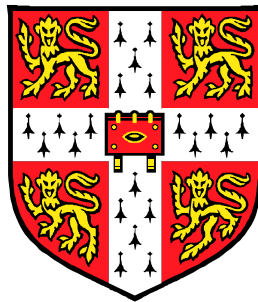


# Focused Ion Beam Fabricated Non-equilibrium Superconducting Devices

*Richard William Moseley*

Darwin College  
Cambridge



A dissertation submitted for the degree of Doctor  
of Philosophy at the University of Cambridge

April 2000

# Summary

## **Focused Ion Beam Fabricated Non-equilibrium Superconducting Devices**

The developments over the last decade in Focused Ion Beam (FIB) instrument technology have reached a point where there is sufficient control of an ion beam to make cuts, trenches, and other shapes in a sample on a scale of tens of nanometers. This work concentrates on the use of an FIB instrument for making superconducting devices. It is shown for the first time that planar-bridge (Nb/Cu/Nb) Superconductor/Normal-metal/Superconductor (SNS) junctions can be reliably fabricated using a standard FIB instrument. This is demonstrated by the responses of junctions to microwaves and magnetic fields; the junctions display the appropriate Josephson behaviour demanded by current technological applications. In addition, the reproducibility in junction behaviour (the variation of critical current is approximately 10%) is the best so far observed for this type of junction. The SNS junction fabrication method has been successfully extended for making high-density SNS junction arrays, dc-SQUIDs, and related devices. A simple model is devised to explain the normal-state resistance and critical current of a junction. The model is based on the geometry of a junction as defined by the FIB instrument and the film deposition. The model is mostly successful in qualitatively explaining many of the geometrical factors that affect the electrical properties of the junction. Nb/Cu/Nb junction series arrays, made using an FIB instrument, are also successfully fabricated. The yield of the junctions forming small arrays is found to be similar to the yield of single junctions. For the series arrays studied here, new observations have been made: the electrical properties of an array have been found to be dependent on the spacing of the junctions and the number of junctions in the array.

This work also investigates the thermal properties of SNS and micron-scale superconductor/insulator/normal-metal junction based devices for use in bolometer device based applications. It is shown that self-heating raises the temperature of the junctions significantly above their operating temperatures. For a device sitting on a low thermally conductive membrane, it is found that the effects of heating, or cooling, in the junctions are exaggerated.

# Preface

This dissertation is submitted for the degree of Doctor of Philosophy in the University of Cambridge. Except where specific reference is made, this work is entirely the result of my own work and includes nothing that is the outcome of work done in collaboration. No part of this work has been or is being submitted for any other qualification at this or any other university. Some of the work contained in this dissertation has been published.

Richard Moseley

*Device Materials Group,*

*Department of Materials Science and Metallurgy,*

*University of Cambridge*

April 2000

I have many people to thank for their help with my research over the last 3 (and a bit) years. Firstly I thank my supervisor, Dr. Mark Blamire, who has shown great patience, and never resorted to giving me a “motivation” talk during my zero-progress moments (months?). I thank Dr. Zoe Barber for helping me with the thin-film deposition systems and clean-room maintenance, the head of the research group, Professor Jan Evetts, and the Department of Materials Science and Metallurgy for providing the laboratory facilities. I have been financially supported by the IRC in Superconductivity and the UK Engineering and Physical Sciences Research Council.

Around the lab there are many people I thank for their good humour and support, especially when I had the all too often “bad research” days. Huge thanks ( $\times 10^\infty$ ) goes to Drs. Gavin Burnell and Wilfred Booij who have helped me “beyond the call of duty” so many times. Thanks to Dr Ed Tarte and Dr. Neil Mathur for all those patient chats with me about superconductivity. Thanks go to all my co-conspirators in the lab: Phil “hamster” McBrien, Noel “mine’s a pint John” Rutter, John “it’s not my round” Durrell, Robert “ding-dong” Kinsey, Neil “transatlantic time” Todd, Robert “nemesis” Hadfield, Steve “doh” Issac,

Adnan “FIB” Latif, Robert “finite analysis” Baranovski, Dolores “thermal-diffusion” Vasquez-Navarro, and all the other members past and present.

Enormous thanks to Darwin College, which has not only been the source of my social life, but has also provided a supportive and learning atmosphere. Several people deserve special mention, without whom Cambridge would have been a duller place. Bruce “trust me” Weir, Vicki “Cranberry juice” Cleave, Pete “rude-boy” Brown, Nicolle “Barbie boatie” McNaughton, Sandy “how are you?” Fung, Rina “Richard, that’s sooo bad!” Knoeff, Helen “cinema?” Pfuhl, Phil “\$90,000” Clarkson, Lori “watch out for my sister” Di-bon, Giudi “that wasn’t very nice, was it Richard?!” Di-bon, Marcus “stroke” Watson, Christy “row harder” Job, John “full metal jacket” Halstead, and Rebecca “coffee-break?” Newby.

Colossal thanks to my house-mates, of three years (is it really that long?!), Mark “Kiwi” Horsburgh and Rob “be good” Harris, who have had to put up with me; apologies for all the times I’ve had a *great*<sup>TM</sup> idea, and made you both listen to it!

Finally, and most importantly, thanks to Mum, Dad, Charlotte, and Splodge. Their love and support, although too rarely acknowledged by me, have been a continuing source of inspiration in my life.

RWM Cambridge, April 2000

# Contents

<b>1. Introduction .....</b>	<b>1</b>
1.1. Background .....	2
1.2. Overview of the work.....	3
1.3. References .....	4
<b>2. Aspects of superconductivity in junction devices.....</b>	<b>5</b>
2.1. Introduction .....	6
2.2. Building blocks of superconductivity .....	6
2.2.1. Historical background .....	6
2.2.2. Ginzburg-Landau theory .....	7
2.2.3. Brief BCS theory.....	8
2.3. Theory and properties of SNS junctions .....	13
2.3.1. The Josephson effect .....	14
2.3.2. The RSJ model .....	17
2.3.3. Magnetic field effects.....	19
2.3.4. Microwave effects .....	20
2.4. Theory and properties of SIN junctions .....	22
2.4.1. Tunneling mechanism .....	22
2.4.2. Current in an SIN junction .....	23
2.4.3. Temperature dependent effects of SIN junctions.....	24
2.5. The proximity effect.....	24
2.5.1. Gor'kov theory .....	26
2.5.2. de-Gennes theory.....	27
2.5.3. McMillan model.....	31
2.5.4. Golubov and Kupriyanov model.....	32
2.5.5. Andreev reflection.....	35
2.6. Review of non-equilibrium superconductivity.....	37
2.6.1. Non-equilibrium quasiparticle and phonon energy distributions.....	37
2.6.2. Quasiparticle recombination .....	39
2.6.3. Knock-on effects of changes in the energy distribution of quasiparticles .....	39
2.6.4. Time Dependent Ginzburg-Landau Theory .....	40

2.7. References .....	43
<b>3. Experimental methods .....</b>	<b>48</b>
3.1. Introduction .....	49
3.2. Substrate Preparation.....	49
3.2.1. Background .....	49
3.2.2. Cleaning .....	50
3.3. Polycrystalline thin film deposition .....	51
3.4. Fabrication of single island SIN junctions .....	54
3.4.1. Base layer definition.....	56
3.4.2. Mesa etch and anodisation .....	56
3.4.3. Wiring layer deposition using lift-off.....	57
3.4.4. Anodisation ring break .....	58
3.5. Fabrication of a silicon nitride membrane.....	58
3.6. The focused ion beam instrument .....	60
3.7. Measurement apparatus.....	64
3.7.1. Devices rig.....	64
3.7.2. Dip probe.....	65
3.7.3. Oxford instruments Heliox™ Instrument.....	66
3.8. References .....	68
<b>4. Using an FIB instrument to fabricate planar-bridge SNS junctions.....</b>	<b>70</b>
4.1. Introduction .....	71
4.2. Fabrication.....	72
4.2.1. Overview .....	72
4.2.2. Early attempts.....	74
4.2.3. Area dose method.....	80
4.3. Summary .....	84
4.4. References .....	84
<b>5. Characterisation of Nb/Cu/Nb junctions .....</b>	<b>86</b>
5.1. Introduction .....	87
5.2. Basic junction characterisation.....	87
5.2.1. Film characterisation .....	87
5.2.2. I-V characteristics of junctions .....	89
5.3. Effect of the junction's geometry on its electrical properties .....	91

5.3.1.	Simple model for the $I_C$ and $R_N$ dependence with the mill time of the trench...	91
5.3.2.	Variation of length .....	94
5.3.3.	Variation of width .....	98
5.3.4.	Variation of the normal-metal thickness .....	101
5.4.	Response to magnetic fields.....	102
5.4.1.	Variation of the mill time.....	103
5.4.2.	Magnetic fields applied in the in-plane directions .....	104
5.4.3.	Variation of width and length.....	104
5.4.4.	Large limit.....	107
5.5.	Temperature dependence of the I-V characteristics.....	108
5.5.1.	$I_C$ and $I_R$ .....	110
5.5.2.	Hysteresis .....	115
5.6.	Comparison with recent results .....	117
5.7.	Summary .....	118
5.8.	References .....	119
<b>6.</b>	<b>Characterisation of Nb/Cu/Nb junction series arrays .....</b>	<b>122</b>
6.1.	Introduction .....	123
6.2.	Background to SNS junction series arrays.....	123
6.2.1.	External phase locking .....	124
6.2.2.	Mutual phase locking .....	125
6.2.3.	Coupling versus disorder.....	129
6.3.	Preliminary studies of junction series arrays.....	129
6.3.1.	Double junction series arrays .....	129
6.3.2.	Small series arrays.....	131
6.3.3.	Large series arrays.....	133
6.4.	Systematic study of double junction series arrays .....	135
6.4.1.	Semi-empirical model of $I_C$ and $R_{ARRAY}$ .....	136
6.4.2.	$I_C$ , $R_{ARRAY}$ , and $I_C R_{ARRAY}$ product dependencies with junction spacing.....	139
6.4.3.	Response to microwaves .....	141
6.4.4.	Magnetic field junction response with junction spacing.....	142
6.5.	Influence of the Nb island in a closely spaced double junction array.....	143
6.5.1.	Prediction and comparison of the I-V characteristics .....	144
6.5.2.	Response to microwaves .....	146

6.5.3. Magnetic field responses.....	146
6.6. Behaviour of closely spaced series arrays.....	148
6.6.1. Semi-empirical model of closely spaced series arrays.....	148
6.6.2. I-V characteristics .....	150
6.6.3. Microwave response.....	151
6.6.4. Magnetic field response .....	151
6.7. Investigation of 3-terminal double junctions .....	152
6.7.1. Method .....	152
6.7.2. Prediction and comparison of the <i>I-V</i> characteristics.....	153
6.7.3. Comparison of coupling mechanisms .....	155
6.8. Summary .....	158
6.9. References .....	158
<b>7. Thermal effects in SNS- and SIN- junction based devices .....</b>	<b>161</b>
7.1. Introduction .....	162
7.1.1. Background .....	162
7.2. Thermal effects in an SIN junction based device.....	163
7.2.1. Theory .....	163
7.2.2. Device fabrication and measurement.....	170
7.2.3. Results and discussion.....	171
7.3. Thermal effects in SNS junction based devices.....	175
7.3.1. Background .....	175
7.3.2. Heater directly and indirectly coupled to a junction .....	178
7.3.3. Electron-phonon coupling at 0.35K.....	179
7.3.4. Heater and junction on a membrane.....	182
7.3.5. Comparison with Morpurgo's hot electron tunable supercurrent device.....	185
7.4. SNS junction dc-SQUIDS.....	186
7.4.1. Design Considerations.....	188
7.4.2. Development work.....	188
7.4.3. Closely spaced junctions dc-SQUID.....	192
7.4.4. Conclusions .....	193
7.5. Summary .....	194
7.6. References .....	194

<b>8. Conclusions .....</b>	<b>198</b>
8.1. Introduction .....	199
8.2. Summary .....	199
8.3. Low $T_C$ junction technology .....	201
8.4. References .....	202
<b>Appendix A. Glossary of Terms.....</b>	<b>203</b>
<b>Appendix B. Conferences Attended and (Un)Published Papers.....</b>	<b>207</b>

# Chapter 1

---

*“There is a theory which states that if ever anyone discovers exactly what the universe is for, and why it is here, it will instantly disappear and be replaced by something even more bizarrely inexplicable.*

*There is another theory which states that this has already happened...”*

Hitchhikers Guide to the Galaxy,  
the BBC radio series, Douglas Adams.

## Introduction

## 1.1. Background

The development of superconducting junctions stems from the work of Giaever and Josephson performed in the early 1960s (Giaever 1960; Josephson 1962). Their independent research earned them the Nobel Prize for physics in 1973.

Giaever described the electrical properties of Superconductor/Insulator/Normal-metal (SIN) junctions, and successfully modeled the flow of current in a junction using an electron tunneling mechanism. Using the model he was able to show that there is an energy gap in a superconductor. SIN junctions have subsequently been extensively investigated because they are a potential candidate for very sensitive bolometer devices, used for applications in astronomy (Booth 1996; Kraus 1996).

Josephson discussed the electrical properties of a junction containing two superconducting electrodes separated by a thin electrical discontinuity. Later, this type of superconducting junction came to be known as a Josephson junction. The electrical properties of a Josephson junction are unique, it is very sensitive to magnetic flux with a resolution of one quantum flux when appropriately positioned in a magnetic field, and it can detect and emit microwaves. These useful properties have many applications, e.g. detectors, mixers, microwave communications, and digital circuits.

One type of junction with Josephson properties is a Superconductor/Normal-metal/Superconductor (SNS) junction. The electrical properties of SNS junctions are difficult to reproduce due to the high sensitivity of the electrical current in a junction to the microstructure and dimensions of the junction. Previously photo-lithographic based techniques were commonly used to pattern junctions. Typically, photolithography has a resolution of 0.5  $\mu\text{m}$ . The resolution is too low to be useful for making reliable planar-type junctions. The excellent control over depositing thin films means, however, that only a stacked SNS junction design can provide suitable junction reliability using photolithography. The drawback of this design, however, is the inherently low impedance of the junction ( $\sim \text{m}\Omega$ ) making them unsuitable for use in many applications. The developments over the last decade in Focused Ion Beam (FIB) instrument technology have reached a point where there is sufficient control of an ion beam to make cuts, trenches, and other shapes in a sample on a scale of  $\sim 10 \text{ nm}$ . For a recent review of this see (Bender 2000). Using an FIB instrument to pattern planar type SNS junctions should increase the reliability of the junctions, and provide an alternative form of SNS junction for use in applications. The majority of the work

presented here focuses on the fabrication and characterisation of planar-bridge low  $T_C$  SNS junctions and related devices using an FIB instrument. For bolometer based applications, work is also presented describing the heating processes that occur in electrically biased SIN and SNS junctions.

## 1.2. Overview of the work

The primary aim of this work is to show how an FIB instrument can be used to make reliable sub-micron scale SNS planar-bridge junctions and related devices. The secondary aims are: understanding the electrical behaviour of planar-bridge SNS junctions and SNS junction devices made using an FIB instrument and; understanding the thermal properties of SIN- and SNS- junction based devices for use in bolometer device applications.

Chapter 2 presents a brief introduction to various aspects of the theory appropriate to superconducting junction devices and concentrates on the principal concepts used in this thesis. These include a brief description of the phenomenological and microscopic theories of superconductivity, the electrical properties of SNS and SIN junctions, the proximity effect, and important aspects of non-equilibrium superconductivity.

Chapter 3 describes the experimental methods and equipment used. The preparation and deposition of the thin-films used for making SNS and SIN junctions are the subjects of the first part of the chapter. The second part describes the fabrication route used for making a SIN junction based device. The third part describes the fabrication of silicon nitride membranes, used for making SIN- and SNS-junction based devices. The fourth part presents an introduction to the use and operation of an FIB instrument. The final part describes the equipment used to measure the devices discussed in this work.

Chapter 4 describes the fabrication of an SNS junction using an FIB instrument. The chapter describes the development of the fabrication route, and the improvements to the methods that were made. Finally, an assessment of the reproducibility is made of the electrical properties of the junctions.

Chapter 5 presents the work characterising (Nb/Cu/Nb) SNS junctions made using the fabrication route described in chapter 4. The first part of the chapter compares the current-voltage ( $I$ - $V$ ) characteristics of the junctions with the resistively shunted junction model. The second part compares a model of the critical current and normal-state resistance of a junction based on the dimensions of the junction with experiment. The third part compares the responses of junctions to an applied magnetic field with two models. The

fourth part investigates the temperature dependencies of certain features observed in the  $I$ - $V$  characteristics. The final part compares the work presented here with the work using the latest developments in junction manufacturing.

Chapter 6 extends the work reported in chapters 4 and 5 by demonstrating that high-density (Nb/Cu/Nb) SNS junction arrays can be made using an FIB instrument. The first part presents a background to junction array theory and describes the various mechanisms that can electrically couple junctions together. The second part describes the work showing that small and large junction arrays can be made using an FIB instrument. The third part describes a systematic study of the junction spacing dependence with the electrical properties of the array. The fourth part compares the electrical properties of closely spaced junctions with similar long junctions. The final part compares the electrical properties of two closely spaced junctions with two widely spaced junctions using three terminal measurements.

Chapter 7 discusses the thermal properties of SIN- and SNS- junction based devices. The first part of the chapter presents work comparing the heat flow in a SIN junction based device sitting on a substrate and a thermally insulating membrane. The second part presents the work discussing the thermal properties of SNS junction made using an FIB instrument. The final part describes the development of a dc-SQUID based bolometer using an FIB instrument.

Chapter 8 discusses the major conclusions made in this work and their implications for further work.

### 1.3. References

H. Bender (2000). "Ions beams focus on semiconductor devices." *Vacuum Solutions*(14 (April 2000)) 11.

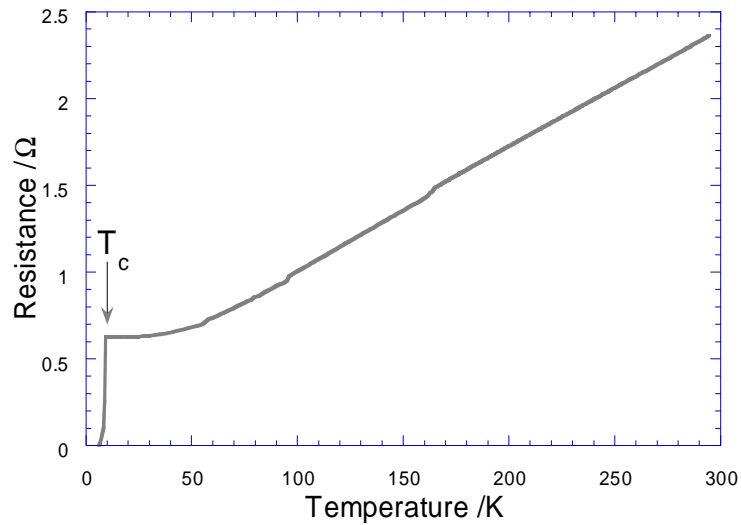
N. E. Booth and D. J. Goldie (1996). "Superconducting Particle Detectors." *Superconductor Science & Technology* **9**(7) 493.

I. Giaever (1960). *Physical Review Letters* **5** 147.

B. D. Josephson (1962). *Physics Letters* **1** 251.

H. Kraus (1996). "Superconductive Bolometers and Calorimeters." *Superconductor Science & Technology* **9**(10) 827.

# Chapter 2



Graph of the resistance of a Nb/Cu track versus temperature showing the transition from its normal state at high temperatures to superconducting state at low temperatures.

## Aspects of superconductivity in junction devices

## 2.1. Introduction

To explain all aspects of superconductivity in junction devices would be prohibitive and, in all probability, a waste of resources; there are copious amounts of materials, in which the reader can find an in-depth analysis of current theories. The author has found, however, the following books that are most useful for understanding superconductivity and its applications: Tinkham (Tinkham 1996), Waldram (Waldram 1996), and Gray (Gray 1981).

The aim of this chapter therefore, is to provide all the background theory that is needed for analysing the experimental work described in later chapters. It also serves to provide the historical context for this work, giving an up-to-date history of the development of superconducting junction devices.

## 2.2. Building blocks of superconductivity

### 2.2.1. Historical background

Superconductivity is a phenomenon that has long held the imagination of not just scientists and engineers, but also the general public. It was discovered in 1911 by Kamerlingh Onnes (Onnes 1911) at Leiden when its best-known property was discovered, the disappearance of electrical resistance in certain materials, normally metals, below a critical temperature. These materials are now known as the low  $T_C$  superconductors. During the 19<sup>th</sup> Century great advances in the understanding of electromagnetism were made, although no prediction about superconductivity was ever made. This did not delay its discovery however, because the phenomenon only occurs at low temperatures that were not obtainable until 1908 when liquefied helium was first produced, also by Onnes. It was the development of cryogenic techniques therefore, that was responsible for the discovery of superconductivity. In 1933 Meissner and Ochsenfeld discovered that superconductors could expel any magnetic field, below a critical magnetic field strength, thus demonstrating the perfect diamagnetic property of a superconductor. This important discovery distinguishes a superconductor from a perfect conductor.

The first serious attempt to model the electrodynamics of a superconductor was made by the London brothers in 1935 (London 1935). This was followed by the very successful model made by Ginzburg and Landau (Ginzberg 1950), which was based on Landau's general theory of second order phase transitions. These attempts used phenomenological

models rather than microscopic theory, and it was not until 1957 that Bardeen, Cooper, and Schrieffer (BCS) produced a successful microscopic model for superconductivity (Bardeen 1957).

In 1987 superconductivity was discovered in some ceramic-like materials, the so-called ‘high temperature superconductors’ due to their high critical temperatures. BCS theory could not explain their properties, and subsequently, a vast amount of research has been geared towards explaining their behaviour. Today, there is no theory that adequately explains their properties.

This study focuses on the transport of electrons through heterogeneous superconductors and normal-metals. The relevant approaches that are best suited for explaining their electro-dynamical properties are based upon the phenomenological model of Ginzburg-Landau and the microscopic theory of BCS, which are discussed in the following sections.

### 2.2.2. Ginzburg-Landau theory

Ginzburg-Landau theory is based upon the premise that a spatially varying complex order parameter in a material can be represented by a single waveform,  $\psi(\mathbf{r})$ .  $|\psi^* \psi|$  represents the local density of superconducting electrons,  $n_s(\mathbf{r})$ . It was then postulated that if  $\psi$  is small and varies slowly in space, the free energy density,  $G_L$ , can be expanded in a series of the form

$$G_L = G_{N0} + \int_V \left[ \alpha_L \psi^* \psi + \frac{\beta_L}{2} (\psi^* \psi)^2 + \frac{\hbar^2}{2m} \left| \left( \nabla - \frac{2e}{\hbar} \mathbf{A} \right) \psi \right|^2 \right] dV + \int \frac{1}{2\mu_0} (\mathbf{B} - \mathbf{B}_E)^2 dV \quad (2.1)$$

where  $\mathbf{A}$  is the vector potential,  $G_{N0}$  is the free energy of the normal state at the same temperature,  $\alpha_L$  and  $\beta_L$  are Landau parameters,  $m$  is the mass of a charge carrier, and  $\mu_0$  is the permeability of free space. The first three terms correspond to the free energy in a field-free homogeneous superconductor and the fourth term is the kinetic energy associated with changes in the pair potential and the magnetic field. The last term is the magnetic self-energy of the supercurrents where  $\mathbf{B}$  is the net field and  $\mathbf{B}_E$  is the externally applied field. In order to determine the equilibrium state of the superconductor it is necessary to minimise  $G_L$  with respect to arbitrary small changes  $d\psi_{GL}(\mathbf{r})$ . This produces the following equation,

$$\frac{1}{2m} (-i\hbar \nabla + 2e\mathbf{A})^2 \psi + (\alpha + \beta \psi^* \psi) \psi = 0. \quad (2.2)$$

This equation is known as the 1<sup>st</sup> Ginzburg-Landau equation and it has the following boundary condition,

$$(-i\hbar\nabla_N + 2e\mathbf{A}_N)\psi = 0, \quad (2.3)$$

where  $\nabla_N$  is a component normal to the surface. Taking into account the presence of magnetic fields and knowing that the supercurrent density,  $\mathbf{J}_S$ , is

$$\mathbf{J}_S = \nabla \wedge \frac{\mathbf{B}}{\mu_0}, \quad (2.4)$$

the second Ginzburg-Landau equation is obtained,

$$\mathbf{J}_S = \frac{ie\hbar}{m}(\psi^*\nabla\psi - \psi\nabla\psi^*) - \frac{4e^2}{m}\mathbf{A}\psi^*\psi \quad (2.5)$$

The fact that  $\psi$  is assumed to only vary slowly means the equation can only be used in non-uniform situations near the superconductor's critical temperature,  $T_C$ . Although the theory of Ginzburg-Landau does give information about the macroscopic properties of a superconductor, it does not give information about its microscopic properties, and presents a significant drawback to the model. It is successful however, in predicting the supercurrent density in an SNS junction (described in sections 2.5.2 and 2.6.4) and to predict the existence of the mixed state of Type II superconductors where normal regions co-exist with superconducting regions.

### 2.2.3. Brief BCS theory

#### 2.2.3.1. Concept

The basis for understanding the microscopic behaviour of the low temperature superconductors, used in this work, is the BCS microscopic theory of superconductivity (Bardeen 1957). The theory centres on the premise that if an attractive potential existed between two electrons and they were placed in the presence of a Fermi sphere of electrons, then they would exist in a bound state, even if the potential were too weak to hold them had they been isolated. The Fermi sea of unbound electrons in this case serves to prohibit the two bound electrons from occupying states with wavenumber  $\mathbf{k}$  less than the Fermi wavenumber,  $\mathbf{k}_F$ , thus, stabilising the bound state irrespective of how weakly attractive the interaction is.

Below a critical temperature,  $T_C$ , electrons whose energies are within a certain range of the Fermi energy,  $E_F$ , will experience an attractive interaction potential. This is created by a phonon mediated attractive electron-electron interaction, which overcomes the repulsive

Coulomb interaction of the electrons. The electrons condense into pairs, named Cooper pairs, and are ordered in momentum space and reduce their overall energy. Each pair has equal and opposite spins  $\mathbf{k}_\uparrow, -\mathbf{k}_\downarrow$ . The approximation is made that the interaction potential ( $V_{\mathbf{k}\mathbf{k}'}$ ) is equal to a negative constant,  $-V_I$ , for all states  $\mathbf{k}, \mathbf{k}'$  with energy  $\varepsilon_{\mathbf{k}}, \varepsilon_{\mathbf{k}'}$  less than a cut-off energy,

$$\varepsilon_C = \hbar\omega_C - E_F, \quad (2.6)$$

where  $\omega_C$  is the Debye frequency.  $V_{\mathbf{k}\mathbf{k}'}$  is zero for other states. Using this approximation the probability of pair occupation of a state  $\mathbf{k}$  in the superconducting ground state,  $v_{\mathbf{k}}^2$ , can be found,

$$v_{\mathbf{k}}^2 = \frac{1}{2} \left( 1 - \frac{\varepsilon_{\mathbf{k}}}{E_{\mathbf{k}}} \right). \quad (2.7)$$

$\varepsilon_{\mathbf{k}}$  is calculated from the Bloch energy relation,

$$\varepsilon_{\mathbf{k}} = \frac{\hbar^2}{2m} (\mathbf{k}^2 - \mathbf{k}_F^2), \quad (2.8)$$

and

$$E_{\mathbf{k}}^2 = \Delta^2 + \varepsilon_{\mathbf{k}}^2 \quad (2.9)$$

where,

$$\Delta = V_I \sum_{\mathbf{k}} v_{\mathbf{k}} \sqrt{1 - v_{\mathbf{k}}^2}. \quad (2.10)$$

The energy required to excite an electron from the ground state to a state  $\mathbf{k}$  is given by  $E_{\mathbf{k}}$ . The relationship between  $E_{\mathbf{k}}$  and  $\mathbf{k}$  is shown in figure 2.1. It shows that the minimum energy required to create an excitation is  $\Delta$  and therefore, a gap in the excitation spectrum of magnitude  $\Delta$  is produced. Commonly  $\Delta$  is known as the energy-gap of a superconductor. The spatial variation of  $\Delta$  is known as the pair potential,  $\Delta_P(\mathbf{r})$ .

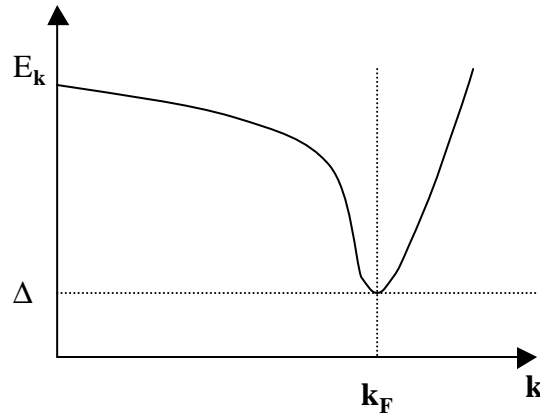


Figure 2.1: Energy-momentum diagram for excitations in a superconductor.

### 2.2.3.2. Quasiparticles

In a superconductor, electron-like and hole-like excitations are found. These are known as quasielectrons and quasiholes, respectively. Their nature is, however, different to any other excitations found in normal-metals and semiconductors. Given that the ground state involves the condensation of single electrons into pair states, it follows that the excitations involve the reverse of this process. A single quasiparticle excitation can be defined as an excitation that involves  $\mathbf{k}\uparrow$  being occupied with probability 1, i.e. a full state, and  $-\mathbf{k}\downarrow$  being occupied with probability 0, i.e. an empty state. Figure 2.2a shows the probability of pair occupation of state  $\mathbf{k}$ , given by equation 2.7, and figures 2.2b and c shows the two distinct types of excitation that can occur from the superconducting ground state. The quasielectron excitation is shown in figure 2.2b. Here a pair is removed from  $\mathbf{k}_e\uparrow$  and  $-\mathbf{k}_e\downarrow$ , and creating an excitation at  $\mathbf{k}_e$ , where  $\mathbf{k}_e > \mathbf{k}_F$ . The empty state created at  $-\mathbf{k}_e\downarrow$  has negligible effect since  $v_k^2$  is nearly zero here. The excitation at  $\mathbf{k}_e\uparrow$  has changed the occupation probability there from nearly zero to unity. This type of excitation, therefore, has strong electron-like properties, hence its name. Similarly, the quasihole excitation is formed when  $\mathbf{k}_h$  is less than  $\mathbf{k}_F$ , shown in figure 2.2c. The empty state at  $\mathbf{k}_h\uparrow$  has negligible effect since  $v_k^2$  is approximately unity here. The creation of an empty state at  $-\mathbf{k}_h\downarrow$  has changed the occupation probability from nearly 1 to 0 thus, creating an excitation with strong hole-like properties.

If the quasiparticle excitation is at  $\mathbf{k}_F$  it is between the electron-like and hole-like branches and so it will have a mixed character. It is these excitations, known as quasiparticles, which are commonly found in superconductors.

Quasiparticles are fermions and there is one-to-one correspondence between the electron states in a normal-metal and the quasiparticle states in the superconductor. Thus,

$$N_S(E)\delta E = N_N(\varepsilon)\delta\varepsilon, \quad (2.11)$$

where  $N_S$  and  $N_N$  are the superconducting and normal densities of states, respectively. Substituting from equation 2.9 into equation 2.11 gives:

$$N_S(E_{\mathbf{k}}) = N(0) \frac{E}{\sqrt{E^2 - \Delta^2}} \begin{cases} E_{\mathbf{k}} > \Delta \\ E_{\mathbf{k}} < \Delta \end{cases}, \quad (2.12)$$

$$N_S(E_{\mathbf{k}}) = 0$$

where  $N(0)$  is the density of states at the Fermi surface. A convenient model when considering the behaviour of quasiparticles in a superconductor is the so-called

semiconductor representation. This uses the relatively obvious analogies between quasiholes and quasielectrons and the holes and electrons in a semiconductor. The superconductor is represented as an ordinary intrinsic semiconductor with a band-gap equal to twice the energy gap  $\Delta$ . The density of states is given by equation 2.12 and the results are shown in figure 2.3. Conventionally, the quasiholes are shown in the bottom half of the diagram, though they have positive excitation energy like the quasielectrons and increasing the energy scales as the distance from the Fermi energy in the diagram. The semiconductor representation is a model of the tunneling of quasiparticles and is only valid when the electron distributions in the superconductor are not significantly perturbed. A large degree of caution must be applied before using the semiconductor model in situations far from equilibrium.

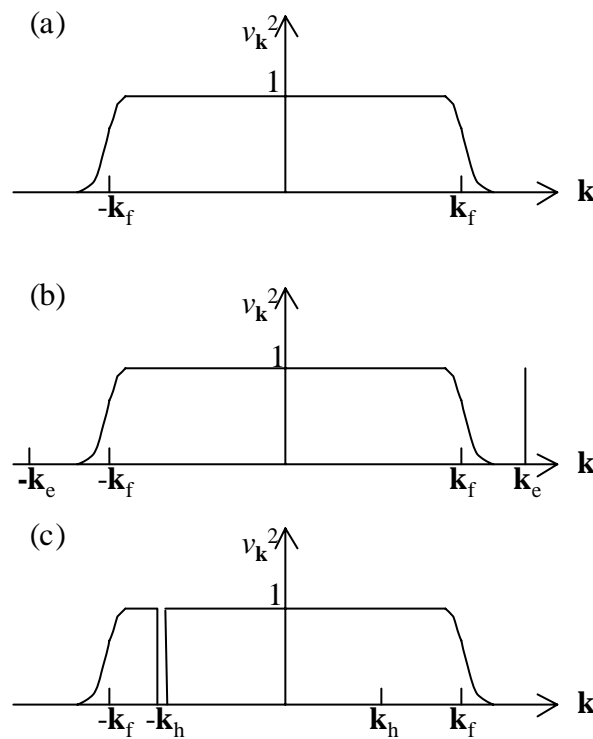


**Figure 2.2:** (a) Ground state probability of pair occupation of a state  $k$  ( $v_k^2$ ). (b) An electron-like excitation from the ground state. (c) A hole-like excitation from the ground state.

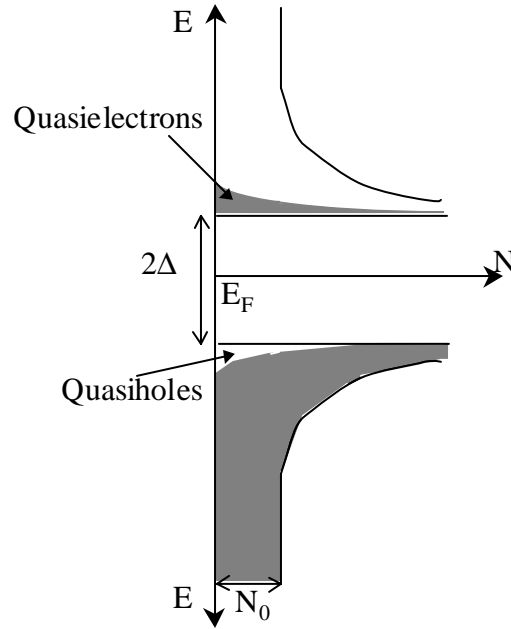


**Figure 2.3: The semiconductor representation of the quasiparticle density of states in a superconductor (i.e. hole-like states shown in the lower half of the diagram in spite of their positive excitation energy).**

### 2.2.3.3. Thermal effects

For  $T > 0$  K the presence of thermally excited quasiparticles modifies the value of the energy gap such that

$$\Delta = V_I \sum_{\mathbf{k}} v_{\mathbf{k}} \sqrt{1 - v_{\mathbf{k}}^2} (1 - 2f_{\mathbf{k}}) \quad (2.13)$$

where  $f_{\mathbf{k}}$  is the Fermi function. By replacing the discrete states  $\mathbf{k}$  with the continuous density of states (equation 2.12) the BCS gap equation is obtained,

$$\frac{1}{N_0 V_I} = \int_{\Delta}^{\hbar\omega_c} \frac{(1 - 2f_{\mathbf{k}}(E))}{\sqrt{E^2 - \Delta^2}} dE, \quad (2.14)$$

where the product of  $N_0 V_I$  gives the strength of the electron-phonon coupling,  $\lambda$ . For weak coupling, in the limit of  $N_0 V_I \ll 1$  the gap equation can be solved to derive the relationship between  $\Delta$  at  $T=0$  K and  $T_C$ ,

$$2\Delta_{(0)} = 3.52 k_B T_C, \quad (2.15)$$

where  $k_B$  is the Boltzmann constant.

## 2.3. Theory and properties of SNS junctions

SNS junctions belong to a subset of the Josephson class of junction, so-called because they exhibit the Josephson effect (see below). SNS junctions have distinct advantages over other types of Josephson junctions due to their non-hysteretic, and high current density nature. They can be used for diverse applications including interferometric logic elements (Morpurgo 1997), Superconducting QUantum Interference Devices (SQUIDs) (Pauza 1993), Single Flux Quantum logic devices (Likharev 1996), junction arrays for the voltage standard (Burroughs 1999) and for high frequency radiation sources (Wan 1989).

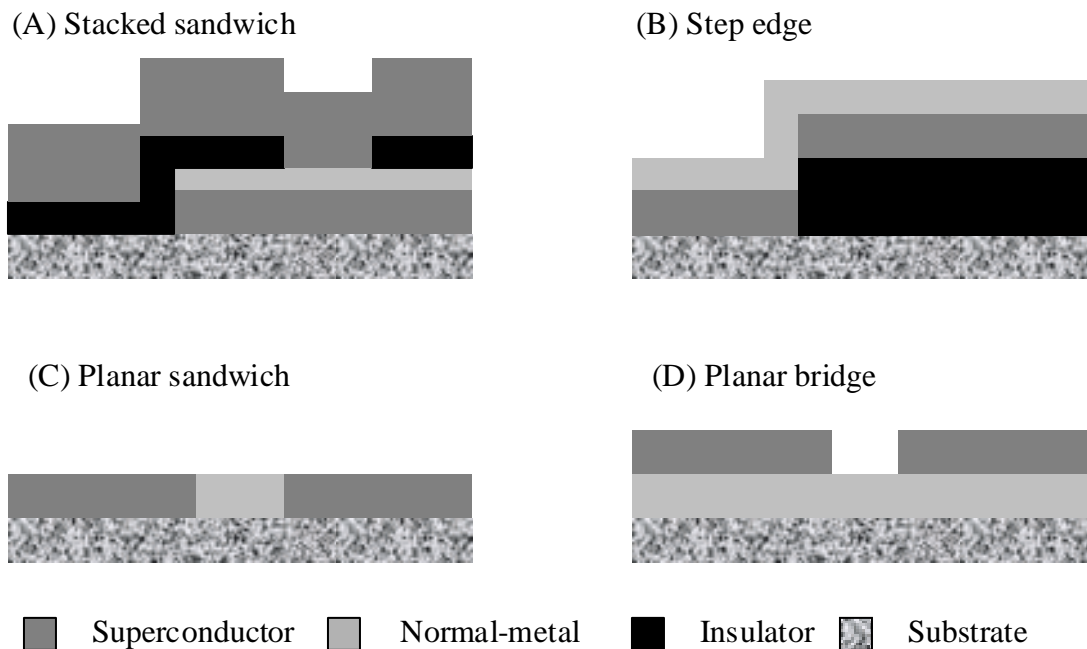


Figure 2.4: Four types of SNS junctions

Research into Josephson junctions started in earnest in the mid-1960s after Josephson's theoretical predictions (Josephson 1962). Initially, research concentrated on the Superconductor/Insulator/Superconductor (SIS) and weak-link superconductor (ScS) junction types. It was not until 1969 that Clarke performed the first study of SNS junctions (Clarke 1969). This study verified that the Josephson effect was present in SNS junctions made in Pb/Cu/Pb thin-film sandwiches. A simplified model using the de-Gennes theory of the proximity effect, detailed in section 2.5.2, was successfully used to quantitatively account for their behaviour. Other structures of SNS junctions were also fabricated and studied. These can be sub-divided into four types: stacked sandwich; step edge; planar sandwich; and planar bridge. Figure 2.4 shows a schematic diagram of each type. Today, the

most common structure used is the sandwich type because of its high reliability. Typically, Nb is used as the superconductor because of its relatively high critical temperature and stability.

Although sandwich type junctions have been fabricated with reproducible electrical properties, their inherently low impedance ( $\sim 1 \text{ m}\Omega$ ) has made them unsuitable for most applications. SIS sandwich junctions are therefore, often favored instead. They can be designed to order through commercial companies, e.g. HYPRES Inc, but their hysteretic Current-Voltage ( $I$ - $V$ ) characteristics are a serious drawback in many applications. The trade-off between hysteresis and low impedance can be difficult so research was carried out, mainly in the late 1970s, into producing high impedance and reliable SNS structures. To-date the edge (Morpurgo 1998) and combined sandwich (Seto 1971) structures do not appear to offer sufficient reproducibility. Suitable planar junctions have been made using electron beam (Hirose 1997), ion beam (Harris 1977), x-ray (Blocker 1978), chemical wet etch, and plasma etch (Vandover 1981) techniques, but in all cases their reproducibility is poor. This is largely due to the high sensitivity of the Josephson current to the microstructure and dimensions of the normal-metal barrier. The difficulty of fabricating reproducible planar SNS junctions is an important reason why they have not been exploited in a wider range of applications.

### 2.3.1. The Josephson effect

In 1962 Josephson (Josephson 1962) predicted phenomena that can only occur at a discontinuity in a superconducting structure where the Cooper pairs can not occupy. The phenomena can be observed experimentally in a variety of superconducting structures where an electrical discontinuity is in series with two superconductors. These can be classed into one of four types: tunnel barrier; normal-metal; semi-conductor; and weak-link superconductor. The Josephson effect arises from Cooper pairs being transferred across the discontinuity. The approach used here to describe the Josephson effect is from Feynmann (Feynman 1965).

Consider the macroscopic wave function of Cooper pairs in a superconductor,  $SC_1$ , given by

$$\Psi = |\Psi(r)| \exp \left[ i \left( \theta_{(r)} - \left( \frac{2E_F}{\hbar} \right) t \right) \right], \quad (2.16)$$

where  $\theta(r)$  is the phase and  $t$  is time. As a second superconductor,  $SC_2$ , is brought closer to  $SC_1$  both wavefunctions penetrate the barrier sufficiently to couple with each other. The overall energy of the system is then reduced by the coupling. If the energy from the coupling exceeds the thermal fluctuation energy, the phases of the wavefunctions become locked and pairs pass from one superconductor to the other. The time evolution of the wave functions of the coupled superconductors for each superconductor are described by the Josephson relations:

$$i\hbar \frac{\partial \Psi_1}{\partial t} = U_1 \Psi_1 + K \Psi_2 \quad (2.17)$$

$$i\hbar \frac{\partial \Psi_2}{\partial t} = U_2 \Psi_2 + K \Psi_1. \quad (2.18)$$

$U_I$  represents the energy of the wave function of the superconductor and  $K$  represents the coupling constant that is a measure of the interaction of the 2 wave functions. Applying a voltage,  $V$ , across the two superconductors gives an energy difference of

$$e^* (V_2 - V_1) = e^* V, \quad (2.19)$$

so

$$U_2 - U_1 = e^* V. \quad (2.20)$$

Here  $e^*$  represents the total charge of a Cooper pair, i.e.  $e^* \equiv 2e$ . Taking the zero energy of the system to be midway between the energies  $U_1$  and  $U_2$  then equations 2.17 and 2.18 become

$$i\hbar \frac{\partial \Psi_1}{\partial t} = -\frac{e^* V}{2} \Psi_1 + K \Psi_2 \quad (2.21)$$

$$i\hbar \frac{\partial \Psi_2}{\partial t} = -\frac{e^* V}{2} \Psi_2 + K \Psi_1 \quad (2.22)$$

Since the pair density,  $n_s$ , is equal to  $|\Psi^* \Psi|$ , rewriting the wavefunction in terms of  $n_s$  gives

$$\Psi = (n_s)^{\frac{1}{2}} \exp(i\theta) \quad (2.23)$$

So substituting equation 2.23 into equations 2.21 and 2.22, separating the real and imaginary parts, and finally introducing the phase difference across the junction as  $\phi = \theta_2 - \theta_1$ , the following relations are obtained:

$$\frac{\partial n_{s1}}{\partial t} = \frac{2}{\hbar} K (n_{s1} n_{s2})^{\frac{1}{2}} \sin \phi \quad (2.24)$$

$$\frac{\partial n_{s2}}{\partial t} = -\frac{2}{\hbar} K (n_{s1} n_{s2})^{\frac{1}{2}} \sin \phi \quad (2.25)$$

$$\frac{\partial \theta_1}{\partial t} = -\frac{K}{\hbar} \left( \frac{n_{S2}}{n_{S1}} \right)^{\frac{1}{2}} \cos \phi + \frac{e^* V}{2\hbar} \quad (2.26)$$

$$\frac{\partial \theta_2}{\partial t} = -\frac{K}{\hbar} \left( \frac{n_{S1}}{n_{S2}} \right)^{\frac{1}{2}} \cos \phi - \frac{e^* V}{2\hbar} \quad (2.27)$$

Equations 2.24 and 2.25 shows that the rate of decrease of the pair density in one superconductor is the negative of the other.

In the case where both superconductors are the same thus  $n_{S1} = n_{S2} = n_S$ , and where the density of Cooper pairs in the superconductors do not change significantly with time so  $n_{S1}$  and  $n_{S2}$  remain close to the constant equilibrium value. Taking equation 2.24 from 2.25 gives:

$$\frac{\partial n_{S1}}{\partial t} = \frac{2K}{\hbar} n_S \sin \phi = -\frac{\partial n_{S2}}{\partial t}. \quad (2.28)$$

This means that there is a net flow of Cooper pairs across the junction that depends on the phase difference between the two superconductors. Multiplying equation 2.28 with the charge of a Cooper pair and an effective distance into the electrode the dc Josephson equation for the supercurrent density ( $J$ ) through the junction is obtained,

$$J = J_C \sin \phi. \quad (2.29)$$

$J_C$  gives the maximum supercurrent density that the junction can sustain before entering the finite voltage state.

The ac Josephson equation can be obtained by substituting the expansion in equation 2.26 from equation 2.27, giving the following relation for the rate of change of the phase difference between the two superconductors:

$$\frac{\partial \phi}{\partial t} = \frac{2e}{\hbar} V. \quad (2.30)$$

This means that when a constant voltage difference is present across the Josephson junction, the phase difference increases linearly with time. Substituting equation 2.30 into equation 2.29 gives:

$$J = J_C \sin \left( \frac{2e}{\hbar} Vt + \phi_0 \right). \quad (2.31)$$

The dc voltage across the junction results in an ac supercurrent density with a frequency ( $f$ ) that is proportional to the applied voltage, i.e.

$$f = \frac{2e}{\hbar}V. \quad (2.32)$$

The reciprocal of the proportionality constant is  $\hbar/2e$ , and the flux quantum constant ( $\Phi_0$ ) is equal to  $2.0679 \times 10^{-15}$  Wb.

At low voltages an extremely high frequency ac current transverses the junction. This relation intertwines frequency and voltage and therefore, the Josephson junction can be utilised in the international standardisation of the Volt.

### 2.3.2. The RSJ model

The Resistively Shunted Junction (RSJ) model derives the  $I$ - $V$  characteristics of a Josephson junction where the weak link is a normal-metal, a conductor that does not superconduct. Stewart (Stewart 1968) and McCumber (McCumber 1968) independently formulated the RSJ model. The model is based on a lumped circuit that consists of an ‘ideal’ SIS-type junction that is placed electrically in parallel with an ohmic resistor ( $R_N$ ), shown schematically in figure 2.5. The full model also includes a capacitor, to include the effects of junction capacitance, but this has been neglected because they are not present in this work.

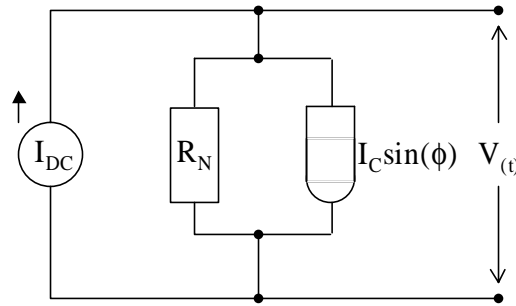


Figure 2.5: The equivalent circuit used in the RSJ model.

Assuming the circuit is dc current biased, commonly the case due to the low impedance of Josephson junctions making measurements involving voltage biasing noisy, the total bias current ( $I$ ) in the absence of noise is the sum of the ac Josephson current and the dc Josephson current or

$$I = \frac{\Phi_0}{2\pi R_N} \frac{d\phi}{dt} + I_C \sin \phi. \quad (2.33)$$

This can be rewritten as a dimensionless equation:

$$\frac{I}{I_C} = \frac{d\phi}{d\theta} + \sin \phi, \quad (2.34)$$

where

$$\theta = \omega_J t \quad (2.35)$$

$$\omega_J = \frac{2\pi}{\Phi_0} I_C R_N. \quad (2.36)$$

For the case where the current is less than the critical current of the junction, i.e.  $I < I_C$ ,  $\phi$  is independent of time so  $V=0$ . However, for  $I > I_C$   $\phi$  changes with time as does  $V$ . To find the time averaged voltage  $\langle V(t) \rangle$  across the junction equation 2.34 is rewritten as

$$d\theta = \frac{d\phi}{\frac{I}{I_C} - \sin \phi} \quad (2.37)$$

Equation 2.37 is integrated, then rearranged to solve for  $\phi(t)$  to give:

$$\phi(t) = 2 \tan^{-1} \left\{ \sqrt{1 - \left(\frac{I_C}{I}\right)^2} \tan \left( \frac{\omega_J t \sqrt{\left(\frac{I}{I_C}\right)^2 - 1}}{2} \right) + \frac{I_C}{I} \right\} \quad (2.38)$$

This equation is similar to the description of an oscillatory driven pendulum system so  $\phi(t)$  and hence,  $V(t)$  are periodic with a period,  $T$ , giving

$$T = \frac{2\pi}{\omega_J \sqrt{\left(\frac{I}{I_C}\right)^2 - 1}} \quad (2.39)$$

and the time averaged voltage is

$$\langle V(t) \rangle = \frac{1}{T} \int_0^T V(t) dt = \frac{\Phi_0}{2\pi T} [\phi(T) - \phi(0)]. \quad (2.40)$$

Substituting expressions for  $\phi(T)$  and  $\phi(0)$   $\langle V(t) \rangle$  is simply expressed as

$$\langle V(t) \rangle = I_C R_N \sqrt{1 - \left(\frac{I_C}{I}\right)^2} \quad \text{for } I > I_C. \quad (2.41)$$

This equation clearly shows the importance of the  $I_C R_N$  product since it determines the ac voltage amplitude at a given operating frequency. Figure 2.6 shows the simulated  $I$ - $V$  characteristics of the junction in the lumped circuit. At high bias the gradient of the curve asymptotically approaches  $R_N$ .

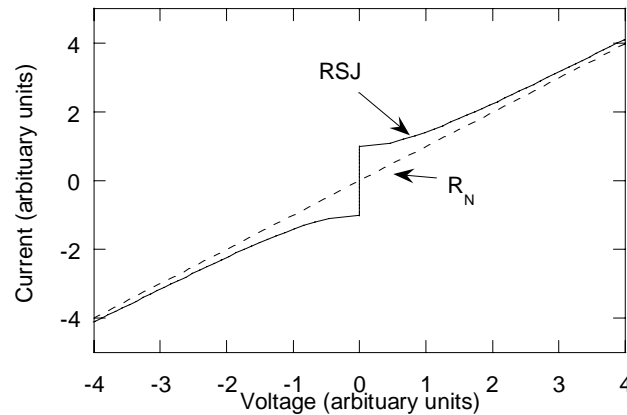


**Figure 2.6: The simulated I-V characteristics predicted by the RSJ model showing that at high bias the model approaches asymptotically the Ohmic line.**

### 2.3.3. Magnetic field effects

When a magnetic field is applied in the direction perpendicular ( $z$ ) to the plane of the supercurrent flow in the junction ( $x,y$ ) the phase difference in the Josephson junction will not only be dependent on time (see above), but also on the local strength of the magnetic field. To analyse this situation it is necessary to first consider whether the supercurrent is uniformly distributed across the width of the junction at zero applied field. If the supercurrent is not evenly distributed across the width of the junction then the junction is considered to be in the *large* limit where the magnetic fields caused by this redistribution would have to be considered (Booij 1997). If the supercurrent is uniformly distributed over the width of the junction then it is in the *small* limit. The cross-over from the small to the large limit occurs when the junction width becomes comparable to the Josephson penetration depth,  $\lambda_J$ . The junction's behaviour in the large limit will be investigated in chapter 5.4.4. Here, only junctions in the small limit are examined.

Consider an applied static magnetic field ( $B$ ) in the  $z$ -direction where the superconducting electrodes are sufficiently thick that screening currents can be neglected (this is not strictly accurate for the thin film junctions studied here and will be discussed in further detail in chapter 5.4). The phase across the junction dependence with the applied magnetic field is found by applying Stoke's law on a small rectangular region crossing the junction barrier so

$$\frac{\partial \theta}{\partial x} = \frac{2\pi\mu_0}{\Phi_0} d' H_z(x). \quad (2.42)$$

where  $H$  is the magnetic field strength, and  $d'$  is the junction's magnetic thickness (the length over which the magnetic field penetrates the barrier and superconducting electrodes in the perpendicular direction to the junction width). In the case of a constant magnetic field equation 2.42 can be integrated and substituted into equation 2.29 to obtain the dependence of the supercurrent density on the applied magnetic field (Barone 1982)

$$J(x) = J_0 \sin\left(\frac{2\pi d'}{\Phi_0} H_z x + c\right), \quad (2.43)$$

where  $c$  is an integration constant.

$I_C$  at a given magnetic field can be found by integrating equation 2.43 with respect to  $x$  and varying the start phase  $\theta(x=0)$  to find its optimal value. This results in the following dependence

$$I_{(\Phi/\Phi_0)} = I_{C(0)} \left| \frac{\sin\left(\frac{\pi\Phi}{\Phi_0}\right)}{\frac{\pi\Phi}{\Phi_0}} \right|. \quad (2.44)$$

Note, there are successive minima for  $I_C(H_z)$  when an integer number of flux quanta are introduced in the junction barrier.

#### 2.3.4. Microwave effects

When a Josephson junction is irradiated with microwaves a current is produced across the junction. The electrons from this current will phase lock with the Josephson supercurrent at certain frequencies. This is observed as a step in the junction's  $I$ - $V$  characteristics. To model them consider the case where the junction is voltage biased (the current biasing case is complicated and will be discussed qualitatively later). The applied time varying voltage is given by

$$V(t) = V_0 + V_{rad} \cos(\omega_s t), \quad (2.45)$$

where  $\omega_s$  is the angular frequency of the radiation,  $V_{rad}$  is the voltage across the junction due to the radiation, and  $V_0$  is a constant. By integrating equation 2.45  $\phi(t)$  is

$$\phi(t) = \phi_0 + \omega_0 t + \left(\frac{2eV_{rad}}{\hbar\omega_s}\right) \sin(\omega_s t). \quad (2.46)$$

$\phi_0$  is a constant of integration. Substituting equation 2.46 into equation 2.29 produces:

$$J_S = J_C \sum (-1)^n J_n \left( \frac{2eV_{rad}}{\hbar\omega_S} \right) \sin[\phi_0 + \omega_0 t - n\omega_S t] \quad (2.47)$$

This only contributes a dc component when  $\omega_0 = n\omega_S$  so current spikes are seen in the  $I$ - $V$  characteristics at:

$$V_{rad} = \frac{n\hbar\omega_S}{2e}. \quad (2.48)$$

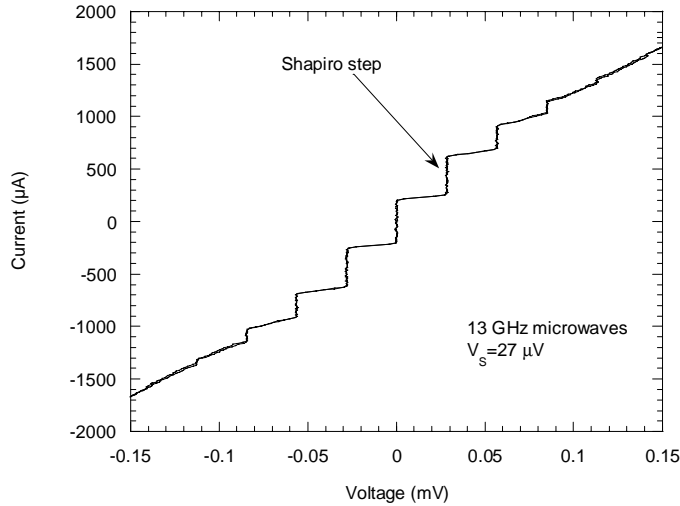


**Figure 2.7: Experimental  $I$ - $V$  characteristics of a Josephson junction showing Shapiro steps. The step interval ( $V_S$ ) is  $27 \mu\text{V}$ .**

For the current driving source case, used in this work, the resulting nonlinear differential equation is difficult to solve. The qualitative  $I$ - $V$  characteristics for the dc component of the resulting voltage versus the dc component of the driving current can be obtained by considering the  $I$ - $V$  characteristics obtained from a current driven irradiated junction shown in figure 2.7. As the driven current exceeds the height of the current spike at zero voltage (shown in figure 2.7) the voltage increases with a slope of the resistance until the voltage reaches the next current spike. At this point the current increases up this current spike as the voltage remains relatively fixed. As the current increases, the voltage will continue this pattern and the rises in the voltage will occur at precisely the voltage frequency relation given by equation 2.48. These steps are commonly known as Shapiro steps, named after their discoverer (Shapiro 1963).

## 2.4. Theory and properties of SIN junctions

Superconductor/Insulator/Normal-metal (SIN) junctions are useful for a variety of applications. Examples include bolometry and instruments for investigating non-equilibrium solid state physics (Booth 1996; Kraus 1996). An important difference between SIN and SNS junctions is that in SIN junctions only quasiparticles are able to tunnel through the sandwich layer. This is because of the lack of a Cooper pair energy state in the normal-metal electrode. This also accounts for the absence of the Josephson effect. Giaever first reported tunneling in SIN junctions and modeled their current-voltage ( $I$ - $V$ ) characteristics (Giaever 1960). The analysis is described in the following sections.

### 2.4.1. Tunneling mechanism

For a 1-dimensional situation, consider an electron tunneling through a barrier. The coupling of the electrons is proportional to the overlap of the exponential tails in the barrier and this determines the transition rate. The hamiltonian of electron tunneling,  $H_T$ , is represented using the BCS creation,  $c^*$ , and annihilation,  $c$ , operators,

$$H_T = \sum_{kk'} T_{kk'} c_{k'}^* c_k + \text{hermitian conjugate}. \quad (2.49)$$

$T_{kk'}$  is a tunneling matrix element, which is determined by the overlap of the wavefunction.  $k$  and  $k'$  refer to states on different sides of the barrier. The first term is the transition rate for an electron across the barrier in one direction while the hermitian conjugate is the inverse transition rate, i.e. for an electron transferred in the opposite direction.

The transition probability is found by substituting equation 2.49 for the hamiltonian in Fermi's golden rule equation. The current is then merely  $2e$ , to account for both spins, multiplied by the transition probability to give,

$$2e \left( \frac{2\pi}{\hbar} \right) \sum_{kk'} |\langle k' | H_T | k \rangle|^2 f_k (1 - f_{k'}) \delta(E_k + eV - E_{k'}). \quad (2.50)$$

$f_k$  gives the probability that the initial state  $k$  is occupied and  $(1 - f_{k'})$  gives the probability that the final state  $k'$  is unoccupied. The delta function serves to conserve energy. For the inverse process, only the distribution functions must be changed into  $f_{k'}(1 - f_k)$ , and upon subtracting, the net current,  $I$ , is

$$I = \frac{4e\pi}{\hbar} \sum_{kk'} |\langle k' | H_T | k \rangle|^2 (f_k - f_{k'}) \delta(E_k + eV - E_{k'}). \quad (2.51)$$

Converting equation 2.51 into an integral, the normal-state conductance,  $\sigma_N$ , is found to be

$$\sigma_N = \frac{4\pi e}{\hbar} |T_{kk}|^2 N(0)N'(0). \quad (2.52)$$

$N(0)$  and  $N'(0)$  are the respective junction electrode's electronic densities of states at  $E_F$ .

#### 2.4.2. Current in an SIN junction

For an SIN junction the current can be derived using the approach detailed above, and is given by

$$I(V) = \frac{\sigma_N}{e} \int_{-\infty}^{\infty} \frac{N_S(E)}{N_S(0)} (f(E) - f(E + eV)) dE \quad (2.53)$$

The current is the contribution of four separate tunneling mechanisms,

$$I = e \int (j_1 - j_2 - j_3 + j_4) dE. \quad (2.54)$$

The components of the current,  $j_{1-4}$ , are shown in a semi-conductor representation form in figure 2.8.  $j_1$  represents the current due to the electrons with energies greater than  $(\Delta - eV)$  that tunnel from the normal-metal into the superconductor.  $j_2$  and  $j_4$  represent the current due to holes being transferred from either side of the barrier.  $j_3$  represents the tunneling of electrons from the superconductor into the normal-metal.  $j_3$  and  $j_4$  therefore, represent back-tunneling events, tunneling that occurs in the reverse direction to the net flow of current, and deposit energetic excitations back into the normal-metal.

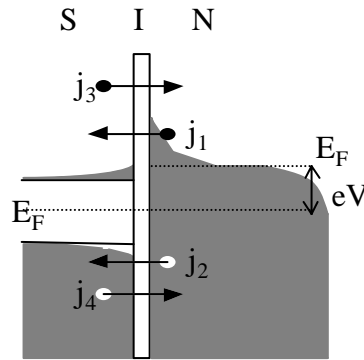


**Figure 2.8: Semiconductor representation of a biased SIN junction showing the various current contributions present ( $j_1, j_2, j_3$  and  $j_4$ ).**

### 2.4.3. Temperature dependent effects of SIN junctions

From equation 2.53 it is apparent that the conductivity of the junction for  $V < \Delta/e$  will change with the junction's temperature. This is shown in figure 2.9 where the  $I$ - $V$  characteristics of a junction were calculated from equation 2.53 for different temperatures.

The differential conductance from equation 2.53 is

$$\frac{dI}{dV} = \sigma_N \int_{-\infty}^{\infty} \frac{N_s(E)}{N_s(0)} \left( \frac{\partial f(E + eV)}{\partial (eV)} \right) dE . \quad (2.55)$$

As  $T \rightarrow 0$  K, the differential conductance measures directly the density of states of the superconductor, since

$$\left. \frac{dI}{dV} \right|_{T \rightarrow 0} = \sigma_N \frac{N_s(e|V|)}{N_s(0)} . \quad (2.56)$$

SIN junctions make good bolometers because their  $I$ - $V$  characteristics are very sensitive to changes in temperature.

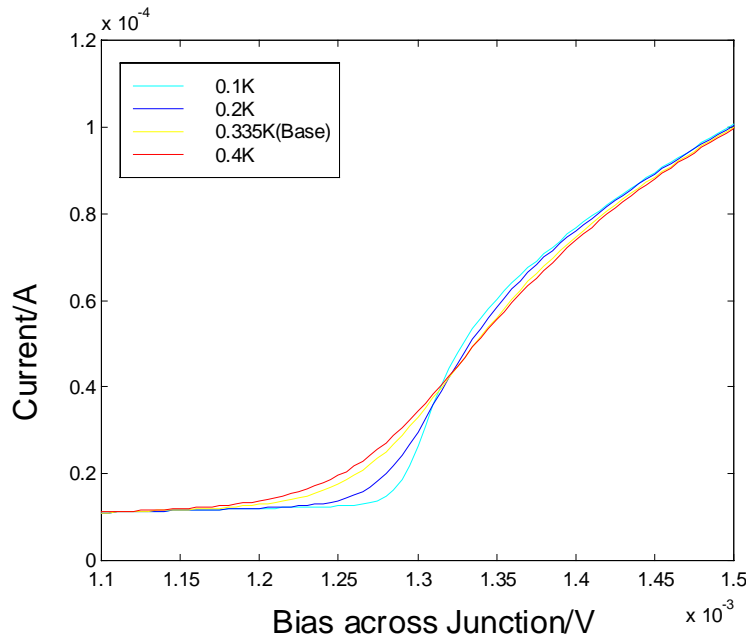


Figure 2.9: Simulated  $I$ - $V$  characteristics (positive branch) of an SIN junction at various temperatures.

## 2.5. The proximity effect

When a superconductor is placed in intimate contact with a normal-metal, a region with both normal metal- and superconductor- like properties will be created around the interface of the two materials. This phenomenon is known as the proximity effect. If a

Superconductor/Normal-metal (SN) bilayer is used then the magnitude of the pair potential,  $\Delta_p(\mathbf{r})$ , is reduced in the superconductor. A finite pair potential may appear in the normal-metal, which in effect means that superconductivity spills into the normal-metal.

Note, for the work described in later chapters, the order parameter ( $\psi$ ) will be used instead of  $\Delta_p$ . The two parameters are related here by

$$|\psi|^2 \propto \Delta_p. \quad (2.57)$$

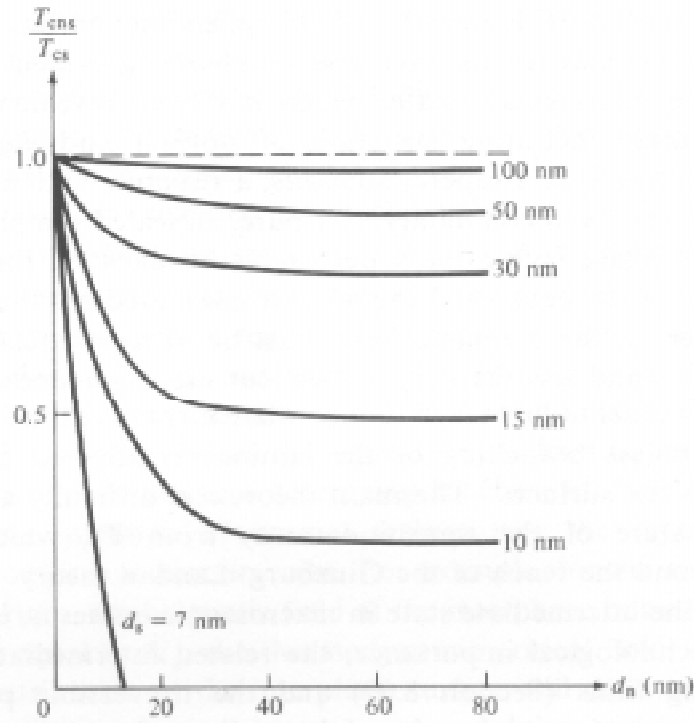


**Figure 2.10: Typical experimental data on the reduction of the critical temperature of a superconductor ( $d_s$ )/normal-metal ( $d_n$ ) layered composite film ( $T_{Cns}$ ) as functions of the component film thicknesses (from Werthamer, 1963).**

As a result of the decrease of the pair potential in the superconductor, the pair density also decreases and consequently the  $T_C$  of the superconductor is reduced. This has been shown experimentally to be true. The results of such an experiment are shown in figure 2.10, which shows how  $T_C$  varies with the thickness of the normal-metal,  $d_N$ . When the superconductor is much thicker than a certain value,  $T_C$  decreases with increasing  $d_N$  until it reaches a limiting value. For thinner films of superconductors however, superconductivity is completely suppressed, shown by  $T_C$  decreasing to zero with increasing  $d_N$ . Interestingly, if the decrease in  $T_C$  were the result of inter-diffusion or alloying then the thickness

dependencies would not be seen. These observations are, therefore, due to the presence of the proximity effect. The results show how deep superconductivity penetrates into the normal-metal from the superconductor, and similarly, how deep superconductivity is perturbed into the superconductor by the normal-metal.

The length over which the proximity effect significantly alters  $\Delta_P(\mathbf{r})$  (and consequently,  $\Delta$  and  $T_C$ ) is known as the coherence length ( $\xi$ ). For a superconductor, where the length is less than the electron mean free path ( $\ell_e$ ) (known as the clean-limit, i.e.  $\xi \ll \ell_e$ ) the length is denoted as  $\xi_{SC}$ . From BCS theory for  $T < T_c$   $\xi_{SC}$  is given by

$$\xi_{SC} = \frac{\hbar v_F}{\pi \Delta_{(0)}}, \quad (2.58)$$

where  $v_F$  is the Fermi velocity and  $\Delta_{(0)}$  is the energy-gap at  $T=0$  K. In the dirty-limit, where  $\xi \gg \ell_e$ ,  $\xi$  is a function of the electron mean free path and is denoted as  $\xi_{SD}$ . From BCS theory for  $T < T_C$ ,

$$\xi_{SD} = \sqrt{\frac{\xi_{SC} \ell_e}{3}}. \quad (2.59)$$

Similarly, for the normal-metal case the length scale is found by modifying equations 2.58 and 2.59, using  $T > T_C$  (for a normal-metal  $T_C = 0$  K). In the clean-limit the characteristic length,  $\xi_{NC}$ , is

$$\xi_{NC} = \frac{\hbar v_F}{2\pi k_B T}, \quad (2.60)$$

and in the dirty-limit the length scale (denoted as  $\xi_{ND}$ ) is,

$$\xi_{ND} = \sqrt{\frac{\xi_{NC} \ell_e}{3}}. \quad (2.61)$$

There is no shortage of theories of the proximity effect (Wolf 1985) so the account presented here is limited to those that attempt to predict the spatial variation of  $\Delta_P$  in a superconductor/normal-metal bilayer.

### 2.5.1. Gor'kov theory

Gor'kov (Gor'kov 1960) produced an equation that gives the spatial variation of  $\Delta_P$ :

$$\Delta_P(\mathbf{r}) = \int K_0(\mathbf{r}, \mathbf{r}') \Delta_P(\mathbf{r}') d\mathbf{r}'. \quad (2.62)$$

Here,  $K_0$  is a kernel and depends upon the value of  $\Delta_P$  in the neighborhood of  $\mathbf{r}$  and  $\mathbf{r}'$ . Gor'kov shows that the first Ginzburg-Landau equation, equation 2.2, can be used to obtain

the variation of the pair potential by applying BCS theory in the limit of small  $\Delta_P$  near  $T_C$ . The length scale is  $\xi_G$  and it is obtained from

$$\xi_G^2(T)\nabla^2\Delta_P(\mathbf{r}) + \Delta_P(\mathbf{r}) - \left|\frac{\Delta_P(\mathbf{r})}{\Delta_{P_\infty}}\right|^2\Delta_P(\mathbf{r}) = 0. \quad (2.63)$$

Here  $\Delta_{P_\infty}$  is the bulk value, deep inside the superconductor. Solving this is difficult for most experimental situations, although a crude approximation for the dirty-limit gives:

$$\xi_G(T) = 0.855\sqrt{l_e\xi_{SC}}\left[1 - \frac{T}{T_C}\right]^{\frac{1}{2}}. \quad (2.64)$$

This theory is limited in its validity. It can be used to describe the macroscopic properties of inhomogeneous superconductors at temperatures close to  $T_C$ , but it only takes account of the superconducting electrons rather than quasiparticles.

### 2.5.2. de-Gennes theory

The work of de-Gennes (de-Gennes 1964) used an approach similar to Gor'kov's, described in the previous section. De-Gennes substituted  $K_0(\mathbf{r},\mathbf{r}')$  for  $K_0(x,x')$  into equation 2.62. This gives the 1-dimensional first-order term in the expansion of  $\Delta_P(x)$ . For the dirty-limit

$$K_0(x,x') = K_0(X) = \frac{N(0)V}{2\xi_{SD(\max)}} \sum_j \sqrt{2j+1} \exp\left[\frac{X\sqrt{2j+1}}{\xi_{SD(\max)}}\right], j>0 \quad (2.65)$$

where  $X=|x-x'|$ . This is an example of an electron correlation function and represents the solutions of a diffusion equation. Using equation 2.65 and a diffusion equation the boundary conditions at an S/N interface can be obtained:

$$\frac{\Delta}{N(0)V} \text{ is continuous} \quad (2.66)$$

$$\frac{D}{V} \frac{d\Delta}{dx} \text{ is continuous,} \quad (2.67)$$

here  $D$  is given by,

$$D = \frac{v_F l_e}{3}. \quad (2.68)$$

These boundary conditions can not be applied to the Gor'kov/Ginzburg-Landau equation 2.64 because of the rapid variation of  $\Delta_P(\mathbf{r})$  near to the interface with the normal-metal. De-Gennes overcame this obstacle by applying a 1-frequency approximation to  $K_0(x,x')$  so only

the longest range exponential  $K_0(x, x')$  was retained and the higher frequency terms were replaced by a single Dirac delta function. This was an appropriate approximation for structures with thick normal-metal layers, and enabled de-Gennes to derive a differential equation with effective boundary conditions for  $\Delta_P(x)$  in the superconductor so,

$$\frac{d^2 \Delta_P}{dx^2} = -q_S^2 \Delta_P, \quad (2.69)$$

with

$$\frac{\Delta_P}{N(0)V} (1 - CN(0)V) = \frac{2\Delta_P}{1 + (q_S \xi_{SC(max)})^2} \text{ is continuous} \quad (2.70)$$

$$\frac{D}{V} \frac{d\Delta_P}{dx} (1 - CN(0)V) = \frac{1}{\rho} \frac{2}{1 + (q_S \xi_{SC(max)})^2} \frac{d\Delta_P}{dx} \text{ is continuous} \quad (2.71)$$

where  $C$  is a normalisation constant,  $\rho$  is the normal state resistivity, and  $q_S$  is a characteristic length scale defined as

$$\frac{1}{q_S} \approx \xi_{SC(max)} \sqrt{2} \left(1 - \frac{T}{T_C}\right)^{\left(\frac{1}{2}\right)}, \quad (2.72)$$

near  $T_C$ .

Similarly, for the normal-metal de-Gennes derived a set of equations comparable to equations 2.69 but  $q_S$  is substituted for  $q_N$ . Here,  $q_N$  is an imaginary function because the normal-metal is above its transition temperature and is defined as

$$q_N = \frac{i}{\xi_{ND(max)}} \left( \frac{\ln\left(\frac{T}{T_{CN}}\right)}{2 + \ln\left(\frac{T}{T_{CN}}\right)} \right)^{\left(\frac{1}{2}\right)}, \quad (2.73)$$

where  $T_{CN}$  is the transition temperature of the normal-metal.

Figure 2.11 shows how  $\Delta_P$  varies at a SN interface. De-Gennes used the previous sets of equations to obtain an expression for the characteristic length,  $b$ , (shown in figure 2.11) of a thick NS bilayer where

$$b = \left( \frac{\Delta_P(x)}{\frac{d\Delta_P(x)}{dx}} \right)_{x=0} = \frac{\rho_N}{\rho_S} K_n^{-1} \coth(K_n d_n) \quad (2.74)$$

and  $K_n^{-1}$  is the decay length of the normal-metal and is, approximately, equal to  $\xi_{ND}$  in the dirty-limit.

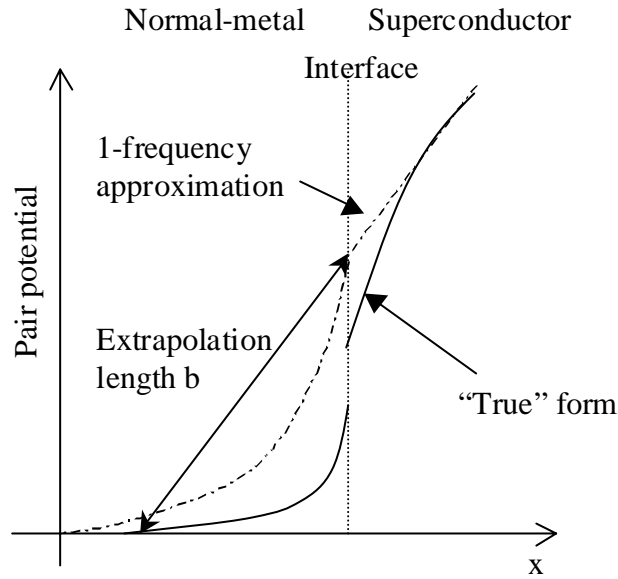


**Figure 2.11:** Comparison of the variation of the pair potential in a proximitised superconductor/normal-metal region with the de-Gennes 1-frequency model.

### 2.5.2.1. Model of a symmetrical SNS structure

De-Gennes also obtained the relevant equations for finding the  $I_C$  of a symmetrical SNS junction, whose geometry is shown in figure 2.12. These equations are coupled and relate the boundary conditions at the two interfaces:

$$\frac{d\Delta_P(d_N/2)}{dx} - \frac{d\Delta_P(-d_N/2)}{dx} = \frac{\rho_S}{\rho_N} K_N (\Delta_P(d_N/2) + \Delta_P(-d_N/2)) \tanh\left(K_n \frac{d_N}{2}\right) \quad (2.75)$$

$$\frac{d\Delta_P(d_N/2)}{dx} + \frac{d\Delta_P(-d_N/2)}{dx} = \frac{\rho_S}{\rho_N} K_N (\Delta_P(d_N/2) - \Delta_P(-d_N/2)) \coth\left(K_n \frac{d_N}{2}\right) \quad (2.76)$$

here  $d_N$  is the thickness of the normal-metal layer, between the two superconductors, and  $\rho_S$  and  $\rho_N$  are the normal state resistivities of the superconductor and normal-metal, respectively. Solving these equations for  $d\Delta_P(d_N/2)/dx$ , and using this as the boundary condition for equation 2.5 at the point  $x=d_N$ , de-Gennes derived an expression for the supercurrent that could flow in the junction,

$$J = \frac{\pi K_n}{4e\rho_N k_B T_C} (\Delta_P^+(d_N/2)\Delta_P(-d_N/2) - \Delta_P(d_N/2)\Delta_P^+(-d_N/2)) \operatorname{cosech}\left(2K_n \frac{d_N}{2}\right). \quad (2.77)$$

de-Gennes obtained the value of  $|\Delta_P(d_N/2)|$  by assuming that  $\Delta$  is real, integrating equation 2.63 and using equations 2.75 and 2.76 in the limit  $d_N K_n \gg 1$  as a boundary condition in order to obtain

$$\left| \frac{\Delta_P}{\Delta_{P\infty}} \right|^2 \left[ 1 + \left( \frac{\xi_{ND}(T)}{b_\infty} \right)^2 + \left| \frac{\Delta_P}{\Delta_\infty} \right|^2 \right] = \frac{1}{2} \quad (2.78)$$

where

$$b_\infty = \frac{\rho_N}{\rho_S} K_n^{-1}. \quad (2.79)$$

If both the normal-metal layer and the superconductor are conventional metals, then  $b_\infty$  is comparable to  $\xi_{SC(max)}$  for the superconductor and if  $T \sim T_C$ ,  $\Delta_P(d_N/2) \ll \Delta_{P\infty}$ . The  $I_C$  of the 1-dimensional junction therefore, is given by

$$\begin{aligned} I_C &= \frac{\pi}{4e} \frac{\rho_N K_n^{-1}}{(\rho_S \xi_{ND}(T))^2} \frac{\Delta_{P\infty}^2}{k_B T_C} \exp(-K_n d_N) \\ &\approx \frac{\pi \Delta_0}{e} \frac{\rho_N K_n^{-1}}{(\rho_S \xi_{SC})^2} \left( 1 - \frac{T}{T_C} \right)^2 \exp(-K_n d_N) \end{aligned} \quad (2.80)$$

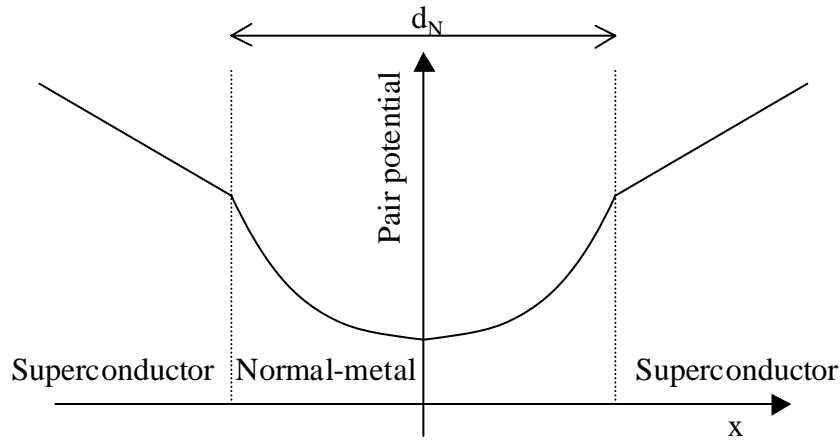


**Figure 2.12: Variation of the pair potential in a SNS junction using the de-Gennes 1-frequency approximation.**

The one frequency approach taken by de-Gennes has been able to model the  $I_C$  in SNS junctions quite well. An example for this was the experimental study of Pb/Cu/Pb by Clarke, discussed in section 2.3, where they were found to accurately model the temperature and thickness dependencies predicted by equation 2.80. The approach does have some drawbacks shown by the requirement that  $d_N \gg K_n^{-1}$ , which sets a limit where the equations

are valid. Below this limit the supercurrent will modify the spatial variation of the pair potential from its form with no current flowing.

### 2.5.3. McMillan model

McMillan (McMillan 1968) devised a model of the proximity effect where the superconductor and normal-metal are only coupled together by electron tunneling through a barrier between the two materials. This is not only applicable to SIN structures but also to disordered SN bilayers. Here, contaminants and defects at the bilayer interface disrupt the normal conduction processes leaving electron tunneling as the only method of electron transport. McMillan assumed that the thickness of the two layers are both less than their respective coherence lengths so that the properties are uniform across the thickness of both films. The further assumption was made that the tunneling is a specular process and therefore, the tunneling matrix elements that couple the electron states in the superconductor with those in the normal-metal are all of equal magnitude. This means that momentum is not conserved and the materials must be in the dirty-limit. By making these approximations, McMillan showed that the self-energy in the normal-metal layer,  $\Delta_{PN}(E)$ , for the pair potential in the normal-metal,  $\Delta_{PN}$ , is given by

$$\Delta_{PN}(E) = \frac{\left( \Delta_{PN} + \frac{i\Gamma_N \Delta_{PS}(E)}{\left[ E^2 - \Delta_{PS}^2(E) \right]^{\left(\frac{1}{2}\right)}} \right)}{1 + \frac{i\Gamma_N}{\left[ E^2 - \Delta_{PS}^2(E) \right]^{\left(\frac{1}{2}\right)}}} \quad (2.81)$$

$\Delta_{PS}(E)$  is the self-energy in the superconducting layer and  $\Gamma_N = \hbar/\tau_n$  where  $\tau_n$  is the tunneling time for an electron in the normal-metal. McMillan showed that

$$\Gamma_N = \frac{\hbar v_{FN} p}{4B_N d_N} \quad (2.82)$$

where  $v_{FN}$  is the Fermi velocity in the normal-metal,  $p$  is the barrier transmission probability, and  $B_N$  is a function of the ratio of the mean-free path to the layer thickness and is of order 1.

The self-consistency equation for  $\Delta_{PN}$  is

$$\Delta_{PN} = \lambda_N \int_0^{\omega_{CN}} \text{Re} \left[ \frac{\Delta_{PN}(E)}{\left( E^2 - \Delta_{PN}^2(E) \right)^{\left(\frac{1}{2}\right)}} \right] \tanh \left( \frac{E}{2k_B T} \right) dE, \quad (2.83)$$

where  $\lambda_N$  is the electron-phonon coupling strength in the normal-metal (for weak coupling this is equal to  $N(0)V$ ), and  $\omega_{CN}$  is the Debye frequency of the normal-metal. By direct substitution into equations 2.81 and 2.83 it is possible to obtain equations for  $\Delta_{PS}(E)$  and  $\Delta_{PS}$ , the self-energy and bulk pair potential in the superconductor. By self-consistently solving the four equations, solutions for  $\Delta_{PS,N}(E)$  may also be obtained. From this the density of states in each region may be determined by using

$$N_{S,N}(E) = \text{Re} \left[ \frac{E}{\left( E^2 - \Delta_{PS,N}^2(E) \right)^{\frac{1}{2}}} \right]. \quad (2.84)$$

McMillan's model can be fitted to experimental data, typically by taking  $B_{N,S}=1$  and selecting a value of the barrier transmission probability,  $p$ , which fits. The fact that  $p$  is a free parameter means the model is not physically correct, and is a consequence of the assumptions used in the model. In most experimental situations the pair potential will not be constant on either side of the barrier. Several experimental studies have, however, found good agreement with experiment by using  $p$  as a fitting parameter (Romagnon 1974; Gilabert 1979; Goldie 1990).

#### 2.5.4. Golubov and Kupriyanov model

Golubov and Kupriyanov (Golubov 1988) developed a microscopic model of the proximity effect in an inhomogeneous thin-film of superconductor. This model can be applied to both superconductor/superconductor and superconductor/normal-metal structures. The advantage of this model is it uses realistic assumptions about the materials that are commonly used by experimentalists. The major assumption used is that the materials are in the dirty-limit (i.e.  $\ell_e \ll \xi$ ), and is true for most real situations. In this limit the normal and anomalous Green's functions ( $G$ ,  $F$ ) will obey the Usadel equations (Usadel 1970), which describe diffusive current flow:

$$\phi_p(\omega_n, x) = \Delta_p(\omega_n, x) + \xi_{SD}^2 \frac{\pi T_C}{\omega_n G(\omega_n, x)} \nabla \left[ G^2(\omega_n, x) \nabla \phi_p(\omega_n, x) \right] \quad (2.85)$$

$$\Delta_p(\omega_n, x) \ln \left[ \frac{T}{T_C} \right] + 2\pi T \sum_{\omega_n} \frac{\Delta_p(\omega_n, x)}{\omega_n} - F(\omega_n, x) = 0 \quad (2.86)$$

$$\phi_P = \frac{\omega_n F}{G} \quad (2.87)$$

$$F = \frac{\phi_P}{\sqrt{\omega_n^2 + \phi_P^2}} \quad (2.88)$$

$$G = \frac{\omega_n}{\sqrt{\omega_n^2 + \phi_P^2}} \quad (2.89)$$

$$\omega_n = \pi T(2n+1) \quad n=0,1,2,\dots \quad (2.90)$$

Equation 2.85 describes the proximity effect as a diffusive process. Equation 2.86 is a self-consistency relationship that is used to determine the order parameter,  $\Delta_P(\omega_N, x)$ .  $\phi_P(\omega_N, x)$  is a convenient parameter with no simple physical meaning.  $\omega_N$  is the Matsubara frequency. Kupriyanov gives an extensive discussion of the properties of these equations (Kupriyanov 1988). The equations provide a foundation for modeling any superconducting interfacial region. To obtain  $F(\omega_N, x)$  and  $G(\omega_N, x)$  the equations must be solved simultaneously for both layers, and numerically for the general case. The density of states can be solved, given that  $N(S) = N(0) \text{Re}[G(S = -i\hbar\omega_N)]$ . It is also possible to calculate the quasiparticle lifetimes in the inhomogeneous superconductor by using these functions as Kaplan (Kaplan 1976) did for the homogeneous case.

Here, Golubov and Kupriyanov (Golubov 1988) used the equations to model an inhomogeneous superconductor, composed of two superconductors. One superconductor,  $S_1$ , is thick and the other,  $S_2$ , is thin with a lower  $T_C$  and energy gap,  $\Delta_P(x=0)$ . The following assumptions were necessary to model this situation:

$$\begin{aligned} d_{S_1} &\gg \xi_{SD_1} \gg l_{S_1} \\ l_{e,S_1} &\leq d_{S_2} \ll \xi^* \\ \xi_{S_2D} &= \xi^* \sqrt{\frac{T_{C,S_2}}{T_C^*}} \\ T_{C,S_1} &> T_{C,S_2} \end{aligned} \quad (2.91)$$

where  $d_x$  is the thickness of layer  $x$ ,  $T_C^*$  is the effective critical temperature of the combined structure, and  $\xi^*$  is the effective coherence length in the thin  $S_2$  electrode. These assumptions mean that  $\Delta_P$  in  $S_1$  will vary across its thickness, whereas in  $S_2$  it will be constant. Golubov solved equations 2.85-2.90 in order to obtain  $\Delta_P(x)$ , which is shown in figure 2.13.

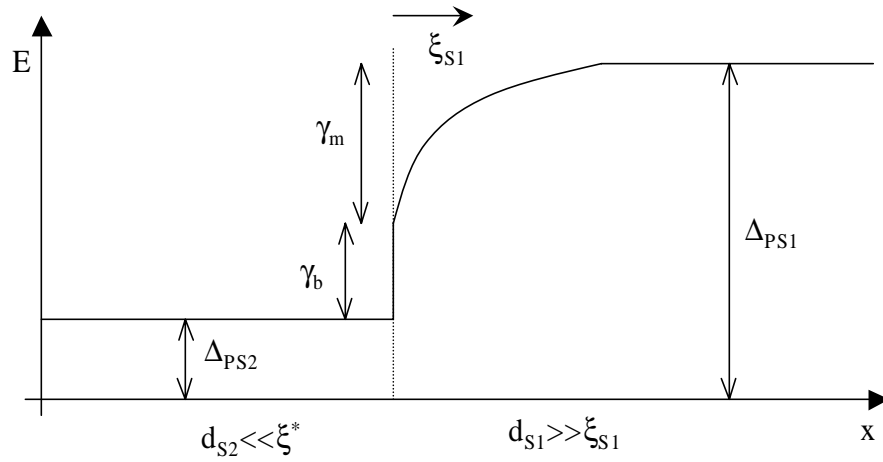


**Figure 2.13: Golubov and Kupriyanov model of a proximitised superconductor/normal-metal region.**

The ratio of the critical temperatures and two parameters,  $\gamma_m$  and  $\gamma_b$ , were found to characterise the proximity effect in this type of structure.  $\gamma_m$  and  $\gamma_b$  are given by

$$\gamma_m = \frac{\rho_{S_1} \xi_{S_1} d_{S_1}}{\rho_{S_2} \xi^{*2}} \quad (2.92)$$

$$\gamma_b = \frac{R^* d_{S_2}}{\rho_{S_2} \xi^{*2}} \quad (2.93)$$

where  $\rho_x$  is the normal state resistivity,  $R^*$  is the resistance area product of the  $S_1S_2$  boundary.  $\gamma_m$  and  $\gamma_b$  reflects the electrical differences between  $S_1$  and  $S_2$ .  $\gamma_m$  is a measure of the difference between quasiparticle densities.  $\gamma_b$  is a measure of the transparency of the interface.

The importance of Golubov and Kupriyanov's microscopic model, is it can model the trapping of quasiparticles in the regions where the local value of  $\Delta_p(x)$  experiences a minimum. This allows quasiparticles to energetically relax, but are then unable to escape until they relax into Cooper pairs.

Golubov and co-workers have found that many structures can be modeled using the Usadel equations: SS'IS''S (Golubov 1995) and SN'IN''S (Golubov 1989). For the SNS structures investigated in later chapters, no microscopic model exists, although it should be possible to extend microscopic theory to this geometry (Golubov 1999). Van Dover did model the proximity effect in an SNS structure based on de-Gennes theory, and is discussed in Chapter 7.

Other models of SNS structures exist, but they are not applicable for most experimental situations. Kieselmann modeled the proximity effect in a clean-limited SN double layer in the framework of the Gor'kov equations (Kieselmann 1987). Ashida and Tanaka also investigated the proximity effect in SNS junctions in the framework of the Gor'kov equations (Ashida 1989; Tanaka 1993).

### 2.5.5. Andreev reflection

Consider a SN bilayer. At low temperatures most of the excitations in a normal-metal will have energies that are lower than the bulk value of  $\Delta$  in a superconductor. Consequently, there are no single particle states available for the excitations to enter on crossing the interface. The process that enables the current carried by these excitations to cross the interface is known as Andreev reflection (Andreev 1964). The processes involved in Andreev reflection are shown in schematic form in figure 2.14.

As the excitation approaches the interface it experiences an increasing local value of the pair potential. The interaction between the excitation and the condensate causes it to become less electron-like as it approaches the interface so that the value of its localised charge ( $q_{ex}$ ) decreases as does its group velocity. The value of its crystal momentum ( $\mathbf{k}_{ex}$ ) also decreases but its energy remains constant. Deep inside the superconductor, there are no single particle states available to the quasiparticle and so at the point where its energy is equal to the local value of  $\Delta_p$ , it comes to rest with  $\mathbf{k}_{ex}=\mathbf{k}_F$  and  $q_{ex}=0$ . In order for the current carried by this excitation to be converted into supercurrent, a pair of electrons must be injected into the superconductor which requires that a charge of  $2e$  must be removed from the normal-metal. This is achieved by the quasiparticle being reflected as a hole-like excitation. The difference between this process and ordinary reflection processes is that all of the components of the original quasiparticle's crystal momentum are reversed instead of only the component perpendicular to the interface (shown in figure 2.14). The hole-like excitation retraces the same path in real space as the original electron-like excitation.

This description of Andreev reflection is slightly misleading however, because the processes described do not happen sequentially. For a clean-limited normal-metal, the process of Andreev reflection creates a ballistic steady bound state of hole and electron excitations in the normal-metal.

Andreev reflections in the normal-metal layer of an SINS tunnel junction can give rise to resonances. The effects of resonances where reflected quasiparticles constructively interfere to give peaks in conductance at certain voltages have been observed by Tomasch (Tomasch 1965) and Rowell and McMillan (Rowell 1973).

For dirty-limited normal-metals, the ballistic steady state system is lost and the effects of Andreev reflection become less obvious. Andreev reflection is still present, however, but in a non-ballistic and chaotic form. This has been discussed by Wilhelm (Wilhelm 1997). Further discussion of Andreev reflection is presented in chapter 7.3.

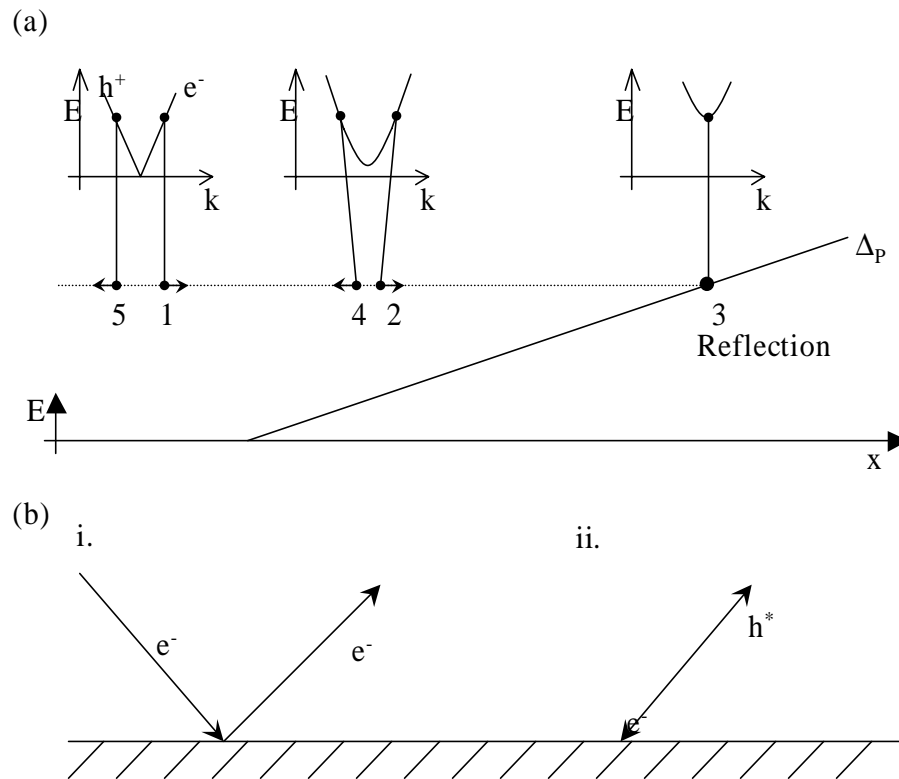


**Figure 2.14: Andreev reflection (a) Changes in the excitation spectrum of a normal-metal as the pair potential rises near to an interface with a superconductor. (b) Real space trajectories in ordinary (i) and Andreev (ii) reflection processes. (after Lean, 1987)**

## 2.6. Review of non-equilibrium superconductivity

Any system that gains energy from an external source will be in non-equilibrium. Many types of external sources will create non-equilibrium superconducting junctions. Examples include, electron-, or phonon-, injection, and microwave-, or optical-, radiation. All the junctions investigated here are in non-equilibrium so it is important to consider the various consequences of non-equilibrium superconductivity in SNS and SIN junctions.

The environments of both non-equilibrium SIN and SNS junctions depend on the properties of the superconductor, the normal-metal, the substrate, and its immediate surroundings. The associated factors that determine their properties are: quasiparticle and phonon lifetimes; quasiparticle and phonon mean free path values; and the phonon escape time.

### 2.6.1. Non-equilibrium quasiparticle and phonon energy distributions

Experimental studies on non-equilibrium phonons and quasiparticles date back to the mid-1960s. Early studies used Superconductor Tunnel Junctions (STJs) where elastic single electron tunneling between two superconducting films, separated by a thin oxide barrier, results in a non-equilibrium distribution of quasiparticles. These quasiparticles decay mainly by phonon emission, resulting in a non-equilibrium phonon-energy distribution. The phonon frequencies typically lie between 50 GHz and 1.5 THz. The phonons either escape from the thin film into the insulator substrate without reabsorption or, thermalise within the superconductor film.

The quasidelectrons and quasiholes branches of  $E(\mathbf{k})$  are symmetrical at small deviations from  $\mathbf{k}_F$ . An excited quasiparticle can decay under spontaneous or stimulated phonon emission into states of lower energy either within the same branch or changing to the other branch. Energies range therefore, from  $\hbar\Omega=0$  to  $\hbar\Omega=E-\Delta$ , where  $\Omega$  is the energy of the phonon. Figure 2.15 shows schematically the possible transitions.

The probability for a quasiparticle to undergo a spontaneous transition is described by  $\tau_T$ , the mean time for the transition to occur, where  $\tau_T^{-1} \propto (E - \Delta)$ . This relationship is a consequence of the decreasing number of phonon states available for the transition for quasiparticles close to the gap edge, and also by the destructive interference in the BCS transition probability.

The reabsorption of phonons by quasiparticles only occurs at high quasiparticle densities, e.g. at temperatures comparable to  $T_C$ , or under conditions of high quasiparticle

population that result in an inelastic decay of non-equilibrium phonons, e.g. by electron injection.

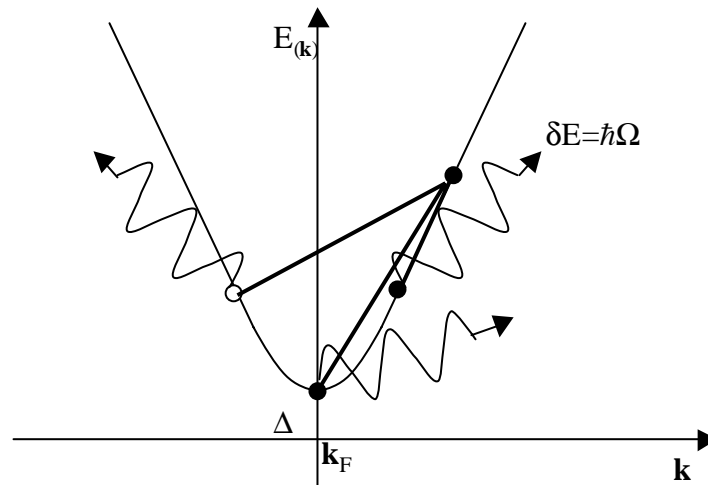


**Figure 2.15: Schematic of a BCS wave relation plot showing the possible relaxation mechanisms of an excited quasiparticle.**

In order to determine the energy distributions of the phonons and quasiparticles it is necessary to solve rate equations for both the phonons and quasiparticles. The important parameters entering these equations are: the energy distribution of the primary quasiparticle excitation rates; the quasiparticle-to-phonon and phonon-to-quasiparticle transition rates; the phonon lifetimes for surface-boundary escape and volume decay; the elastic scattering rates for quasiparticles and phonons. The energy distribution of the primary quasiparticle excitation depends upon the type of excitation process e.g. by electron tunneling, phonon, or photon injection.

Experimentally, it is often difficult to determine these parameters precisely so work to date has used rate models that either neglect the parameters or over-simplify them. Two popular examples of these models are the Rothwarf-Taylor equations (Rothwarf 1967) and the Chang and Scalapino coupled kinetic equations (Chang 1977). The major assumption used in the Rothwarf-Taylor equations is that only phonons with energy  $2\Delta$  exist in the superconductor. While this is not true, the equations have been remarkably successful for analysing experimental work (Twerenbold 1986). The Chang and Scalapino coupled kinetic equations extend the Rothwarf-Taylor equations by taking into account the non-equilibrium phonon population energy distribution. The equations are very difficult to solve and normally require other assumptions to be made that depends upon the experimental situation.

### 2.6.2. Quasiparticle recombination

Quasiparticle recombination is an important process that takes place in superconductors. Two quasiparticles of energy's  $E_1$  and  $E_2$  form a Cooper pair in its ground-state under the emission of 1 recombination phonon of energy  $\hbar\Omega=E_1+E_2$ . The minimum phonon energy therefore, is  $2\Delta$ . These phonons can consequently be easily reabsorbed via Cooper pair-breaking to reform two quasiparticles. For the low  $T_C$  superconductors used throughout this work, the phonon mean free path for pair-breaking is in the range 10-100 nm. The process of quasiparticle recombination, therefore, enhances the effective lifetime of quasiparticles. This enhanced lifetime in superconducting thin-films can be up to 2 orders of magnitude larger than the intrinsic lifetime.

The excitation energy will be eventually lost due to phonon surface escape and volume decay either by quasiparticle excitation or anharmonic phonon interactions. It is the quasiparticle recombination process however, that normally governs the non-equilibrium distribution of quasiparticles and phonons in most superconducting systems.

### 2.6.3. Knock-on effects of changes in the energy distribution of quasiparticles

When a superconductor is in non-equilibrium, the change in the quasiparticle population energy distribution can alter the superconducting state. First, consider how the quasiparticle distribution function affects the energy gap. The quasiparticle energy distribution can be described by the Fermi function,

$$f_k(E) = \frac{1}{1 + \exp\left(\frac{E - u^*}{k_B T_e}\right)}. \quad (2.94)$$

Here  $T_e$  is the electronic temperature, and  $u^*$  is the effective chemical potential. This gives a simple analytical approximation for  $f_k(E)$  in non-equilibrium states, although  $u^*$  loses its physical significance.  $\Delta$  can be found by inserting equation 2.94 into the BCS approximated equation 2.13,

$$\ln\left(\frac{\Delta_{(0)}}{\Delta}\right) = \int_0^\infty \frac{N(E)f(E)}{E} dE \quad (2.95)$$

However, equation 2.95 will not be valid if there is a significant imbalance in the quasiparticle population.

Other examples of the changes caused by the shift in the quasiparticle population energy distribution are branch- and charge- imbalance. Branch imbalance refers to a

difference in the relative populations of the branches of quasiparticle spectra for  $\mathbf{k}$  above and below  $\mathbf{k}_F$  (Tinkham 1972). Charge imbalance refers to the probability that a quasiparticle state is either a hole in, or an addition to, the pair distribution (Pethick 1979). This represents the exchange of charge between the Cooper pairs and quasiparticles, although overall charge neutrality is maintained. The difference between these two types of imbalance originates from the fact that a quasiparticle charge does not change sign discontinuously as  $\mathbf{k}$  crosses from  $\mathbf{k}_F$ , because the distribution of electrons at  $T=0$  K is not discontinuous at  $\mathbf{k}_F$  as in a normal-metal. In real systems charge imbalance is the most relevant with a relaxation time for a system experiencing charge imbalance of  $\sim 10^{-10}$  s (Clarke 1972).

Charge imbalance is responsible for an extra resistance in studies of SNS sandwich structures (above that of the normal-metal layer itself as inferred from its known resistivity and thickness) (Pippard 1971). Pippard *et al.* argued that although some current is converted by Andreev reflection at the S/N interface, an extra resistance arose from the non-equilibrium region in the superconductor in which a quasiparticle current was converted to a supercurrent. This simple interpretation has very effectively explained the measurements of SNS resistance values by Hsiang and Clarke (Hsiang 1980) and will be used to explain similar observations in chapter 5.

#### 2.6.4. Time Dependent Ginzburg-Landau Theory

Although there are many shortcomings with the Ginzburg-Landau theory it has had remarkable success in describing many real superconducting systems. The equations can be modified to take into account many non-equilibrium situations, e.g. non-equilibrium quasiparticle populations (Gray 1981), and show how the properties of the system will change over time. The Time Dependent Ginzburg-Landau (TDGL) equations were originally derived by Schmid (Schmid 1966) for superconductors near  $T_C$ . Gor'kov and Eliashberg (Gor'kov 1968) then extended them to be rigorously valid at all temperatures in a superconductor rendered gapless by paramagnetic impurities. Kramer and Watts-Tobin (Kramer 1978) obtained a more generalised version that is valid for a dirty superconductor near  $T_C$ , taking into account inelastic electron-phonon scattering. Finally, Schon and Ambegaokar (Schon 1979) derived a TDGL equation, which included various pair-breaking mechanisms: electron-phonon scattering, paramagnetic impurities, supercurrent depairing, magnetic fields and spatial variation of the order parameter. The generalised pair-breaking parameter is given by

$$\Gamma = \frac{1}{2\tau_E} + \frac{1}{\tau_S} + \frac{D}{2}\mathbf{Q}^2 - \frac{D}{2}\frac{\nabla^2\psi}{\psi}, \quad (2.96)$$

where  $\tau_E$  is the inelastic electron-phonon scattering time,  $\tau_S$  is the magnetic spin flip time,  $D$  is a diffusion coefficient,  $\psi$  is the temperature-dependent equilibrium order parameter and

$$\mathbf{Q} = \nabla\theta + 2e\mathbf{A} \quad (2.97)$$

is proportional to the superfluid momentum. The general TDGL equation (Schon 1979) is given by

$$\frac{\pi}{8k_B T} \left[ \frac{\eta}{2|\psi|\tau_E} \left( \frac{\partial}{\partial t} + 2ie\Phi_{eff} \right) + \left( 2|\psi|\tau_E\zeta - \frac{\eta}{2|\psi|\tau_E} \right) \frac{|\dot{\psi}|}{|\psi|} \right] \psi = \left[ \alpha - \beta|\psi|^2 + \xi_{(0)}^2 (\nabla - 2ie\mathbf{A})^2 \right] \psi, \quad (2.98)$$

where  $\Phi_{eff}$  is the effective potential, relating to the gauge invariance of the chemical and electric potentials. Other parameters are given by

$$\begin{aligned} \eta &= (2\gamma\tau)^{\left(\frac{1}{2}\right)} \left( 1 + \frac{\gamma}{2\psi_0^2\tau} \right)^{\left(-\frac{1}{2}\right)} & \alpha &= (T_C - T) / T_C \\ \zeta &= \left( 1 + \left[ \frac{\gamma}{\psi_0} \right]^2 \right)^{\left(\frac{1}{2}\right)} - \frac{\gamma}{\psi_0} + \frac{1}{2\psi_0\tau} & \beta &= \frac{7\zeta(3)}{8\pi^2 k_B^2 T_C^2} \\ \gamma &= \frac{i\omega}{2} + \Gamma & \xi_{(0)}^2 &= \frac{\pi\hbar D}{8k_B T_C} \\ \frac{1}{\tau} &= -i\omega + \frac{1}{\tau_E} \end{aligned} \quad (2.99)$$

The current is determined by

$$I = \frac{\pi\sigma_N}{4ek_B T} \mathbf{Im} \left\{ \psi^* (\nabla - 2ie\mathbf{A})\psi \right\} - \sigma_N (\nabla\Phi_{eff} - \mathbf{A}), \quad (2.100)$$

where  $\sigma_N$  is the normal state conductance.

Using the TDGL equations it is possible to qualitatively model the electrical characteristics of an SNS junction. The reason why it is only a qualitative model is that the material parameters can only be treated phenomenologically because the equations are not valid for an SNS structure, e.g. the normal-metal does not have a  $T_C$ . By treating the normal-metal as a gapless superconductor it is possible to model the current in an SNS structure because the pair-breaking mechanisms in the normal-metal are still valid. By taking into

account the relaxation time governing current transfer between the normal and superconducting layers (Vandover 1981), it is possible to investigate the effects of a varying order parameter in the proximitised region.

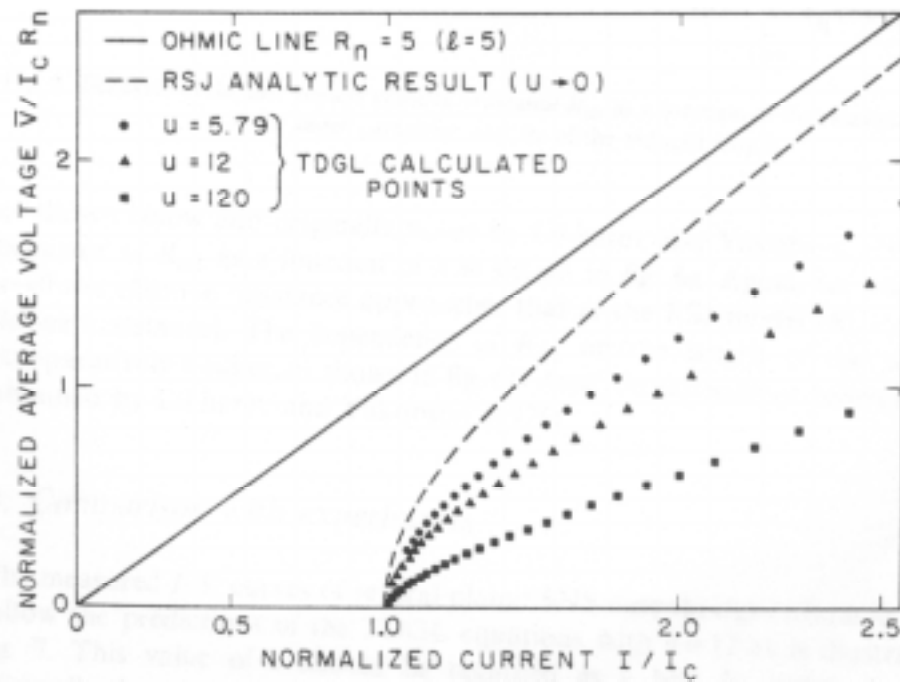


**Figure 2.16:** Effects of the relaxation time ( $u$ ) on the I-V characteristics near the critical current. As the relaxation time is decreased the TDGL curves approach the RSJ result (dashed curve). From (Vandover, 1981).

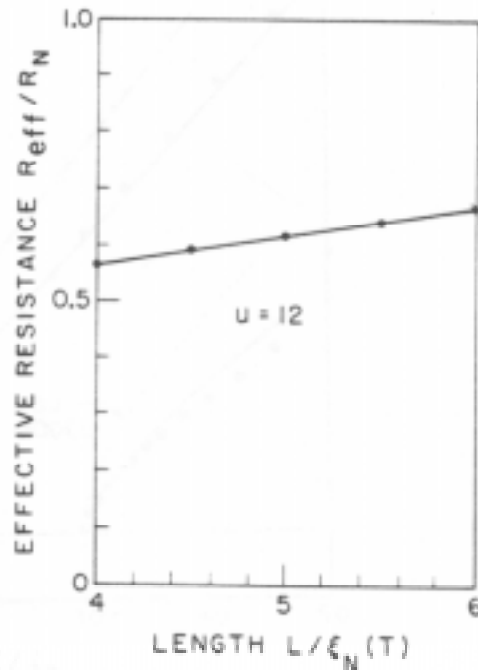


**Figure 2.17:** Behaviour of the low voltage effective resistances ( $R_{EFF}$ ) as a function of the relaxation time ( $u$ ) with the variation of the reduced length ( $L/\xi_N$ ). From (Vandover, 1981).

The equations are solved by numerical analysis. The resulting  $I$ - $V$  characteristics of planar-bridge SNS junctions for different order parameter relaxation times, treated as an adjustable parameter, can be found. Lozanne performed this analysis and the results are shown in figure 2.16. It shows that the  $I$ - $V$  characteristics obtained from the TDGL equations increasingly deviates from the RSJ model. This deviation increases as the relaxation time of the order parameter is increased. At higher voltages, the effective resistance,  $R_{EFF}$ , of the junction is different to the  $R_N$  of the junction, calculated from the RSJ model. The dependence of  $R_{EFF}$  on the length of the bridge is comparatively weaker, shown in figure 2.17.

## 2.7. References

- A. F. Andreev (1964). "The Thermal Conductivity of the Intermediate State in Superconductors." *Soviet Physics Journal of Experimental Theoretical Physics* **19**(5) 1228.
- M. Ashida, S. Aoyama, J. Hara and K. Nagai (1989). *Phys. Rev. B* **40** 8673.
- J. Bardeen, L. N. Cooper and J. R. Schrieffer (1957). "Microscopic Theory of Superconductivity." *Physical Review* **108** 1175.
- A. Barone and G. Paterno (1982). "Physics and the applications of the Josephson effect." (New York, Wiley).
- T. K. Blocker, R. K. Watts and W. C. Holton (1978). "Future Trends in Superconductive Electronics." (New York, AIP).
- W. E. Booij (1997). PhD Thesis "Josephson junctions and Devices Fabricated by Focussed Electron Beam Irradiation." Dept. Materials Science. Cambridge, University of Cambridge 208.
- N. E. Booth and D. J. Goldie (1996). "Superconducting Particle Detectors." *Superconductor Science & Technology* **9**(7) 493.
- C. J. Burroughs, S. P. Benz, T. E. Harvey and C. A. Hamilton (1999). "1 volt dc programmable Josephson voltage standard." *IEEE Transactions on Applied Superconductivity* **9** 4145.
- J. J. Chang and D. J. Scalapino (1977). "Kinetic-Equation Approach to Non-Equilibrium Superconductivity." *Physical Review B* **15**(5) 2651.
- J. Clarke (1969). "Supercurrents in lead-copper sandwiches." *Proc. Roy. Soc.* **308** 447.

- J. Clarke (1972). *Phys. Rev. Lett.* **28** 1363.
- P. G. de-Gennes (1964). *Rev. Mod. Phys.* **64** 225.
- R. P. Feynman (1965). "The Feynman Lectures on Physics." (Reading, Massachusetts, Adison-Wesley).
- I. Giaever (1960). "Energy gap in superconductors measured by electron tunneling." *Phys. Rev. Letts.* **41** 1509.
- A. Gilabert, C. Van Hasendonck, L. Ven den Dries and Y. Bruynserade (1979). *Solid State Comm.* **31** 109.
- V. L. Ginzberg and L. D. Landau (1950). *Zh. Eksperim. i Teor. Fiz.* **20** 1064.
- D. J. Goldie, N. E. Booth, C. Patel and G. L. Salmon (1990). *Physical Review Letters* **64** 954.
- A. A. Golubov (1999). "Personal Communication."
- A. A. Golubov and M. Y. Kupriyanov (1988). "Theoretical Investigation Of Josephson Tunnel-Junctions With Spatially Inhomogeneous Superconducting Electrodes." *Journal Of Low Temperature Physics* **70**(1-2) 83.
- A. A. Golubov, E. P. Houwman, J. G. Gijbetsen, V. M. Krasnov, J. Flokstra, H. Rogalla and M. Y. Kupriyanov (1995). "Proximity Effect In Superconductor-Insulator-Superconductor Josephson Tunnel-Junctions - Theory and Experiment." *Physical Review B-Condensed Matter* **51**(2) 1073.
- A. A. Golubov and M. Y. Kupriyanov (1989). "Josephson effect in SNINS and SNIS Tunnel-Junctions with Finite Transparency of the SN Boundaries." *Zhurnal Eksperimentalnoi I Teoreticheskoi Fiziki* **96** 1420.
- L. P. Gor'kov (1960). *Soviet Physics: Journal of Experimental and Theoretical Physics* **10** 998.
- L. P. Gor'kov and G. M. Eliashberg (1968). *Zh. Eksp. Teor. Fiz* **54** 612.
- K. E. Gray (1981). "Nonequilibrium Superconductivity, Phonons, and Kapitza Boundaries." (New York and London, Plenum Press).
- E. P. Harris and R. B. Laibowitz (1977). *IEEE Trans. Magn.* **MAG-13** 724.

- N. Hirose, H. Ohta, T. Matsui and M. Fukuda (1997). "S-N-S weaklink junctions fabricated by nanometer lithography." *IEEE Transactions On Applied Superconductivity* **7**(2 Pt3) 2635.
- T. Y. Hsiang and J. Clarke (1980). "Boundary resistance of the superconducting phase slip center." *Phys. Rev. B* **21** 945.
- B. D. Josephson (1962). *Physics Letters* **1** 251.
- S. B. Kaplan, C. C. Chi and D. N. Langenberg (1976). "Quasiparticle and Phonon Lifetimes in Superconductors." *Physical Review B* **14**(11) 4854.
- G. Kieselmann (1987). "Self-Consistent Calculations of the Pair Potential and the Tunneling Density of States in Proximity Contacts." *Phys. Rev. B* **35** 6762.
- L. Kramer and R. J. Watts-Tobin (1978). *Phys. Rev. Lett.* **40** 1041.
- H. Kraus (1996). "Superconductive Bolometers and Calorimeters." *Superconductor Science & Technology* **9**(10) 827.
- M. Y. Kupriyanov and V. F. Lukichev (1988). *Sov. Phys. JETP* **67** 1163.
- H.W. Lean (1987). PhD Thesis. "The transport properties of superconducting-normal interfaces" Department of Physics, University of Cambridge.
- K. K. Likharev (1996). "Ultrafast superconductor digital electronics: RSFQ technology roadmap." *Czech. Jnl. Phys.* **46** 3331.
- F. London and H. London (1935). "The Electromagnetic Equation of the Supraconductor." *Proceedings of the Royal Society (London)* **A149** 71.
- D. E. McCumber (1968). "Effect of ac impedance on dc Voltage-Current characteristics of superconductor weak-link junctions." *J. Appl. Phys.* **39** 3113.
- W. L. McMillan (1968). "Tunneling Model of the Superconducting Proximity Effect." *Physical Review* **175**(2) 537.
- A. F. Morpurgo, S. Holl, B. J. van Wees, T. M. Klapwijk and G. Borghs (1997). *Phys. Rev. Lett.* **78** 2636.
- A. F. Morpurgo, T. M. Klapwijk and B. J. van Wees (1998). *Appl. Phys. Lett.* **72** 966.
- H. K. Onnes (1911). *Leiden Communications* **120b, 122b, 124c**.
- A. J. Pauza (1993). PhD Thesis "The Fabrication of Josephson Junctions with an Electron Beam." Department of Engineering, University of Cambridge.

- C. J. Pethick and H. Smith (1979). "Relaxation and collective motion in superconductors: a two-fluid description." *Annals Phys. (NY)* 119.
- A. B. Pippard, J. G. Shepherd and D. A. Tindall (1971). "Resistance of Superconducting-normal interfaces." *Proceedings of Royal Society, (London)* **A 324** 17.
- J. P. Romagnon, A. Gilabert, J. C. Noiray and E. Guyon (1974). *Solid State Communications* **14** 83.
- A. Rothwarf and B. N. Taylor (1967). *Physical Review Letters* **30** 167.
- J. M. Rowell (1973). *Physical Review Letters* **30** 167.
- A. Schmid (1966). "A time dependent Ginzburg-Landau equation and its application to the problem of resistivity in the mixed state." *Phys. Kond. Materie* **5** 302.
- G. Schon and V. Ambegaokar (1979). *Phys. Rev. B* **19** 3515.
- J. Seto and T. van Duzer (1971). *Appl. Phys. Lett.* **19** 488.
- S. Shapiro (1963). *Phys. Rev. Lett.* **11** 80.
- W. C. Stewart (1968). "Current-Voltage characteristics of Josephson junctions." *Appl. Phys. Lett.* **12** 277.
- Y. Tanaka and M. Tsukada (1993). *Phys. Rev. B* **47** 287.
- M. Tinkham (1996). "Introduction to Superconductivity." Singapore, McGraw-Hill Book Co.
- M. Tinkham and J. Clarke (1972). *Phys. Rev. Lett* **28** 1366.
- W. J. Tomasch (1965). *Physical Review* **139** 746.
- D. Twerenbold (1986). *Physical Review* **B34** 7748.
- K. Usadel (1970). *Physical Review Letters* **25** 560.
- R. B. Vandover, A. Delozanne and M. R. Beasley (1981). "Superconductor-Normal-Superconductor Microbridges - Fabrication, Electrical Behavior, and Modeling." *Journal Of Applied Physics* **52**(12) 7327.
- J. R. Waldram (1996). "Superconductivity of metals and cuprates.", (Bristol, Institute of Physics Publishing).

K. Wan, A. K. Jain and J. E. Lukens (1989). "Submillimeter wave generation using Josephson junction arrays." *App. Phys. Lett.* **54** 1805.

N.R. Werthamer (1963). *Phys. Rev.* **132** 2440

F. K. Wilhelm, A. D. Zaikin and A. A. Golubov (1997). "Coherent charge transport in superconducting/normal proximity structures." *J. Low Temp. Phys.* **106** 297.

E. L. Wolf (1985). "Principles of Electron Tunneling Spectroscopy." (New York, OUP).

# Chapter 3

---



Picture of the Devices rig.

## Experimental methods

## 3.1. Introduction

This chapter describes the majority of the experimental methods that were used for the work reported in later chapters. To avoid device failure there are many factors during the fabrication and measurement processes that must be controlled exactly. For device engineering, sound experimental methods are, therefore, crucial.

The first part of the chapter gives a detailed guide for the preparation of substrates, and the deposition of thin-films. Second, a detailed procedure is given for the patterning of trilayer films for use in the SIN tunnel junction work. Third, the fabrication of silicon nitride ( $\text{Si}_3\text{N}_4$ ) membranes, used for making SIN- and SNS- junction based devices on membranes, is explained. Fourth, a brief background is given to the operation and uses of a Focussed Ion Beam (FIB) instrument, used in all the SNS junction based work. Finally, an explanation is given of the apparatus used to measure the devices.

## 3.2. Substrate Preparation

### 3.2.1. Background

As in any construction process one of the keys to success is to use good foundations. There are a number of considerations that have to be made when choosing a suitable substrate. Some of these considerations are: thermal and electrical properties; robustness; availability; and cost. In this work different substrates have been used. For the single island SIN tunnel junction work r-plane sapphire and double-sided 1- $\mu\text{m}$  thick  $\text{Si}_3\text{N}_4$  coated Si (100) substrates were used. R-plane sapphire was used during the early development work of making SIN devices on membranes due to the laboratory's familiarity with it and its robustness. For most of the SNS junction work, Si and oxidised Si coated Si substrates were used due to its low cost, and good availability in the laboratory. For both the SIN- and SNS-junction based work making devices on membranes,  $\text{Si}_3\text{N}_4$  (1  $\mu\text{m}$  thick) coated Si was used. Twente MicroProducts Ltd. supplied these substrates, which were fabricated using low-pressure chemical vapour deposition to coat Si with  $\text{Si}_3\text{N}_4$ . Although this type of substrate is not as robust as any of the other substrates used here, the low thermal conductivity of  $\text{Si}_3\text{N}_4$  makes it a very attractive material for use in the non-equilibrium experiments pursued in chapter 7. In addition, the fabrication of  $\text{Si}_3\text{N}_4$  membranes is well understood, making fabrication relatively straight forward and is discussed later in section 3.5.

### 3.2.2. Cleaning

For each type of substrate used, the same procedure that is described here was employed to clean and prepare it for film deposition. Great care had to be employed, as any contaminants or defects on the substrates' surfaces could severely degrade the resulting electrical performance of a fabricated device. Firstly, the substrates were cut into useful sample sizes from the delivered wafers, using a dicing saw. Two protective layers of resist and wax were coated onto the wafers before cuttings so as to minimise damage to the wafer's surface. The sizes used varied, and depended upon the device being made. Table 3.1 displays the type of device with the corresponding substrates and dimensions used.

DEVICE TYPE	SUBSTRATE(S) USED	SUBSTRATE SIZE (LENGTH × WIDTH)
Single island SIN tunnel junction	r-plane sapphire	12.5 mm × 3.5 mm
SNS junction	Si and Oxidised Si coated Si	5 mm × 10 mm and 10 mm × 10 mm
SIN- and SNS- junction based devices on a membrane	Si <sub>3</sub> N <sub>4</sub> (1 μm thick) coated Si	10 mm × 10 mm

**Table 3.1: The types of devices, substrates and sizes used**

Secondly, the substrates were given a thorough cleaning to remove any resist, wax or other contaminants remaining from the cutting process. The cleaning process consisted of:

- Careful warming of the samples until the wax melts and then dipped in acetone to dissolve the resist.
- Leave substrates to soak in chloroform over-night.
- Ultrasound substrates in chloroform for at least ½ hour.
- Ultrasound substrates in acetone for at least ½ hour.
- Gentle wiping with a cotton bud soaked in acetone on a clean glass microscope slide and vigorous airbrushing with acetone.
- Previous step is repeated, but use absolute alcohol instead of acetone.
- Dry samples using filtered compressed air and place immediately in a glass dish ready for transfer to the deposition system.

The use of Si<sub>3</sub>N<sub>4</sub> coated Si substrates was new to the lab so a quality check of the substrates was made by the author. A sample of the substrate was cleaned and examined in microscopic detail, using an atomic force microscope. A typical image of the surface is shown in figure 3.1. It shows that the majority of the surface is reasonably flat with bumps

present every 1-3  $\mu\text{m}$ . These are probably by-products of the coating process, and did not seriously inhibit the electrical performance of the membrane-based devices.

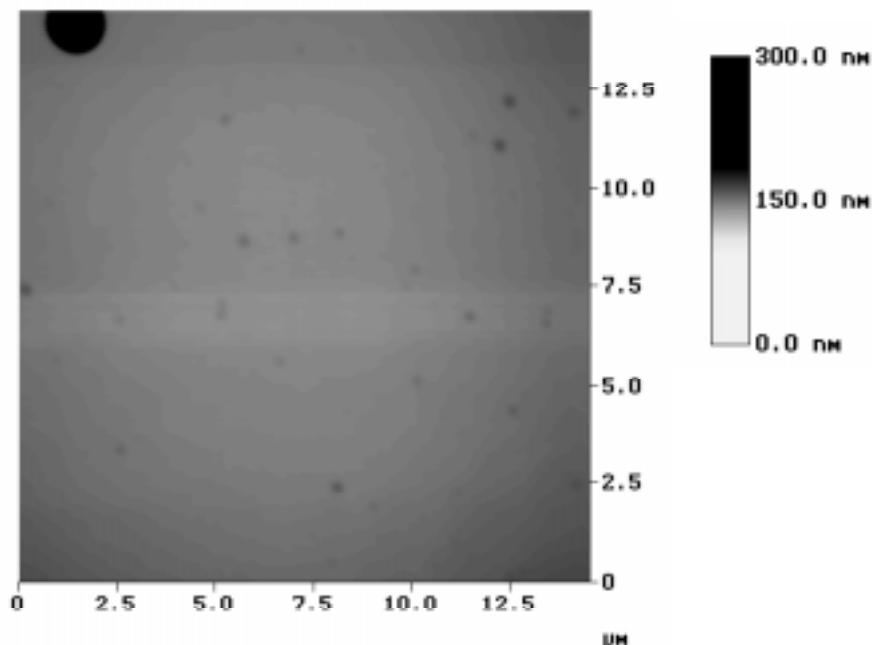


**Figure 3.1:** Image of the surface of a  $\text{Si}_3\text{N}_4$  coated Si substrate taken using an atomic force microscope (taken by the author with the aid of Mr. John Durrell).

### 3.3. Polycrystalline thin film deposition

The thin-films described here were deposited, with the assistance of Dr. Mark Blamire, Dr. Gavin Burnell, and Dr. Zoe Barber, using an Ultra-High Vacuum (UHV) magnetron sputtering system, and is shown schematically in figure 3.2. The system is fully described in (Blamire 1988). The liquid  $\text{N}_2$  jacket around the inner chamber, shown in the figure, was designed to trap contaminating gases. Pressures as low as  $2 \times 10^{-7}$  Pa were routinely reached.

The system could be used for magnetron sputtering of many different kinds of materials and substrates by simply swapping one sputtering flange, containing the magnetron targets and substrates, for another. Two flanges, one containing two targets and the other containing four targets, were used. Both were operated in the same way and a schematic of the dual system is shown in figure 3.3. For most depositions the substrate holder was rotated during the film deposition, and the rate of film growth could be controlled by controlling the speed of rotation and thus the length of time of the substrates were exposed to the target. A

computer controlled stepper motor mounted to the axle allowed the necessary precise rotation speed of the stage. Blanking of the substrates was achieved by rotating the stage away from the active magnetron.

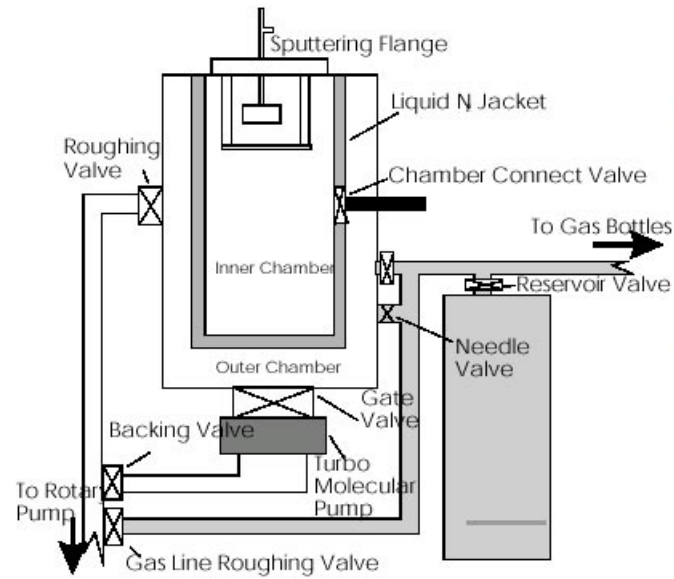


Figure 3.2: Schematic of the UHV magnetron sputtering system (picture courtesy of Dr. Gavin Burnell).

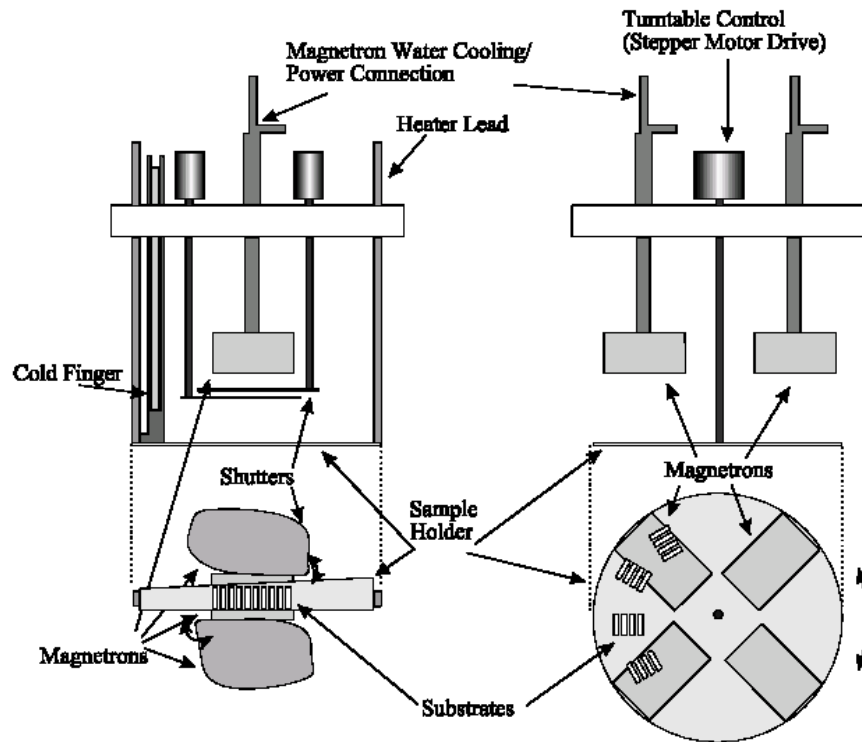


Figure 3.3: Schematics of the two flanges used in this work (picture courtesy of Dr. Gavin Burnell).

Before commencing the deposition, the system was allowed to pump overnight (i.e. at least 9 hours), during which it was heated to approximately 120 °C for 4 hours during a bake out procedure. After this point a test for any leaks in the system were made by checking the partial pressure of O<sub>2</sub> was  $<5 \times 10^{-8}$  Pa. Sputtering was carried out in Ar gas (>99.999 999 % purity), at pressures between 0.5 and 2 Pa, with either a static, or a continuous flow of gas, depending on the material being sputtered. For deposition of polycrystalline Nb and W, a constant sputtering power was maintained using computer controlled power supplies. The interface electronics between the computer and power supply was designed and built by the author. The oxide barriers used in the SIN tunnel junction work were formed by thermal oxidation, using a constant pressure of 99.999 99 % O<sub>2</sub> at ambient temperature. All the stages in the trilayer deposition process (SIN work) and the bilayer process (SNS work) were carried out without breaking the vacuum. This had the advantage of forming clean interfaces between layers and minimising the chance of defects in processed devices.

RUN NUMBER	SUBSTRATES USED	BOTTOM LAYER (Thickness/ nm)	MIDDLE LAYER (Thickness/nm)	TOP LAYER (Thickness/nm)
8917	r-plane sapphire Si <sub>3</sub> N <sub>4</sub> coated Si	Nb(90)	Al(12)/Al <sub>2</sub> O <sub>x</sub> /Al(12) Using O <sub>2</sub> at 1kPa for 30 minutes	W (110)

**Table 3.2: Trilayer deposition parameters**

RUN NUMBER	SUBSTRATE(S) USED	BOTTOM LAYER (Thickness /nm)	TOP LAYER (Thickness /nm)
8960	Si	Au (100, 200, 400)	Nb (75 )
9029	Si	Au (50, 100, 125)	Nb (75)
9235	Si	Au (125)	Nb (75)
9136	Si	Cu (20,30,70,100)	Nb(75)
9333	Oxidised Si coated Si	Cu (70)	Nb (75)
9633	Oxidised Si coated Si	Cu(70)	Nb(75)
9901	Oxidised Si coated Si Si <sub>3</sub> N <sub>4</sub> coated Si	Cu(70)	Nb(75)

**Table 3.3: Bilayer film deposition parameters**

The deposition rates for most of the materials used were already known (Burnell 1998). The details of the deposition runs from which SIN- and SNS- junction based devices were made, are listed in tables 3.2 (trilayer) and 3.3 (bilayer), respectively. Each table details the

types of substrates used, the materials that were deposited, the order they were deposited in, and their thicknesses.

### 3.4. Fabrication of single island SIN junctions

The fabrication of the SIN tunnel junctions used in the devices, described here, used a mask design, designed by Dr. Ikuo Kanno, and is shown schematically in figure 3.4. The devices were made using conventional optical photolithographic techniques and standard thin film processing routes. Figure 3.5 shows schematically the fabrication process used.

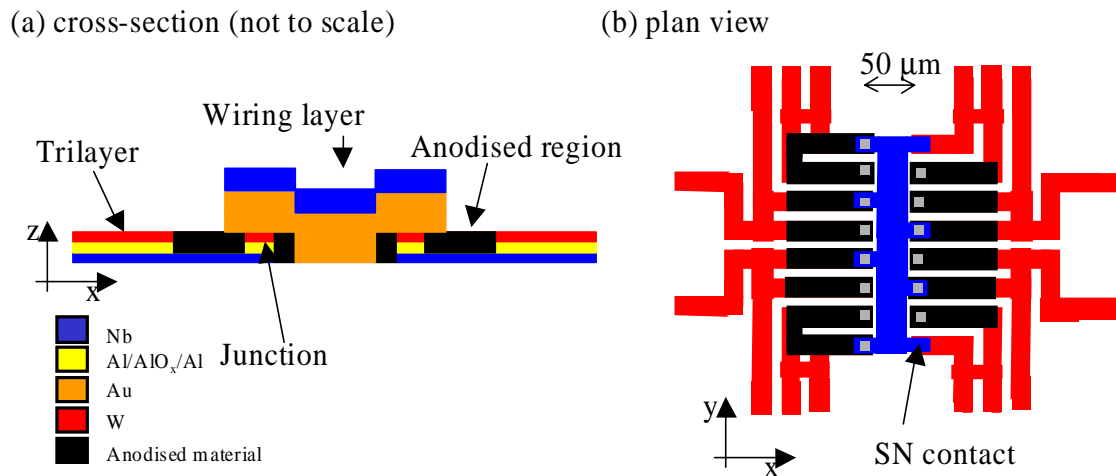


**Figure 3.4:** Schematics of (a) cross-section and (b) plan view of the single island SIN junctions design.

Hoechst AZ 1529 resist was used for most of the work described here, however, in the initial developmental work Shipley S1400-31 microposit resist was used. It was discontinued by the manufacturer, hence the change to AZ1529. Changing the resists caused considerable fabrication problems, which were very time consuming to solve. This meant changing the original process, which used a trilayer containing a top layer of Nb to W. This was due to the incompatibility of Nb with the modified process, and the reasons for the change are reported by Burnell (Burnell 1998). The sputtering deposition parameters of W had to be fully characterised by the author and are shown in table 3.4.

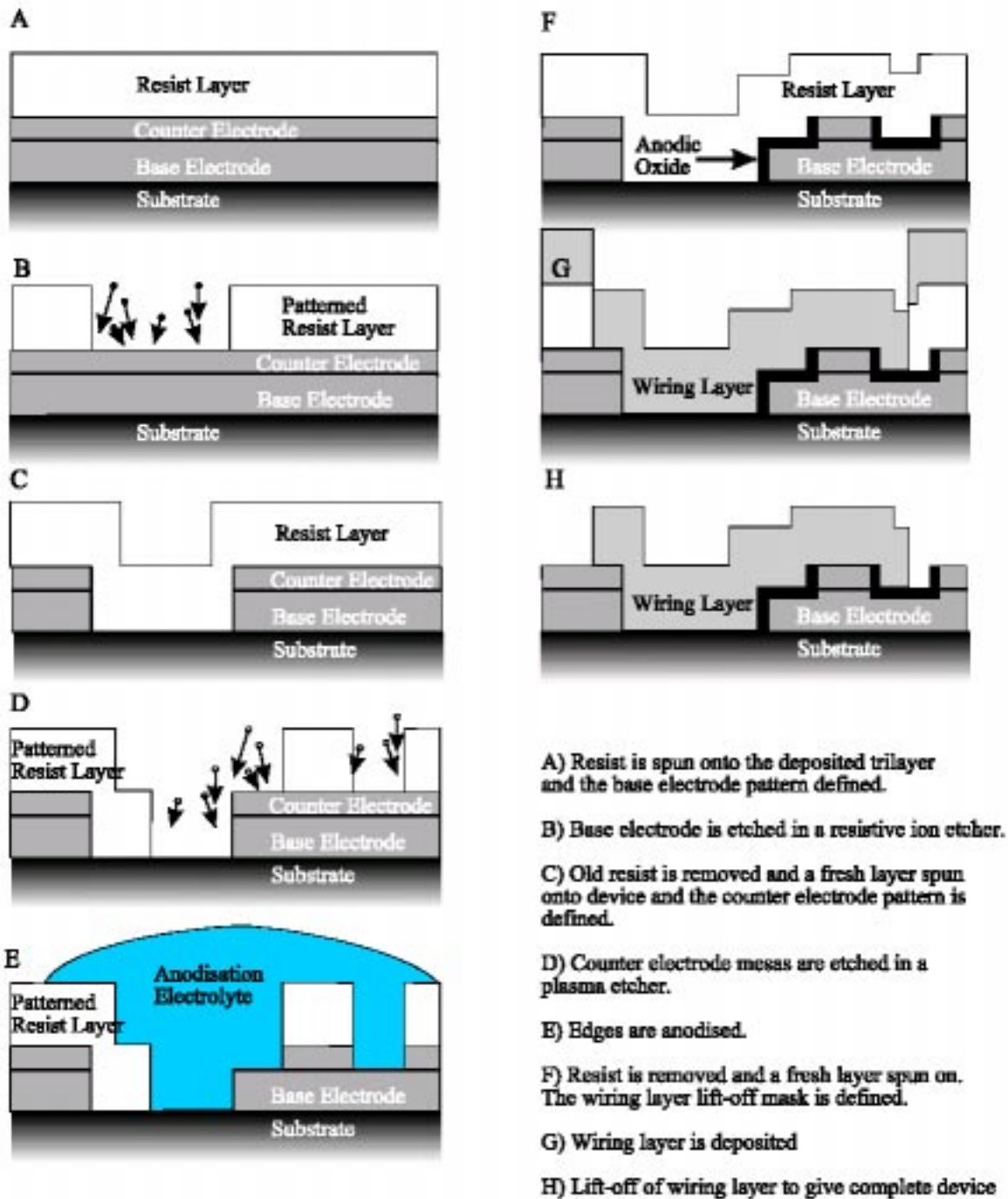


Figure 3.5: Processing steps for a typical device (picture courtesy of Dr. Gavin Burnell)

MATERIAL	AR PRESSURE (Pa)	GAS	SPUTTERING	POWER (W)	DEPOSITION RATE (nm min <sup>-1</sup> )
W	2.5			30	0.3

Table 3.4: Deposition parameters for polycrystalline W

### 3.4.1. Base layer definition

Resist was placed onto a cleaned sample, spun at 6,000 rpm for 30 s, baked at 100 °C for 1 minute. The sample was then placed in a mask projection system, which had a resolution of approximately 2  $\mu\text{m}$ . A mask that defined the base layer was loaded into the system, and then carefully focused onto the sample. Light from a Hg vapour lamp was projected through the mask and onto the sample for 35 s. The sample was developed, using developer solution in the ratio developer to water of 4:1. The sample was dried with compressed air and placed in a Reactive Ion Etcher (RIE). A 10 minute etch of  $\text{SiCl}_4$  plasma, at a pressure of 64 Pa and power of 60 W, was used. After this a 2½ minute plasma of  $\text{CF}_4$ , at 68 Pa was run to passivate any chlorine radicals remaining in the chamber. Any remaining radicals could form Nb chloride “worms”, defects which reduced the resulting device’s performance (Warburton 1993). Finally, the sample was sprayed with acetone, in order to strip the remaining resist, and then it was dried.

### 3.4.2. Mesa etch and anodisation

A mask defining the geometry of the junctions was patterned onto the sample. The exposed W layer had to be removed before anodisation, due to its incompatibility with anodisation. This was achieved by plasma etching with  $\text{CF}_4$ , for which Al is an effective etch-stop. Prior to etching with the  $\text{CF}_4$  plasma, a cleaning stage in an  $\text{O}_2$  plasma (85 W power, for one minute) was employed to remove any residual organic material from the region. This was followed by the  $\text{CF}_4$  etch (85 W for 2 ½ minutes). The completeness of the etch could be easily verified as Al is significantly brighter when viewed under white light than W.

To seal any holes, formed in the resist during the plasma etches, the sample was then re-baked at 110 °C. A drop of buffered electrolyte was carefully pipetted onto the exposed area of the sample (Kroger 1981). The resist on one of the electrical pads was carefully stripped off using a cotton bud soaked in acetone. Electrical contact probes were placed in contact with the pad and the droplet. Using the probes a current of approximately 15  $\mu\text{A}$  was then passed through the sample and a chart recorder measured the changes in the resistance of the sample. The changes in resistance were due to the systematic oxidation of the trilayer by the electrolyte. As time proceeded the oxide built up further down into the material and changes in the rate of resistance change corresponded to the different layers. Anodisation was stopped as soon as the oxidation process had reached the bottom layer.

This technique not only electrically isolated the material around the junctions but, also, provided a good diagnostic of the deposited film's quality, as shown by the sharpness of the resistance changes. Finally, the resist was stripped off the sample and then it was dried.

### 3.4.3. Wiring layer deposition using lift-off

The wiring layer design consisted of an island, covering half of the junctions, and small wires connecting the other junctions to their adjacent, connected, junctions. A resist layer was spun onto the substrate at 4,000 rpm for 30 s, baked at 100 °C for 1 minute, soaked in chloro-benzene for 2 minutes, and then re-baked for 1 min. This process hardened the top layer of the resist and resulted in an overhang of around 1  $\mu\text{m}$  at the edges of the resist. This overhang ensured the lift-off layer was removed successfully.

The sample was then put into an UHV sputter and ion mill deposition system, housed in the cleanroom. Using an oil diffusion pump the system reached a base pressure of approximately  $5 \times 10^{-5}$  Pa. The system contained an Ar ion beam milling gun and two magnetrons, equipped with Nb and Au targets. In order to achieve a high Nb deposition rate the magnetron with the Nb target and the sample holder was water-cooled. This was required to produce superconducting Nb in what tended to be a relatively dirty system.

Prior to deposition, the two targets were cleaned, by pre-sputtering. To avoid contaminating the sample the chip holder was carefully angled away from the targets. After this the chip was subjected to a brief Ar ion mill to remove any organic contaminants from the surface to be deposited on. The mill time and the beam's voltage and current were critical in the success of the device. Too little milling and the surfaces would not be cleaned and there would be a significant contact resistance between the surface and the deposited layer. Too much milling disrupted the oxide barrier, creating micro-shorts in the barrier and ultimately, harming the device's performance. After considerable effort the optimum mill time was found to be 5 s with a beam voltage of 500 V and current of 7.5 mA. After the ion mill an Au layer of approximately 500 nm was deposited, followed by a Nb layer of approximately 150 nm.

The chip was unloaded from the system and placed in ultra-sounded acetone for 10 seconds before being left to soak for at least an hour, or until the film around the wiring pattern lifted-off the chip. To prevent the wiring layer from peeling off, the sample was carefully dried, using a cloth rather than compressed air.

#### 3.4.4. Anodisation ring break

A wire ring, defined in the base layer stage, connected all the junctions together for the purposes of anodisation. It was necessary, therefore, to remove the ring before any characterisation of the junctions could be performed. A layer of resist was applied to the sample in the usual way and a mask containing the ring-break design was exposed onto the sample and developed. It was then placed into the RIE system and a plasma etch was performed, using the same procedure as described in section 3.4. Once completed, the resist was carefully removed by placing the sample in ultra-sounding acetone for 5 seconds and then left to soak for 20 minutes.

### 3.5. Fabrication of a silicon nitride membrane

Both the thin films used for the SNS- and SIN- junction based devices were successfully deposited onto  $\text{Si}_3\text{N}_4$  coated Si substrates, allowing devices on membranes to be fabricated and characterised.  $\text{Si}_3\text{N}_4$  has a very low thermal conductivity so by placing a device on a  $\text{Si}_3\text{N}_4$  membrane the effect of thermal transport in the substrate can be neglected. The advantage of this will be explained in further detail in chapter 7.

The membrane although strong was very brittle so it was always manufactured after the device had been fabricated. A hole in the  $\text{Si}_3\text{N}_4$  was made on the backside of the sample exposing the Si underneath which was then chemically etched. Given a suitable etchant, the etching would stop at the  $\text{Si}_3\text{N}_4$  on the front-side of the sample (where the device was sitting) producing a membrane. Unfortunately, the only known etchants, also, etch the metals in the thin films. Great care was, therefore, taken in order to avoid contact between the film and the etchant. The following procedure was adopted to make the membrane.

A layer of resist was spun and baked onto both sides of the sample. A square was defined in the resist on the backside of the sample. The sample was put in the RIE with the square exposed. A  $\text{CF}_4$  plasma was used for 25 minutes to etch through the  $\text{Si}_3\text{N}_4$ . The sample was then cleaned using acetone and then a protecting layer of resist was spun and baked onto the front-side of the sample. The sample was placed in a holder, specially designed by the author, shown in figure 3.6. The holder was put into a beaker, and then submerged in 33%(wt) KOH heated to 87-93 °C. KOH acts as the etchant so the sample holder was designed so the alkali could not reach the device side of the sample.

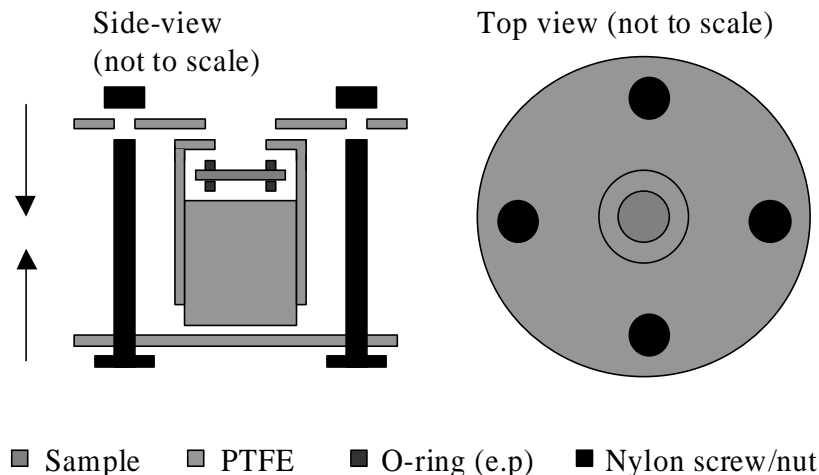
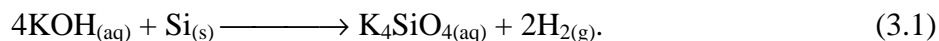


**Figure 3.6: Schematic of the chip holder.**

The reaction of Si with KOH is well documented as an anisotropic etch of Si (Finne 1967; Bassous 1977). The reaction at standard temperature and pressure is



KOH etches the (100) surface of Si at a rate about 400 times its etch rate on the (111) surface (Green 1994). A schematic diagram of the cross-section of a Si etched substrate with the membrane is shown in figure 3.7.

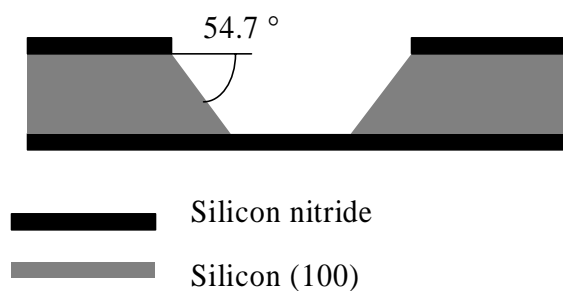


**Figure 3.7: Schematic of a cross section of a  $\text{Si}_3\text{N}_4$  membrane.**

The etch rate was found to be  $1.8 \pm 0.2 \mu\text{m min}^{-1}$ . This agreed well with documented results e.g.  $1 \mu\text{m min}^{-1}$  for 20%(wt) KOH at  $80^\circ\text{C}$  (Gajda 1994). Other more exotic chemicals exist for selectively etching Si including hydrazine (Gajda 1994). These were not investigated because of the additional hazards associated with them.

The e.p. O-rings, used to cushion the sample inside the holder, were quite resistant to KOH. They acted also to trap air around the front side of the sample in order to prevent contact between the etchant and the device.

The etch finished when there were no more hydrogen bubbles emanating from the sample. The sample holder was then taken out of the KOH solution while observing the necessary safety precautions associated with the highly corrosive solution. The holder was placed immediately in hot water (approximately 70°C) to prevent crystallisation of  $K_4SiO_4$  onto the membrane. The holder was opened, and the resist on the sample was removed by placing the sample in a beaker of acetone for a short while.

Experience showed that the membranes would withstand the sample being dropped, lightly airbrushed, and could be heated to temperatures between 0.3 and 400 K, all with no ill-effects to the membrane. Ultrasound, vigorous airbrushing, and poking the membrane, however, were all found to be destructive.

### **3.6. The focused ion beam instrument**

In recent years the FIB instrument has become an essential tool for the microelectronics industry. Their flexibility in allowing both in-situ high resolution imaging, and modification of fine features on a sample, makes them powerful tools. Since the late 1980s when commercial FIB instruments first became available, they have become popular in the semiconductor industry. Huge commercial effort has been saved through their use because they can be used to quickly inspect and modify faulty circuits that arise from problems in their manufacture. These problems can then be swiftly addressed and the manufacture process can be corrected. As the increasing popularity and sophistication of these instruments increases it will become routine practice to make complex sub-micron scale devices with a high accuracy and reproducibility, pushing the frontiers of device physics further.

Examples of research where FIB instruments have been used include; lithography mask development (Speaks 2000); sample preparation for use in transmission electron microscopy (Altmann 1999); field emission transistors (Kim 1998); fabrication of tools for use in microsurgery (Vasile 1999).

A standard FIB instrument (FEI Inc. FIB200) was used throughout this work. An abridged version of the theory and operation, given in the instrument's manual, is given here.

A detailed description of the theory and operation of a FIB instrument can be found elsewhere (Young 1993; FEI 1996).

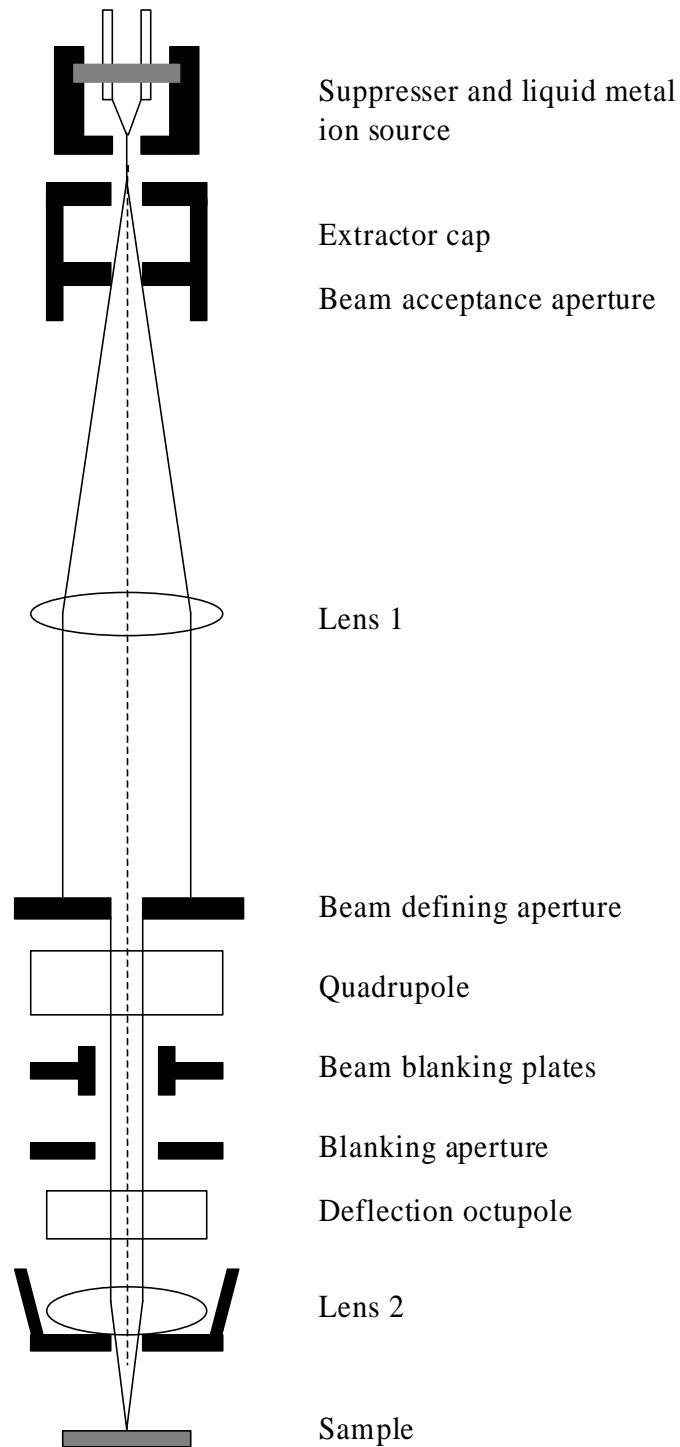


**Figure 3.8: Schematic diagram of a focused ion beam instrument**

The heart of an FIB instrument is the focusing column, shown schematically in figure 3.8. The column produces a beam of focused ions that travel to the sample. The column operates in a high vacuum environment ( $< 7 \times 10^{-5}$  Pa) to avoid interference with the beam from atmospheric gas molecules. A strong electric field is applied to the liquid metal (Ga) ion source at the top of the column. This extracts positively charged ions, normally at an extraction current of 2.2  $\mu$ A. They are then focused into a beam by two electrostatic lenses, a steering quadrupole, and an octupole deflector in the column. The ion beam passes through a small opening into the sample chamber (base pressure  $< 5 \times 10^{-4}$  Pa) where it strikes the sample, removing material through the physical sputtering process, also known as ion milling.

To minimise the diameter of the beam it is necessary to use the highest beam voltage and the smallest possible working distance. The column is operated at 30 kV, and the working distance is between 15 to 75 mm. The rate at which ions from the ion beam strikes the sample, known as the beam current, is controlled automatically by the variable aperture. The beam current setting can be changed in the range from 1 to 1,000 pA. For most of the work reported here beam currents of 1pA, 4pA, and 11 pA were used.

The ions striking the surface also generate secondary electrons and ions. The secondary electrons are detected and processed to form an image of the sample as the ion beam scans across the surface. The quadrupole steering plates controls the positioning of the beam and the octupole stigmator/deflection assembly provides scan and shift for fine field of view movement, as well as beam astigmatism correction. A scan control system enables milling of specified patterns into the sample.

To protect the sample from constant milling there is a beam blanking system in the focusing column. This system, when activated, diverts the beam away from the blanking aperture and into a Faraday cup. This system not only blanks the beam from the sample but, also, allows the beam current to be measured.

Although the construction of a FIB instrument has many similarities to a scanning electron microscope's, the limiting factor that determines the spatial resolution of the instrument is chromatic aberration rather than spherical aberration found in most scanning electron microscopes. This is due to the energy spread ( $\sim 5$  eV) in the ion beam. This means that the beam's diameter increases with larger apertures, and consequently, with increasing beam current.

The depths that the gallium ions penetrate the material can be calculated using Monte Carlo based calculations. Table 3.5 shows the calculated depths, using the SRIM2000 program (Biersack 1980), of Ga in various materials.

ELEMENT	STOPPING DISTANCE (NM)	LONGITUDINAL STRAGGLING (NM)	LATERAL STRAGGLING (NM)
Ta	8.4	7.3	5.7
Mo	9.9	6.4	4.6
Pd	8.8	6	4.3
W	7.2	6.3	4.9
Pt	6.8	6.1	4.7
Hf	10.3	8.8	6.8
Au	7.5	6.8	5.3
Nb	11.3	7	5.1
Fe	10	4.9	3.6
Zr	14.9	9.2	6.7
Si	25.7	8.7	6.7
Al	22.6	7.5	5.8
Ag	10.1	7	5
Zn	12	6.4	4.7
Pb	12.9	11.8	9.1
Cu	9.5	5	3.7

Table 3.5: Penetration distances of 30 keV Ga ions in different materials

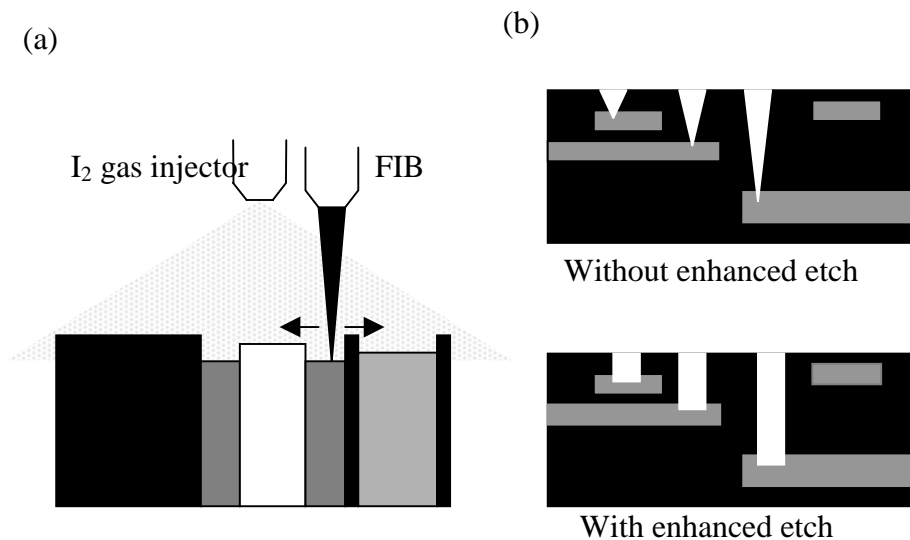


Figure 3.9: Schematic of cross-sections using (a) enhanced etch on different materials and (b) comparing trenches milled with and without enhanced etch.

The FIB instrument also has an  $I_2$  gas injection system. Using this system in conjunction with the ion beam, and an appropriate source gas, it is possible to deposit metal

or insulator films/structures onto the sample. In addition, the  $I_2$  gas injection system can be used with the ion beam to enhance the etching process. This enhanced etching process can be used for milling high aspect ratio holes, and increasing the chemical selectivity of the beam. Figure 3.9 shows the differences between milling with and without enhanced etch.

## 3.7. Measurement apparatus

### 3.7.1. Devices rig

The devices rig, built by Dr. Wilfred Booij and Dr. Gavin Burnell, contained all the room temperature electronics, needed by the various cryogenic probes used. The electronics were computer controlled, along with data acquisition and processing.

Measurements were obtained using an integrated dual current supply and low noise voltage amplifier set, connected to the device being measured. The current monitor signal and amplified voltage response, coming from the set, was digitised using a National Instruments LabNB<sup>TM</sup> 12 bit digitising analogue to digital converter board and the data processed by a LabVIEW<sup>TM</sup> program, largely written by Dr. Gavin Burnell and running on an Apple Macintosh<sup>TM</sup> Quadra 650. The software program is capable of recording up to 4 channels of data simultaneously whilst controlling a separate magnetic coil power supply and/or providing a controlled current to the device. Figure 3.10 shows a schematic of the measurement set-up.

#### 3.7.1.1. Computer analysis

The acquired data was saved to disc as a series of  $I$ - $V$  characteristics and was then analysed offline using various custom written LabVIEW<sup>TM</sup> programs that extracted and processed the desired data. For the work based on SNS junctions a program written by Dr. Wilfred Booij was used, and for the work based on SIN tunnel junctions a program written by Gavin Burnell and the author was used.

For the SNS work the junction's critical current was determined using a finite voltage criterion of  $0.5 \mu\text{V}$  and the normal state resistance was found by determining the slope at high bias.

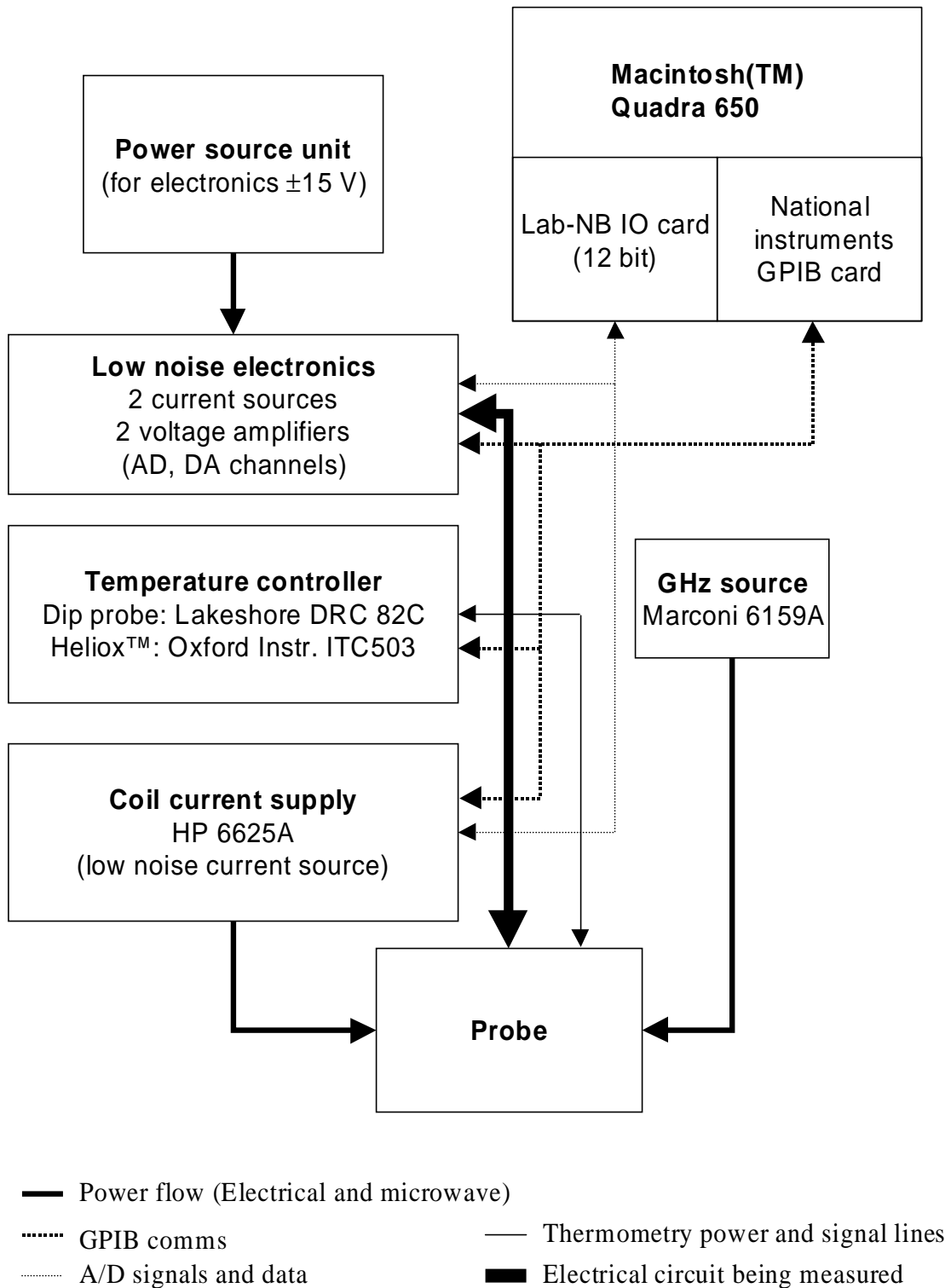


Figure 3.10: Schematic diagram of the devices rig

### 3.7.2. Dip probe

A dip probe, built by Dr. Wilfred Booij, was used for much of the work. It fits into a standard liquid helium dewar, and has a low thermal mass, making it easy and quick to use

compared with flow cryostat based systems. The bottom assembly of the probe consists of a Cu block to which a thin-film high power heater is attached. The sample that contained the devices was mounted, using either silver dag or nail varnish, on a custom designed sample holder that attached to the probe with a 19-way D-connector. Electrical connections between this and the holder were made by ultrasonic wiring bonding with 30  $\mu\text{m}$  Al wire.

Once the sample holder was clamped to the Cu block, a cylinder containing two pairs of Helmholtz coils could be slid over the sample. These coils were used to apply a magnetic field in both the perpendicular ( $z$ ) and in-plane directions ( $x$  and  $y$ ) of the order of 100 mT. Over this cylinder a  $\mu$ -metal cylindrical shield was placed. This reduced the ambient magnetic field to less than 320 nT (at room temperature). Microwave irradiation with a maximum frequency of 20 GHz could be applied to the sample through a rigid coaxial cable that ends in a dipole antenna that was directly situated above the sample. The microwave source used was a Marconi Instruments 6159A.

### 3.7.3. Oxford instruments Heliox™ Instrument

For some experiments temperatures below 4.2 K were needed so it was necessary to use an Oxford Instruments Heliox™  $^3\text{He}$  instrument. This is designed to fit into a standard helium dewar and can reach a base temperature of 0.3 K, although in practice this temperature is in the range 0.34-0.36 K, depending upon the thermal load on the instrument's sample holder and surrounding wiring. A schematic of this system is shown in figure 3.11. A condensed version of the operating manual is described here.

The sample space is pumped and then is cooled to 150 K using liquid  $\text{N}_2$ . The probe is then transferred to a helium dewar, and cooled by liquid He to 4.2 K. The  $^3\text{He}$  sorption charcoal is then heated while the 1 K pot is being constantly filled with helium from the dewar via a capillary and needle valve. A rotary pump is also constantly pumping the 1 K pot. The 1 K pot temperature then falls so that  $^3\text{He}$  condenses and runs down to the  $^3\text{He}$  pot on which the sample is mounted. The sample can then be cooled to base temperature by ceasing to heat the charcoal sorption pump, which will then start to pump on the  $^3\text{He}$ . The entire operation from loading to reaching base temperature takes between 3 and 4 hours. Temperatures in the range 0.3-1.5 K are achieved by heating the charcoal sorption pump to reduce its efficiency. For temperatures above this temperature control is more complicated. The sample can be directly heated by a heater mounted next to the probe holder and indirectly cooled by the 1 K pot. With practice, the full range of temperatures between 1.5 K

and 10 K was achieved, although stability could be a problem, with temperatures swings of up to 5% over periods of minutes were observed.

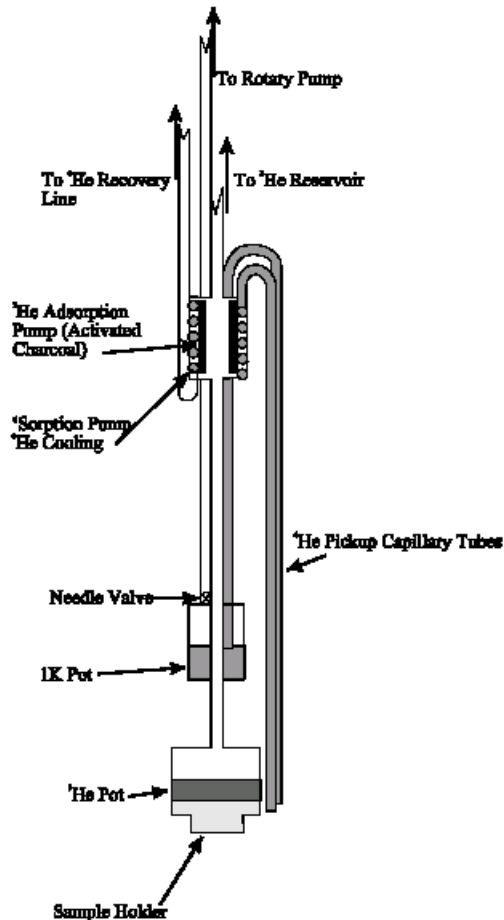


Figure 3.11: Schematic diagram of the Oxford instruments Heliox™ probe (picture courtesy of Dr. Gavin Burnell)

The sample was stuck down using either silver dag or nail varnish from the Colorgirl™ range onto a specially designed sample holder that fitted onto the probe's holder, designed by Dr. Gavin Burnell (Burnell 1998). The sample holder was then attached to the probe's holder using a 0.9" dual-in-line socket and two connecting bolts. Electrical signals pass from the sample to the electronics system through wire bonds from the sample to a printed circuit board on the sample holder. The DIL socket has permanently connected copper wires from the socket to a permanently mounted D-socket housed in the Heliox™. To reduce the thermal load of the wires they are thermally anchored to the 1K pot. In later measurements Nb alloy superconducting wires were used in order to reduce the thermal load further. The signal wires are then passed through an in-built connection port inside the probe

where the signals are then carried through the rest of the Heliox™ by standard copper cabling to a socket where the rig's electronics could be connected to.

A further improvement, made by the author, to the set-up was to reduce the electronic noise caused by the connecting electronics. A breakout box was mounted directly onto the probe's socket so the meter long cabling between the rig's electronics and probe's socket used previously was not needed. The breakout box contains shielding and in series 1 nF RC feedthroughs that reduce high frequency interference, a major source of noise.

### 3.8. References

- F. Altmann and D. Katzer (1999). "Cross-sectional specimen preparation from ICs downside for SEM and TEM-failure analyses using focused ion beam etching." *Thin Solid Films* **344** 609.
- E. Bassous, H. Taub and L. Kuhn (1977). *Appl. Phys. Lett.* **31** 135.
- J. P. Biersack (1980). "SRIM2000." Computer Program.
- M. G. Blamire, R. E. Somekh, Z. H. Barber, G. W. Morris and J. E. Evetts (1988). "Microstructure Effects On Electronic-Properties Of Nb/Al<sub>2</sub>O<sub>3</sub>/Nb Tunnel-Junctions." *Journal Of Applied Physics* **64**(11) 6396.
- G. B. Burnell (1998). PhD Thesis "Quasiparticle and phonon transport in superconducting particle detectors." Department of materials science and metallurgy. University of Cambridge, Cambridge.
- FEI (1996). "Focused ion beam workstation user's guide." 7451 N.E. Evergreen Parking, Hillsboro, OR, USA, FEI Company.
- R. M. Finne and D. L. J. Kline (1967). *J. Electrochem. Soc.* **114** 965.
- M. A. Gajda, H. Ahmed, J. E. A. Shaw and A. Putnis (1994). "Anisotropic etching of silicon in hydrazine." *Sensors and Actuators A-Physical* **40** 227.
- J. A. Green and B. E. Burns (1994). *J. Electrochem. Soc.* **141** 3182.
- H. Kim, T. Noda and H. Sakaki (1998). "Formation of GaAs/AlGaAs constricted-channel field-effect transistor structures by focused Ga implantation and transport of electrons via focused ion beam induced localized states." *Journal of vacuum science and technology B* **16** 2547.
- H. Kroger, L. N. Smith and D. W. Jillie (1981). "Selective Niobium Anodisation Process for Fabricating Joesphson Tunnel Junctions." *Applied Physics Letters* **39**(3) 280.

- R. Speaks (2000). CPGS report. Department of Materials Science and Metallurgy. University of Cambridge, Cambridge.
- M. J. Vasile, R. Nassar, J. Xie and H. Guo (1999). "Microfabrication techniques using focused ion beams and emergent applications." *Micron* **30** 235.
- P. A. Warburton (1993). PhD Thesis "Quasiparticle Trapping in Superconducting Heterostructures.", University of Cambridge.
- R. J. Young (1993). "Micro-machining using a focused ion beam." *Vacuum* **44** 353.

# Chapter 4

---



Picture of the FIB instrument used in this work.

## Using an FIB instrument to fabricate planar-bridge SNS junctions

## 4.1. Introduction

In the past four decades since Josephson junctions were first discovered there has been an on-going search for a fabrication route that produces reliable and high-quality junctions. The first junctions to be investigated were of the tunnel (SIS) type, as discussed in chapter 2.3. Today the most commonly used Josephson junction is the stacked tunnel junction, using Nb- and Al- based fabrication technologies (Kroger 1981; Schulze 1998; Fritzsche 1999; Zehnder 1999). For many applications, however, a junction with high impedance and no electrical hysteresis is desired. The SNS class of junction will, potentially, display both of these features. To-date the most reliable type of SNS junction has a stacked geometry, which has the inherent drawback of having low impedance.

The planar-bridge SNS junctions, described in chapter 2.3, has the potential to provide a high impedance, if a suitable material with a high resistivity is chosen. Van Dover (Vandover 1980; Vandover 1981) made the first systematic study of these types of junctions and confirmed they had good electrical properties. The junctions were made using wet-etch and plasma etch techniques on superconductor/normal-metal bilayer tracks. For each technique, they found that the electrical properties of junctions were not reproducible. This poor reproducibility made the junctions useless for most applications. Other attempts at making suitable planar junctions were made using electron- (Hirose 1997), ion- (Harris 1977), and x-ray-(Blocker 1978) beam based techniques. In all cases, however, their reproducibility was found to be poor. This was largely due to the high sensitivity of the Josephson current to the microstructure and dimensions of the normal-metal barrier.

In this chapter a novel fabrication route for making planar-bridge Josephson junctions using an FIB instrument, has been developed and investigated. It is demonstrated that a junction can be made with a variation in its critical current,  $I_C$ , and normal state resistance,  $R_N$ , of less than 10 %. The fabrication process is, therefore, more reliable than any other previously documented one for this type of junction. This is due to the high degree of control, allowed by the FIB instrument, over the dimensions of the junctions. The closest study to this work is that of Van Dover (Vandover 1980; Vandover 1981). For their Nb/Cu bridges measured at 1.5 K they recorded poorer electrical properties than the junctions measured here at 4.2 K.

## 4.2. Fabrication

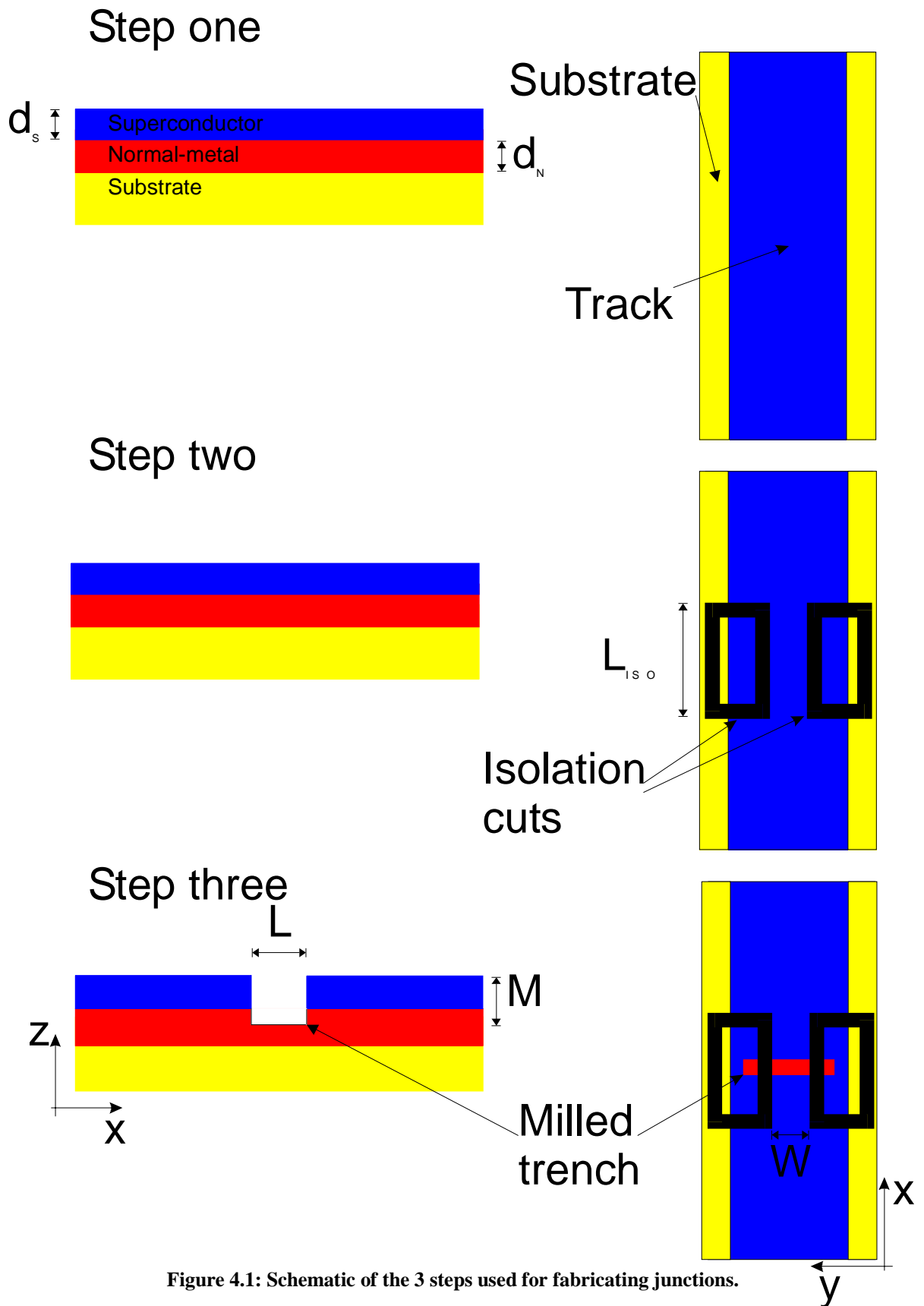
### 4.2.1. Overview

Although the detail of the fabrication process described here has evolved considerably, the essence of the process has remained the same and can be described in 3 consecutive steps, shown schematically in figure 4.1. The first step defines the conventional wiring of the sample, and the second and third steps are performed using the FEI200 Inc. FIB instrument, as described in chapter 3.6.

In the first step, a patterned bilayer (superconductor/normal-metal) thin-film sample containing tracks and connecting tracks is made. The bilayer is deposited onto a Si based substrate in a UHV magnetron sputtering system (chapter 3.3), and consists of a bottom layer of normal-metal and a top layer of superconductor. The tracks where the junctions would be eventually placed and connecting tracks are patterned onto the bilayer using AZ1529 resist and a Karl Suss MJB3 contact mask aligner (resolution  $\sim 1 \mu\text{m}$ ). The exposed regions of the bilayer are then removed by ion milling using the UHV sputter and ion mill system, described in chapter 3.4. The same ion mill gun parameters described in chapter 3.4.3, and a mill time of 2 minutes are used.

The second step consists of using the FIB instrument to make two rectangular cuts through the film and into the substrate, along the edges of a track where the junction would eventually be placed. The cuts restrict the width of the junction, providing a uniform path for the current to cross the junction, and isolating the edge of the track from the junction. It is important to isolate the edges of the tracks from the junction region to prevent any unwanted electrical micro-shorts around the edge degrading the junction's performance.

Finally, in the third step, the FIB instrument is used to make the junction by milling a trench through the superconductor layer, across the width of the track thus, leaving a normal-metal link under the trench.



## 4.2.2. Early attempts

### 4.2.2.1. Junction fabrication using the FIB instrument

Initially junctions were made in Nb (75 nm)/Au tracks on a Si substrate. The thickness of the Au layer and the width of the junction were varied in order to optimise their electrical performance. In the initial attempts the rectangular cuts (step 2) were made by removing entire rectangular blocks of film around the edges of the track. This proved to be time consuming, and increased the risk of damaging the rest of track due to drift of the beam. Instead, deep rectangular cuts through the bilayer and into the substrate were made. The junction trench (step 3) was made using a beam current of 1 pA and enhanced etch was employed, described in chapter 3.6, to make a *line* cut. Here, the beam is swept back and forth along a line and stops when it has made a pre-calculated number of sweeps.

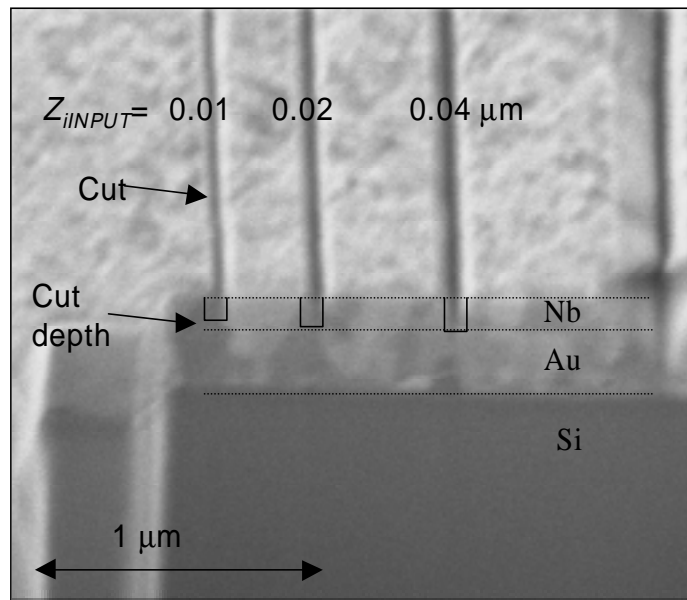


**Figure 4.2:** View taken from a  $45^\circ$  tilted elevation of cuts made into a Nb(75 nm)/Au (200 nm) thin-film on a silicon substrate using an FIB instrument.

The software controlling the beam uses a calibrated mill rate of the material and the beam current to convert the user-specified depth,  $Z_{INPUT}$  [ $\mu\text{m}$ ], into the required number of sweeps made by the beam. Figure 4.2 shows a series of cuts of varying depths into a Nb/Au track; each cut is labeled with the value of  $Z_{INPUT}$  used. The image shows that the junction length (i.e. the width of the cut's cross-section) also varied with depth; the deeper the cut the longer the junction. This is thought to be due to the increased effect of erosion on both sides of the trench by material from the bottom of the trench resputtering around the trench. This

effect increases as the beam cuts into the Au layer because more material is ejected from the bottom of the trench, a consequence of the Au mill rate being higher than Nb.

Initially, the widths of the junctions were varied from 4-8 $\mu\text{m}$ . The  $R_N$  of each junction was found, however, to be very low ( $\sim\text{m}\Omega$ ) resulting in a low  $I_C R_N$  product, typically between 0.6 to 3.1  $\mu\text{V}$  at 4.2 K. The typical  $I$ - $V$  characteristics of a junction whose width was 4  $\mu\text{m}$  is shown in figure 4.3. It clearly shows there is a lot of electronic noise present because the  $I_C R_N$  product is comparable to the voltage noise of the rig ( $\sim 1$   $\mu\text{V}$ ). To increase the signal to noise ratio  $R_N$  was, therefore, increased by reducing the width to 0.5  $\mu\text{m}$ .

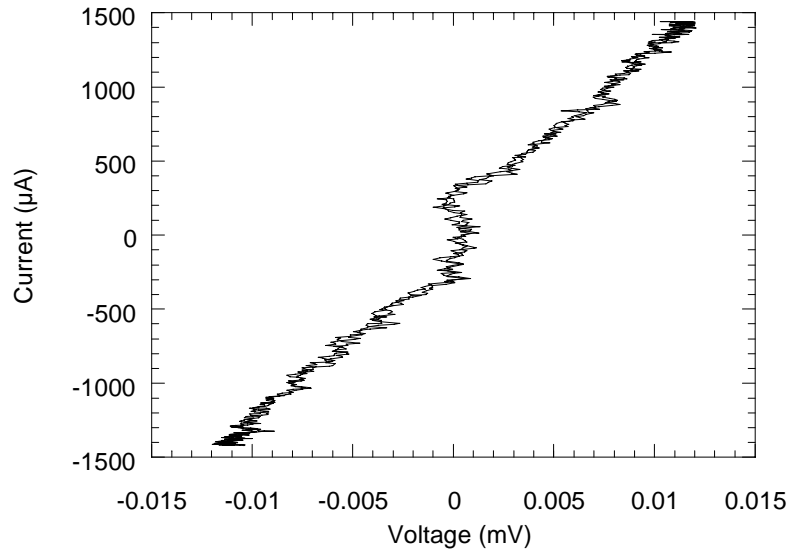


**Figure 4.3: I-V characteristics at 4.2 K of a Nb/Au(200 nm)/Nb junction,  $Z_{\text{INPUT}}=0.07$   $\mu\text{m}$  and  $W=4$   $\mu\text{m}$ .**

#### 4.2.2.2. Junction characteristics

Confirmation of the existence of junctions were made by measuring the current-voltage ( $I$ - $V$ ) characteristics of the junctions using the 4.2 K dip probe described in chapter 3.7.2, which included both magnetic field coils and a microwave antenna. All measurements were taken at 4.2 K. Figure 4.4 shows an image of a typical junction, taken using a scanning electron microscope, and clearly shows the fine isolating cuts made by the FIB instrument. Figure 4.5 shows the  $I$ - $V$  characteristics of a typical junction together with its response to microwaves (13 GHz), and figure 4.6 shows its response an applied magnetic field

perpendicular to the plane of the film ( $z$ -direction). Shapiro steps, as described in chapter 2.3.4, were observed in its  $I$ - $V$  characteristics when the junction was irradiated with microwaves at a voltage spacing of  $\hbar\omega/2e$ . At certain magnetic field strengths the  $I_C$  was almost completely suppressed. Overall, the response resembles the expected Fraunhofer pattern, and any deviations are due to the noise present in the  $I$ - $V$  characteristics; a voltage criterion was used to measure the  $I_C$ . The suppression of  $I_C$  in both the magnetic and microwave responses clearly demonstrates the Josephson junction behaviour.

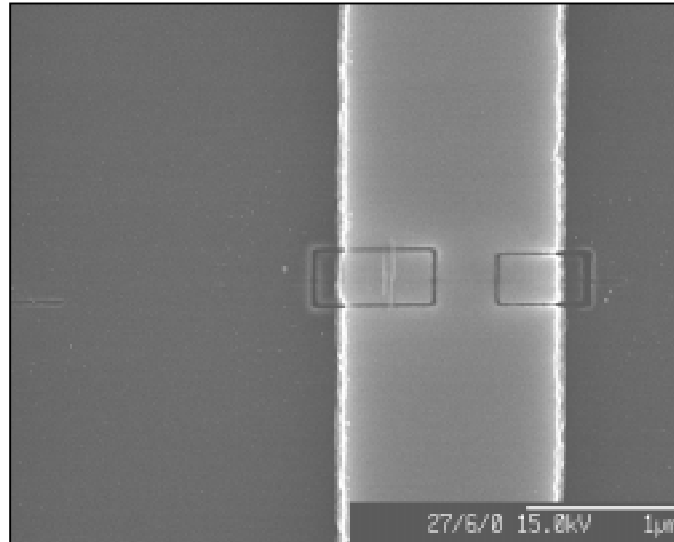


Figure 4.4: Image of a completed junction taken using a scanning electron microscope

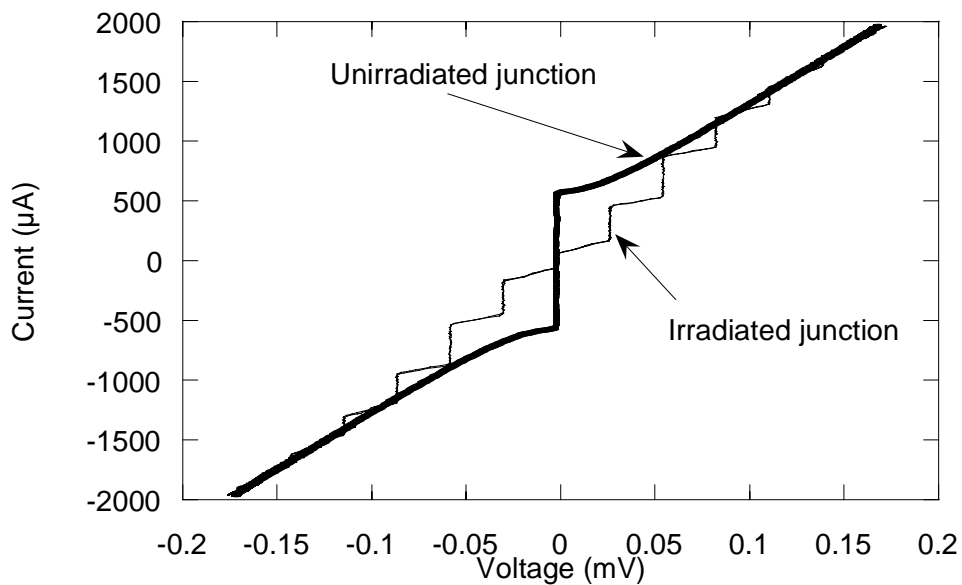
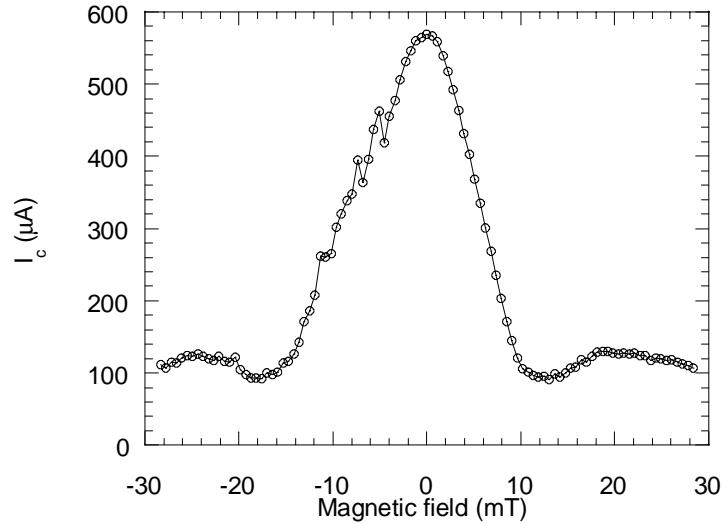


Figure 4.5:  $I$ - $V$  characteristics at 4.2 K of a Nb/Au(100 nm)/Nb junction ( $Z_{\text{INPUT}}=0.01$ ,  $W=0.5 \mu\text{m}$ ) showing both the unirradiated junction  $I$ - $V$  and the Shapiro response to microwave radiation (13 GHz).



**Figure 4.6: The variation of the critical current ( $I_c$ ) with an applied magnetic field at 4.2 K of a Nb/Au(100 nm) junction,  $W=0.5 \mu\text{m}$ .**

#### 4.2.2.3. Effects of Ga on junction properties

Thermal diffusion of Ga into a sample can both reduce the quality and reliability of a junction. To test for these effects two experiments were performed. Firstly, one sample was measured before and after it had been subjected to oven baking for 12 hours at 100 °C. Secondly, two samples were measured and re-measured over a period of weeks. In both experiments there were no apparent differences observed in the junction  $I$ - $V$  characteristics. This indicates that the effects of thermal diffusion of Ga are not significant although this experiment does not preclude the effects of Ga scattered into the junction region during the ion beam mill. The range over which Ga scatters into the junction region was found using Monte Carlo simulations of Ga ion with a normal incidence onto Au, shown in table 3.5. It shows that the average penetration depth of Ga was 8 nm with a lateral spread,  $\sigma_L$ , of 7 nm. Similar calculations for Nb gave a penetration depth of 11 nm and  $\sigma_L=7$  nm. The effect of scattered Ga in a junction is thought to be detrimental to the junction's electrical properties, but this will not affect a junction's reliability due to its systematic nature.

#### 4.2.2.4. Variation of $Z_{INPUT}$

A systematic study was made of junctions by varying  $Z_{INPUT}$ . The  $I_C$ ,  $R_N$ , and  $I_C R_N$  products at 4.2 K as  $Z_{INPUT}$  was varied are shown in figure 4.7. Both the  $I_C$  and  $I_C R_N$  products decrease with  $Z_{INPUT}$ , as expected, although the great variation of  $R_N$  with  $Z_{INPUT}$  does not show any particular trend with  $Z_{INPUT}$ . Indeed, the electrical properties of the junctions studied here showed their lack of reproducibility, demonstrated by the spread in  $I_C$  and, especially,  $R_N$ . In addition, the temperature dependencies of the  $I_C$ ,  $I_C(T)$ , of three junctions were measured using the Oxford Instruments Heliox™ probe from just below 0.35 K to 6 K and are shown in figure 4.8a. The general form of each junction's  $I_C(T)$  was the same, although the relative values of the currents were very different. This also shows the lack of reproducibility of the junctions. In two of the junctions studied here hysteresis in the  $I_C$  was observed at temperatures below 2 K. Both of these observations are discussed in further detail in chapter 5.5.

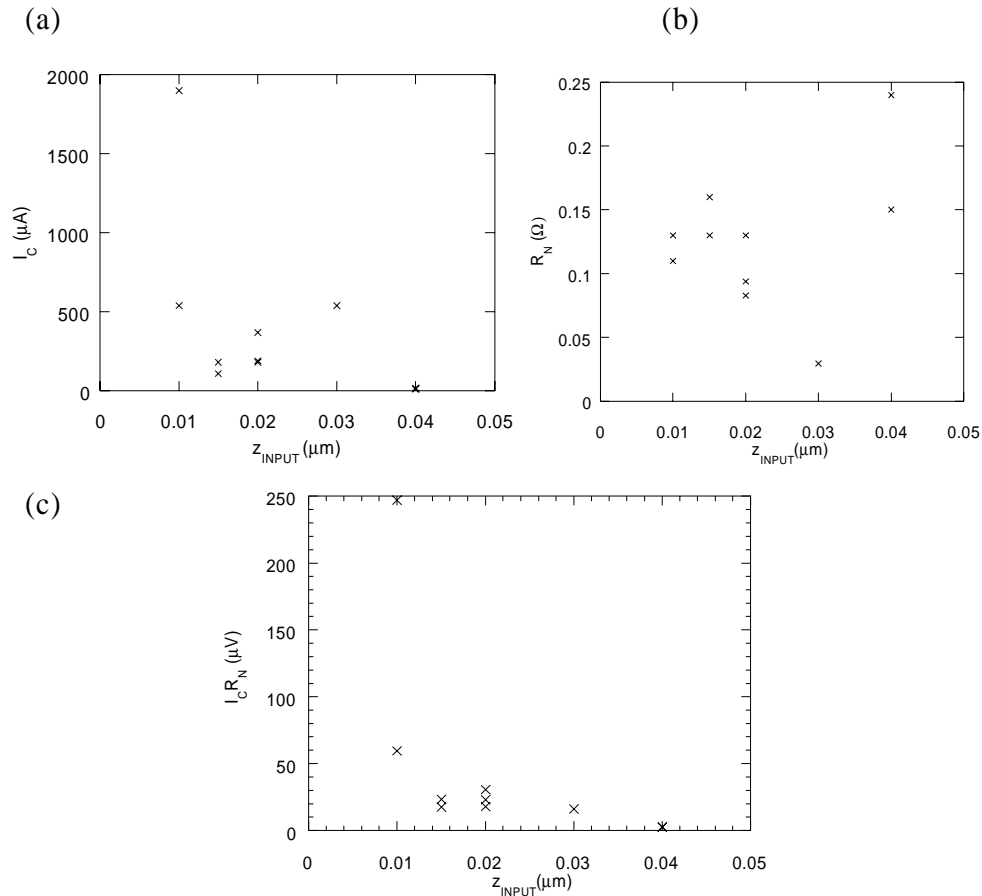


**Figure 4.7:** The variation of (a) the critical current,  $I_C$  (b) normal state resistance,  $R_N$  and (c)  $I_C R_N$  product with  $Z_{INPUT}$  at 4.2 K in Nb/Au(100nm)/Nb junctions ( $W=0.5 \mu\text{m}$ ).

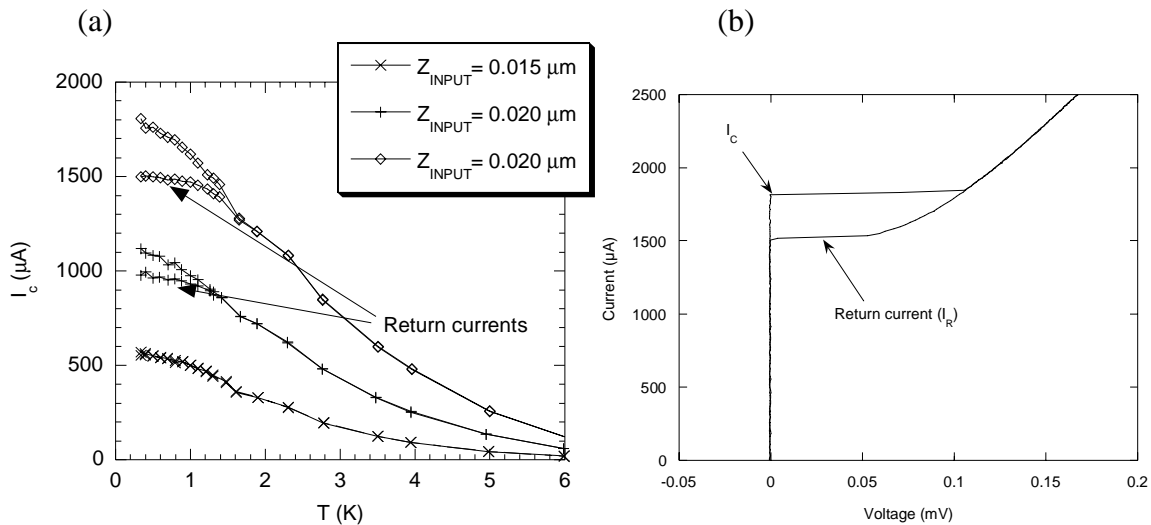


**Figure 4.8:** (a) The variation of  $I_c$  with temperature for different Nb/Au(100 nm)/Nb junctions (b) An example of the hysteretic I-V characteristics observed at 0.35 K.

#### 4.2.2.5. Improvements to the method

The poor reproducibility of the junction behaviour meant it was necessary to assess the method and make improvements. Six changes were made:

1. Insulating oxidised Si coated Si substrates were used instead of Si because the Si substrates were found to be slightly electrically conductive.
2. The normal-metal was changed from Au to Cu, as Cu was found to have better adhesion on both Si and oxidised Si. The enhanced etch technique was not used on Cu because Cu reacts with  $\text{I}_2$  to form insulating, crystalline  $\text{CuI}$ .
3. To reduce the effects of any current density fluctuations on a junction's performance,  $L_{\text{ISO}}$  (shown in figure 4.1) was standardised to 3  $\mu\text{m}$ .
4. The line cut technique to define the junction trench was abandoned because the junction length,  $L \sim 12 \text{ nm}$ , (shown in figure 4.1), was not much larger than the spot size of the beam ( $\sim 5 \text{ nm}$ ). Since the focusing of the beam determines the spot size any change in focusing can vary it considerably, e.g. tiny electronic fluctuations in the focusing electrodes, or alternatively, the consistency in focusing by the user. No systematic study of this was ever made, although it was often found that there was a variation of 5-10 nm in the sides of the junction trenches, made on the same sample. By widening the trench, or in other words, increasing  $L$  to 50 nm, greater control was obtained over its dimensions.

5. A 12-bit digital-analogue controller card in the FIB instrument's computer converts pixels on its computer screen into individual beam coordinates onto the sample so the beam size is dependent upon the magnification used. To increase the consistency of the cuts they were made at standard magnifications and beam currents. The isolation cuts were made at 25 k $\times$  with a beam current of 11 pA and the trenches were made at 65 k $\times$  with a beam current of 1 pA. This results in pixel sizes of 3 nm and 1 nm respectively. In later experiments the 4 pA beam current was used because the 1 pA aperture had sufficiently eroded (after 2 years) that its true beam current was actually greater than 4 pA. This only affected the mill time of the cut and did not make any apparent difference in the precision of the cuts.
6. Before each cut is made the beam current is automatically sampled by the FIB instrument's software so a calibration factor can be made to convert  $Z_{INPUT}$  into the number of beam sweeps required to produce a trench of depth,  $M$ . At the low currents used significant electrical noise was found to be associated with the sampled current mainly due to the insufficiently shielded leads from the FIB instrument's stage to the current meter for such low currents (1 pA). The noise was found to have a signal to noise ratio of approximately 2:1 and, hence, the precision in the depth of the cut was low. Fortunately it was possible to overcome this problem and the precision in the depth was greatly improved by using the area dose method (Presser 1997) and is discussed in the next section.

#### 4.2.3. Area dose method

It is apparent from the initial experiments that the milled depth of the trench in the bilayer ( $M$ ) is critical in determining the electrical performance of a junction. Insufficient milling leaves some superconducting Nb, while over-milling leads to no measurable Josephson coupling at 4.2 K. To calibrate the Nb mill rate a  $1 \mu\text{m}^2$  area of bilayer track was milled elsewhere on the sample (magnification of 65 k $\times$  and beam current of 1 pA) using the standard end point detection technique of measuring the stage current in the FIB instrument as a function of mill time (Presser 1997). The stage current measures the current from the electrons that are knocked-out of the material. This makes it possible to make a distinction between the materials and therefore it is possible to find the mill time to remove only the Nb layer. Figure 4.9 shows a typical end point detection graph and has been annotated to highlight the various layers as the beam mills through the sample.

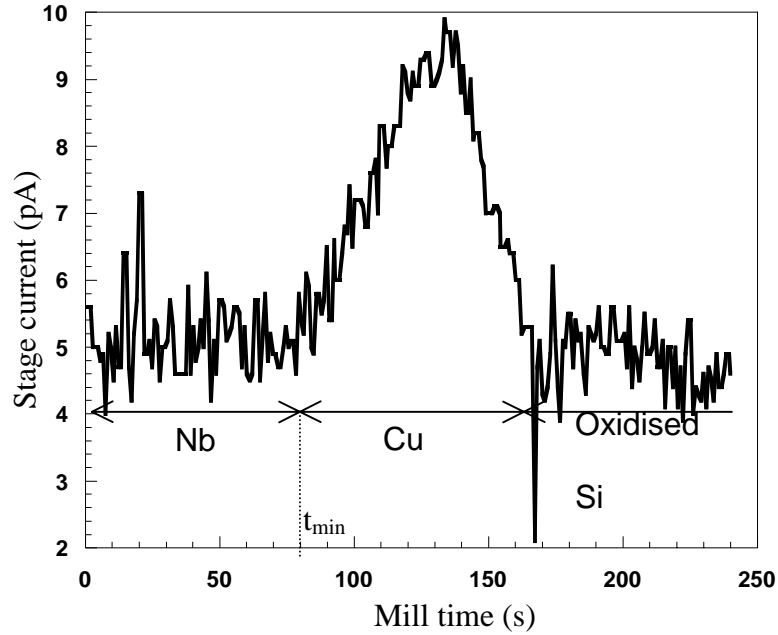


**Figure 4.9:** End point detection of  $1 \mu\text{m}^2$  Nb(75 nm)/Cu(70 nm) bilayer on oxidised Si coated Si. The stage current gives an indication of how deep the ion beam has milled into the bilayer.

The mill time to remove only the Nb layer ( $t_{min}$ ) for a trench of arbitrary area can be calculated by scaling the result from the end point detection graph. This procedure made it possible to test the reproducibility of milling small volumes, i.e. junction trenches, and therefore ultimately the reproducibility of junction properties. The mill rate of Nb and Cu was calculated to be  $9.4 \times 10^{-10} \text{ m}^3\text{C}^{-1}$  and  $8.8 \times 10^{-10} \text{ m}^3\text{C}^{-1}$ , respectively. By repeatedly measuring the stage current profile as a function of mill time on the same highly uniform sample, there was found to be no significant variation over many weeks (as long as the emission current of the Ga source was maintained at a constant value ( $2.2 \mu\text{A}$ ) and the FIB instrument's column was kept carefully aligned). This demonstrated the excellent control over the beam properties and milling of small volumes of material. To distinguish between weak-link (ScS) and SNS behaviour  $I$ - $V$  characteristics of junctions were measured with the mill time,  $t$ , less than, equal to, or greater than  $t_{min}$ .

Figure 4.10 shows the  $I_C R_N$  product versus the mill time of the junction trench ( $50 \text{ nm} \times 1 \mu\text{m}$ ) for junctions made on the same sample Nb (75 nm)/Cu (70 nm). It shows that there is good reproducibility with the  $I_C R_N$  product for junctions made under the same conditions. It, also, shows that the  $I_C R_N$  product decreases with increasing mill time. From end point detection it is found that  $t_{min}=4 \text{ s}$  and the mill time to mill through the entire bilayer,  $t_{max}$ , is 8

s. Separating the effect of mill time on  $I_C$  and the normal state conductance,  $\sigma_N=1/R_N$ , shown in figure 4.11, a linear decrease of  $I_C$  with increasing mill time is found. Also observed is a sharp drop in  $\sigma_N$  at  $t=4$  s from a constant value to a linearly decreasing value with increasing mill time. This is discussed in further detail in chapter 5.3.

Figure 4.12 shows the  $I$ - $V$  characteristics of a typical junction and its response to microwave radiation. Figure 4.13 shows its response to a magnetic field. Both responses show that the junction has Josephson like characteristics. The microwave response clearly shows Shapiro steps. The magnetic response gives a reasonable fit to the ideal sinc dependence as described by equation 2.44, also shown in figure 4.13. The reappearance of  $I_C$  at higher fields indicates there is a Josephson current. This is discussed in more detail in chapter 5.4.

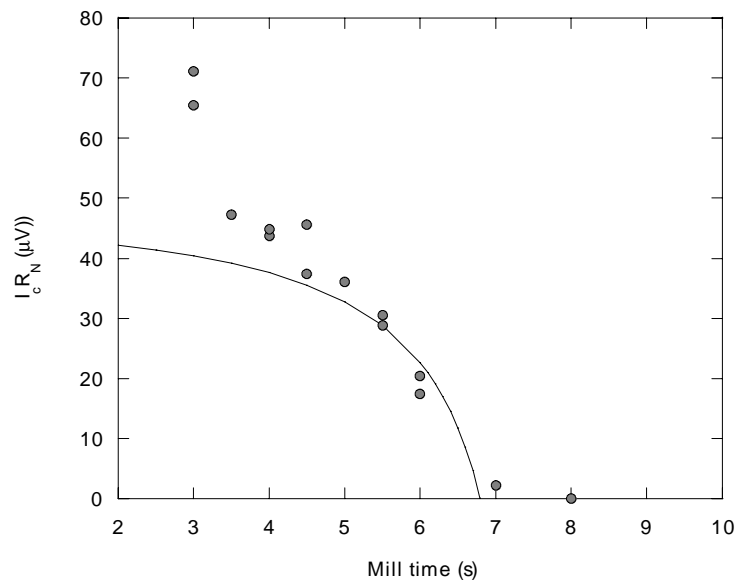


**Figure 4.10: Nb(75 nm)/Cu(70 nm)/Nb junction  $I_C R_N$  product at 4.2 K versus mill time. The junctions were made using the area dose method. The difference between the  $I_C R_N$  products of junctions made with the same mill time is small (~10 %). The line shows the results from the geometrical model, discussed in chapter 5.**

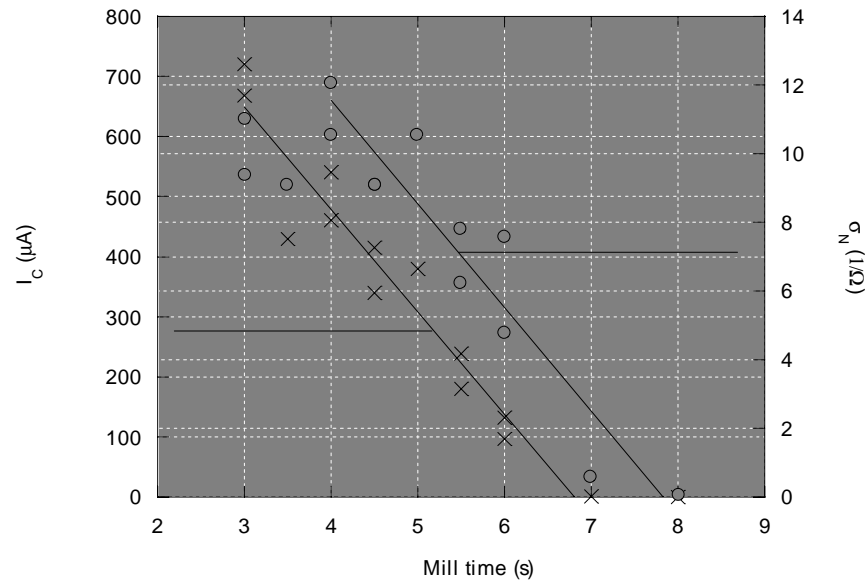


**Figure 4.11: The variation of the critical current,  $I_C$  (x), and the normal state conductance,  $\sigma_N$  (o) versus mill time (t) at 4.2 K in Nb(75 nm)/Cu(70 nm)/Nb(75 nm) junctions using the area dose method.**

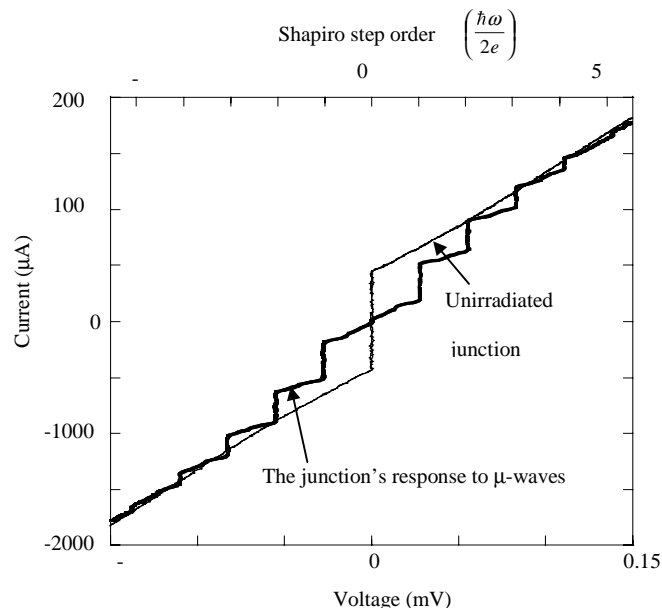


**Figure 4.12: I-V characteristics at 4.2 K of a typical Nb(75 nm)/Cu(70 nm)/Nb (75 nm) junction showing both the unirradiated junction I-V and the Shapiro response to microwave radiation.**

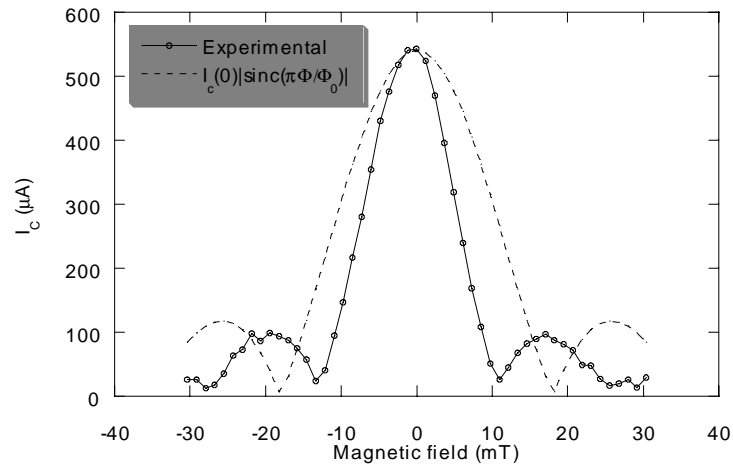


**Figure 4.13:** The variation of  $I_C$  with an applied magnetic field at 4.2 K. The dashed line shows the sinc dependence of an ideal Josephson junction using the geometrical dimensions of the junctions.

### 4.3. Summary

Nb/Cu/Nb SNS junctions can be reliably fabricated using a standard FIB instrument. As demonstrated by the responses to microwaves and magnetic field, the junctions display the appropriate Josephson behaviour demanded by current technological applications. In addition, the reproducibility in junction behaviour ( $I_C$  to within ~10%) is the best so far observed for this type of junction using low  $T_C$  superconductors.

### 4.4. References

- T. K. Blocker, R. K. Watts and W. C. Holton (1978). "Future Trends in Superconductive Electronics." (AIP, New York).
- L. Fritsch, H. Elsner, M. Schubert and H. G. Meyer (1999). "SNS and SIS Josephson junctions with dimensions down to the submicron region prepared by a unified technology." *Superconductor Science & Technology* **12**(11) 880.
- E. P. Harris and R. B. Laibowitz (1977). *IEEE Trans. Magn.* **MAG-13** 724.
- N. Hirose, H. Ohta, T. Matsui and M. Fukuda (1997). "S-N-S weaklink junctions fabricated by nanometer lithography." *IEEE Transactions On Applied Superconductivity* **7**(2 Pt3) 2635.

- H. Kroger, L. N. Smith and D. W. Jillie (1981). "Selective Niobium Anodisation Process for Fabricating Josephson Tunnel Junctions." *Applied Physics Letters* **39**(3) 280.
- N. Presser and M. R. Hilton (1997). *Thin Solid Films* **308-309** 369.
- H. Schulze, R. Behr, F. Muller and J. Niemeyer (1998). "Nb/Al/AlO<sub>x</sub>/AlO<sub>x</sub>/Al/Nb Josephson junctions for programmable voltage standards." *Applied Physics Letters* **73**(7) 996.
- R. B. Vandover, A. Delozanne and M. R. Beasley (1981). "Superconductor-Normal-Superconductor Microbridges - Fabrication, Electrical Behavior, and Modeling." *Journal Of Applied Physics* **52**(12) 7327.
- R. B. Vandover, A. Delozanne, R. E. Howard, W. L. McLean and M. R. Beasley (1980). "Refractory-Superconductor S-N-S Microbridges." *Applied Physics Letters* **37**(9) 838.
- A. Zehnder, P. Lerch, S. P. Zhao, T. Nussbaumer, E. C. Kirk and H. R. Ott (1999). "Proximity effects in Nb/Al-AlO<sub>x</sub>-Al/Nb superconducting tunneling junctions." *Physical Review B-Condensed Matter* **59**(13) 8875.

# Chapter 5

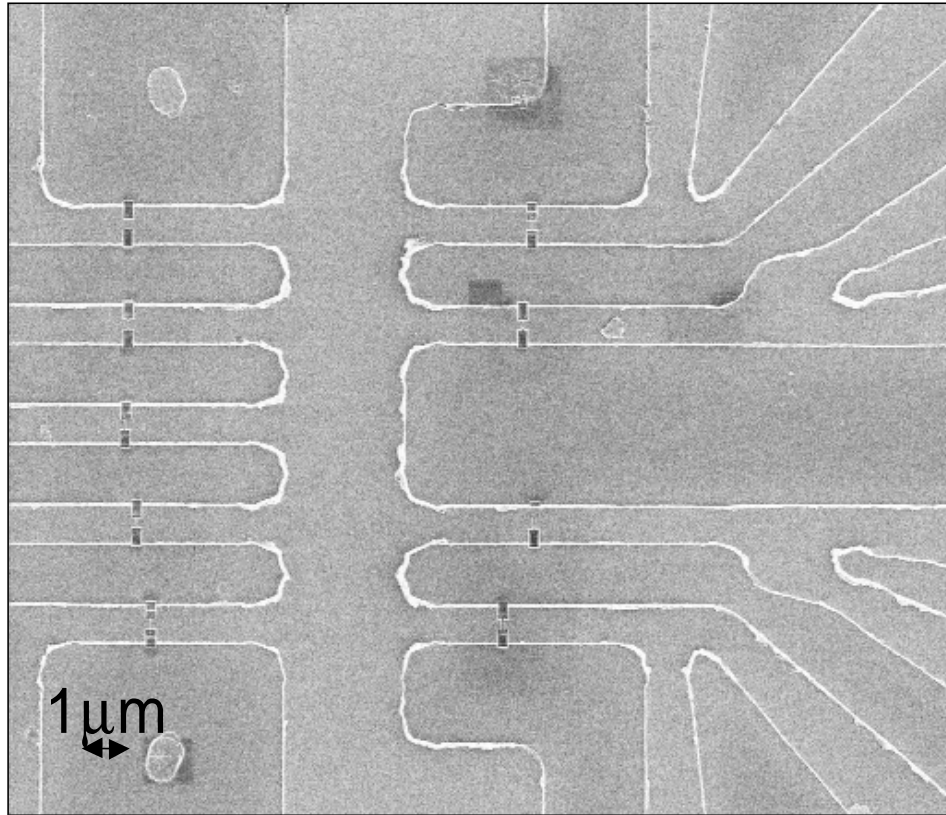


Image of a patterned sample of SNS junctions made using an FIB instrument.

## Characterisation of Nb/Cu/Nb junctions

## 5.1. Introduction

This chapter extends the work described in chapter 4 by characterising the Nb/Cu/Nb junctions fabricated using an FIB instrument. The aims of the experiments described here are: firstly, to investigate the relationships between the electrical properties of a junction and its geometry (junction width, length, trench depth, normal-metal thickness) as defined by the FIB instrument and deposition process; secondly, to characterise the junctions' responses to magnetic fields and operating temperatures. A clear understanding of this is useful for improving the fabrication method and to give insight into the electrical dynamics of this type of junction.

All the junctions described in this chapter, unless otherwise stated, are made using Nb (75nm thick)/ Cu (70nm thick) bilayers deposited on oxidised Si substrates. Basic characterisation of the junctions is made by performing systematic studies of changes to their geometry and by varying the operating temperature. Firstly, the electrical properties of the unpatterned and patterned films are examined. Secondly, the general  $I$ - $V$  characteristics of the junctions are studied. Thirdly, the results from junctions fabricated using the area dose method (described in chapter 4.2.3) are analysed so a qualitative model can be made to describe the relationship between the mill time,  $t$ , used for making the trench, and the resulting junction's  $I_C$ ,  $R_N$ , and  $I_C R_N$  product. Fourthly, the dependencies of  $I_C$  and  $R_N$  with the junction's width, length, and the Cu layer thickness are examined. Fifthly, the responses of junctions to magnetic fields are investigated. Sixthly, the temperature dependencies of  $I_C$  and  $R_N$  to a systematic variation of  $L$  are investigated. Finally, the interpretation of the junction properties are summarised and compared with the recent work of Hadfield *et al.* (Hadfield 2000).

## 5.2. Basic junction characterisation

### 5.2.1. Film characterisation

The changes in resistance with temperature of a single junction (with  $t = 4$  s) were recorded at the end of each step in the fabrication process (described in chapter 4.2.1) and are shown in figure 5.1. The resistance of the track as expected, increased after each

successive step in the fabrication process. The  $T_C$  and resistance ratio of  $R_{T=285\text{ K}}$  to  $R_{T=T_C}$  were taken and are displayed in table 5.1.

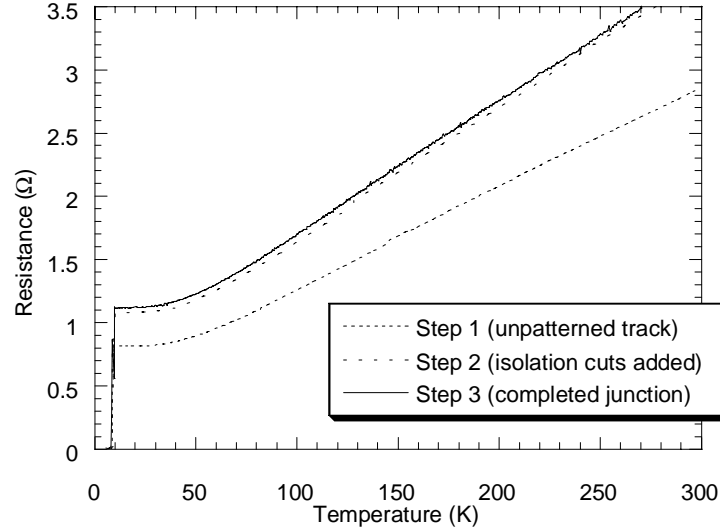


**Figure 5.1: Variation of temperature with the resistance of a Nb/Cu track after each junction fabrication step.**

STEP NUMBER	$T_C$ (K)	$R_{T=285\text{ K}} : R_{T=T_C}$
1	$8.9 \pm 0.1$	3.43
2	$8.2 \pm 0.3$	3.35
3	$8.1 \pm 0.3$	3.34

**Table 5.1: Critical temperature ( $T_C$ ) and resistance ratio values of a Nb/Cu track after each junction fabrication step.**

There is a slight decrease in the resistance ratio after each successive step. This is thought to be caused by Ga ions from the ion beam damaging the track. The  $T_C$  decreases with each subsequent step, and can be interpreted as an indication that the effect of Ga in Nb is to attenuate its superconducting properties. Meyer found that the  $T_C$  of Nb was generally decreased using ion implantation, although interestingly it was found for Mo the  $T_C$  could be increased from 0.9 K to 7 K (Meyer 1974).

Singh (Singh 1999) made a systematic study of the dependence of  $T_C$  with variable thickness Nb/Cu (70 nm) unpatterned thin-films. The  $T_C$  of each film was found to be dependent upon the niobium thickness up to a limiting value of approximately 85 nm. This

indicates the importance of the proximity effect in the junctions studied here. Using a different experimental setup to the one used here they recorded the  $T_C$  of 3 Nb (75 nm)/Cu(70 nm) thin-films to be  $7.9 \pm 0.2$  K. The difference between the value recorded in table 5.1 and Singh's is attributable to systematic temperature errors present in both setups. Taking the errors into account, the  $T_C$  of a completed junction is  $7.9 \pm 0.3$  K.

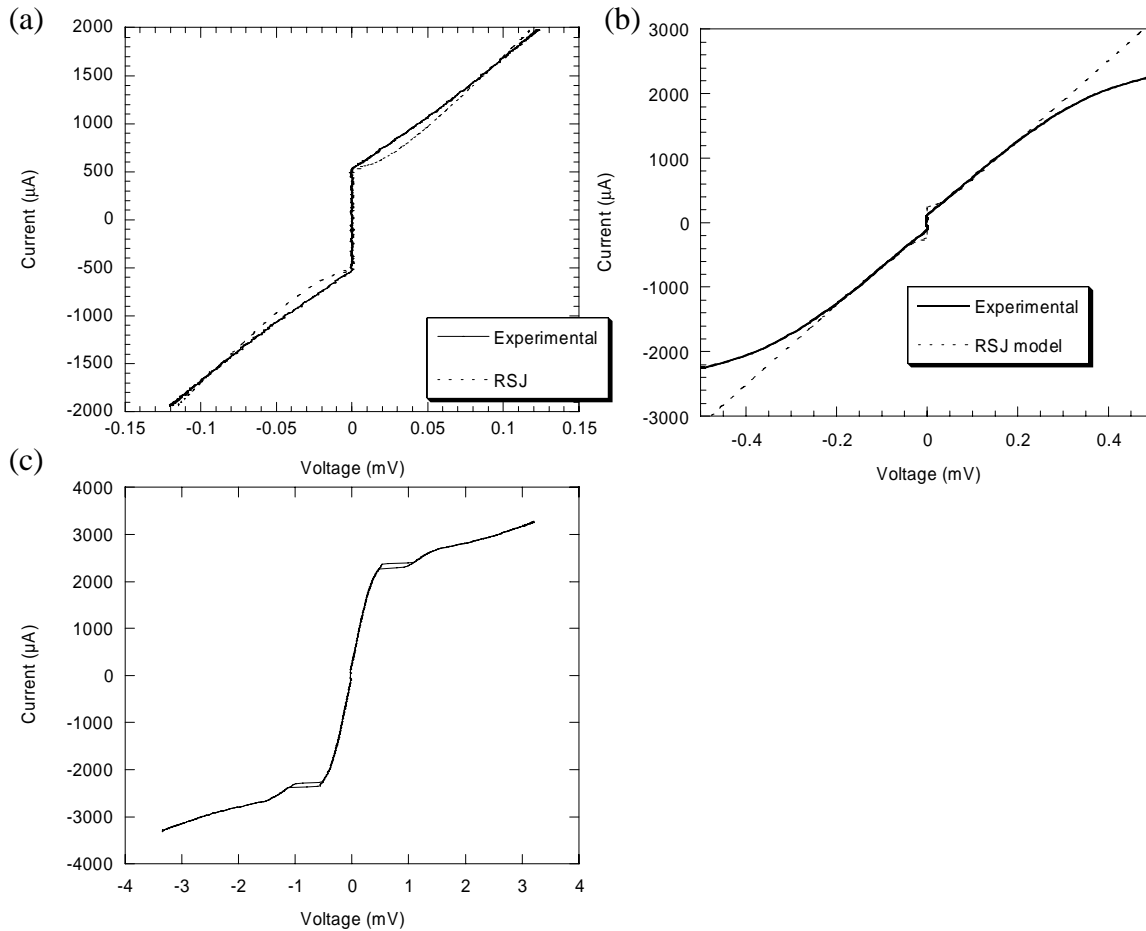


**Figure 5.2: The I-V characteristics at 4.2 K of typical junctions at (a) low bias (b) medium bias and (c) high bias. For comparison, the I-V characteristics obtained from the RSJ model are also shown in (a) and (b).**

### 5.2.2. I-V characteristics of junctions

The  $I$ - $V$  characteristics of junctions were studied at low, intermediate and high biases at 4.2 K. The results from typical junctions studied are shown in figure 5.2.

Fitted lines, using the RSJ model (described in chapter 2.3.2) are also shown in figure 5.2a and b for the low and medium biases. The resistance used for calculating the RSJ  $I$ - $V$  characteristics was taken from the junction's resistance at medium bias. The experimental

results showed that the junctions deviated from the RSJ model, which are discussed separately.

### 5.2.2.1. Low bias case

For all the junctions studied here, the  $I$ - $V$  characteristics of the transition from the zero- to finite- voltage states were rounded. Deviations from the RSJ model are to be expected because it is a very simple model; it does not take into account the effects of thermal noise or any of the non-equilibrium processes that take place in the junction, e.g. order relaxation around the Nb electrodes. Any of these processes will potentially, alter the  $I$ - $V$  characteristics.

A possible cause of the rounding in the  $I_C$  has been investigated. An approach described by Colclough (Colclough 1998) has been used to take into account the effects of thermal noise in the RSJ model. The presence of thermal noise will round the  $I$ - $V$  characteristics at the transition from the zero- to the finite- bias states. The best fit made to the  $I$ - $V$  characteristics of a junction of 4.2 K, not shown, corresponds to an unlikely noise temperature of approximately 2,000 K.

Some processes can give rise to the appearance of excess current in the  $I_C$ . Excess currents are non-Josephson currents and can arise from a variety of mechanisms. They are generally related to strong coupling effects (Ivanov 1981; Kupriyanov 1981) and can be distinguished from a Josephson component by the fact that they are insensitive to the phase difference between the two superconducting electrodes. However, this possibility can be neglected as  $I_C$  can be completely suppressed by comparatively low magnetic fields (described in chapter 2.3.3 and demonstrated in figure 4.13).

It is more likely that the  $I$ - $V$  characteristics can be explained using the Time Dependent Ginzburg-Landau (TDGL) theory. For comparison, the  $I$ - $V$  characteristics derived from the TDGL equations (equations 2.96-2.100) are shown with the ones obtained from the RSJ model in figure 2.16. This shows that increasing the non-equilibrium state of the junction will decrease the effective resistance at low voltages. It is observed in figure 5.2a that the resistance of the junction at low voltages is lower than the resistance obtained by the RSJ model. This observation supports, at least qualitatively, the argument that the non-equilibrium state of the junction is responsible for the apparent rounding in the  $I_C$ .

### 5.2.2.2. Medium bias case

As the current amplitude was increased so that the maximum junction bias approached  $\sim 0.2$  mV the slope of the curve progressed towards a limiting value, as expected by the RSJ model. This value was used as the value of  $R_N$  in all the junctions reported here. Above  $\sim 0.2$  mV, however, the  $I$ - $V$  characteristics deviated from the model, the slope changed and became increasingly resistive. Deviations in the experimental  $I$ - $V$  characteristics from the RSJ model are often seen, and various mechanisms have been suggested to account for these, and many are based on the presence of multiple Andreev scattering (Blonder 1982; Klapwijk 1982; Octavio 1983; Flensberg 1989) and heating (Skocpol 1974).

### 5.2.2.3. High bias case

At higher bias ( $\sim 0.5$  mV) there was a hysteretic voltage rise, similar observations were observed by Van Dover (Vandover 1981). They attributed it to self-heating and attempted to model this using the heating theory of Skocpol (Skocpol 1974). At biases above the voltage rise there is a “bump”, followed by an ohmic dependence. The resistance was  $\sim 2$   $\Omega$  and corresponded to the resistance of the fully normal region around the junction (i.e. a bilayer region of  $3 \mu\text{m} \times 0.5 \mu\text{m}$ ). A possible explanation for this was the formation of a “hot-spot” in the region of the junction, that at sufficient biases was enough to locally heat the surrounding Nb above its  $T_C$ . This will be examined in further detail in a later section 5.5.2.

## 5.3. Effect of the junction’s geometry on its electrical properties

### 5.3.1. Simple model for the $I_C$ and $R_N$ dependence with the mill time of the trench

To explain the  $I_C$ ,  $R_N$  and  $I_C R_N$  product as a function of mill time a simple, geometrically based model has been made. It uses the following assumptions: firstly, it is only valid for the situation where the superconductor in the trench has been entirely removed, and normal-metal is still present, i.e. for the range  $t_{max} > t > t_{min}$ ; secondly, a damaged region of normal-metal is present that is a result of the Ga ions, from the beam penetrating the Cu layer and forming a damaged layer. This layer is sufficiently damaged to

reduce the electronic inelastic mean free path. This means there is no Josephson current, although normal electronic conduction is still possible. Figure 5.3 shows a schematic of the cross-section of a junction.



**Figure 5.3: Schematic diagram of the cross-section of a SNS junction.**

The model also, assumes that the current path across the junction is fixed with mill time and follows the geometrical length of the junction,  $L$ .

The variation of  $I_C$  with mill time,  $I_C(t)$ , is given by

$$I_C(t) = J_0 W (d(t) - d_{dam}) \quad (5.1)$$

where  $J_0$  is the critical current density of the junction at  $t_{min}$ .

The variation of  $R_N$  with mill time,  $R_N(t)$ , is the sum of the contributions of both the damaged and undamaged normal-metal regions in the trench. The resistivity of the two layers was assumed to be approximately the same. Hence

$$R_N(t) = \frac{L \rho_N}{W d(t)} \quad (5.2)$$

where

$$d(t) = d_N \left( 1 - \frac{t - t_{min}}{t_{max} - t_{min}} \right). \quad (5.3)$$

Combining equations 5.1 and 5.2 the  $I_C R_N$  product is given by,

$$I_C R_N(t) = J_0 \rho_N L \left( 1 - \frac{f_{dam}}{1 - \frac{t - t_{min}}{t_{max} - t_{min}}} \right) \quad (5.4)$$

where  $J_0 \rho_N L$  was the  $I_C R_N$  product at  $t=t_{min}$  and  $f_{dam}$  is the fraction of the damaged layer over the original thickness of the normal-metal layer, i.e.

$$f_{dam} = \frac{d_{dam}}{d_N}. \quad (5.5)$$

The model predicts that  $I_C(t)$  will reduce to zero before the normal state conductance,  $\sigma_N$ , ( $1/R_N$ ) becomes zero by a time,

$$\Delta t = f_{dam}(t_{max} - t_{min}). \quad (5.6)$$

The results from the model are shown with the experimental data in figures 4.10 and 4.11. The trends of both the  $I_C$  and  $\sigma_N$  curves show a linear decrease with increasing mill time, due to the corresponding linear decrease in cross-sectional area of the Cu link. A time disparity between the complete suppression of  $I_C$  at  $t=6.8$  s and  $\sigma_N$  at  $t=7.8$  s was seen. By comparing the times at which  $I_C$  and  $\sigma_N$ , and knowing  $t_{min}=4$  s and  $t_{max}=8$  s, it is calculated from equations 5.5 and 5.6 that there is 18 nm of Cu remaining when  $I_C$  is completely suppressed. From Monte Carlo calculations the average penetration depth of 30 keV Ga ions into Cu is 9.5 nm and  $\sigma_L=5$  nm (table 3.5). It is probable that the true thickness of the damaged layer however, is greater than this value due to further disruption caused deeper in the Cu layer, e.g. creation of dislocations and other lattice defects, and electro-migration of Ga ions.

The  $I_C R_N$  product as a function of mill time, calculated from equation 5.4, is plotted over the entire range of  $t$ , and shown in figure 4.10. It highlights the sharp drop observed at  $t=4$  s. Knowing the mill rate of Nb, at  $t=3$  s the trench is calculated to be 56 nm deep leaving a thin, 19 nm thick layer of Nb. From table 3.5, the average penetration depth of Ga into Nb is 11 nm. This means that at  $t=3$  s the junction will be more SNS- rather than weak link- like, discussed in chapter 2.3. Any remaining Nb would not have any superconducting properties because of damage and the proximity of the Cu layer. This means also, that the sudden drop in  $I_C$  at  $t=4$  s is not a consequence of the junction character changing from weak link (ScS) to SNS, but instead, is the result of damage to the Cu layer.

This model does have some major drawbacks however, and they are evident by the assumptions used in the derivation. It is quite successful though in predicting the electrical character of a junction in terms of the parameters used by the FIB instrument so it is useful for manufacturing purposes. The major drawback of the model is it treats the flow of current within the junction to be 1-dimensional, whereas the geometry of the junction does not allow this approximation to be made. The presence of Cu underneath the Nb layer means charge carriers in the junction are not localised in the region of Cu directly underneath the junction trench. If an accurate model describing the current flow in a junction was to be made, a 3-dimensional transmission line approach must be used.

### 5.3.2. Variation of length

Junctions were made with a systematic variation of  $L$  in the range 30 to 150 nm. The depths of the trenches were kept constant by scaling their mill times to a trench of area  $50 \text{ nm} \times 1 \text{ }\mu\text{m}$  with a mill time of 4 s, so that only the Nb layer was removed. This assumes that the scaling factor is independent of the geometry of the trench regardless of how close the walls of the trench are e.g. the profile of the cuts have steep sides. It is thought that the steepness of the sides will decrease as  $L$  decreases because of the effects of increased sidewall erosion. Figure 5.4 shows the  $I_C R_N$  products versus  $L$  of these junctions at  $T=4.2 \text{ K}$ . The  $I_C R_N$  products show an approximate inverse linear relationship with increasing  $L$  between 50 and 130 nm.

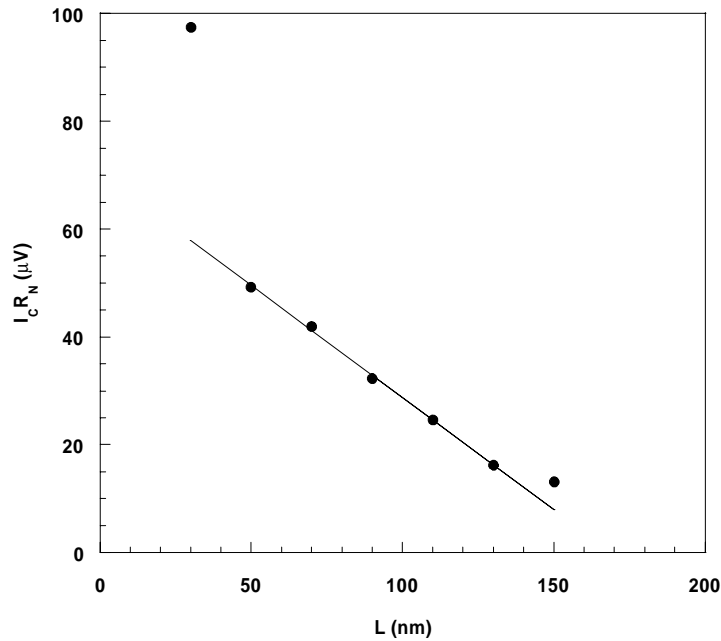


**Figure 5.4: The variation at 4.2K of the  $I_C R_N$  product with the junction length ( $L$ ). The fitted line shows that the  $I_C R_N$  product has an inverse linear relationship with increasing  $L$ .**

A simplified model given by Tinkham (Tinkham 1996) of SNS junctions assumes a 1-dimensional geometry for the junction so that  $I_C$  falls with  $L$  as  $\exp[-L/\xi_{ND}]$ . Figure 5.5 shows how  $I_C$  varies with  $L$  in its logarithmic form. The slope of the fitted line, also shown in the figure, is used to calculate  $\xi_{ND(T=4.2K)}$ , and is found to be  $53(\pm 3) \text{ nm}$ . From equation 2.61 the value of  $\xi_{ND(T=4.2K)}$  is  $60 \pm 2 \text{ nm}$ , calculated from the properties of the materials. The difference between the two values, although small, is significant, and is attributable to the

assumption that the geometry of the junction is not 1-D, making the simple exponential relationship inappropriate.

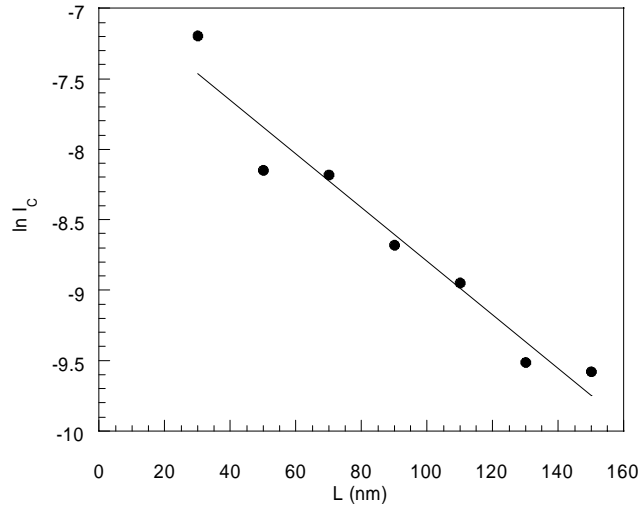


**Figure 5.5: Dependence of  $\ln I_C$  with junction length ( $L$ ). A fitted line is added to show the inverse linear relationship with increasing  $L$ .**

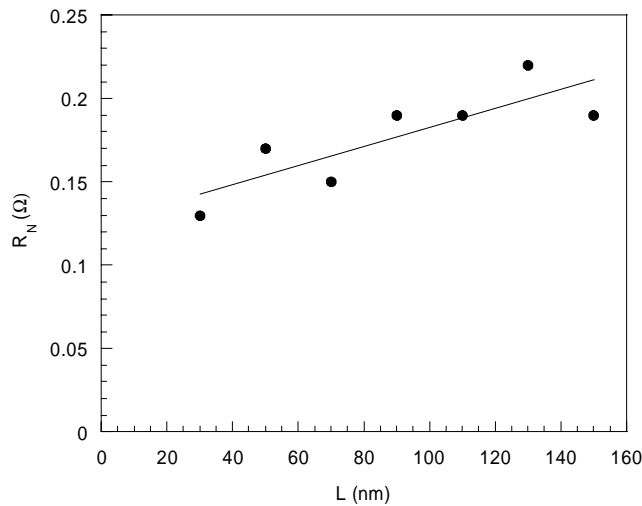


**Figure 5.6: The variation of the normal state resistance ( $R_N$ ) with junction length ( $L$ ). The fitted line shows the offset linear dependence with increasing  $L$ . The offset is  $0.12 \pm 0.01 \Omega$ .**

The dependence of  $R_N$  with  $L$  is shown in figure 5.6. The predicted dependence of  $R_N$  with increasing  $L$  is a directly proportional one (equation 5.2). The experimental results shows a linear dependence with an offset present at  $L=0$  nm of  $0.12 \pm 0.01 \Omega$ . The slope of

the line fitted to  $R_N$ , also shown in the figure, is used to calculate the apparent resistivity of Cu and found to be  $2.0 \pm 0.5 \times 10^{-8} \Omega\text{m}$ . This value compares favorably with the measured resistivity of Cu, found to be  $2.8 \pm 0.3 \times 10^{-8} \Omega\text{m}$ . The offset in the graph is therefore, an excess resistance, and not attributable to the geometrical length of the barrier. Two possible effects that could be responsible for the additional resistance are: first, there is a region of bilayer on both sides of the trench that is effectively part of the junction's normal-metal region, resulting from quasiparticles diffusing into the superconducting electrodes. This is similar to observations made by Pippard (Pippard 1971), and is discussed in chapter 2.6.3; second, contact resistance at the Nb/Cu interfaces due to impurities and defects. Consideration of both effects is made here, using the parameters of the materials that are shown in table 5.2.

Material	$k_F$ ( $\times 10^6 \text{ m}^{-1}$ ) <sup>a</sup>	$v_f$ ( $\times 10^6 \text{ ms}^{-1}$ ) <sup>a</sup>	$n_e$ ( $\times 10^{28} \text{ m}^{-3}$ ) <sup>a</sup>	$\rho$ ( $\times 10^{-9} \Omega\text{m}$ )	$l_e$ (nm)	$\mathcal{E}_{ND(T_c)}$ (nm)
Nb	1.18	1.37	5.56	$130 \pm 10$	$7 \pm 1$ <sup>(†)</sup>	$57 \pm 8$
Cu	1.36	1.57	8.45	$28 \pm 3$	$24 \pm 2$	$42 \pm 2$

**Table 5.2: Nb and Cu parameters of the Fermi wavenumber ( $k_F$ ), Fermi velocity ( $v_F$ ), electron density ( $n_e$ ), electrical resistivity ( $\rho$ ), inelastic electron mean free path ( $l_e$ ) and the dirty limit coherence length ( $\xi_{ND}$ ) [<sup>a</sup>(Ashcroft 1976) <sup>†</sup>(Warburton 1993)].**

To consider both effects a transmission line model developed by Berger (Berger 1972) is used. Two parameters are used here: the resistance area products,  $R^*$ ; and the characteristic transmission length,  $L_{TL}$ . The model uses a transmission line approach, and has been previously used in studying normal-metal/semiconductor interfaces. It has also, been successfully used to study superconductor/normal-metal interfaces, particularly for junctions of the step edge geometry where contact resistance is important (Tarte 1992). The contact resistance,  $R_C$ , using the appropriate geometry (assuming the bilayer extends to infinity and the geometry of the junction is symmetrical) is given by

$$R_C = \frac{1}{W} \sqrt{\frac{R^* \rho_N}{d_N}}. \quad (5.7)$$

Assuming that the observed excess resistance is solely due to contact resistance so that  $R_C = 0.06 \Omega$ , (half of the apparent offset resistance)  $R^*$  is  $2.0 \pm 1.5 \times 10^{-15} \Omega\text{m}^2$  from equation 5.7. Clarke (Clarke 1969) prepared sandwich structured Pb/Cu/Pb junctions using an ultra-high vacuum evaporator, similar to the junctions studied here. Tarte (Tarte 1992) calculated  $R^*$  for Clarke's junctions to be  $\sim 2 \times 10^{-14} \Omega\text{m}^2$ , comparing favorably to the

experimental value. Given the agreement with similarly deposited bilayers in ultra-high vacuum, the presence of impurities at the interface contributing to a contact resistance can be excluded.

The characteristic transmission line length,  $L_{TL}$ , is given by

$$L_{TL} = \sqrt{\frac{d_N R^*}{\rho_N}}, \quad (5.8)$$

and is found here, to be  $70 \pm 40$  nm. From the offset present in figure 5.6, if no interfacial resistance is present, the inferred extra length traveled by the charge carriers in the Cu layer is  $\sim 100$  nm.

The question therefore is; is the calculated value for  $R^*$  reasonable for it to be due to contact resistance? There will always be an intrinsic interfacial resistance between two different materials due to the mismatch of their fermi wave vectors,  $\mathbf{k}_F$ . Waldram (Waldram 1992) calculated  $R^*$  between a normal-metal and superconductor by considering the probability of an electron undergoing either Andreev reflection (chapter 2.5.5) or specular reflection at the interface. The resistance area product for this case is given by

$$R^* = \rho_{(Nb)} l_{e(Nb)} \frac{R_S}{R_A} \quad (5.9)$$

where  $R_S$  and  $R_A$  denotes the probability of specular reflection or Andreev reflection, respectively.  $R_A$  is given by

$$R_A = \frac{4\mu^2}{(1+\mu^2)^2} \quad (5.10)$$

and  $\mu$  is given by

$$\mu = \frac{k_f(Nb)}{k_f(Cu)}. \quad (5.11)$$

Knowing  $R_A + R_S = 1$  it is possible to solve equation 5.9. This gives  $R^* = 2 \times 10^{-17} \Omega m^2$ , 2 orders of magnitude smaller than the experimental value. Tarte (Tarte 1992) similarly, also found difficulty in calculating  $R^*$  for noble metal-YBCO edge type contacts, and argued that any irregularities in the interface and the geometry of the contact would seriously affect the reflection and transmission processes at the interface. It is therefore, concluded that although the experimental value of  $R^*$  is much larger than the value calculated using Waldram's model, it is sufficiently low to exclude the possibility of an extrinsic resistance at the interface due to impurities.

Evidence is shown later in section 5.5, however, to support the explanation that there is a region of bilayer on both sides of the trench that is effectively part of the junction's normal-metal region.

### 5.3.3. Variation of width

When the isolation cuts are made (step 2 in figure 4.1) ions from the ion beam, erode regions along both sides of the track resulting in damage in the bilayer. This means that the apparent width of the junction (the width defined by the FIB instrument's user) is not the same as the actual width. Typically, a completed junction will show an eroded region of approximately 100 nm on both sides of the trench in the junction, and is shown pictorially in figure 5.7. Assuming that the dimensions of the eroded regions stay constant, as expected if they were caused by the ions from the ion beam, then  $I_C$  will be completely suppressed when the eroded regions overlap, i.e. when the junction circuit is broken.

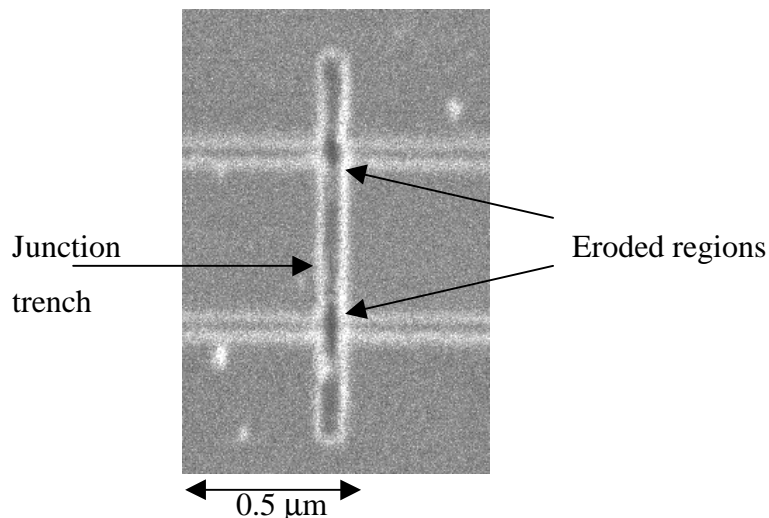
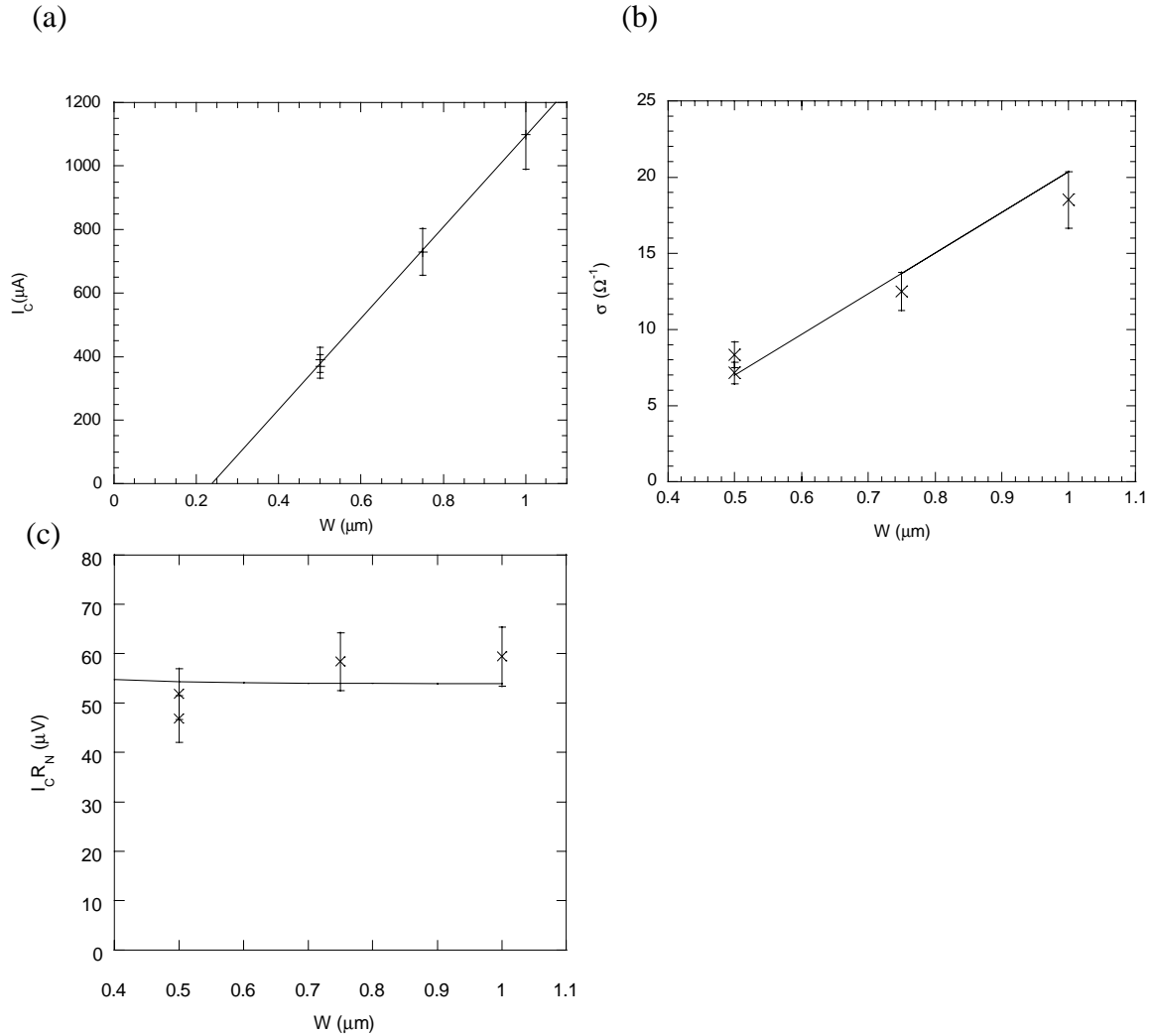


Figure 5.7: Image of a junction taken using an FIB instrument showing the eroded regions.

An experiment was performed to confirm this observation and also, to investigate how the electrical properties of the junctions changed with width. Junctions were made on one sample and for each junction the depth of the trench,  $M$ , and the length,  $L$ , were kept constant as the FIB user-defined width was varied. Figure 5.8 shows the variation of  $I_C$ ,  $\sigma_N$  and  $I_C R_N$  product as a function of the width. A line can be fitted to  $I_C$  as the width is increased, shown in figure 5.8a. This agrees with the model described in section 5.3.1, and means that  $J_0$  is constant, and consequently, the current density across the width of each junction is the same. By extrapolating the fitted line it is apparent that  $I_C$  is completely

suppressed at  $W < 240$  nm, giving the width of each eroded region to be 120 nm, which corresponds to the observed value found from figure 5.7.

Lines calculated using the model were fitted to the plots and are shown in figure 5.8b and c. In order to take account of the eroded regions the value of  $W$  in equation 5.2 has to be modified by subtracting  $0.24 \mu\text{m}$ . Successful fits are only possible by relaxing the  $L$  parameter because the current path does not follow the geometrical length of the junction as discussed in the previous section. The curves of best fits used  $L=100$  nm, although the relevance of this value is not thought to be significant due to the inaccuracies of the model.



**Figure 5.8: The variation of (a) the critical current,  $I_C$  (b) the normal state conductance,  $\sigma_N$ , and (c) the  $I_C R_N$  product with junction width ( $W$ ) less than  $1 \mu\text{m}$  at  $4.2$  K in Nb/Cu/Nb junctions (Junction length= $50$  nm). Error bars are  $\pm 10\%$ . For comparison, the results from the geometrical model are also plotted using  $W$  with  $240$  nm subtracted from the geometrical value and  $L=100$  nm.**

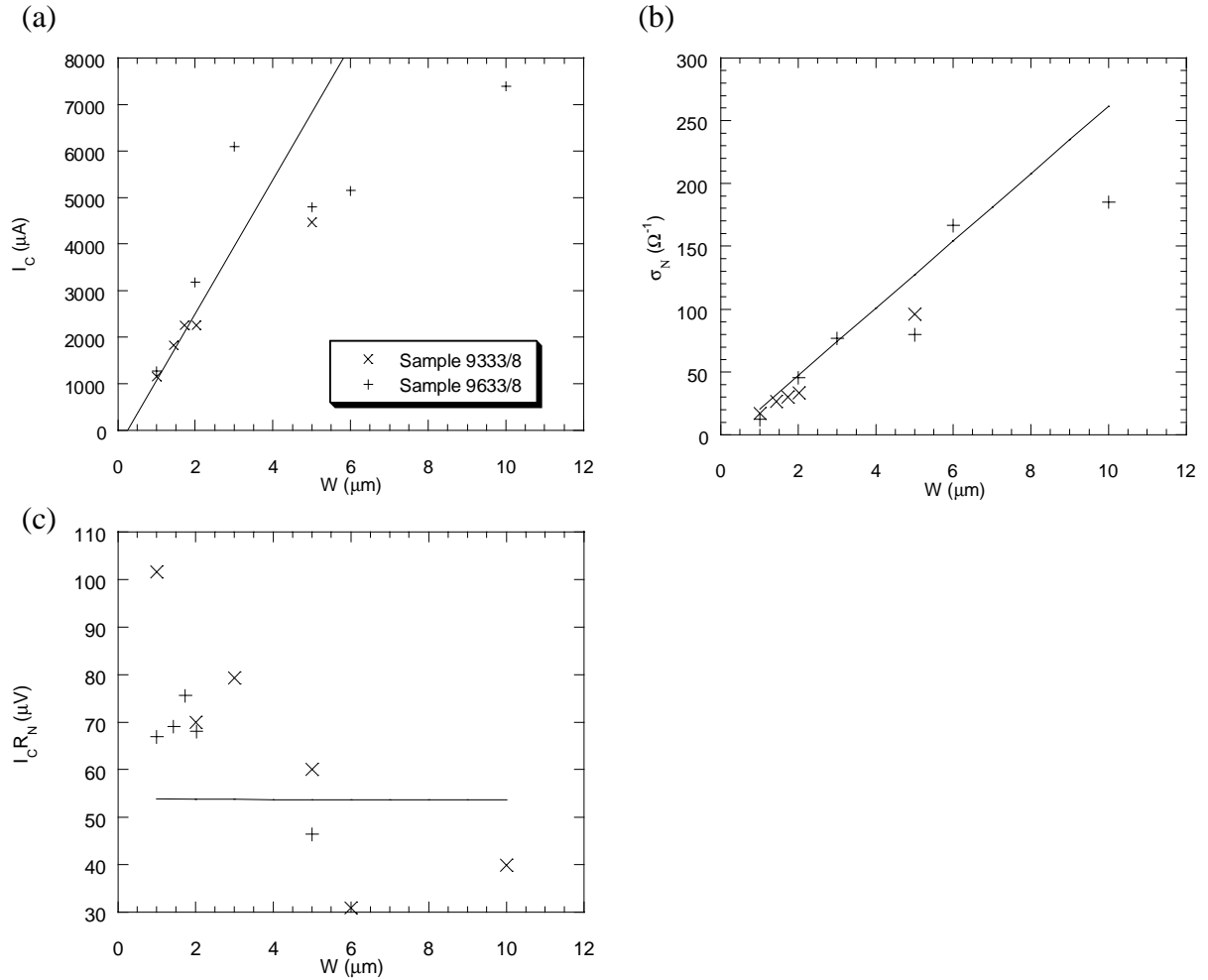


**Figure 5.9: The variation of (a) the critical current,  $I_C$  (b) the normal state resistance,  $\sigma_N$  and (c) the  $I_C R_N$  product with junction width ( $W$ ) less than  $10 \mu\text{m}$  at  $4.2 \text{ K}$  in Nb/Cu/Nb junctions (junction length is  $50 \text{ nm}$ ). For comparison the results from the model are also shown (Error is  $\sim 10\%$ , not shown).**

The next experiment is to find the dependence of  $I_C$ ,  $\sigma_N$  and the  $I_C R_N$  product as the width varies over a larger range,  $W=1-6 \mu\text{m}$ . Two sets of samples were used and were patterned using a mask design containing wide tracks. For each junction, the value of  $I_C$  was taken as the maximum  $I_C$  observed from the responses to an applied magnetic field in the  $z$ -direction,  $I_C(B)$  ( $z$ -direction is defined in figure 4.1). Plots showing  $I_C$ ,  $\sigma_N$  and the  $I_C R_N$  product versus  $W$  are shown in figure 5.9. For  $W < 2 \mu\text{m}$ ,  $I_C$  increased linearly with  $W$ , as predicted by the model. There is a departure from the linear dependence however, for  $W \geq 2 \mu\text{m}$ ; the rate of increase in  $I_C$  decreases with  $W$ . Similarly,  $\sigma_N$  shows a similar deviation from the model, although this is not as strong as in  $I_C$ . For  $W \geq 2 \mu\text{m}$  the  $I_C R_N$  product therefore, decreases with increasing  $W$ , whereas the model predicts no dependence with  $W$ .

The results show that the model is not valid for large  $W$ . A possible reason for this is  $J_0$  is no longer constant with junction width. This could be due to the effect of current redistribution in the junction region, and is examined in further detail in section 5.4.2.

### 5.3.4. Variation of the normal-metal thickness

Samples of varying Cu thickness,  $d_N$ , were deposited (9136 deposition run, detailed in table 3.3), and then junctions were fabricated in the usual way. For each junction trench, only the Nb layer was removed. This ensured that the depths of the junction's trenches were kept constant. For each junction, the  $I_C$  and  $R_N$  were measured in the usual way and in figure 5.10 the  $I_C$ ,  $\sigma_N$ , and  $I_C R_N$  product are plotted as a function of  $d_N$ .

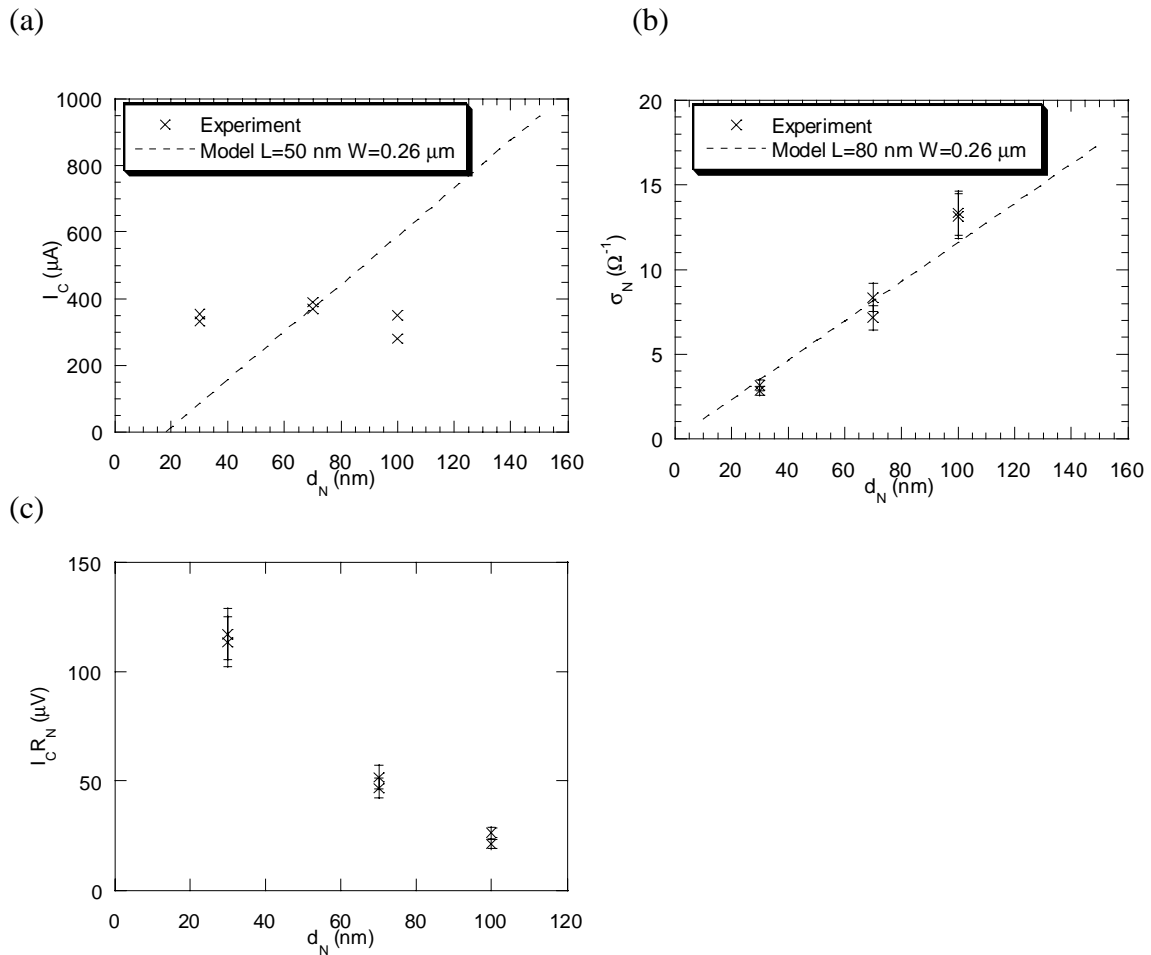


**Figure 5.10:** The variation at 4.2 K of (a) the critical current,  $I_C$  (b) the normal state resistance,  $\sigma_N$  and (c) the  $I_C R_N$  product with the normal-metal thickness ( $d_N$ ) in Nb/Cu/Nb junctions. For comparison, the results from the geometrical model are also shown (dotted lines) in (a) and (b).

Using the model, fitted lines have been added to the  $I_C$  and  $\sigma_N$  plots to show the discrepancies between the model and experiment. From equations 5.1 and 5.2 both the  $I_C$  and  $\sigma_N$  are expected to increase linearly with  $d_N$ .  $\sigma_N$  does indeed increase proportionally with  $d_N$  and a line can be fitted to the data, calculated using the model with suitable fitting parameters. The variation of  $I_C$  shows however, no significant dependence with  $d_N$ . This discrepancy between the experiment and the model highlights the major drawback of the main assumption used in the model; the junction does not have a 1-dimensional geometry.

A possible qualitative explanation of  $I_C$  being independent of  $d_N$  can be given using the proximity effect, as described in chapter 2.5. A region of Cu directly below the Nb will be proximitised to roughly a depth of a coherence length ( $\xi_{ND}$ ). Electronic transport in the proximitised layer may therefore, possess more coherent properties than the rest of the normal-metal layer. In effect, the electronic contribution to the Josephson supercurrent would come mainly from current transport between the two proximitised regions on either side of the junction.

The problem with this explanation, however, is there is no observed decrease in  $I_C$  when  $d_N=30$  nm, i.e. for  $d_N < \xi_{ND}$ , ( $\xi_{ND}$  is calculated to be  $\sim 60$  nm at 4.2 K). This may be due to the low range of  $d_N$  used, and will be discussed further in section 5.6.

An important conclusion, however, is a junction's  $I_C R_N$  product will decrease with increasing  $d_N$  in the range studied.

## 5.4. Response to magnetic fields

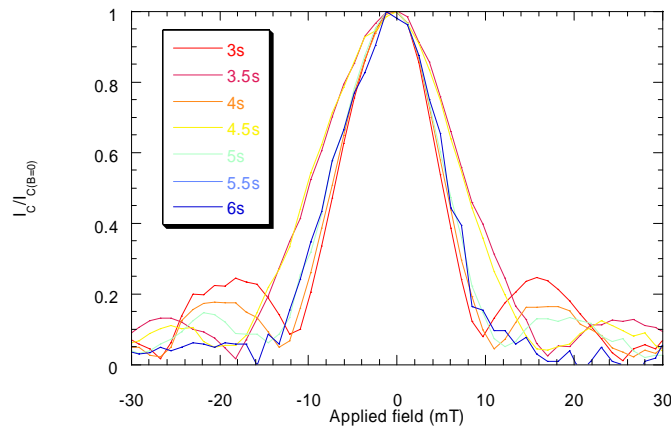
The response of a junction to a magnetic field conveys useful information about the current distribution across its width, and the current-transport mechanisms in the junction. A systematic survey of the responses of junctions to magnetic fields was carried out.

Figure 4.13 shows the  $I_C(B)$  plot of a typical junction, with the corresponding theoretical sinc dependence curve described by equation 2.44. Only the first minima were recorded because of the current limit in the probe's magnetic coils. Although the experimental  $I_C(B)$  results showed dependencies similar to the ones expected from the theoretical dependence, the 1<sup>st</sup> minima positions were significantly smaller than the theoretical ones. The thin-film and sub-micron geometry of the junction makes this discrepancy unsurprising because the  $I_C(B)$  model (chapter 2.3.3) describes the case for an ideal junction where shielding currents and its geometry are ignored.

### 5.4.1. Variation of the mill time

The effect of varying mill time is now investigated. Figure 5.11 shows the  $I_C(B)$  responses of junctions with different mill times. They show that the basic shape of the  $I_C(B)$  response remains similar; virtually all of the junctions display at least 2 minima on either side of the central maximum, and then as the magnetic field strengthens the  $I_C$  increases. The junctions that do not appear to display this behaviour (at longer mill times) do show however, a strong reduction in the  $I_C$  as the magnetic field increases, but as the field is increased further the  $I_C$  appears to level off with increasing field. This effect is thought to be the result of electronic noise swamping the very low  $I_C$  observed at higher fields.

The average magnitudes of the first minima positions were recorded as a function of mill time and are plotted in figure 5.12. The figure shows that there are significant fluctuations in the positions of the first minima, but the fluctuations appear to be independent of the mill time, and so may be due to trapped flux, or other extraneous sources.



**Figure 5.11: The normalised responses at 4.2 K of junctions to an applied magnetic field,  $I_C(B)$ , with varying junction trench milling times.**

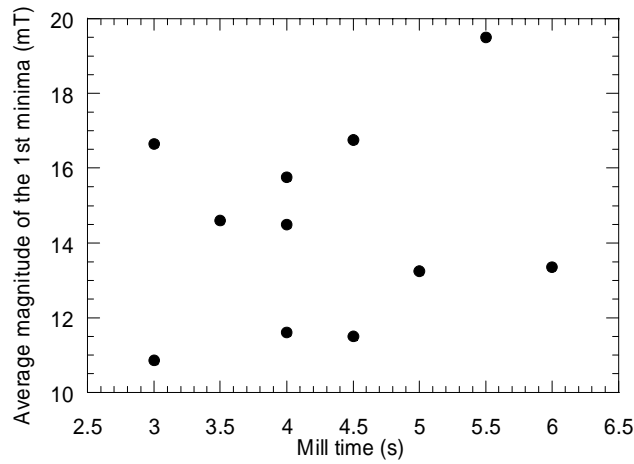


**Figure 5.12: Variation at 4.2 K of the average magnitude of the first minima (taken from the  $I_C(B)$ ) with the junction trench mill time in Nb/Cu/Nb junctions.**

#### 5.4.2. Magnetic fields applied in the in-plane directions

Magnetic fields were also applied in the  $x$  and  $y$  directions, defined in figure 4.1, but no significant changes in  $I_C$  were observed when the field was applied in either direction. There was a small reduction in the bilayer track's critical current however, when strong fields were applied in the  $y$  direction.

#### 5.4.3. Variation of width and length

A quantitative approach can be used to explain how the responses of a junction to a magnetic field change with  $W$  and  $L$ . A systematic study of this has been made and the average magnitude of the positions of the first  $I_C(B)$  minima versus  $W$  and  $L$  are plotted in figures 5.13 and 5.14, respectively. Only the positions of the first minima are recorded because of the greater uncertainty in the position of higher order minima due to the presence of electronic noise, as mentioned in section 5.4.1. The estimates of the uncertainty in the positions of the minima are 10%, and are displayed in both plots as error bars. Both plots in figures 5.13 and 5.14 show that  $W$  and  $L$  affect the positions of the minima. For increasing  $W$ , the average magnitude of the minima positions decrease non-linearly, and for increasing  $L$ , the positions linearly decrease. This is unsurprising as even the simplified Josephson junction model, described in chapter 2.3.3, predicts a width dependence with a minimum interval,  $B_0$ , given by

$$B_0 = \frac{\Phi_0}{W(2\lambda_L + L)}. \quad (5.12)$$

$\lambda_L$  is the London penetration depth, and is taken to be 90 nm, reported for similar polycrystalline Nb thin films (Schneider 1994). Comparison with the minima positions predicted from equation 5.12 with  $W$  and  $L$  can be made, and are also shown in their respective figures. It is apparent from the two plots that there is a large discrepancy between the results from the experimental and the theory. This is probably a consequence of the thin-film geometry and micron scale of the junctions.

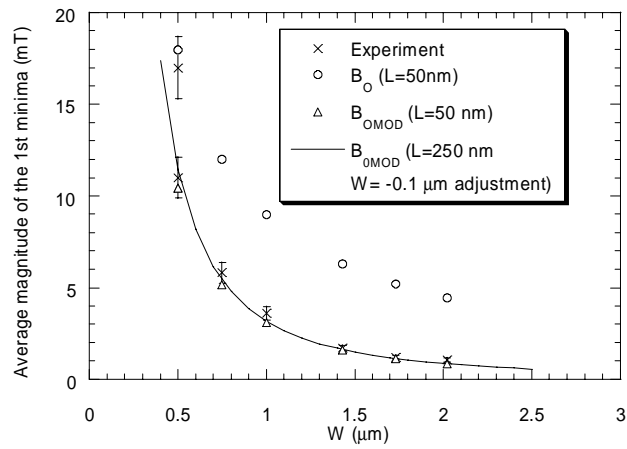


**Figure 5.13:** The variation at 4.2 K of the average magnitude of the first minima (taken from the  $I_C(B)$ ) with width ( $W$ ) in Nb/Cu/Nb junctions. The results from several models are also plotted.

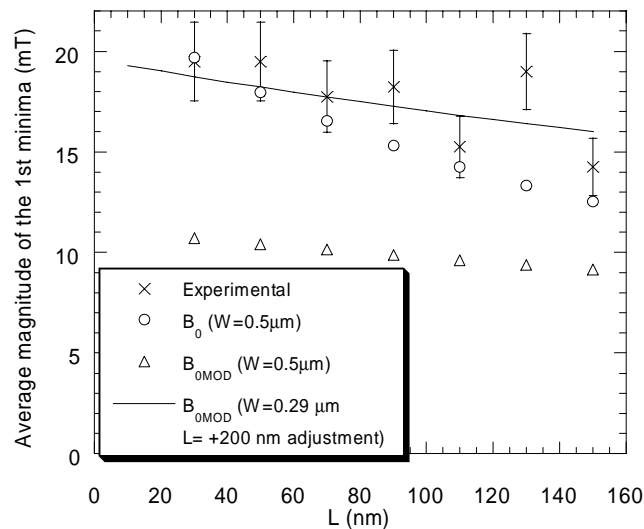


**Figure 5.14:** The variation at 4.2 K of the average magnitude of the first minima (taken from the  $I_C(B)$ ) with length ( $L$ ) in Nb/Cu/Nb junctions. The results from several models are also plotted.

### 5.4.3.1. Comparison with the Rosenthal model

Rosenthal *et al.* (Rosenthal 1991) successfully modeled the  $I_C(B)$  of synthetic planar thin-film grain boundary Josephson junctions. Although this is not the same type of junction as the one studied here, the geometry is similar, and as will become clear, the model is applicable to most thin-film Josephson junctions. They simplified the geometry of their junction to a planar geometry, where the thickness of the thin-film superconductor,  $d_S$ , is comparable to  $\lambda_L$ . This means that the variation of the phase difference across the width of the junction is independent of the film's thickness, and also the shielding currents at the edges of the junction significantly change the current density across the width of the junction. To take these effects into account they solved the London equations (London 1935) for two unconnected semi-infinite slabs in the limit  $d_S < \lambda_L$ , and found that the two dimensional flow of the shielding currents severely affected the current distribution across the width of the junction. This had the effect of changing the interval between minima and is denoted as  $B_{0MOD}$  where

$$B_{0MOD} = 1.84 \frac{\Phi_0}{W^2 + W(2\lambda_L + L)} \quad (5.13)$$

Values of  $B_{0MOD}$  have been calculated using the fixed parameters  $L = 50$  nm (for varying  $W$ ) and  $W = 0.5$   $\mu\text{m}$  (for varying  $L$ ). These are plotted for comparison with the experimental results in figures 5.13 and 5.14.

For varying  $W$ , the model agrees remarkably well with experiment, as shown in figure 5.13. It is noted that for low values of  $W$  ( $W \sim 0.5$   $\mu\text{m}$ ) there were significant spreads in the experimental positions of the minima. Possible causes for these spreads are thought to be: firstly, a low precision in  $W$  due to poor focusing of the FIB instrument during the isolation cuts fabrication step; and secondly, magnetic shielding by circulating currents in the nearby electronically isolated, rectangular bilayer cuts. Both causes would have a greater effect on the response of a junction with low  $W$ .

For varying  $L$  (figure 5.14) there is no agreement with the model, and the trend in the experimental data shows a significant deviation from the decreasing trend. This is thought to be related to the magnetic observations in junctions of  $W = 0.5$   $\mu\text{m}$ , described above.

By changing the fixed parameters and systematically adjusting  $L$  and  $W$ , lines of best fit were made, and plotted, in both figures. The adjustments are also, displayed in the figures. Unsurprisingly, no adjusted values for  $L$  and  $W$  can be found that model both sets of data successfully, for the reasons previously given above. It is clear, especially from the

more reliable  $W$  dependence case, that the effects of circulating currents around the edges of a junction play an important role in the junction's response to a magnetic field.

#### 5.4.4. Large limit

When the Josephson penetration depth,  $\lambda_J$ , becomes greater than the width of the junction, i.e.  $\lambda_J > W$ ,  $I_C$  becomes large compared with the Meissner screening currents so the central part of the junction becomes shielded from an externally applied magnetic field. In this situation the junction is considered to be in the large limit.  $\lambda_J$  is also temperature dependent, increasing with decreasing temperature, so a crossover between the two limits can be observed in the same junction. The crossover is gradual over temperature and  $W$ , and consequently, it is often difficult to know precisely its position. A junction can be characterised as being in the large limit by examining its  $I_C(B)$ . In the large limit the sinc dependence changes to a linear one thus, the plot traces out triangular profiles. A detailed explanation for this is found in Barone and Paterno (Paterno 1982). It was apparent that for  $W \geq 2 \mu\text{m}$ , junctions at 4.2 K displayed large limit-like behaviour as demonstrated by their  $I_C(B)$  behaviour. An example is shown in figure 5.15 of a junction with  $W=2 \mu\text{m}$ . An offset in the central maximum was observed in all these junctions. This can arise from two causes; trapped flux in the junction; and self-field effects due to the geometry of the junction. Since the  $I_C(B)$  plots are fairly symmetrical it is unlikely to be a result of the latter; if it were the result of geometry the positions of the minima would not shift with the central maximum.

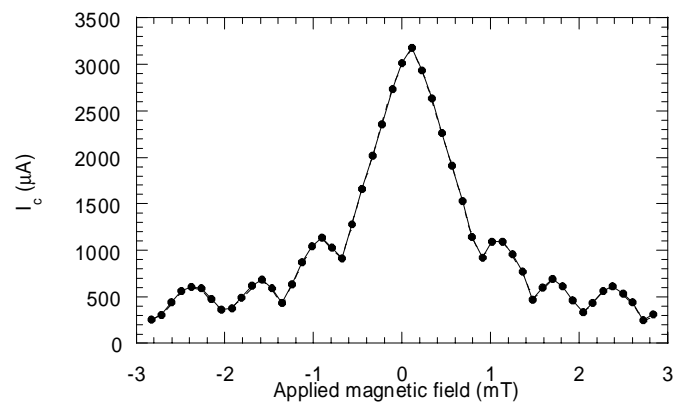


**Figure 5.15: The responses of a junction to an applied magnetic field,  $I_C(B)$ , at 4.2 K of a Nb/Cu/Nb junction ( $W=2 \mu\text{m}$ ,  $L=50 \text{ nm}$ ). The  $I_C(B)$  shows large limit behaviour.**

## 5.5. Temperature dependence of the I-V characteristics

SNS junction  $I$ - $V$  characteristics have complex temperature dependencies, even with junctions of the simplest geometry. The non-equilibrium electrical environment in a junction means there are many contributing processes to be considered when modeling their temperature dependencies. Indeed, there has been a significant body of work published on this subject, mainly in the mid-1970s to early-1980s, when RSJ-like junctions were being considered for commercial and scientific exploitation. Two review articles discussed this research in-depth (Likharev 1979) (Delin 1996).

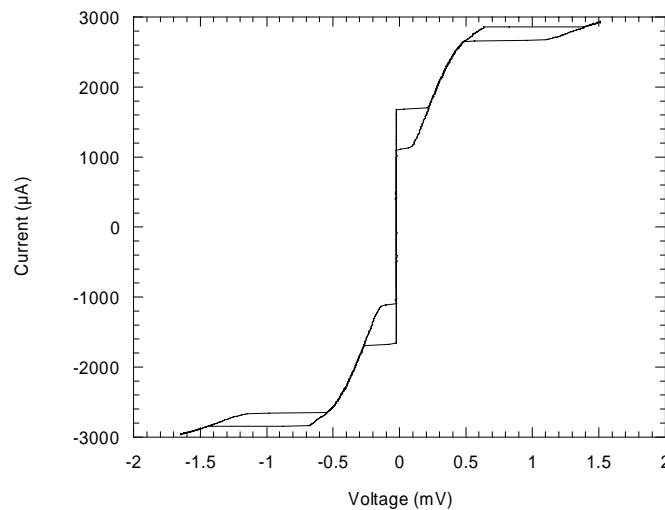


**Figure 5.16: I-V characteristics at 0.40 K of a Nb/Cu/Nb junction ( $W=0.5 \mu\text{m}$ ,  $L=90 \text{ nm}$ ) showing hysteresis at zero- and finite- bias.**

As seen previously (section 5.2.2),  $R_N$  is difficult to measure. Fortunately, most models of SNS junctions assume  $R_N$  to be independent of temperature, and also, assume that non-equilibrium junction effects do not affect  $R_N$ . This means that the theoretical  $I_C R_N$  product can be scaled to the readily obtainable  $I_C$ .

The  $I$ - $V$  characteristics of three junctions of varying  $L$ , previously examined in section 5.3.2, were recorded in the temperature range  $0.35 \text{ K} < T < 9 \text{ K}$  using the Oxford Instruments Heliox<sup>TM</sup> probe (chapter 3.7.3). There are two important features found in all of the junctions studied: first, hysteresis develops in the  $I_C$  at low temperatures ( $< 2 \text{ K}$ ), the lower branch is the return current ( $I_R$ ) from finite voltages, and the upper branch is the critical current ( $I_C$ ) as current increases through the junction (this is shown graphically in figure 4.8b); second, hysteresis in the  $I$ - $V$  characteristics at high biases are always present

(section 5.2.2.3), and their onsets vary with temperature. Figure 5.16 shows a typical example of  $I$ - $V$  characteristics containing both hysteretic features. These features have been observed separately in two previous studies, by Warlaumont (Warlaumont 1979a) and Van Dover (Vandover 1981). Warlaumont (Warlaumont 1979b), made planar-sandwich type Pb(150 nm)/Cu(60 nm)/Pb(150 nm) junctions, and Van Dover made planar bridge junctions. The dimensions of the junctions were similar however, with  $L=200$  nm and  $W=200$  nm. Possible reasons for the development of hysteresis are examined later in this section, but firstly, the temperature dependencies of  $I_C$  and  $I_R$  are examined.

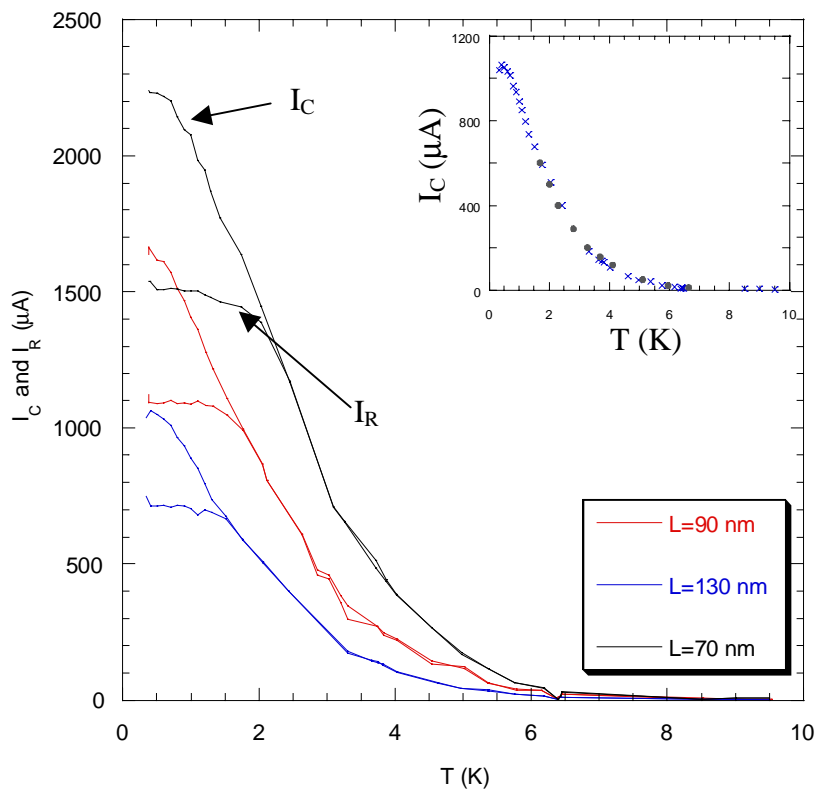


**Figure 5.17: Variation of the critical current ( $I_C$ ) and the return current ( $I_R$ ) with temperature ( $T$ ) of Nb/Cu/Nb junctions of varying length ( $L$ ). Inset shows a comparison with Warlaumont's data( $\bullet$ ), taken from (Warlaumont 1979a).**

### 5.5.1. $I_C$ and $I_R$

The  $I_C(T)$  and  $I_R(T)$  of the 3 junctions studied here are plotted in figure 5.17. Modeling their behaviour starts with the well-known model of SNS junctions devised by Likharev (Likharev 1976). Likharev developed a model for a planar- sandwich type junction by solving the Usadel equations (chapter 2.5.4), which describe the current flow between superconductors as diffusive. This is appropriate for the case where the normal-metal is in the dirty limit, i.e.  $\ell_e < \xi_{NC}$ . Four important assumptions were made:  $J_0$  does not depend on the parameters of the normal-metal; the temperature dependent energy gap,  $\Delta(T)$ , in the thick superconducting electrodes determines  $J_0$ ; the proximity effect is negligible in both materials; and  $R_N$  is always constant. Using these assumptions, appropriate boundary conditions could be made and solutions to the equations were made in certain limiting cases. The relevant equations for the two temperature limiting cases are:

$$I_C = \frac{4\Delta^2(T)}{\pi e k_B T R_N} \frac{L_{eff}}{\xi_{ND}} \exp\left[-\frac{L_{eff}}{\xi_{ND}}\right], \quad (0.3T_C < T < T_C) \quad (5.14)$$

$$I_C = \frac{29\Delta(0)}{eR_N} \left(\frac{\xi_{ND(T_C)}}{L_{eff}}\right)^2 \quad (T < 0.05T_C; L_{eff} > 6\xi_{ND}). \quad (5.15)$$

Here,  $L_{eff}$ , is the effective length of the junction. The adjustable parameters in this model are  $\Delta$ ,  $L_{eff}$ , and  $\xi_{ND}$ . In the absence of any direct measurements of  $\Delta(0)$  it can be estimated from measurements of  $\Delta$  in Nb(90nm)/Al(12nm)/AlO<sub>x</sub>/Al(6nm)/Nb(60nm) tunnel junctions to be 1.3 meV (Moseley 1997). This is a reasonable value to take given that the bulk value of  $\Delta$  is 1.5 meV (Kittel 1976). The dependence of  $\Delta$  with temperature can be calculated using a power series law given by Mühlischlegel (Mühlischlegel 1959). The actual value of  $\Delta(T)$  in the bilayer structure will probably be smaller than the estimate value because of the intrinsic differences between the junctions; the presence of a normal-metal (Cu) in intimate contact with the superconductor (Nb) instead of another superconductor (Al).

Using the adjustable parameters however, no fit from equations 5.14 and 5.15 can be made to the data. This is not unsurprising, as the assumptions used in the model are not appropriate for this case. The presence of the proximity effect, confirmed by  $T_C$  measurements of similar bilayer films (Singh 1999), in the bilayer structure must have a significant effect on  $I_C$ .

### 5.5.1.1. Comparison with the Van Dover $I_C(T)$ model

Van Dover (Vandover 1981) attempted to include the proximity effect in Likharev's model. Using a similar approach to the one used by Fink (Fink 1976) the induced Ginzburg-Landau order parameter in the normal-metal,  $\psi_N$ , by the superconductor was calculated. Assuming  $\psi_N$  to be constant throughout the thickness of the normal-metal, a 1-D potential well across the normal-metal in the junction region was constructed.  $\psi_N$  was used as the boundary values on either side of the well. This is shown schematically in figure 5.18. In previous discussions of the proximity effect the BCS pair potential,  $\Delta_P(x)$ , was used (chapter 2.5). For this case, Ginzburg-Landau theory was used and here  $|\psi|^2$  is the density of pairs and is proportional to  $\Delta_P(x)$ .

The relationship between  $\psi_N$  and the order parameter in the thin-film superconductor,  $\psi_S$ , is given by

$$\psi_N = A\psi_S, \quad (5.16)$$

where  $A$  is an empirical parameter whose value was in the range  $0 < A < 1$ .  $\psi_S$  is given by

$$\psi_S = f(T)\psi_{S\infty} \quad (5.17)$$

where  $f(T)$  is a temperature dependent function that represents the degree to which the order parameter of the superconductor is depressed at the superconductor/normal-metal boundary, otherwise known as the softness of the boundary condition.  $\psi_{S\infty}$  is the order parameter far from the junction region and here, it is equal to  $\Delta$ .  $f(T)$  was calculated by numerical analysis by Van Dover and is given as

$$f_{(T)}^2 = \frac{2\cos^4\left(\frac{d_S}{\xi_{SD}}\right)}{\cos^4\left(\frac{d_S}{\xi_{SD}}\right) - 1} \left[ \left( \frac{A^2\xi_{SD}}{\gamma\xi_{ND}} \right)^2 \tanh^2\left(\frac{d_N}{\xi_{ND}}\right) - \tan^2\left(\frac{d_S}{\xi_{SD}}\right) \right], \quad (\psi_S \ll \psi_{S\infty}) \quad (5.18)$$

where  $\gamma$  is the effective mass ratio of electrons in the superconductor and normal-metal, which in this case is equal to unity.

The differences between the normal state parameters of the two materials were also taken into account and combined with the proximity model to form a prefactor,  $F_P$ , to equations 5.14 and 5.15 given by

$$F_P = \frac{\rho_N f_{(T)}^2 A^2}{\rho_S \gamma}, \quad (5.19)$$

where  $\rho_N$  and  $\rho_S$  are the normal-state resistivities of the normal-metal and superconductor, respectively.

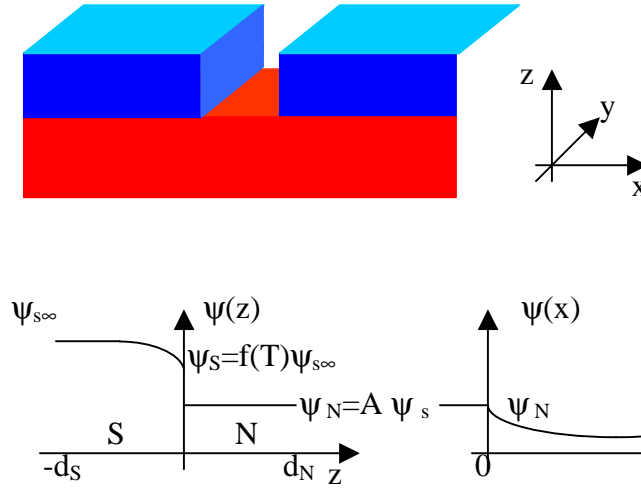


**Figure 5.18: Schematic diagrams of a planar bridge SNS junction showing how the order parameter ( $\psi$ ) varies across the width of the junction and the depth of the Nb/Cu bilayer according to Van Dover's model.**

Application of Van Dover's model to the data has been made by multiplying Likharev's hard-boundary reduced temperature and length solutions for different ratios of  $L_{eff}/\xi_{ND(T=TC)}$  over their whole temperature range by the extrapolated  $I_{C(T=0K)}$  and equation 5.19.  $F_P$  is sub-divided into three parts,  $f(T)$ ,  $A^2$ , and  $\rho_N/(\rho_S\gamma)$ , to act as fitting parameters. The fits and the fitting parameters used for all three junctions are displayed in figure 5.19 and table 5.3, respectively.

$L$ (nm)	$I_C$ ( $T=0K$ )	A	$\rho_N/(\rho_S\gamma)$ Theoretical	$\rho_N/(\rho_S\gamma)$ Experimental	$L/\epsilon_{ND}$	$L_{EFF}/\epsilon_{ND}$
70	2370	0.8	0.21	$0.71 L/\epsilon_{ND}=6$ $1.3 L/\epsilon_{ND}=8$	1.7	$\sim 7$
90	1830	0.8	0.21	0.91	2.1	8
130	1170	0.8	0.21	0.60	3.1	$\sim 8$

**Table 5.3: Comparison of the fitting parameters from the model and the results.**

The best fit is made to the junction with  $L=90$  nm, shown in figure 5.19b, and the other two agreed less well. This is probably because the data for the better fitting curves from Likharev's model for  $(L_{eff}/\xi_{ND})=7$  and 9 were not available. The values of the fitting

parameters calculated using the measured values of  $\rho_N$  and  $\rho_S$ , are also displayed in table 5.3 and show great disagreement with the actual fitted values used. This was also found by Van Dover, and can not be solely attributed to the choice of  $A$  here, as this would have to be greater than 1 in each case.

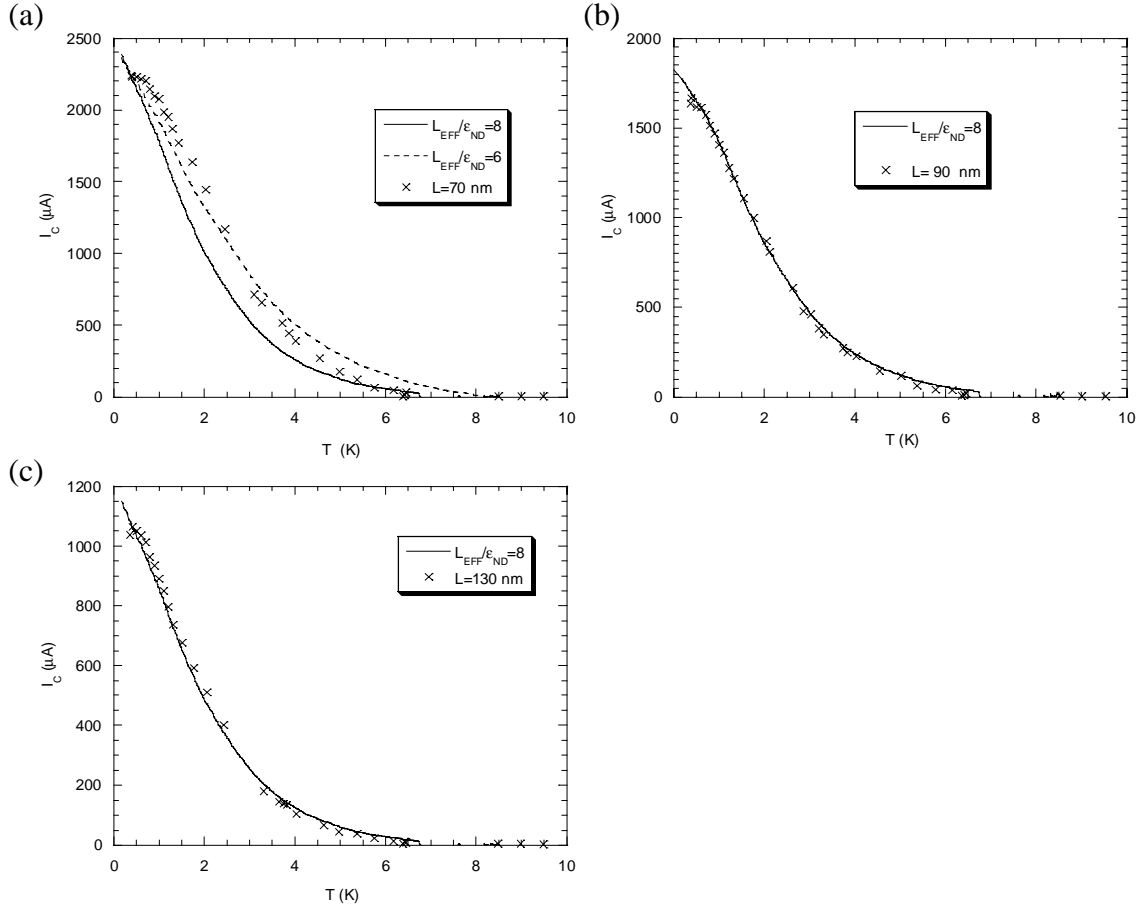


**Figure 5.19: Variation of the critical current ( $I_C$ ) with temperature ( $T$ ) for various Nb/Cu/Nb junctions with junction length ( $L$ ) (a)  $L=70$  nm (b)  $L=90$  nm, and (c)  $L=130$  nm. Fitted lines from Van Dover's model are also shown. The legend includes the reduced length ( $L_{EFF}/\xi_{ND}$ ) used.**

### 5.5.1.2. Comparison with other models

For planar-sandwich type junctions Kupriyanov *et al.* (Kupriyanov 1983) investigated the influence of the effective electron interaction on  $I_C$  inside the normal-metal. They incorporated the BCS electron-phonon relation,  $\lambda=N(0)V_i$ , (chapter 2.2.3.3) into the Usadel equations and applied the same hard boundary conditions as Likharev did. For a normal-metal that does not superconduct at any temperature  $\lambda$  is negative, which is appropriate for Cu. They applied their model to the work of Warlaumont (Warlaumont

1979a) and found a better fit using the ratio  $L_{eff}/\xi_{ND} = 6.5$ . This compared with the ratio of 8.2, obtained using Likharev's basic model. The sensitivity of the model to  $\lambda$  at  $\lambda < 0$  was found to be poor, and it was not possible to determine  $\lambda$  from the data.

Warlaumont, however, scaled the curve from Likharev's model in order to gain a best fit to their data. Scaling Likharev's model was shown using Van Dover's model to be valid if the induced order parameter in the normal-metal is constant with temperature, and the differences between the materials' normal states are also, constant with temperature. While the latter assumption is reasonable, the former depends upon the softness of the boundary condition, described in equation 5.18. This means the scaling procedure is only valid at low temperatures where  $f(T)$  is largely unaffected by temperature. At higher temperatures  $f(T)$  is strongly dependent on temperature, especially as  $T$  approaches  $T_C$ . It means that the scaling procedure made by Warlaumont is therefore, only valid for the low temperature regime, and given the good fit in this temperature regime the effective electron-phonon interaction effect does play a significant role in determining the effective length of the junction,  $L_{eff}$ .

For all three cases studied here, the ratios  $L_{eff}/\xi_{ND}$  are around 8, and are much greater than the predicted values of between 1 and 4 where  $L \equiv L_{eff}$ . This was also found by Van Dover and Warlaumont, and must be a direct consequence of neglecting, or over-simplifying the junction's physical geometry in the frame-work of Likharev's model so that  $L_{eff} > L$ . The prefactor,  $F_P$ , devised by Van Dover to soften Likharev's hard boundary model was based upon a static 2-dimensional proximitised bilayer structure. A major omission in their model was to neglect heating in the region of the junction. This will have a significant effect upon the electrical dynamics of the superconductor/normal-metal boundary. As the temperature decreases more heat must be dissipated in the surroundings, which reduces  $\psi_N$ . Also, the geometry of the planar-bridge junction means that the transmission of the current does not necessarily occur only at the edges of the Nb banks in the trench, as discussed in section 5.3.2. Taking this into account, by making the crude assumption that  $L_{eff} = L + 200$  nm, gives values of  $L/\xi_{ND}$  in the range 6 to 8, roughly in agreement with the experimental  $L_{eff}/\xi_{ND}$  values, and are shown for comparison in table 5.3.

This excess distance of 200 nm supports the explanation given in section 5.3.4 that there is a region of bilayer on both sides of the trench that is effectively part of the junction's normal-metal region.

### 5.5.2. Hysteresis

Attention is now paid to the hysteresis observed in the  $I$ - $V$  characteristics. Warlaumont *et al.* (Warlaumont 1979a) observed similar hysteresis in the  $I_C$  and proposed three possible causes: first, the result of capacitive shunting (McCumber 1968; Stewart 1968); second, the result of time relaxation effects in the junction, described in chapter 2.6.4; third, the result of self-heating due to heat dissipation in the normal-metal region of the junction caused by the high current density, described by Skocpol (Skocpol 1974).

Warlaumont *et al.* ruled out the first cause for the hysteresis observed at zero-bias because there were no capacitive materials present. The third cause, self-heating, was found to be unsuitable because  $I_R$  did not vary with temperature as predicted by Sckpol where  $I_R \propto (I_C)^{1/2}$ . They believed the probable cause of hysteresis in their junctions was due to the second cause; time-relaxation effects. Song (Song 1976) developed a model using a Time-Dependent Ginzburg-Landau (TDGL) framework (chapter 2.6.4) made by Baratoff and Kramer (Baratoff 1977) in Warlaumont). The model states that hysteresis will begin to develop when the time taken for electron pairs to cross the normal-metal region of the junction,  $\tau_{eff}$ , becomes sufficiently greater than the Josephson period,  $\tau_J$  (the reciprocal of the Josephson frequency). Warlaumont's results disagreed with this model however, because the onsets of hysteresis were observed at higher temperatures than expected, and also, there was little dependence on the length of the junction.

More recently, a model was developed by Kummel (Kummel 1990). They calculated the  $I$ - $V$  characteristics of SNS junctions using a relaxation-time model based on the Bogoliubov-de Gennes equations (Svidzinsky 1973) instead of the Ginzburg-Landau model. In this model the transport of current through the normal-metal is by quasiparticle wave packets via Andreev reflection, and the density of states of these charge carriers are calculated using a 1-dimensional potential well approach. The  $I$ - $V$  characteristics calculated from this model show regions of negative-differential resistance and other features, which would be seen as hysteresis in the current-biased  $I$ - $V$  characteristics. Hysteresis was found to be only achievable however, in clean limited materials and where  $L_{eff} \ll \xi_{NC}$ .

Skocpol *et al.* (Skocpol 1974) developed a self-heating hotspot model for ScS junctions, although this model can be applied to SNS junctions. The model assumes that the heat generated by the current in the normal region of the junction can only be transported away by two mechanisms: thermal conduction within the film; and surface heat transfer across the temperature discontinuity, developed at the boundaries with the substrate and

cryogen, if present. The limiting cases where the thermal healing length, the characteristic length over which the combination of heat conduction within the film and surface heat transfer occurs, is greater or less than  $L_{eff}$  were both considered. The model calculates the current that can generate sufficient heat to balance surface heat transfer from the normal region. Above this current, known as the scaling current ( $I_{scale}$ ), the hotspot will locally heat the superconducting electrodes above their  $T_C$ , which increases the normal region of the junction. The thermal healing length for the thin-film devices studied here, are typically of the order of microns (Wellstood 1994) so the appropriate scaling current is given by

$$I_{scale}^2 = T(T_C - T) \left( \frac{k_B}{e} \right)^2 \frac{\pi^2}{3R_\phi^2}, \text{ for } T \sim T_C, \quad (5.20)$$

where  $R_\phi$  is the sheet resistance. For the three junctions studied, the current where the onset of the strong curvature in the  $I$ - $V$  characteristics is taken to be  $I_{scale}$  and were recorded as a function of temperature. Plots of  $I_{scale}^2/T$  versus  $T$  were made and are shown in figure 5.20. Equation 5.20 predicts that the plots will have a straight line fit with a slope of  $-0.15 \times 10^{-6} \text{ A}^2\text{K}^{-2}$  using the measured value of  $R_\phi = 0.4 \text{ } \Omega\phi^{-1}$ . For comparison, the results from equation 5.20 were also plotted in figure 5.20. For temperatures above 6 K, the hot-spot model fits with the experimental data. The results showed no inverse linear dependence at low temperatures; as the temperature was lowered the rate of change in  $I_{scale}^2/T(T_C - T)$  increased.

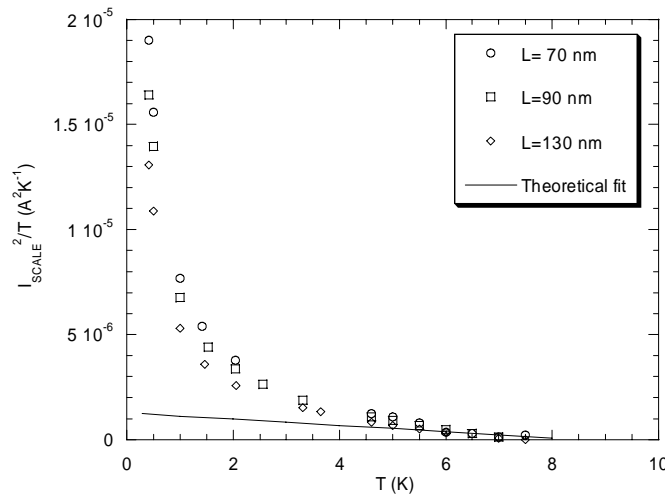


**Figure 5.20: The temperature ( $T$ ) dependence of the scaling current ( $I_{SCALE}$ ) with junction length ( $L$ ).**

**It shows the expected result that  $I_{SCALE}^2/T$  is only linear with temperature near  $T_C$ .**

Van Dover *et al.* also observed this deviation between the model and their results, and they attributed it to the non-validity of equation 5.20 at low temperatures.

Skocpol *et al.* (Skocpol 1974), also, described the hysteresis observed in ScS junctions in the transition between the zero- and finite- voltage states, at low temperatures. They argued that at low temperatures,  $I_C$  can exceed the current required to sustain a normal hotspot,  $I_H$ . As long as the junction is superconducting there will be no dissipation of heat, but once  $I > I_C$  then heat will be dissipated, causing a hot-spot to form, which can be sustained at much lower temperatures. The progressive development of hysteresis as the temperature was lowered arises because of the different temperature dependencies of  $I_C$  and  $I_H$ ;  $I_H$  has a temperature dependence of  $(1-T/T_C)^{1/2}$ . For the junctions studied here, the results show no such temperature dependencies; as the temperature decreases  $I_R$  only rises slightly before reaching a constant value.

No model can be fitted to the observed temperature dependence of the hysteresis at zero-bias. The most likely cause for hysteresis is, however, local heating and is demonstrated to be the case in chapter 7.3.4.

## 5.6. Comparison with recent results

Using the *in-situ* resistance measurement technique (Latif 2000), Hadfield *et al.*, have improved the method for fabricating a junction (Hadfield 2000). The depth of a cut, or a trench, made by an FIB instrument can be controlled more accurately than was possible using the end point detection technique, used here. In addition, they found that the depth of a trench made using end-point detection was over-estimated. This was probably due to the assumption that the size of the milling area did not affect the mill rate. Here, a mill time of 4 s does not correspond to the thickness of the Nb layer, but instead to 70 % of the thickness. The properties of the junction, however, are not ScS-like. To show this, two junctions were made by Hadfield, one in a Nb(125 nm)/Cu(75 nm) film and another in a Nb (125 nm) film. The junction geometry as defined by the FIB instrument are the same, including the trench depth ( $M=90$  nm). The  $I$ - $V$  characteristics at 4.2 K of both junctions are plotted together in figure 5.21. The  $I$ - $V$  characteristics of the junction made in the Nb film compared to the one in Nb/Cu show: smaller  $I_C$ ; hysteresis present in the  $I_C$ ; and higher  $R_N$ . In addition, they have found that the junction made in the Nb film had a poorer response to microwaves. Hadfield *et al.* have also shown that magnetic impurities are present in the Cu layer. If there is a

sufficient concentration of magnetic impurities, the proximity effect will be suppressed in the Cu layer (Yang 1984).

Very recently, Hadfield *et al.* repeated the experiment reported in section 5.3.4 using

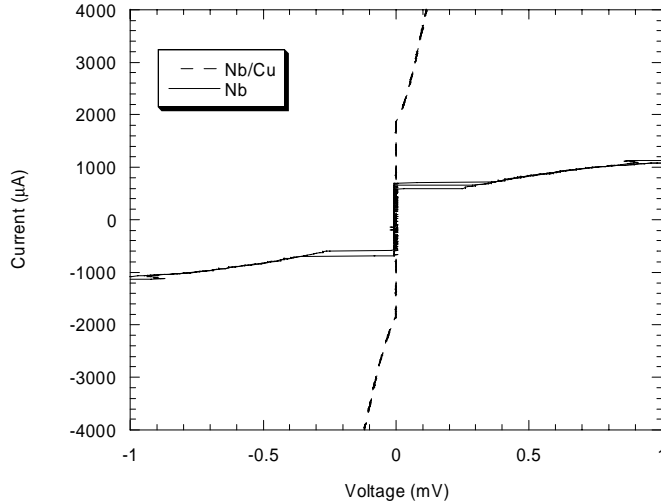


**Figure 5.21: Comparison of I-V characteristics for junctions made in Nb(125 nm) and Nb(125 nm)/Cu(75 nm) films (courtesy of R.H. Hadfield).**

junctions made from their more reliable fabrication method. They made junctions similar to the junctions studied here, but over a wider range ( $0 < d_N < 120$  nm), and found that the Cu layer did attenuate  $I_C$  for  $d_N < \xi_{ND}$ . This confirmed that the Cu was proximitised.

Using the observations made by Hadfield to the junctions studied here at 4.2 K, the additional amount of Nb in the junction trench does not affect the interpretation of the junctions. The remaining Nb in the junction trench is non-superconducting. This is because of its thinness, the presence of Ga impurities and defects caused by the ions during fabrication, and the proximity of Cu.

## 5.7. Summary

Most of the electrical properties of a Nb/Cu/Nb junction have been successfully characterised in terms of the geometry of the junction as defined by the FIB instrument and the thin-film deposition process. In a junction, the effective length of the normal region is greater than its geometrical length. It is shown, however, that the effective length of the normal region can be better described using a transmission line approach for the transport of current through the junction. The response of a junction to an externally applied magnetic

field has been successfully modeled using Rosenthal's model of thin-film Josephson junctions. The temperature dependence of the  $I_C$  has been adequately described using the model devised by Van Dover. It is found that at low temperatures hysteresis at zero- and finite- bias develops in the  $I$ - $V$  characteristics of a junction. The hysteresis at finite bias can be explained using a hot-spot model. The hysteresis at zero-bias can not be satisfactorily explained in terms of the non-equilibrium, time dependent state of the junction, or alternatively, self-heating but it is investigated later in chapter 7.3.

## 5.8. References

- N.W. Ashcroft and N.D. Mermin (1976). "Solid state physics." New York, Saunders College Publishing.
- A. Baratoff and L. Kramer (1977). "Superconducting quantum interference devices and their applications." New York, Walter de Gruyter 51.
- H. H. Berger (1972). *Solid-State Electronics* **15** 145.
- G. E. Blonder, M. Tinkham and T. M. Klapwijk (1982). *Phys. Rev. B* **25** 4515.
- J. Clarke (1969). "Supercurrents in lead-copper sandwiches." *Proc. Roy. Soc.* **308** 447.
- M. Colclough (1998). "Efficient calculation of the current-voltage characteristic of a resistively shunted Josephson junction." in the proceedings of the informal meeting of the UK SQUID community, IRC in superconductivity, University of Cambridge.
- K. A. Delin and A. W. Kleinsasser (1996). *Superconductor Science and Technology* **9** 227.
- H. J. Fink (1976). *Phys. Rev. B* **14** 1028.
- K. Flensberg and J. B. Hansen (1989). *Phys. Rev. B* **40** 8693.
- R. Hadfield, G. Burnell, W. E. Booij and M. G. Blamire (2000). "Personal Communication." University of Cambridge.
- Z. G. Ivanov, M. Y. Kupriyanov, K. K. Likharev, S. V. Meriakri and O. V. Snigirev (1981). *Sov. J. Low Temp. Phys.* **7** 274.
- C. Kittel (1976). "Introduction to solid-state physics." (New York, John Wiley & Sons).
- T. M. Klapwijk, G. E. Blonder and M. Tinkham (1982). *Physica B and C* **109&110B** 1657.
- M. Y. Kupriyanov, K. K. Likharev and V. F. Lukichev (1983). "Influence of effective electron interaction on the critical current of Josephson weak links." *Sov. Phys. JETP.* **1** 235.

- M. Y. Kupriyanov and F. Lukichev (1981). *Sov. J. Low. Temp. Phys.* **7** 137.
- A. Latif, W. E. Booij, J. Durrell and M. G. Blamire (2000). "In-situ resistometric measurements using FIB." *J. Vac. Tech. B*(To be published).
- K. K. Likharev (1976). "The relation of critical current for SNS bridges of variable thickness." *Sov. Tech. Lett.* **2** 12.
- K. K. Likharev (1979). *Rev. Mod. Phys.* **51** 101.
- F. London and H. London (1935). "The Electromagnetic Equation of the Superconductor." *Proceedings of the Royal Society (London)* **A149** 71.
- D. E. McCumber (1968). "Effect of ac impedance on dc Voltage-Current characteristics of superconductor weak-link junctions." *J. Appl. Phys.* **39** 3113.
- O. Meyer, H. Mann and E. Phrlingos (1974). "Applications of Ion Beams to Metals." (New York, Plenum).
- R. W. Moseley (1997). CPGS "Superconducting tunnel junctions." Materials science, Cambridge.
- B. Mühlischlegel (1959). *Zeitschrift Physik* **155** 313.
- M. Octavio, M. Tinkham, G. E. Blonder and T. M. Klapwijk (1983). *Phys. Rev. B* **27** 6739.
- B. A. Paterno (1982). *Physics and applications of the Josephson effect* (New York, Wiley) Chapter 5.
- A. B. Pippard, J. G. Shepherd and D. A. Tindall (1971). "Resistance of Superconducting-normal interfaces." *Proceedings of Royal Society, London* **A 324** 17.
- P. A. Rosenthal, M. R. Beasley, K. Char, M. S. Colclough and G. Zaharchuk (1991). "Flux focusing effects in planar thin-film grain-boundary Josephson-junctions." *Appl. Phys. Lett.* **59** 3482.
- C. Schneider (1994). PhD Thesis "Inductive characterisation of thin superconducting films and bilayers." Department of Materials Science and Metallurgy, University of Cambridge.
- L. Singh and G. B. Burnell (1999). "*Personal communication.*"
- W. J. Skocpol, M. R. Beasley and M. Tinkham (1974). "Self-heating hotspots in superconducting thin-film microbridges." *J. Appl. Phys.* **45** 4054.
- Y. Song (1976). "Origin of "capacitance" in superconducting microbridges." *J. Appl. Phys.* **47** 2651.

W. C. Stewart (1968). "Current-Voltage characteristics of Josephson junctions." *Appl. Phys. Lett.* **12** 277.

A. V. Svidzinsky, T. N. Antsygina and E. N. Bratus (1973). *J. Low Temp. Phys.* **10** 131.

E. J. Tarte (1992). PhD Thesis "The Electrical Properties of Interfaces Between Nobel Metals and  $\text{YBa}_2\text{Cu}_3\text{O}_{7-\delta}$ ." Dept. Physics. Cambridge, UK, University of Cambridge.

M. Tinkham (1996). "Introduction to Superconductivity." (Singapore, McGraw-Hill Book Co.)

R. B. Vandover, A. Delozanne and M. R. Beasley (1981). "Superconductor-Normal-Superconductor Microbridges - Fabrication, Electrical Behavior, and Modeling." *Journal Of Applied Physics* **52**(12) 7327.

J. R. Waldram and S. J. Battersby (1992). *J. Low Temp. Phys.* **86** 1.

P.A. Warburton (1993). PhD Thesis "Quasiparticle trapping in superconducting heterostructures." Dept. Materials science and metallurgy. Cambridge, UK, University of Cambridge.

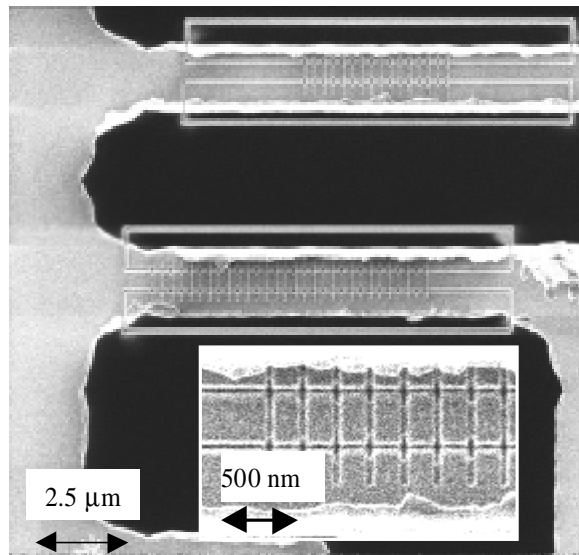
J. Warlaumont, J. C. Brown and R. A. Buhrman (1979a). "Response times and low voltage behavior of SNS microbridges." *Appl. Phys. Lett.* **34** 415.

J. M. Warlaumont, J. C. Brown, T. Foxe and R. A. Buhrman (1979b). "Microwave-enhanced proximity effect in superconductor-normal-metal-superconductor microjunctions." *Phys. Rev. Lett.* **43** 169.

F. C. Wellstood, C. Urbina and J. Clarke (1994). "Hot-Electron Effects In Metals." *Physical Review B-Condensed Matter* **49**(9) 5942.

H. C. Yang and D. K. Finnemore (1984). "Pair-breaking mechanisms in superconductor normal-metal superconductor junctions." *Phys. Rev. B* **20** 1260.

# Chapter 6



FIB image of two arrays made using an FIB instrument.

## Characterisation of Nb/Cu/Nb junction series arrays

## 6.1. Introduction

This chapter shows that Nb/Cu/Nb junctions, made using an FIB instrument, can be placed closely together to make high-density arrays. It is an extension to the study of single Nb/Cu/Nb junctions, reported in chapter 5. The study provides evidence of the important role of quasiparticles and the order parameter in determining the electrical properties of the junctions.

There has long been interest for using Josephson junctions arrays in microwave and voltage standard applications (Benz 1996; Barbara 1999; Darula 1999). Currently, the frequency range of mm and sub-mm wavelengths has attracted interest because of some specific applications, e.g. in environmental monitoring and military communications. The basic techniques of these applications are well known, however, there is a lack of compact radiation sources, especially in the sub-mm range. According to the Josephson equations, the Josephson junction is an ideal voltage-to-frequency transducer (chapter 2.3.1). Typical frequencies are in the mm and sub-mm wavelength range, and therefore, a radiation source based on the Josephson junctions is a good candidate for the next generation of low power consumption THz generators.

The work presented here has not been performed before, although most of their electrical properties can be explained, if not quantitatively, at least qualitatively from previous studies of planar weak links structures performed in the 1970s. All the arrays used in this section were made using Nb(75 nm)/Cu(70 nm) bilayer films.

## 6.2. Background to SNS junction series arrays

A Josephson junction can act as a microwave source due to the ac Josephson effect. If a Josephson junction is biased above its  $I_C$ , a high frequency oscillation with frequency  $f$  is generated that is strictly related to the average voltage across the junction (equation 2.32). Jain (Jain 1984) showed that the maximum power  $P_M$  that can be delivered by a single junction to a matched load is

$$P_M = \frac{1}{8} I_C^2 R_N. \quad (6.1)$$

A typical Josephson junction with the parameters given in chapter 5, should deliver a power of only  $\sim 1$  nW. Although this power is low, the line-width,  $\Delta f$ , of the generated radiation is very low, and therefore, is very attractive for the applications mentioned above. Since the frequency of a Josephson junction is controlled by the junction's voltage, any

voltage fluctuation will cause broadening of  $\Delta f$ . Considering the only fluctuations are due to thermal noise,  $\Delta f$  equates to

$$\Delta f = \frac{1}{2} \left[ \frac{2\pi}{\Phi_0} \right]^2 R_d \left( \frac{2k_b T}{\pi R_N} \right), \quad (6.2)$$

where  $R_d$  is the differential resistance at the bias point. For the Nb/Cu/Nb junctions described in chapters 4 and 5  $\Delta f \sim 30$  MHz at 4.2 K, taking  $R_d \equiv R_N$ . To overcome the low power output and the large frequency spread more junctions can be added to form an array. The available power should increase with the number of junctions, and at the same time  $\Delta f$  should decrease. The condition is that the junctions must oscillate coherently, i.e. they must be mutually phase locked. Mutual phase locking refers to not only the average frequencies of all the junctions being equal but the fluctuating frequencies,  $f_i$ , of the oscillations are also equal over a short time. This does not imply that  $d\phi/dt$  are equal at each instant. Such phase locking, often referred to as the coherent state of the array, can be maintained even in the presence of perturbations e.g. thermal noise, and random variation in the junction parameters. The main mechanism for interaction between junctions is high-frequency electromagnetic coupling (Likharev 1981). Before discussing the various mechanisms for Josephson junction interaction, it is necessary to examine two independent (non-interacting) junctions that are placed closely together to form a series array.

### 6.2.1. External phase locking

Figure 6.1 shows the series connection of the 2 Josephson junctions and the equivalent circuit of this. The phase difference  $\phi_1$  and  $\phi_2$  across the two junctions are given by

$$\phi_1 = \chi_B - \chi_A \quad (6.3)$$

$$\phi_2 = \chi_C - \chi_B \quad (6.4)$$

and  $\chi_A$ ,  $\chi_B$ , and  $\chi_C$  are the phases of the order parameter of the 3 electrodes. The time evolution of the phase difference ( $\phi$ ) across a junction is determined by the current through that junction. If the current source has impedance, which is large compared to the junction impedance (normally the case) then the junction currents are determined by the current fixed by the current source and not the high-frequency currents due to the junctions themselves. This highlights the point that the system has no restoring force coupling  $\phi_1$  and  $\phi_2$  against the inevitable perturbations. If such an array is irradiated by an external ac (microwave) source,

$f_i$  can be simultaneously synchronised by the external source, and thus, be made equal to each other. This is referred to as *external* phase locking.

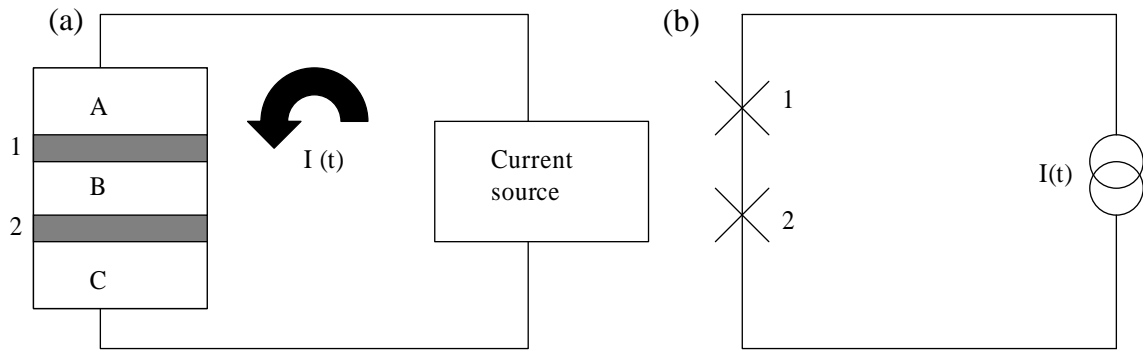


**Figure 6.1:** (a) Series connection of 2 Josephson junctions and (b) the equivalent circuit. Diagrams taken from Jain (Jain 1984)

### 6.2.2. Mutual phase locking

There are many possible mechanisms, however, that can lead to *mutual* phase coherence. The dominant coupling mechanism and its strength will depend upon the electrical properties of the junction and its environment. Various mechanisms that can lead to mutual phase locking are considered below.

#### 6.2.2.1. Order parameter coupling

In the middle electrode, shown in figure 6.1, the order parameter ( $\psi$ ) can be suppressed by the two junctions. A qualitative picture of this time and space dependence of  $\psi$  is shown in figure 6.2. The amplitude of the suppression is dependent on  $\phi(t)$ , resulting in  $\Delta$  oscillating with the Josephson frequency. These oscillations penetrate into the electrodes to a depth of approximately  $\xi_{ND}$ , for a superconductor in the dirty limit. If another Josephson junction is located within this distance, an interaction between the two junctions results, which can cause mutual phase locking. Some evidence for this mechanism has been found in experiments with closely spaced weak-links (Smith 1990), although its strength is usually much smaller than that of the quasiparticle coupling mechanism which is discussed below.

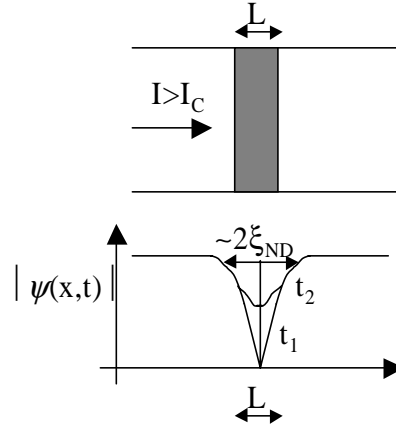


**Figure 6.2:** (a) Schematic diagram showing order parameter coupling and (b) variation of the order parameter ( $\psi$ ) with time in the junction and electrodes. Diagrams taken from Jain (Jain 1984).

### 6.2.2.2. Quasiparticle coupling

The order parameter is not the only parameter to vary with the Josephson frequency. The quasiparticle current in the electrodes will also oscillate with the same frequency. Since the ac Josephson effect is essentially the oscillation of the junction supercurrent at the Josephson frequency, a fixed bias current (constant in time) implies that part of the junction current must be carried by quasiparticles counter-oscillating with the same frequency, shown in figure 6.3. These quasiparticles diffuse into the electrodes, decaying due to branch relaxation in a time  $\tau_Q$ , which is of the order of  $10^{-10}$  s for most practical superconductors (chapter 2.6.3). The corresponding decay length of the quasiparticles is the quasiparticle diffusion length ( $\lambda_Q$ ). If two Josephson junctions are located within a distance of the order of  $\lambda_Q$  they will interact. Quasiparticles generated by one of the junctions will penetrate through the other junction, inducing a quasiparticle current  $I_Q$ . Conservation of charge, however, means that a supercurrent of the same amplitude must flow in the opposite direction. Since the supercurrent is directly related to the Josephson phase difference across the junction, the quasiparticles generated by one junction induce a variation of  $\phi$  across the second junction, acting as a coupling force, and vice versa.

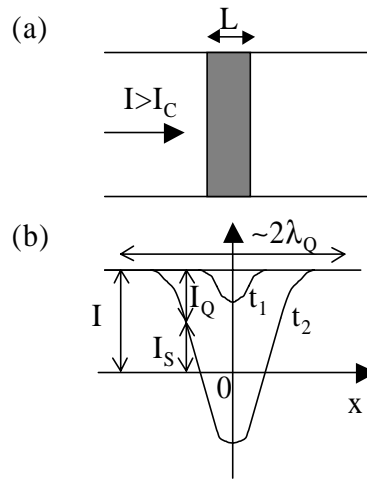


**Figure 6.3:** (a) Schematic diagram showing quasiparticle coupling: current ( $I$ ) through the junction redistributes periodically between superconducting ( $I_S$ ) and quasiparticle ( $I_Q$ ) components, which results in the periodic injection of quasiparticles into the electrodes. Diagrams taken from Jain (Jain, 1984).

### 6.2.2.3. High-frequency electromagnetic coupling

High-frequency electromagnetic coupling is the direct result of the changing phase difference across one junction that changes the current through another junction, and vice-versa. The processes in these junctions, therefore, will be interdependent. This mechanism is a direct effect of the Josephson effect, rather than a secondary effect, and is, therefore, much stronger. To consider the high-frequency (of the order of the Josephson frequency) interaction, consider the circuit shown in figure 6.4. This is very similar to that of figure 6.1, but has a linear shunt with finite impedance  $Z_e(\omega)$  connecting the junctions. The shunt impedance should be of the order of the junction impedance,  $Z$ , at the frequency of the Josephson oscillations of the junction, i.e.

$$|Z_e(\omega)| \approx R_N. \quad (6.5)$$

In this case, oscillations of the voltage across the junction will produce an appreciable ac current,  $I_e$ , containing components with frequencies  $f_1$  and  $f_2$ . This current, flowing through both junctions, tends to lock the oscillation phases, thus acting as a coupling force. At these high frequencies the dimensions of the coupling circuit can be comparable to the Josephson radiation wavelength ( $\sim$ mm). Here, ac coupling can be qualitatively described in the following terms: Josephson oscillations of a junction are partly radiated to the surrounding space and part of this radiation induces oscillations in another junction. The electromagnetic

coupling can only be altered by changing the environment, and not the Josephson junctions themselves.

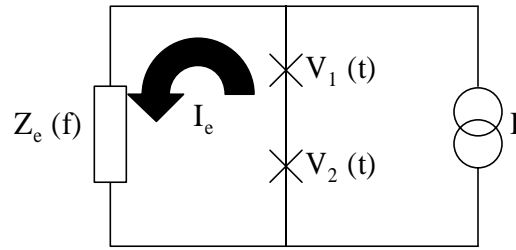


**Figure 6.4: Electrical diagram to show high-frequency electromagnetic coupling. Josephson voltage oscillations across each of the junctions induce a current  $I_e$  of the same frequency flowing through the coupling circuit  $Z_e$  and both junctions. This current can then lock the phases of the 2 junctions. Diagram taken from Jain (Jain, 1984).**

#### 6.2.2.4. Low-frequency electromagnetic coupling

Low-frequency electromagnetic coupling occurs as a result of low-frequency currents. An example of a situation where this occurs is shown in figure 6.5 where 2 junctions are connected together by a closed superconducting path. This circuit is equivalent to that of the well-known dc Superconducting QUantum Interference Device (SQUID). Since no dc voltage drop can exist across the superconductors, the dc voltages across the junctions are equal:  $\text{average}(V_1) \equiv \text{average}(V_2)$ , and consequently the average Josephson oscillation frequencies are also equal. This is because a loop current,  $\text{average}(I_e)$ , is automatically established to compensate for any difference of external bias currents or junction parameters. The presence of additional high-frequency interactions, however, destroys the phase coherence in this circuit.

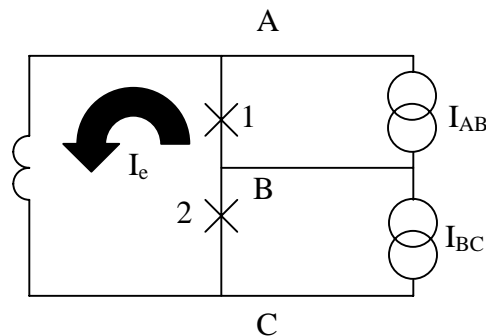


**Figure 6.5: Electrical diagram to show low-frequency electromagnetic coupling. The current  $I_e$  through the superconducting loop automatically establishes equal average voltages ( $V_1$ ) and ( $V_2$ ) across the junctions. Diagram taken from Jain (Jain 1984).**

### 6.2.3. Coupling versus disorder

Wisensfeld *et al.* showed that the key feature of the dynamics of arrays is the competition between the intrinsic disorder of the junctions and the coupling between the junctions mediated by the load (Wisensfeld 1996). They showed that a model, devised by Kuramoto (Kuramoto 1975), could be applied to understand how much disorder a coupled junction system can tolerate. If the disorder is too much for a weakly coupled system the junctions will act independently of one another.

## 6.3. Preliminary studies of junction series arrays

A preliminary study of series arrays was made. All the arrays studied here, unless otherwise stated, used the same type of junction and fabrication method as discussed in chapters 4 and 5. The dimensions of the Nb(70 nm)/Cu(75 nm)/Nb(70 nm) junctions were kept uniform with  $W=0.5\ \mu\text{m}$ ,  $L=50\ \text{nm}$ . The depth of each trench corresponded to  $\sim 90\%$  of the thickness of the Nb layer, as determined by the end point detection method (this corresponds to a mill time of 3.5 s in figure 4.3). The true depth of the trench may not be this deep (discussed in chapter 5.6), but since this does not affect the Josephson properties of the junction this is not important here.

### 6.3.1. Double junction series arrays

The first experiment was to compare the  $I$ - $V$  characteristics of a number of double junction series arrays. Figure 6.6 shows the  $I$ - $V$  characteristics at 4.2 K of two different arrays. They both show an  $I_C$  at zero-bias, but only in figure 6.6b is a symmetrical voltage rise seen ( $V=\pm 15\ \mu\text{V}$ ). This was often observed in the early array attempts and thought to be the result of the spread of  $I_C$  in the junctions forming the array.

Possible causes for the mismatches of the  $I_C$  in an array are: poor reproducibility in the junction parameters; trapped flux; differences in the circulating currents in the electrodes. Voltage steps were routinely seen in arrays that were poorly manufactured, e.g. caused by beam drift in the FIB instrument whilst milling. For arrays where there were no obvious fabrication problems, only a rounding in the  $I_C$  around zero-bias was observed.

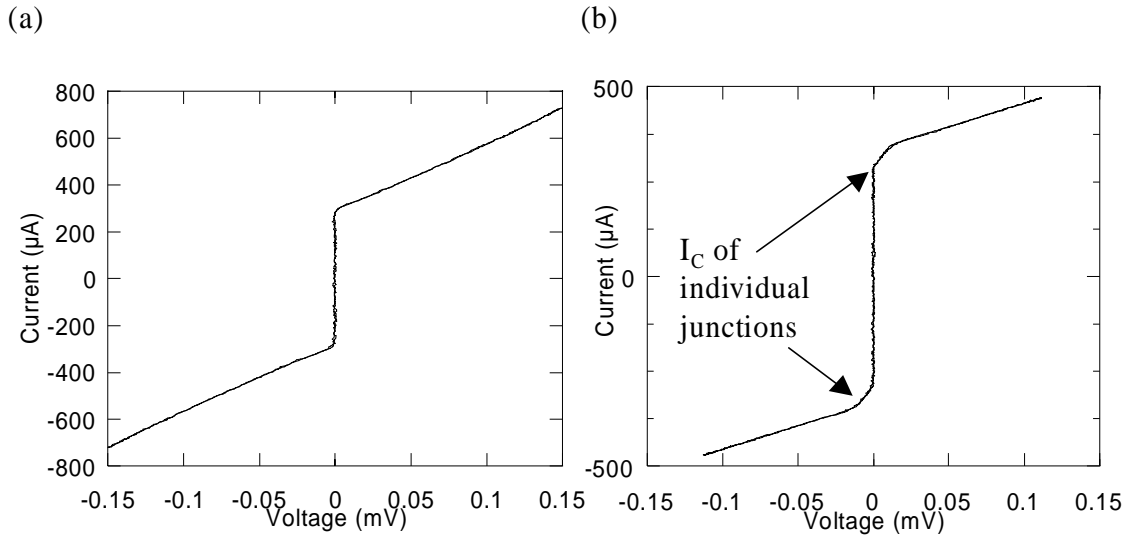


**Figure 6.6: I-V characteristics at 4.2 K of (a) uniform junction series array and (b) non-uniform junction series array.**

### 6.3.1.1. $I_C$ and $R_{ARRAY}$ with $L_{SPACE}$

A study of the effect of varying the spacing of two junctions ( $L_{SPACE}$ ) in series was made. These were made on a single sample where  $L_{SPACE}$  was varied between 0.2 and 8  $\mu\text{m}$  and, for comparison, a single junction was made on the same sample. For each double junction array, the  $I_C$ , the normal state resistance ( $R_{ARRAY}$ ), and the  $I_C R_{ARRAY}$  product were recorded from their  $I-V$  characteristics, and are shown in table 6.1. The  $I_C$  was measured using a voltage criterion of  $V=0\pm 5 \mu\text{V}$ .

$L_{SPACE}$ ( $\mu\text{M}$ )	$I_C$ ( $\mu\text{A}$ )	$R_{ARRAY}$ ( $\Omega$ )	$I_C R_{ARRAY}$ PRODUCT ( $\mu\text{V}$ )
0.2	320	0.25	80
0.5	300	0.23	69
1	270	0.27	73
8	390	0.25	98
Single junction	350	0.12	42

**Table 6.1: Variation of the junction spacing ( $L_{SPACE}$ ) with the electrical properties of double junction arrays at 4.2 K.**

The average  $I_C R_{ARRAY}$  product of the double junctions was calculated to be  $80 \mu\text{V}$  from table 6.1. This was to within 10 % of twice the product of the single junction's  $I_C R_N$  product,  $84 \mu\text{V}$ . The electrical properties of one junction are, therefore, not perturbed by the other junction in this range of spacing.

### 6.3.1.2. Microwave response

Casting microwaves (13.3 GHz) onto the sample produced Shapiro steps in the  $I$ - $V$  characteristics of the arrays at double the normal voltage, known as 'double Shapiro steps' (chapter 2.3.4). These steps occurred at a voltage spacing of  $2V_S$ , where  $V_S$  is the interval between single Shapiro steps, i.e.

$$V_S = \frac{\hbar\omega}{2e}. \quad (6.6)$$

Double Shapiro steps were expected here because they should occur when the two junctions are either electrically- coupled, or identical, because they will change from the zero- to finite-voltage states at the same bias current.

### 6.3.2. Small series arrays

Another sample, containing arrays of 2, 3, and 4 junctions with a spacing of  $1 \mu\text{m}$  was made. The  $I_C$ ,  $R_{ARRAY}$ , and  $I_C R_{ARRAY}$  products, as before, did not deviate from the expected values, calculated from a single junction's  $I_C$ ,  $R_N$  and  $I_C R_N$  product. The responses of the arrays to microwaves were also recorded and are shown in figure 6.7. As expected, the  $I$ - $V$  characteristics of a single junction had only single steps, and the double junction had double steps. It was found, however, that for 3 junctions in series there was a sequence of steps consisting of a single step followed by a double step. For 4 junctions in series, double Shapiro steps were observed. For 3 and 4 junctions in an array, the responses are characteristic of 2 junctions in the array either not being phase locked, or not being electrically identical, to the other junctions.

An explanation for this observation is that it was due to the geometrical consequence of the 2 junctions at the ends of the array being in a different environment to the rest of the junctions inside the array. Another possible explanation for these observations is that the electrical properties of the junctions are inherently non-uniform. Ions from the focused ion beam instrument during the manufacture of an array could cause this; ions resputter from the junction trench being milled into other trenches that have already been made. The last explanation is not supported by observation, however, because it means that the  $I_C$  of each

subsequent junction made would be higher than the one made previous to it; only single Shapiro steps would be seen in the response of the array to microwaves.

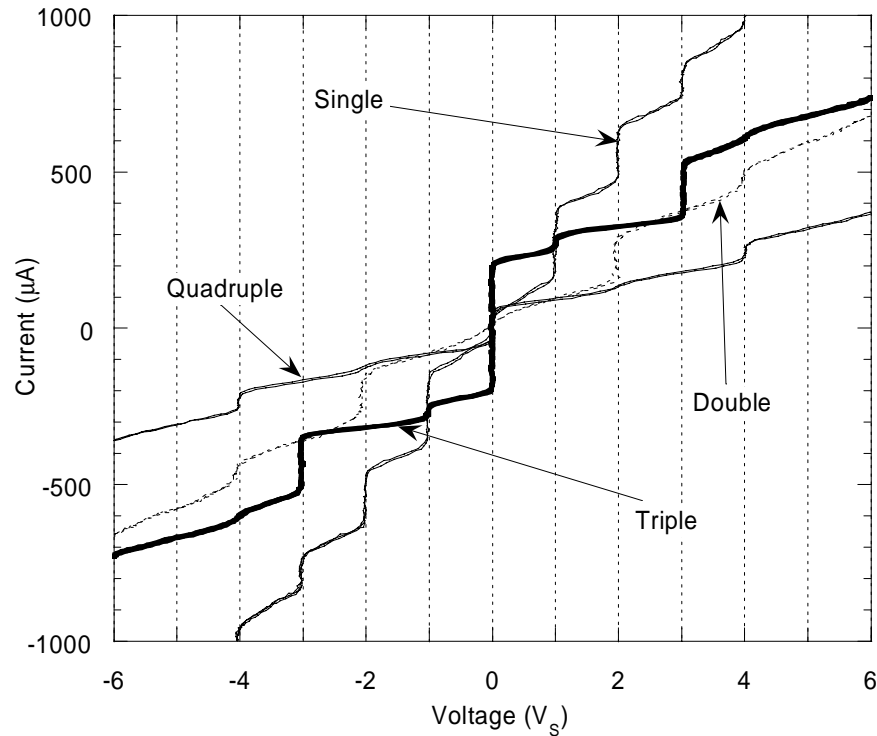


**Figure 6.7:** Shapiro step ( $V_S$ ) I-V characteristic responses of 1,2,3,4 junctions in series arrays to microwaves (13.3 GHz and  $V_S=27 \mu\text{V}$ ) at 4.2 K. The response of each array is dependent on the number of junctions forming the array.

### 6.3.2.1. Magnetic field response

In most cases, the electrical response of an array to a magnetic field was recorded. For each array, a plot was made of  $I_C$  as a function of the applied magnetic field ( $I_C(B)$ ).

Booij (Booij 1997) showed that for the situation described here the  $I_C(B)$  should be similar to the one obtained from a single junction. However, the lobes will widen as a function of  $L_{SPACE}$ . This is because of the junction with the lower  $I_C$  causes current redistribution around the junction with the higher  $I_C$  as it changes from its zero- to finite-voltage states.

The  $I_C(B)$  of all the arrays studied here were qualitatively similar to the ones obtained from a single junction. No trend was observed in the variation of the positions of the first

minima, contrary to expectation. This is probably due to the voltage criterion used, and the low impedance of each junction.

A two junction array with a spacing of 5  $\mu\text{m}$ , made on a similar sample showed, however, an interesting  $I_C(B)$  not seen in the other results. It is displayed in figure 6.8, along with the  $I_C(B)$  of a single junction, also from the same sample. The double junction  $I_C(B)$ , although similar to the single junction's, displays two small lobes on either side of the central lobe that superimpose over the single junction's minima. This would be expected if the two junctions were magnetically coupled (Pauza 1993).

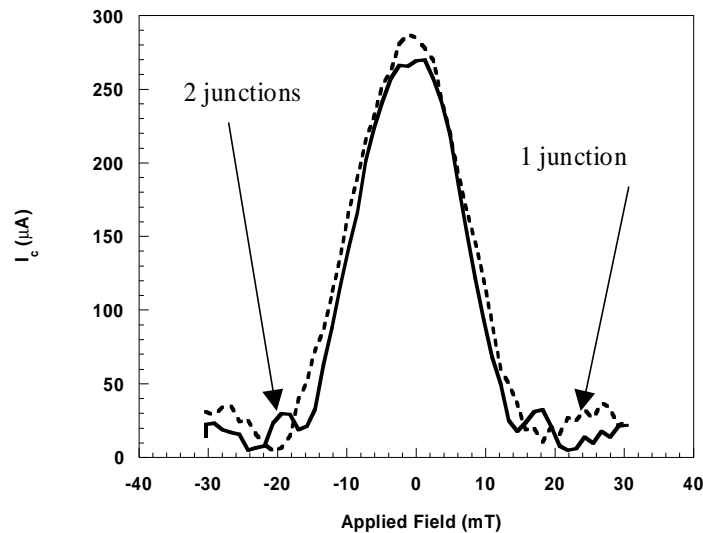
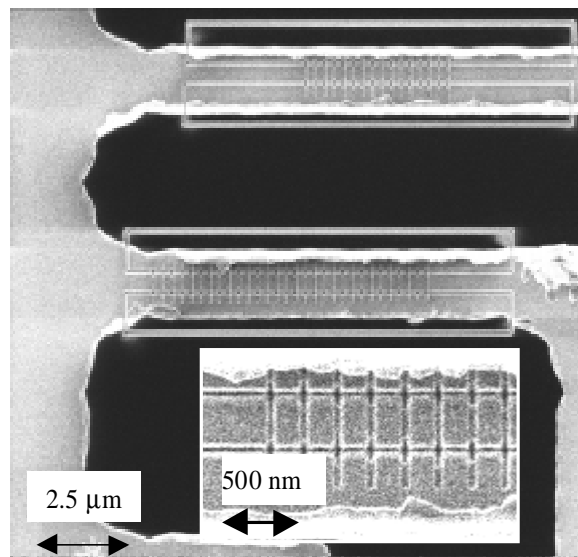


Figure 6.8: Comparison of the  $I_C(B)$  responses of a 2 junction series array with a single junction at 4.2 K.

### 6.3.3. Large series arrays

Two large series arrays containing 16 and 30 junctions with a junction spacing of 0.2  $\mu\text{m}$  were made and an FIB scanned image of the two arrays was taken, shown in figure 6.9. The low voltage  $I-V$  characteristics of both arrays are shown in figure 6.10. A model, constructed by Bennett, a project student under the author's supervision, was used to model the  $I-V$  characteristics of both arrays. A brief description of the model is given here but a full description can be found elsewhere (Bennett 1999). A 7th order polynomial function was fitted to the  $I-V$  characteristics of a single junction. The general form of this function was

assumed to be the same for all junctions in the array. The  $I_C$  of each junction, however, was expected to vary between junctions with a gaussian form. Using these assumptions a model was made and fitted to the medium bias  $I$ - $V$  characteristics of the 16 junction array and to the, only available, low bias  $I$ - $V$  characteristics of the 30 junction array. The model uses 3 parameters, the mean  $I_C$  of the junctions,  $I_{C0}$ , the gaussian spread around  $I_{C0}$ ,  $\sigma$ , and  $R_{ARRAY}$ . Table 6.2 shows the parameters used in order to get the best fit. The  $I_C$  of the junctions in both arrays has a spread of 20 %.  $R_{ARRAY}$  of the 16 junction array is slightly less than the expected value of  $\sim 1.6 \Omega$  (i.e.  $R_N \times 16$ ), although for the 30 junction array the actual value is greater than the expected value of  $\sim 3 \Omega$ . It was thought, as will become apparent, that  $R_{ARRAY}$  would be less than the sum of the normal state resistance of each junction. The lack of any trend between  $R_{ARRAY}$  and  $R_N$  is probably due to the difference in the bias ranges used for modeling the two arrays. A more rigorous study was made and is reported in the next section.



**Figure 6.9:** FIB image of 16 and 30 series junction arrays with a junction spacing of 200 nm. Inset shows an enlargement of one of the arrays.

NUMBER OF JUNCTIONS IN ARRAY	$I_{C0}$ ( $\mu\text{A}$ )	$\sigma$ ( $\mu\text{A}$ )	$R_{ARRAY}$ ( $\Omega$ )
16	225	43	1.3
30	310	65	4

**Table 6.2:** The electrical ( $R_{ARRAY}$ ) and statistical parameters ( $I_{C0}$  and  $\sigma$ ) of a 16 and 30 junction series array.

The microwave response of the 16 junction array was recorded and showed only faint current steps at voltages of approximately  $\pm 340 \mu\text{V}$ . This corresponded to Shapiro steps of

12  $V_S$ . No current steps were seen at lower voltage steps but this may have been due to the poor voltage resolution at the high voltage gains used. While this did not agree with the expected steps at 14 $V_S$ , it did not disprove the explanation given previously; it is conceivable that the two outer junctions on either end of the array were in a different electromagnetic environment to the other junctions inside the array, given the very close spacing. Unfortunately, during the experiment a large static discharge destroyed the array containing 30 junctions, hence no response to microwaves was recorded. This does demonstrate, however, the sensitivity of these types of devices to static.

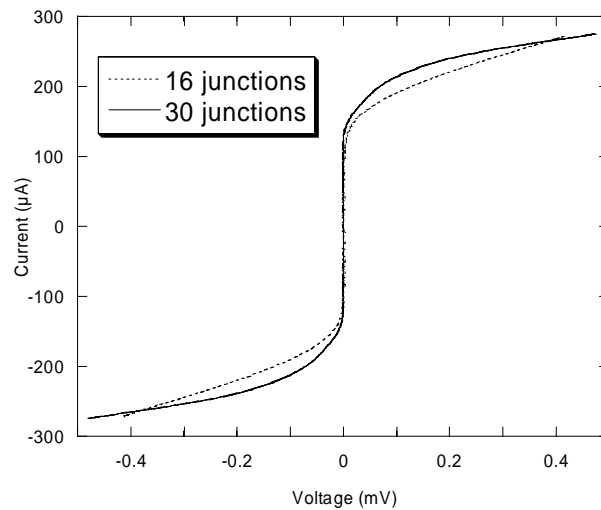


**Figure 6.10: Comparison of the low bias I-V characteristics of a 16 junctions series array with a 30 junctions series array at 4.2K.**

## 6.4. Systematic study of double junction series arrays

A survey of double junction series arrays with a systematic variation in the spacing of the junctions ( $L_{SPACE}$ ) of 0.01 to 1  $\mu\text{m}$  was made using the same junction parameters used in section 6.3. For each array, the  $I_C$ ,  $R_{ARRAY}$ , and  $I_C R_{ARRAY}$  product, and responses to microwaves and an applied magnetic field were recorded and are discussed separately. Before discussing the results, however, a semi-empirical model is made to explain  $I_C$  and  $R_{ARRAY}$  of a double junction array. This will form the basis for understanding the observations made in this section and the subsequent sections of this chapter.

### 6.4.1. Semi-empirical model of $I_C$ and $R_{ARRAY}$

The preliminary study, discussed in the previous section, showed that the electrical properties of double junction arrays were independent of the junction spacing in the range studied. Evidence in chapter 5 shows that the path of the current in the normal region of the junction extends approximately 100 nm along both sides of the bilayer track. This was attributed to the effects of quasiparticle diffusion increasing the normal region of the junction, i.e.  $\lambda_Q=100$  nm. It is expected, therefore, that the electrical properties of an array will change as the junction spacing decreases below 200 nm (i.e.  $L_{SPACE} < 200$  nm). As the paths of the quasiparticles from each junction overlap, the quasiparticle density distribution will increase in the region of overlap and, possibly, alter the current paths in the two junctions. This is shown schematically in figure 6.11a.

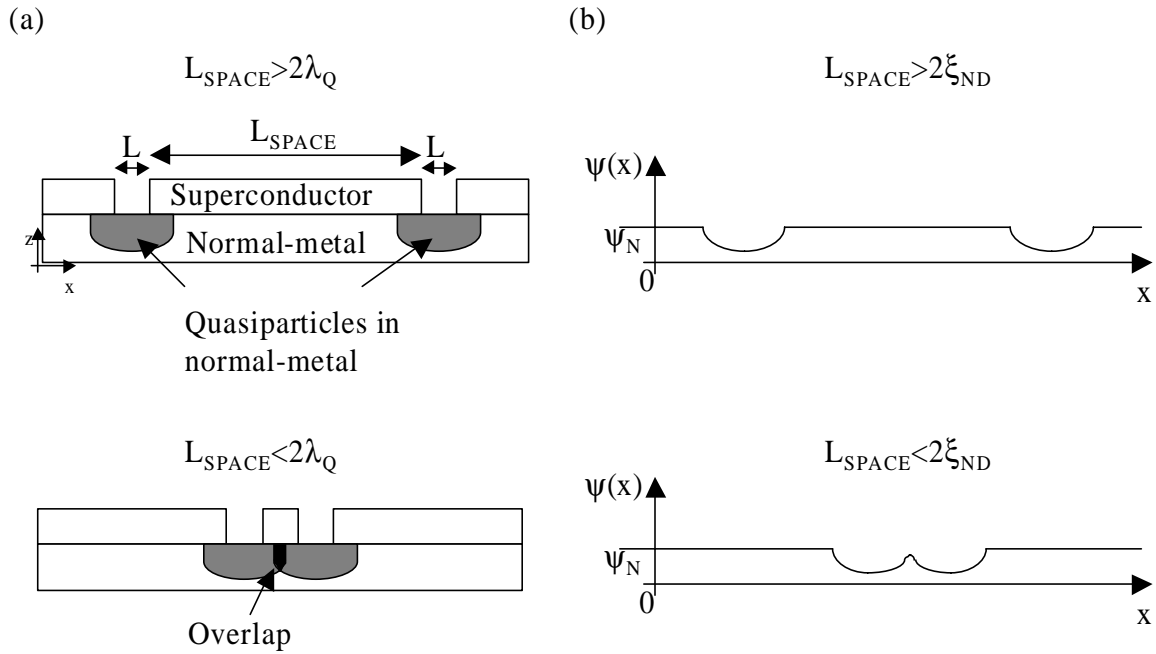


**Figure 6.11: Schematic diagrams showing the quasiparticle (a) and order parameter (b) interactions between two junctions. (a) The quasiparticles from both junctions merge where the junction spacing ( $L_{SPACE}$ ) is less than twice the quasiparticle diffusion length ( $2\lambda_Q$ ). (b) The order parameter in the central Nb/Cu island region is perturbed where  $L_{SPACE}$  is less than two coherence lengths ( $2\xi_{ND}$ ).**

A change in the current path will alter the normal state resistance of the array. There are various ways of modeling  $R_{ARRAY}(L_{SPACE})$  based on the geometry of the array. The author has explored these models, but in order to save resources only the most successful model is discussed here.

Consider a circuit representation of the array, shown in figure 6.12. For both cases  $R_{ARRAY}$  is given by

$$R_{ARRAY} = 2R_{C1} + 2R_G + \left( \frac{1}{R_P} + \frac{1}{2R_{C2}} \right)^{-1} \quad (6.7)$$

where  $R_G$  is the geometrical resistance of the Cu region in each junction, i.e.  $R_G = \rho_N L / W d_N$ , and  $R_P$  is the resistance of the Cu below the Nb island. Assuming the resistivity of this region is unchanged  $R_P = \rho_N L_{SPACE} / W d_N$ .  $R_{C1}$  and  $R_{C2}$  represents the interfacial resistance at each of the outer Nb/Cu electrodes and the Nb/Cu island region, respectively. When  $L_{SPACE}$  is large it is expected that  $R_{C1} \cong R_{C2}$ . As  $L_{SPACE}$  decreases and the quasiparticles from both junctions merge, quasiparticle scattering will increase. This is due to the increase in the local quasiparticle population, so more quasiparticles can pass through the Nb/Cu interface and thus  $R_{C2}$  decreases.

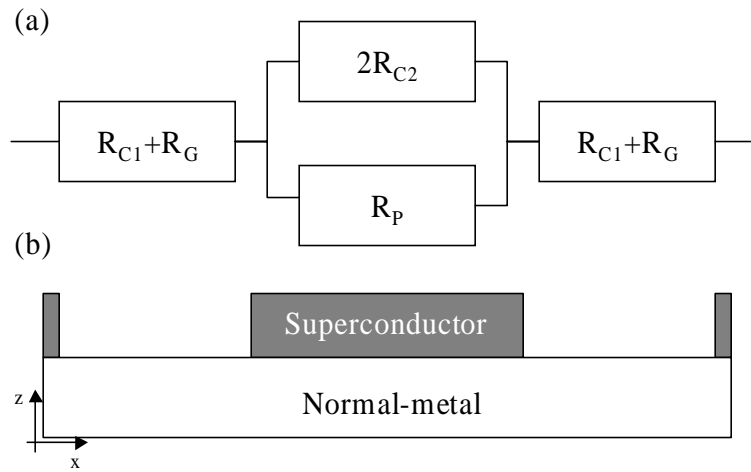


**Figure 6.12: (a) Electrical diagram of a double junction array compared with (b) the schematic of the array.  $R_C$  represents the interfacial resistance,  $R_P$  is the resistance of the Cu region below the Nb island, and  $R_G$  is the resistance of the Cu region below the trench.**

A semi-empirical model, based on the model described in chapter 5.5.1, was used to qualitatively model the induced order parameter ( $\psi$ ) in the x-direction for the two types of double junction arrays examined: large junction spacing,  $L_{SPACE} > 2\xi_{ND}$ , and; small junction spacing,  $L_{SPACE} < 2\xi_{ND}$ . Both situations are shown in schematic form in figure 6.11b.

For the large junction spacing case, the induced order parameter in both junctions is unperturbed. For the small junction spacing case, the order parameter in one junction is perturbed by the order parameter the other junction. The Nb/Cu island region, in-between the

two junctions, will have a higher order parameter than the Cu regions on either side of it. This is because of the presence of Nb in the Nb/Cu island region. The order parameter in the Nb/Cu island region will, however, be less than the order parameter in the two, outer electrodes due to its size. The  $I_C$  of each junction will depend upon the minimum value of the order parameter in the junction's order parameter well, shown in figure 6.11b. The  $I_C$  of both junctions will, therefore, decrease as a result of the decrease in the order parameter in the central Nb/Cu island region.

In the arrays studied here the junctions are assumed to be the same so that  $\psi(x)$  is symmetrical about the middle of the array. A crude way of representing the  $I_C$  of an array can be made by multiplying the critical current of a single, unperturbed junction ( $I_{C(JUNCTION)}$ ) by a prefactor  $B$ , i.e.

$$I_{C(ARRAY)} = B(L_{SPACE} / \xi_{ND}) I_{C(JUNCTION)}, \quad (6.8)$$

$B$  is a function that is related to the decrease in the minima of the order parameter as the junction spacing decreases and is, therefore, dependent upon how similar  $L_{SPACE}$  is to  $2\xi_{ND}$ . Calculating  $B$  requires complex numerical analysis, which has been attempted, but found to be beyond the capability of the author. In the absence of knowing  $B(L_{SPACE}/\xi_{ND})$  quantitatively, a qualitative analysis has been performed using boundary conditions.

For  $L_{SPACE}=0$ , the device is no longer a double junction series array, but instead is a single junction. For  $L_{SPACE} \gg 2\xi_{ND}$ , the induced order parameter in the Nb/Cu island region will be equal to the induced order parameter in the Nb/Cu track, far from the junction region, i.e.  $\psi_N(x=\infty)$  in figure 6.11b.  $B$  has, therefore, the following boundary conditions,

$$B = \frac{I_{C(JUNCTION,2L)}}{I_{C(JUNCTION)}}, \quad L_{SPACE}=0 \quad (6.9)$$

$$B = 1, \quad L_{SPACE} \gg 2\xi_{ND}. \quad (6.10)$$

$I_{C(JUNCTION,2L)}$  is the  $I_C$  of a junction whose length is twice that of the single, unperturbed, junction (for the junctions studied here  $2L=100$  nm). From chapter 5.3.2, it was calculated that at 4.2 K  $2\xi_{ND}$  is approximately 100 nm. The exact dependence of  $B$  with  $L_{SPACE}/\xi_{ND}$  is unknown so a linear one was used here for the closely spaced junction limit. For the two limits,  $B(L_{SPACE}/\xi_{ND})$  is,

$$B = kL_{SPACE} + c \quad \text{for } L_{SPACE} \leq 2\xi_{ND} \quad (6.11)$$

$$B = 1 \quad \text{for } L_{SPACE} > 2\xi_{ND} \quad (6.12)$$

where  $k$  and  $c$  are both constants that obey the boundary conditions, given in equations 6.9 and 6.10.

#### 6.4.2. $I_C$ , $R_{ARRAY}$ , and $I_C R_{ARRAY}$ product dependencies with junction spacing

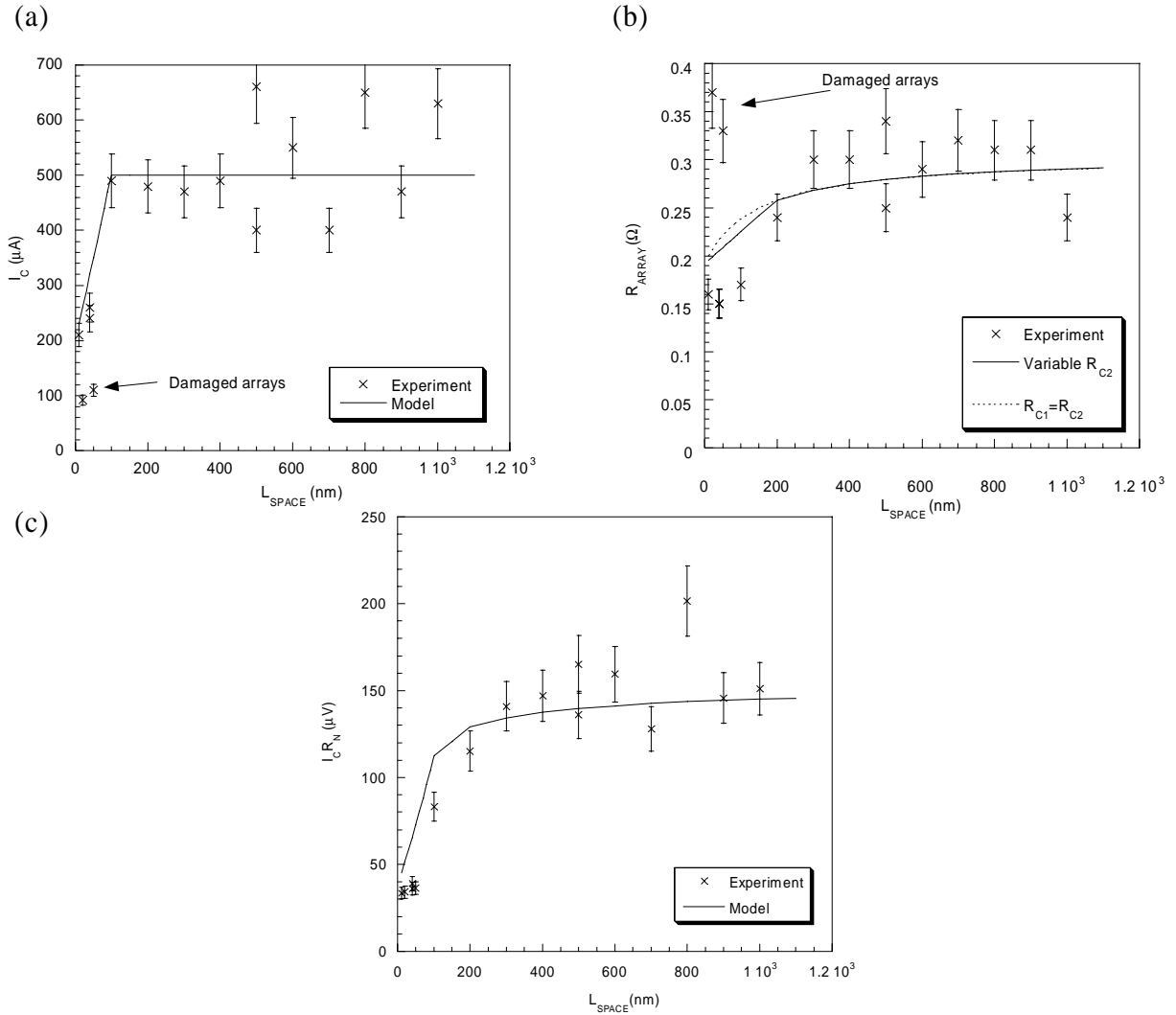


**Figure 6.13: Variation with junction spacing ( $L_{SPACE}$ ) of (a) the critical current ( $I_C$ ) (b) the normal state resistance ( $R_{ARRAY}$ ) and (c) the  $I_C R_{ARRAY}$  product of double junction arrays at 4.2 K. A semi-empirical model describing the quasiparticle and order parameter interactions are also plotted with the results. For (b), a comparison is made between a fixed and variable interfacial resistance in the Nb/Cu island region ( $R_{C2}$ ) resistance.**

Figure 6.13 shows how  $I_C$ ,  $R_{ARRAY}$ , and the  $I_C R_{ARRAY}$  product varied with  $L_{SPACE}$ . The error bars have a range of 10%, estimated from the reproducibility of a single junction (chapter 4). The plots in figure 6.13 show that the electrical properties of an array, as

expected, change at low spacing. Both the  $I_C$  and  $R_{ARRAY}$  of an array dramatically decrease at low spacing and reduce to a limiting value as  $L_{SPACE} \rightarrow 0$ . The decrease in  $I_C$  was observed at  $L_{SPACE} < 100$  nm, and the reduction in  $R_{ARRAY}$  was seen at  $L_{SPACE} < 300$  nm. Both reductions are combined in the  $I_C R_{ARRAY}$  product and result in a significant reduction at  $L_{SPACE} < 300$  nm.

Both the  $I_C$  and  $R_{ARRAY}$  plots show, however, that two arrays whose spacing was small were obviously different to the others; they both had a higher  $R_{ARRAY}$  and lower  $I_C$  than other similar arrays. This may be because they were both damaged by ions from the FIB instrument when high-resolution images were taken of these devices. This is supported by the fact that it was only these two devices that were imaged in this way.

The semi-empirical model, described in the previous section, was plotted with the results. The  $I_C$  of the double junction array was calculated from equation 6.8 using the boundary conditions in equations 6.11 and 6.12. To calculate the boundary conditions  $I_{C(JUNCTION)}$  was taken as the  $I_C$  of a single junction ( $t=3.5$  s) from figure 4.11. In the absence of results for single junctions with  $L=100$  nm,  $I_{C(JUNCTION,2L)}$  was estimated from the  $I_C$  as  $L_{SPACE} \rightarrow 0$  (200  $\mu$ A). Knowing  $I_{C(JUNCTION)}$  and  $I_{C(JUNCTION,2L)}$  values were estimated for  $k$  and  $c$  in equation 6.11 of  $k=3.0 \times 10^6$  m<sup>-1</sup> and  $c=0.4$ .

The change in  $R_{ARRAY}$  was modeled using equation 6.8, where  $R_{C1} \equiv R_{C2} = 0.056 \Omega$ ,  $\rho_N = 2.8 \times 10^{-8}$   $\Omega$ m, and  $d_N = 70$  nm. The fit is not very good but a better fit, also shown in figure 6.13, was obtained by assuming  $R_{C2}$  linearly decreased as the quasiparticles from each junction merged. Here,  $R_{C2}$  was represented by

$$R_{C2} = R_{C1} \quad , \quad L_{SPACE} > 2\lambda_Q \text{ (200 nm)}, \quad (6.13)$$

$$R_{C2} = \left( \frac{L_{SPACE}}{200 \times 10^{-9}} \right) R_{C1} \quad , \quad L_{SPACE} < 2\lambda_Q \text{ (200 nm)}. \quad (6.14)$$

The  $I_C R_{ARRAY}$  products were calculated from the modeled  $I_C$  and  $R_{ARRAY}$  results and are plotted along with the results in figure 6.13c. The differences between the  $I_C R_{ARRAY}$  products obtained by experiment and the semi-empirical model become less conspicuous. Both the trends from the semi-empirical model and the results, however, are similar, resembling the same line-shaped dependence with  $L_{SPACE}$ . The semi-empirical model, although crude in its construction, does agree surprisingly well with the observations.

The errors of the semi-empirical model are partly due to the over-simplification of the  $R_{ARRAY}$  and  $I_C$  dependencies with  $L_{SPACE}$ . A better understanding of  $B(L_{SPACE}/\xi_{ND})$  would help model  $I_C$ .  $R_{ARRAY}$  can not be explained using the simple geometrical semi-empirical model. This is because at  $L_{SPACE}=0$  the resistance is similar to a single junction whose

resistance is half that of the array. However, this does not mean that only one of the junctions was working in the arrays because the critical current is too low for an equivalent ( $L=50$  nm) junction. A possible explanation for this decrease is that the injection of quasiholes and quasielectrons on both sides of the Nb/Cu island region causes a huge athermal population distribution of quasiparticles. This would increase the quasiparticle recombination rate, described in chapter 2.6.2, and cause the quasiparticle diffusion length in the Nb/Cu island region to decrease. The shortening of the quasiparticle diffusion length means that the quasiparticles decay into Cooper pairs over a shorter distance, which causes the normal-state resistance of each junction to decrease. This is investigated in further detail in the next two sections.

#### 6.4.3. Response to microwaves

For  $L_{SPACE} \geq 200$  nm, almost all of the arrays showed double Shapiro steps in their  $I$ - $V$  characteristics when they were irradiated with microwaves. For arrays with  $L_{SPACE} < 200$  nm, their  $I$ - $V$  characteristics contained only single Shapiro steps, and for  $L_{SPACE} \leq 100$  nm only a single  $I_C$  was seen in their  $I$ - $V$  characteristics. This suggests that in the range  $100 \geq L_{SPACE} \geq 0$  nm, the device is a single, long junction whose  $I_C$  is enhanced due to the central Nb island. This will happen if the induced order parameter in the Nb/Cu island region is too small to support two independent potential wells in the  $\psi(x)$ , but large enough to increase the local coherency length of the supercurrent carrying charge carriers. To show this,  $\psi(x)$  is shown qualitatively in the two limits for  $L_{SPACE}$  in figure 6.14.

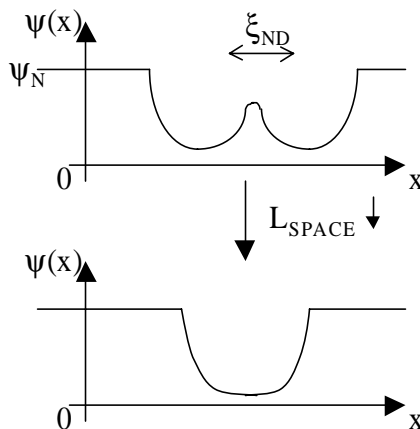


**Figure 6.14: Schematic diagrams showing how the induced order parameter ( $\psi$ ) changes as the junction spacing ( $L_{SPACE}$ ) decreases. The two potential wells merge to form a single one, producing a single junction.**

#### 6.4.4. Magnetic field junction response with junction spacing

For each array the response to an applied magnetic field was recorded. To discuss their behaviour it is necessary to refer back to chapter 5.4. Rosenthal *et al.* (Rosenthal 1991) showed that the geometry of a junction affected the circulation of current, and furthermore, its electrical behaviour in the presence of a magnetic field. The region where the current is most severely affected is known as the flux-focusing region and extends about a junction width, along the track. If the junctions are placed too close to one another, i.e.  $W > L_{SPACE}$ , the flux focusing regions will be squashed together and their areas will become smaller. This means that the response of these arrays will be similar to an array of junctions whose dimensions are smaller than the junctions in a larger spaced junction arrays. Pauza (Pauza 1993) demonstrated the effect of flux focusing in high  $T_C$  planar junction arrays, and a schematic of this situation is shown in figure 6.15. The effects of flux focusing means that the average positions of the 1<sup>st</sup> minima of each array are expected to increase as  $L_{SPACE}$  decreases below  $W$ , i.e.  $L_{SPACE} < 500$  nm. However, when the junctions exhibit single junction behaviour at  $L_{SPACE} < 100$  nm the  $I_C(B)$  behaviour should change to that expected from a long single junction. The presence of circulating currents in the Nb island will shield part of the junction so the apparent length of the junction will be smaller.

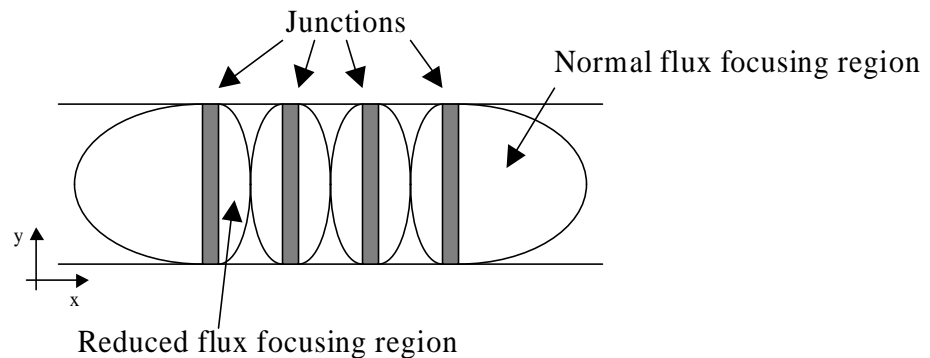


**Figure 6.15: Schematic plan view diagram of an array showing the normal flux focusing regions at the ends of the array and the reduced flux focusing regions in-between the junctions.**

From the  $I_C(B)$  plots of the arrays, the average magnitudes of the two positions of the first minima were plotted as a function of  $L_{SPACE}$ , and are shown in figure 6.16. The results from the arrays that showed dubious behaviour in their  $I-V$  characteristics, as described in the previous section, were ignored in order to simplify observation of any trends. The certainty in each position was estimated from the resolution of the  $I_C(B)$  measurement and found to be  $\pm 1$  mT. The results show that as  $L_{SPACE}$  decreases below 200 nm the positions of

the first minima are on the whole greater than the values for  $L_{SPACE} > 200$  nm. For  $L_{SPACE} > 200$  nm, the positions do not significantly vary. Both of these observations are contrary to the predicted ones. The lack of certainty in the results may be responsible for this. It is more likely, however, that they are the result of the unexplained shielding effects observed in junctions with small width. This was discussed in chapter 5.4.3.1, where the positions of the minima were also much larger than expected.

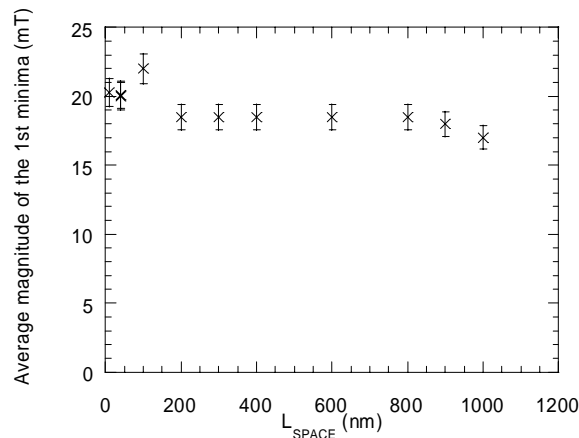


**Figure 6.16: Average magnitude of the 1<sup>st</sup> minima from an  $I_C(B)$  plot versus  $L_{SPACE}$  of 2 junction series arrays at 4.2 K (width=0.5  $\mu\text{m}$ , error bars= $\pm 1$  mT).**

## 6.5. Influence of the Nb island in a closely spaced double junction array

Extending the work described in the previous section the influence of the Nb island in a closely spaced double junction array is now investigated. To do this a comparison was made of the electrical properties of an array to a long, single junction whose Nb electrodes are the same distance apart ( $L_{TR}$ ) as the outer Nb electrodes in the array. This is shown schematically in figure 6.17. For each device, the  $I$ - $V$  characteristics and responses to microwaves and an applied magnetic field were recorded.

To increase the confidence of the results, for each configuration of the outer Nb electrodes three double junction arrays and three long, single junctions were made. The arrays are similar to the arrays used in the previous experiment, with  $L=50$  nm. Initially,  $W$  was 0.5  $\mu\text{m}$  but then it was increased to 1  $\mu\text{m}$ , to further improve the reliability of the results.

This was expected, however, to alter  $R_C$ , which was recalculated from equation 5.7 to be  $0.030 \pm 0.015 \Omega$ .

### 6.5.1. Prediction and comparison of the I-V characteristics

It was thought that as the spacing between the Nb electrodes increases the induced order parameter in the middle of a long, single junction would be less than the order parameter in a closely spaced array. This means that as  $L_{TR}$  increases the  $I_C$  of a double junction increases and the  $I_C$  of a long single junction would decrease and, therefore, the difference between the two would increase.

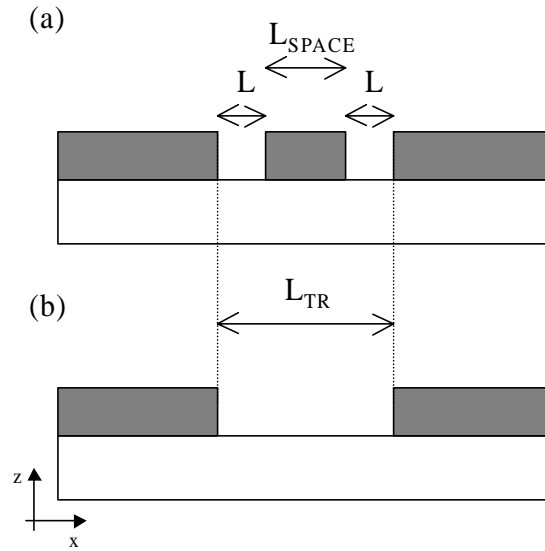


**Figure 6.17: Annotated schematic diagram of (a) double junction array and (b) long single junction.**

The semi-empirical model, discussed in section 6.4.1, predicts that there is a difference between the normal state resistance of the array,  $R_{ARRAY}$ , and the normal state resistance of the long single junction,  $R_N$ . From equation 6.7 the ratio of  $R_{ARRAY}$  to  $R_N$  is

$$\frac{R_{ARRAY}}{R_N} = \frac{2R_{C1} + 2R_G + \left( \frac{1}{R_P} + \frac{1}{2R_{C2}} \right)^{-1}}{2R_{C1} + R_L} \quad (6.15)$$

where  $R_L$  is the geometrical resistance of the long single junction, i.e.  $R_L = \rho L_{TR} / W d_N$ .

The differences between the electrical properties of a double junction and an equivalent long single junction as a function of  $L_{TR}$  were evaluated. This was done by taking the average ratios of the  $I_C$ , normal state resistances, and the  $I_C R_{N(ARRAY)}$  products of the array

to the junction. For  $L_{TR}=100$  nm, the Nb island vanishes so that each ratio will be equal to unity. Figure 6.18 shows the experimental normalised ratios of the  $I_C$  of a double junction to the single junction ( $I_{C(ARRAY)}/I_{C(JUNCTION)}$ ),  $R_{ARRAY}/R_N$ , and  $I_C R_{ARRAY}/I_C R_N$ . The plot of  $R_{ARRAY}/R_N$  includes a line obtained from equation 6.15 for  $W=1$   $\mu\text{m}$ .

The results followed the expected trends as the electrode spacing was increased;  $I_{C(ARRAY)}/I_{C(JUNCTION)}$  and  $I_C R_{ARRAY}/I_C R_N$  increased and  $R_{ARRAY}/R_N$ , stayed reasonably constant, as predicted for the range of  $L_{SPACE}$  studied here.

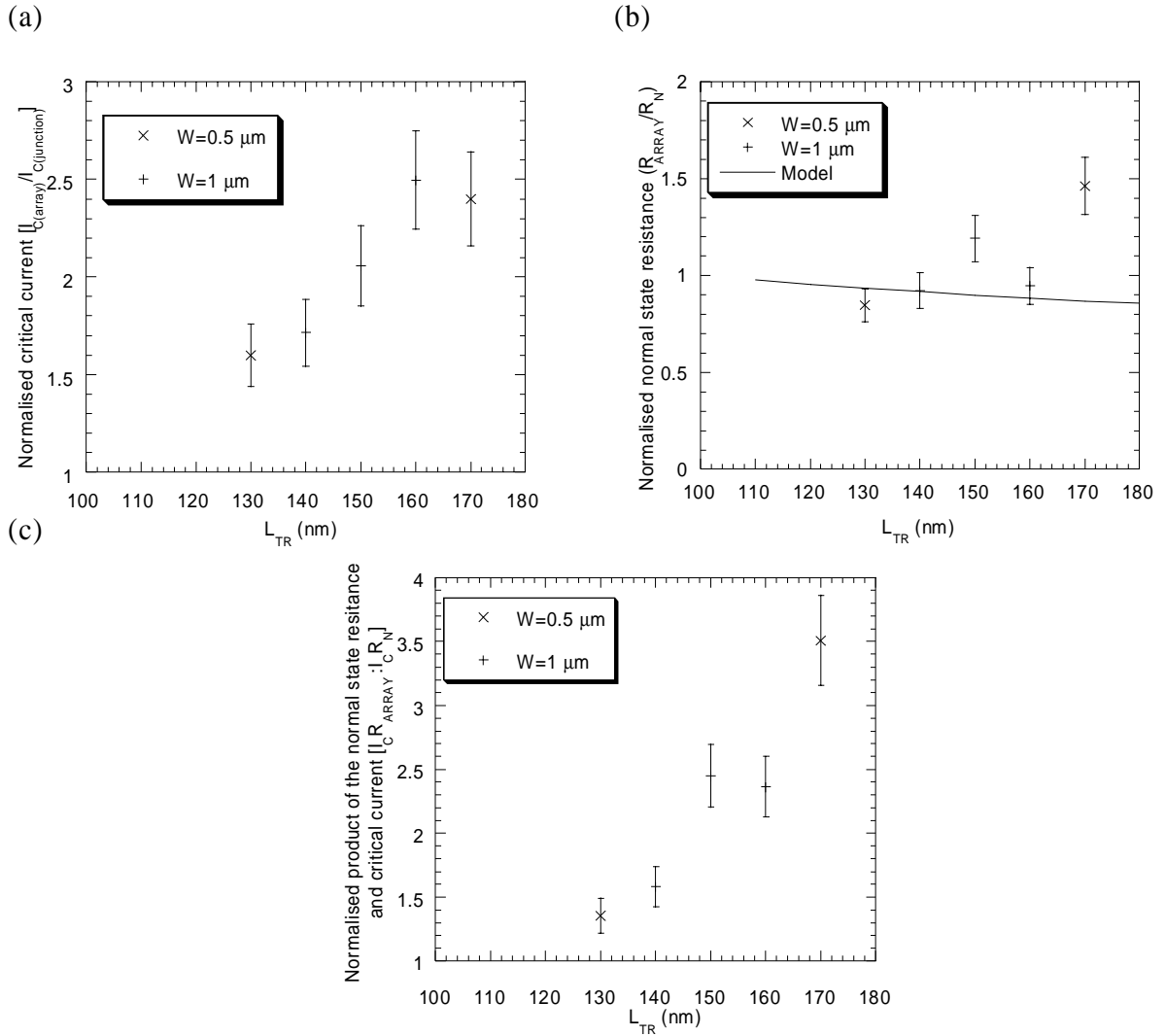


**Figure 6.18:** The variation at 4.2 K of (a) the normalised critical currents,  $I_{C(ARRAY)}/I_{C(JUNCTION)}$ , (b) the normal state resistances ( $R_{ARRAY}/R_N$ ) and (c) the product of the critical current and normal state resistance,  $I_C R_{ARRAY}/I_C R_N$ , with the outer Nb/Cu electrode spacing ( $L_{TR}$ ). Line shown in (b) was derived from a semi-empirical model using  $W=1$   $\mu\text{m}$ .

### 6.5.2. Response to microwaves

For both types of devices with  $W=1\ \mu\text{m}$ , current steps at a spacing of  $\frac{1}{2}V_S$  were observed in their  $I$ - $V$  characteristics when they were irradiated with microwaves. An example of this is shown in figure 6.19. Sub-harmonic Shapiro steps will occur if the Josephson phase relationship (equation 2.29) no longer holds. This has been observed in weak link structures where phase slip centres are present (Hamilton 1972). Sub-harmonic steps have also been predicted to occur in SNS structures where the normal-metal region in the junction is proximitised (Lempitskii 1983).

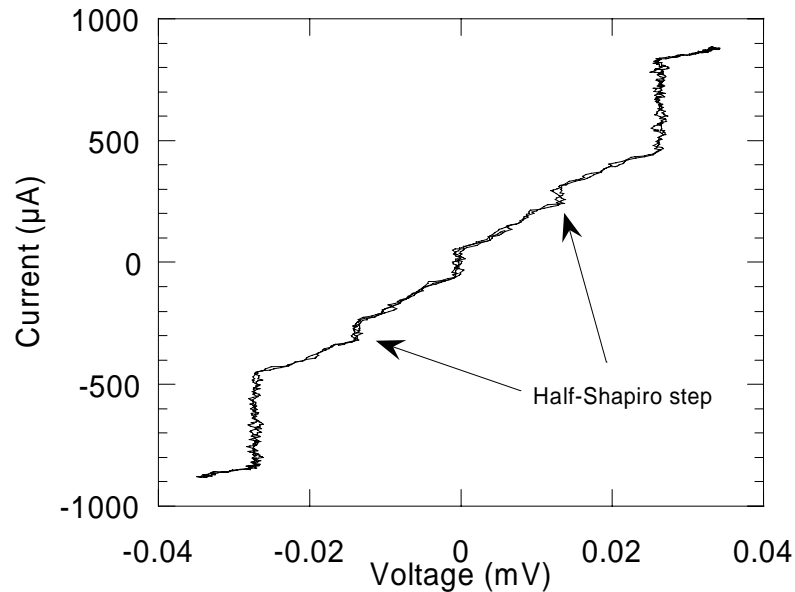


**Figure 6.19:**  $I$ - $V$  characteristics at 4.2 K of a Nb/Cu/Nb junction ( $L=150\ \text{nm}$ ,  $W=1\ \mu\text{m}$ ) showing the  $\frac{1}{2}$  integer Shapiro step response to microwave radiation (13 GHz,  $V_S=0.027\ \text{mV}$ ).

### 6.5.3. Magnetic field responses

The magnetic responses of the arrays and junctions were recorded and found to have significant differences. For comparison, the typical  $I_C(B)$  of each device with the same  $L_{TR}$  is shown in figure 6.20. For the arrays, the minima are at higher field strengths than for the corresponding single junction. This suggests that there is greater magnetic shielding in the array due to the presence of the Nb island.

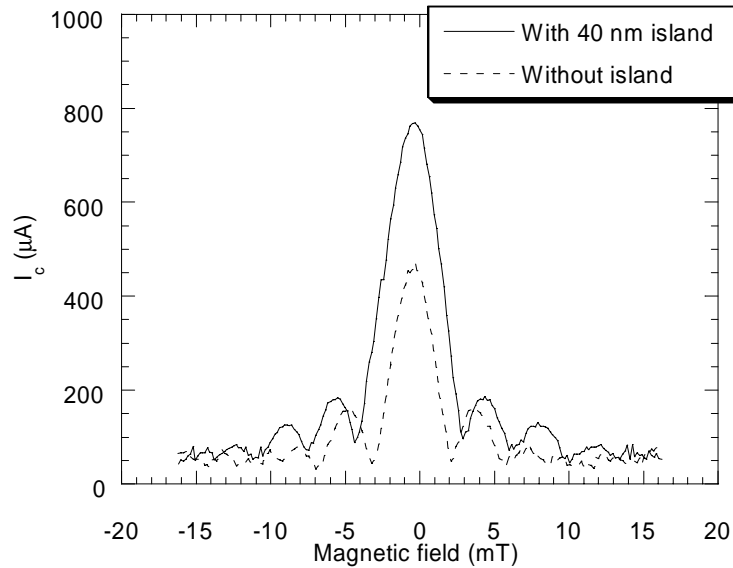


**Figure 6.20: Comparison of the magnetic field responses ( $I_C(B)$ ) of a 2 junction array (junction length=50 nm and junction spacing=40 nm) with an equivalent long junction (junction length=140 nm)**

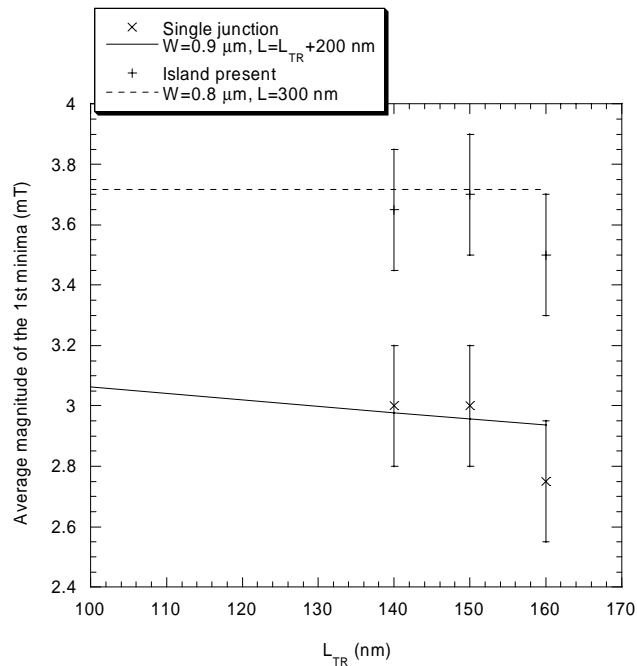


**Figure 6.21: Variation at 4.2 K of the average magnitude of the 1<sup>st</sup> minima from an  $I_C(B)$  plot with the Nb/Cu outer electrode spacing ( $L_{TR}$ ). The error bars are  $\pm 0.2$  mT. Fits are made to each device using the width ( $W$ ) and junction length ( $L$ ) as fitting parameters.**

The dependence of the average position of the first minima versus  $L_{TR}$  is plotted in figure 6.21. Fits are made to both sets of results from the Rosenthal's equation (equation 5.13) using  $L=300$  nm and  $L=L_{TR}+200$  nm for the array and the single junction, respectively. 200 nm was added to the geometrical length of each device due to the contribution of the quasiparticle diffusion currents at the ends of the array/junction, as discussed in chapter 5.4.3.1. As expected, the values obtained from the equation show that the minima interval for the array was greater than the minima interval for the corresponding junction. The theoretical differences between the intervals were not, however, as large as the observed values. A possible explanation for this is that the presence of a Nb island will also affect the magnetic width of the junctions because the circulating currents constrict the flow of supercurrent. Best fits were made to the curves by using  $W=0.8$   $\mu\text{m}$  and  $0.9$   $\mu\text{m}$  for the arrays and the junctions, respectively.

## 6.6. Behaviour of closely spaced series arrays

The work performed thus far has shown that the presence of a Nb/Cu island region renders a closely spaced double junction different to an equivalent long single junction. To extend this work, a further study of the electrical behaviour of closely spaced junctions in series arrays was undertaken. The number of junctions,  $n$ , in the arrays was systematically varied so the cumulative effect of superconducting islands in an array could be examined.

Series arrays containing 1 to 6 junctions, where  $L_{SPACE}=50$  nm,  $L=50$  nm, and  $W=1$   $\mu\text{m}$  were made. For each array, the  $I$ - $V$  characteristics and responses to microwaves and an applied magnetic field were recorded. In order to keep the current uniform across the width of the track the isolation rectangular cuts were extended in length ( $L_{ISO}$ , shown in figure 4.1) from 3  $\mu\text{m}$  to 5  $\mu\text{m}$ .

### 6.6.1. Semi-empirical model of closely spaced series arrays

The semi-empirical model, developed in sections 6.4.1 and 6.5.1 can be extended qualitatively to take into account the presence of multiple islands. Adding more Nb/Cu island regions will create more potential wells in the induced order parameter profile along the  $x$ -axis, shown schematically in figure 6.22. For the large  $L_{SPACE}$  case, the value of each minimum will be dependent only on the two neighbouring Nb/Cu island regions and/or outer Nb/Cu electrode. For the small  $L_{SPACE}$  case, the induced order parameter at any point along the array will be equal to the summation of contributions from all the islands and electrodes

in the array. For a double junction array, evidence in section 6.4.2 suggests that at  $L_{SPACE} < 100$  nm the two potential wells merge to become a single well. In this case adding more junctions to this structure would create a very long potential well. The minimum of the well would, therefore, be expected to initially decrease with increasing  $n$  because of the major contribution to the induced order parameter from the outer Nb electrodes. As  $n$  increases the minimum will reach a limiting value. This is because the contributions from the islands dominate the induced order parameter along the array. In effect,  $I_C$  will decrease until it reaches a limiting value as  $n$  is increased.

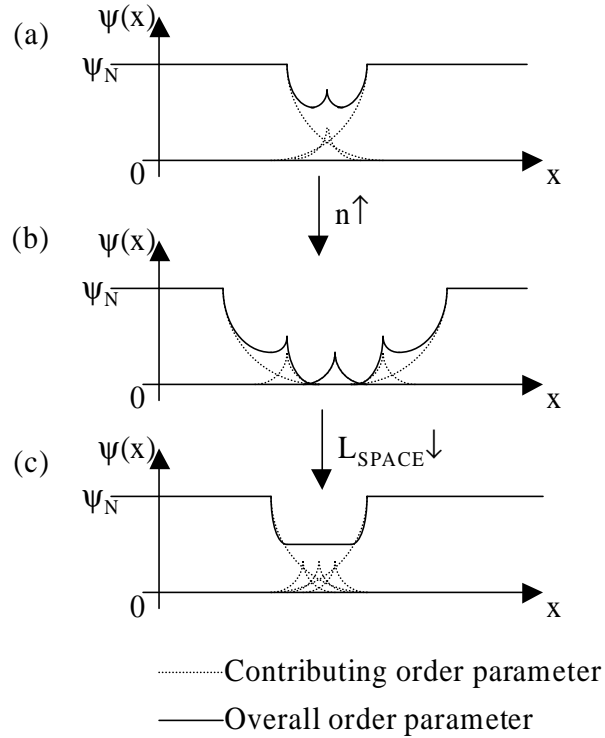


**Figure 6.22:** For  $L_{SPACE} < 2\xi_{ND}$ , the variation of the induced order parameter ( $\psi$ ) along the  $x$ -axis of (a) 2 closely spaced junction array, (b) as more junctions are added to the array (more potential wells are formed) and (c) as the junctions are placed closer together (a single well forms).

$R_{ARRAY}$  is simply given by the sum of the geometrical resistance of the distance between the superconducting electrodes, i.e.

$$R_{ARRAY} = 2R_{C1} + nR_G + (n-1) \left[ \frac{1}{R_P} + \frac{1}{2R_{C2}} \right]. \quad (6.16)$$

The effects of  $I_C$  and  $R_{ARRAY}$  on the  $I_C R_{ARRAY}$  product with increasing  $n$  will, therefore, decrease initially, but as the  $I_C$  reaches a constant value the increase in  $R_{ARRAY}$  will act to increase the  $I_C R_N$  product.

## 6.6.2. I-V characteristics

Figure 6.23 shows the variation with  $n$  of  $I_C$ ,  $R_{ARRAY}$ , and  $I_C R_{ARRAY}$  product of each array. For  $n < 3$ ,  $I_C$  and the  $I_C R_{ARRAY}$  products decreases as the number of junctions increases, whilst  $R_{ARRAY}$  increases. Beyond  $n=3$ ,  $R_{ARRAY}$  continues to increase, whilst  $I_C$  and the  $I_C R_{ARRAY}$  products remain constant. The expected increase in the  $I_C R_{ARRAY}$  products is not seen but is probably due to the low range of  $n$  used here.

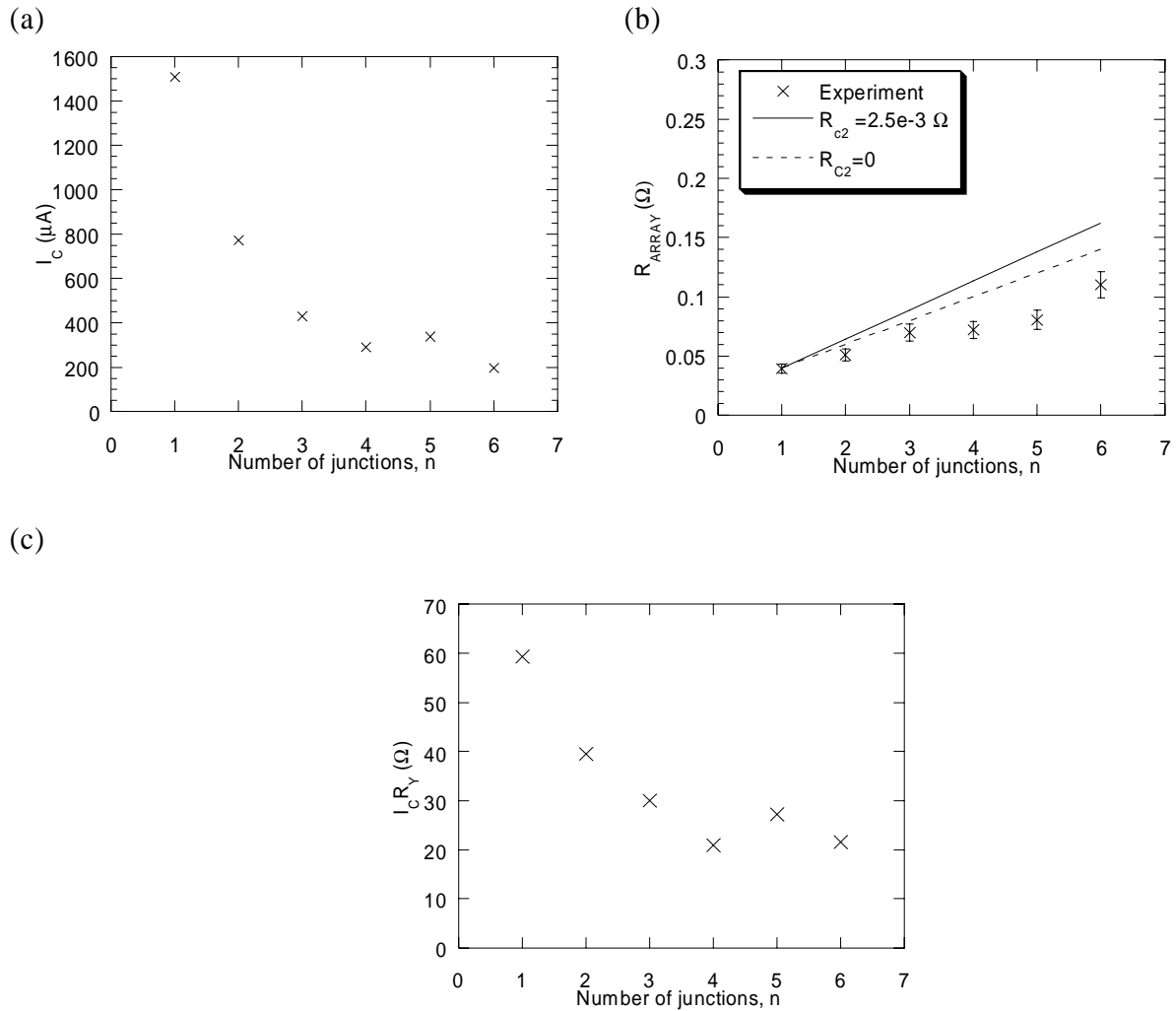


**Figure 6.23: Variation at 4.2 K of the number of junctions ( $n$ ) in an array with (a) the critical current ( $I_C$ ) (b) the normal state resistance ( $R_{ARRAY}$ ) and (c) the  $I_C R_{ARRAY}$  product. For (b), the results from a semi-empirical model are also plotted. A comparison is made between a fixed and variable interfacial resistance in the Nb/Cu island region ( $R_{C2}$ ) resistance.**

$R_{ARRAY}$  versus  $n$  was fitted using equation 6.16, using  $\rho_N = 2.8 \times 10^{-8} \Omega\text{m}$  and  $R_{CI} = 0.01 \Omega$ .  $R_{CI}$  is taken from the data, and is within the range of values expected for  $R_C$

calculated from equation 5.7.  $R_{C2}$  was calculated from equation 6.14 to be  $2.5 \times 10^{-3} \Omega$ . The fit, also shown in figure 6.23b, shows that the semi-empirical model consistently over-estimates  $R_{ARRAY}$ . This is probably due to the same discrepancy seen in section 6.4.2 where the semi-empirical description for  $R_{ARRAY}$  over estimated the observed  $R_{ARRAY}$  for  $L_{SPACE} < 200$  nm. This means that  $R_{C2}$  is much lower than expected.

A better fit where  $R_{C2}=0$  was made, and is also shown in figure 6.23b. However, this fit also over-estimates  $R_{ARRAY}$ . Interestingly, for  $L_{SPACE} < 100$  nm, the effective resistance of each junction in the array ( $R_{ARRAY}/n$ ) decreases below the normal-state resistance of a single junction ( $R_N$ ). The over-estimation of the resistance by the semi-empirical model is likely to be due the over-simplification of the contributions to the resistance, as discussed in section 6.4.2.

### 6.6.3. Microwave response

All of the arrays, with the exception of the 6-junction array, showed half-integer Shapiro steps, as previously reported in section 6.5.2. The 6-junction array showed a similar response to that discussed in section 6.3.2; a double Shapiro step followed by a quadruple Shapiro step. This would indicate that at large  $n$  the induced order parameter may not be as straightforward in form as described here. If time dependent effects are considered the order parameter and the quasiparticle populations will oscillate, as described in section 6.2.2. The induced order parameter may, therefore, oscillate from a form where there is one minimum to a form where there are multiple minima, producing the observed microwave response. If the array does behave like this then the junctions in the array may be mutually phase locked.

### 6.6.4. Magnetic field response

The  $I_C(B)$  of each array was recorded and are shown in figure 6.24a, and the average positions of the first minima (error  $\pm 0.2$  mT) are shown in figure 6.24b. The positions of the minima decrease with increasing number of junctions in the array.

In the single junction case the minima appear at larger values than found for equivalent single junctions. Previous studies showed that the positions of the first minima appeared at field strengths of  $\pm 3.0$  mT, but in this case they were at  $\pm 4.8$  mT. From equation 5.13 this corresponds to  $W$  being  $0.72 \mu\text{m}$ , instead of  $1 \mu\text{m}$ . The reduction in width may be due to the larger rectangular isolated regions that act to increase the magnetic shielding around the junctions.

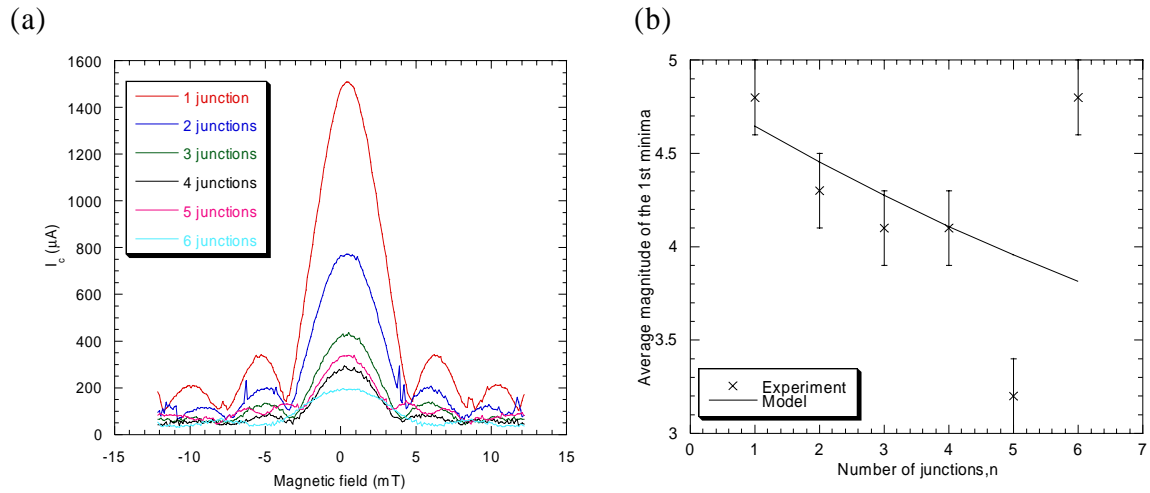


**Figure 6.24:** The variation of the number of junctions at 4.2 K with (a)  $I_c(B)$  of each array and (b) average magnitude of the 1<sup>st</sup> minima obtained each  $I_c(B)$ . For comparison, the results from a planar thin-film model were also plotted using the length and width of each array.

The decreasing trend in the positions of the minima with increasing  $n$  is significant and a possible explanation for this is the distance between the outer Nb electrodes,  $L_{TR}$ , increases as more junctions are added. The effective length of the junction is equal to the sum of the length of the junctions and the quasiparticle diffusion length at the ends of the array (i.e.  $nL+2\lambda_Q$ ). From equation 5.13 it is seen that the minima positions will fall as the number of junctions forming the array increases. A reasonable fit was made to the data using equation 5.13 where  $d'=2\lambda_L+2\lambda_Q+nL$ .

## 6.7. Investigation of 3-terminal double junctions

The final experimental investigation of junction arrays was to make 3-terminal measurements of double junction arrays. This type of measurement allows the electrical properties of a junction in an array to be recorded as current is passed through the array. In order to do this, it was necessary to make 3-terminal devices so that the individual junctions in an array could be measured. The wiring of a 3-terminal device is similar to the designs discussed so far except there is another track that is linked to the main track that allows current and voltage measurements to be taken through only part of the array.

### 6.7.1. Method

The devices were made using a similar fabrication method to that used in the previous array studies, but with some additional stages. Figure 6.25 shows a schematic of a fabricated 3-terminal device. Firstly, the rectangular isolation cuts were made along the main

track, leaving a  $1\ \mu\text{m}$  wide gap where the side track joins the main track. For  $L_{SPACE} > 1\ \mu\text{m}$  the junction trenches can be placed on both sides of the side track so electrical measurements of each junction can be made. For  $L_{SPACE} < 1\ \mu\text{m}$  it was necessary to narrow the gap between the isolation cuts, before the junctions were placed, by making two isolating line cuts, at a higher magnification of  $65\ \text{k}\times$  (see figure 6.25). Devices with  $L_{SPACE}$  in the range  $5\ \mu\text{m}$  to  $130\ \text{nm}$  were made.

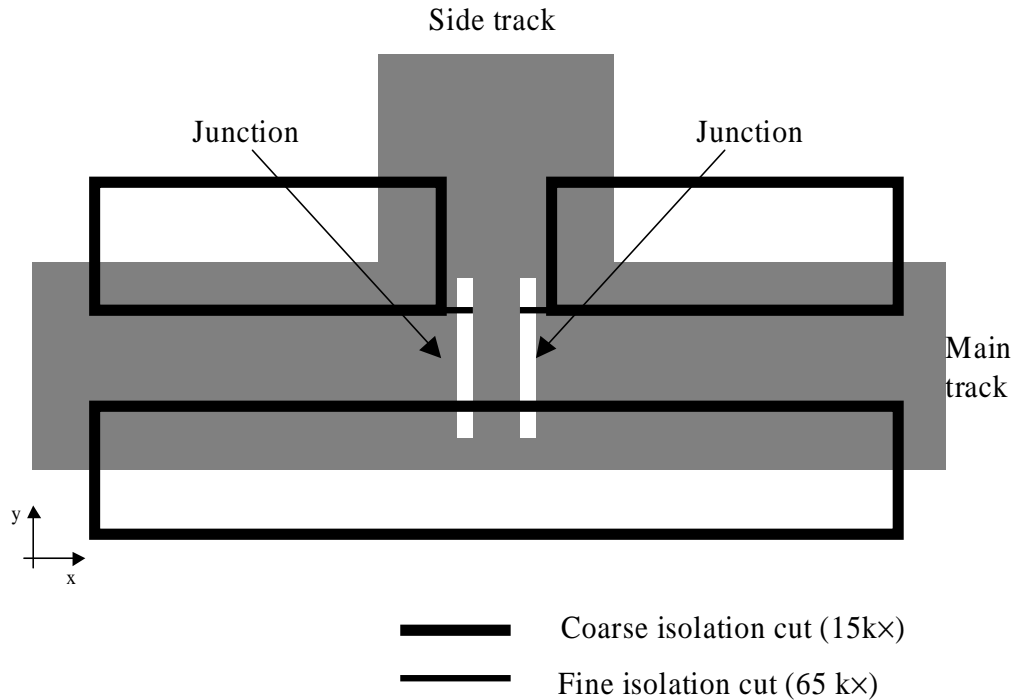


**Figure 6.25: Plan-view schematic diagram of the 3-terminal measurement set-up.**

### 6.7.2. Prediction and comparison of the $I$ - $V$ characteristics

For  $L_{SPACE} > 200\ \text{nm}$ , it is expected that the  $I$ - $V$  characteristics of each junction in an array should be independent of other junctions. For  $L_{SPACE} < 200\ \text{nm}$ , the junctions will interact so the  $I$ - $V$  characteristics of individual junctions may show new features, not seen in independent junctions.

A comparison of the  $I$ - $V$  characteristics of two arrays with  $L_{SPACE} = 1.5\ \mu\text{m}$  and  $130\ \text{nm}$  are shown in figures 6.26a and 6.26b, respectively. Each figure shows the  $I$ - $V$  characteristics of the device, together with the  $I$ - $V$  characteristics of the individual junctions.

For  $L_{SPACE} = 1.5\ \mu\text{m}$ , both junctions display the same single junction behaviour found in chapter 5. The  $I$ - $V$  characteristics of the array show the expected result if the two junctions were independent of one another. The  $I_C$  is equal to the junction with the lowest  $I_C$  and there

is a slight bump in the array's finite voltage state where the other junction enters its finite voltage state.

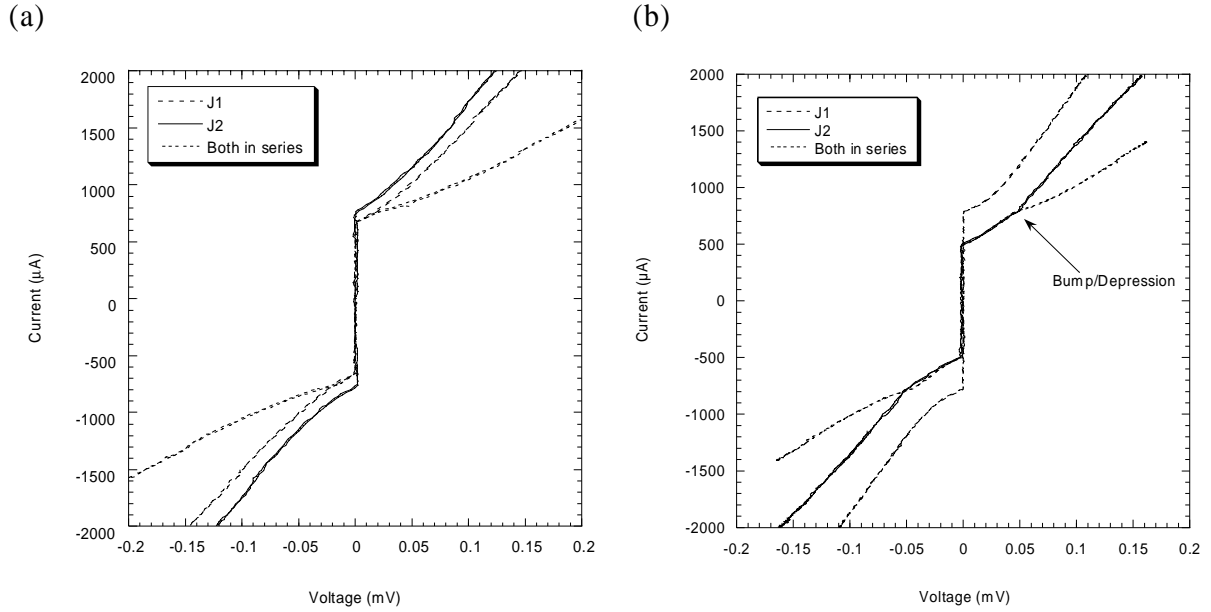


**Figure 6.26: The I-V characteristics at 4.2 K of an array, and its constituent junctions. For junction spacing ( $L_{SPACE}$ ), (a)  $1.5 \mu\text{m}$  and (b)  $130 \text{ nm}$ . For  $L_{SPACE}=130 \text{ nm}$ , a bump is observed at finite-voltage ( $\pm 0.05 \text{ mV}$ ) in the junction with the lower critical current. This may be due to the effects of a quasiparticle interaction with the neighbouring junction.**

For  $L_{SPACE}=130 \text{ nm}$ , the  $I$ - $V$  characteristics of the junctions and array show interesting features not seen in the results for  $L_{SPACE}=1.5 \mu\text{m}$ . First, the junction with the lower  $I_C$  has a broad depression at  $\pm 0.05 \text{ mV}$ . The depression is centred on the current-bias point of the  $I_C$  of the other junction. Magnetic field measurements showed that the position of the depression changed in accordance with the  $I_C$  of the other junction. No similar feature is seen in the  $I$ - $V$  characteristics of the junction with the larger  $I_C$ . Second, comparison of the  $I$ - $V$  characteristics of the array with the junction of lowest  $I_C$  shows that they are the same in the range  $-0.05 < V < 0.05$ . For the array, a bump is observed in the  $I$ - $V$  characteristics centred also at  $\pm 0.05 \text{ mV}$ . At higher biases the normal state resistance reverts to a higher normal state resistance, as expected for a double junction configuration.

### 6.7.3. Comparison of coupling mechanisms

The presence of the depression seen in one junction that is dependent on the  $I_C$  of another junction means these junctions are coupled by some interaction between the two junctions. The interaction can either be quasiparticle, order parameter, or high frequency electromagnetic coupling, as described in section 6.2.2. High frequency electromagnetic coupling can be ignored because of the impedance mismatch between the load and junctions (Benz 1991). Order parameter coupling can be ruled out for two reasons. First, the junction spacing is too large, i.e.  $L_{SPACE} > 2\xi_{ND}$ . Second, if order parameter coupling were responsible then the  $I_C$  of the double junction would be expected to be less than the  $I_C$  of both junctions, as detailed by Lindelof and Bindslev-Hansen (Lindelof 1981). Given the evidence that suggests quasiparticles play an important role in understanding these types of arrays it is, therefore, unsurprising that the only remaining coupling mechanism that can explain the situation here is based on quasiparticles.

#### 6.7.3.1. Modeling the quasiparticle coupling

The explanation of the quasiparticle coupling mechanism given in section 6.2.2.2 is brief, partly because a quantitative theory has been developed only for certain types of Josephson junctions, e.g. planar weak links junctions with a very low  $I_C$  (Artemenko 1978). This is due to the complex nature of the interaction and the lack of experimental results for other type of junctions. Experiments using planar weak link junctions have also been found to be in qualitative agreement with this interaction (Jillie 1976; Jillie 1977a; Jillie 1977b; Palmer 1977; Lukens 1978). Jillie *et al.* (Jillie 1980) investigated the short-range interaction between two weak links. The quasiparticle interaction between closely spaced junctions was examined and a model that included the quasiparticle current injected from one weak link to the other in the RSJ model was constructed. A schematic of the model is shown in figure 6.27. The bias current,  $I_I$  that passes through the junction, labelled J1 in figure 6.27 is given by

$$I_1 + i_{q2} = I_{c1} \sin \phi_1 + \frac{V_1}{R_{N1}}, \quad (6.17)$$

and similarly for J<sub>2</sub>

$$I_2 + i_{q1} = I_{c2} \sin \phi_2 + \frac{V_2}{R_{N2}}, \quad (6.18)$$

where  $i_{q1}$  and  $i_{q2}$  is the part of the quasiparticle current generated in the other bridge that flows through the bridge being measured. The total quasiparticle current through  $J_2$  is

$$I_{q2} = I_2 - I_{c2} \sin \phi_2 + i_{q1}, \quad (6.19)$$

of which a fraction  $\alpha_2$  flows through  $J_1$ . Hence

$$i_{q2} = \alpha_2 I_{q2} = \alpha_2 (I_2 - I_{c2} \sin \phi_2 + i_{q1}), \quad (6.20)$$

and similarly for  $J_1$ ,

$$i_{q1} = \alpha_1 I_{q1} = \alpha_1 (I_1 - I_{c1} \sin \phi_1 + i_{q2}). \quad (6.21)$$

Combining these equations and assuming that  $\alpha_1$  and  $\alpha_2$  are small so that  $\alpha_1 \alpha_2$  can be neglected  $I_1$  and  $I_2$  can be obtained,

$$I_1 = I_{c1} \sin \phi_1 + \frac{V_1}{R_1} - \alpha_2 (I_2 - I_{c2} \sin \phi_2), \quad (6.22)$$

$$I_2 = I_{c2} \sin \phi_2 + \frac{V_2}{R_2} - \alpha_1 (I_1 - I_{c1} \sin \phi_1). \quad (6.23)$$

When the  $I$ - $V$  characteristics of  $J_1$  are measured  $I_2=0$ , and similarly for  $J_2$   $I_1=0$ , therefore equations 6.22 and 6.23 can be rewritten as

$$I_1 = I_{c1} \sin \phi_1 + \frac{V_1}{R_1} + \alpha_2 I_{c2} \sin \phi_2 \quad (6.24)$$

$$I_2 = I_{c2} \sin \phi_2 + \frac{V_2}{R_2} + \alpha_1 I_{c1} \sin \phi_1. \quad (6.25)$$

Inspection of these equations shows that they describe two Josephson junctions and a resistor all in parallel and so can not account for the presence of a depression in the  $I$ - $V$  characteristics in one junction that occurs at the  $I_C$  of the other junction. This could be due to the assumption that the strength of the quasiparticle interaction (represented by the product of  $\alpha_1 \alpha_2$ ) is small, which is not the case in this situation.

A better interpretation of the quasiparticle interaction can be made if the energy distribution of the quasiparticles is considered. It is based on the explanation for dc injection locking, described by Lindelof and Bindslev-Hansen (Lindelof 1981); the energy distribution of the quasiparticles diffusing through the region between the bridges is not a smooth function. Instead the energy distribution has a sharp maximum at the energy corresponding to the gap singularity in the superconductors beyond the junctions. Assuming that the majority of the quasiparticles do diffuse through both junctions then for the situation where  $I_{C1} > I_{C2}$  the semiconductor representation, shown in figure 6.27a, is applicable. The small

peaks in the distributions correspond to quasiparticle injection from the gap singularity through a bridge to another superconductor. As  $I$  is increased further so that  $I > I_{C1}$ , shown in figure 6.27b, a voltage will develop across the junction not being measured,  $J_1$ , which will inject quasiparticles into the central region. The energy population of these quasiparticles will differ to the quasiparticles being generated in  $J_2$  and, therefore, a decrease in the normal state resistance is expected, and is observed here (figure 6.26b).

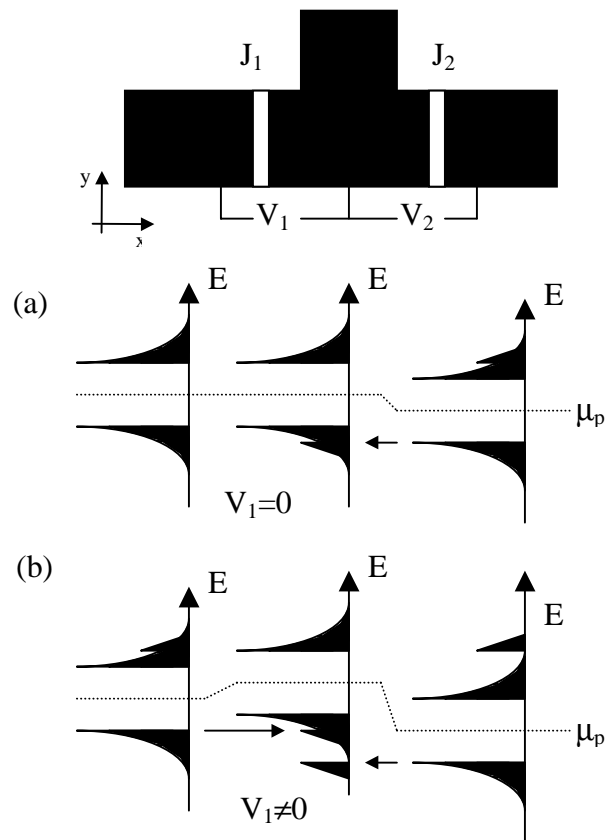


**Figure 6.27: Qualitative illustration of the quasiparticle dc locking mechanism. The junction layout is shown at the top. The quasiparticle distribution in the three regions, with the injected peaks due to the diffusive currents, is also shown. (a) For  $I_{C1} > I > I_{C2}$  (b) For  $I > I_{C1} > I_{C2}$ .**

This qualitative explanation does fit with the observations made, but it is noted that this does not mean the junctions are necessarily mutually phased locked. Indeed, there is no evidence of mutual phase locking because deviations in the  $I$ - $V$  characteristics of both junctions at fixed voltages were not observed. 3-terminal measurements were made where currents were injected into one junction and the voltage across one or both junctions were recorded but these did not show any fixed voltage behaviour. If the energies of the interfering quasiparticles were the same there would be a greater coupling force between the

junctions, so that dc-injection locking could take place. This could be achieved by improving the uniformity of the junctions.

## 6.8. Summary

Nb/Cu/Nb junction series arrays, made using an FIB instrument, were successfully manufactured. The reproducibility of the junctions forming the arrays is found to be similar to the individual junctions reported in chapter 4. New observations have been made for this array geometry. The electrical properties of an array have been found to be dependent on the spacing of the junctions and the number of junctions in the array. For all the arrays studied, there is evidence of current redistribution between junctions. For arrays where the spacing between junctions is less than  $2\lambda_Q$  (200 nm), as the junction spacing decreases the normal-state resistance decreases. Similarly, below a junction spacing of  $2\xi_{ND}$  (100 nm), the critical current decreases. A semi-empirical model was made and explains the electrical behaviour of an array in terms of the changing order parameter and quasiparticle interference. The semi-empirical model was only successful for predicting the trends in the junction spacing dependencies of the critical current and normal-state resistance. For arrays consisting of junctions with spacing below 100 nm, each array behaves like a single junction. It is thought that this can be explained in terms of the changing nature of the order parameter in the array. This could be exploited to make a novel sensor based on switching the device from a single junction to a multiple junction array configuration. There is no evidence of mutual phase locking in the arrays, although it is believed that dc-injection locking may occur if the electrical behaviour of the junctions were made more uniform.

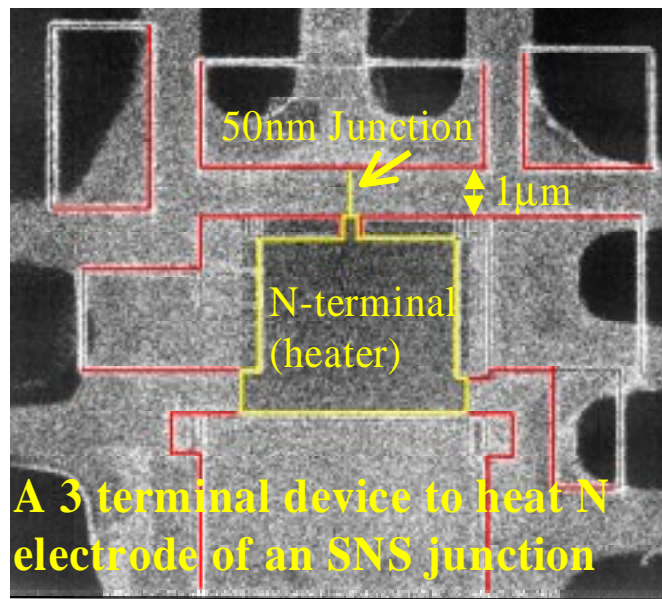
## 6.9. References

- S. N. Artemenko, A. F. Volkov and A. V. Zaitsev (1978). *J. de Phys.* **39** 588.
- P. Barbara, A. B. Cawthorne, S. V. Shitov and C. J. Lobb (1999). "Stimulated emission and amplification in Josephson junction arrays." *Physical Review Letters* **82**(9) 1963.
- A. Bennett (1999). Part III project report, "Fabrication of SNS junction series arrays using a focused ion beam.", University of Cambridge.
- S. P. Benz and C. J. Burroughs (1991). "Coherent emission from two-dimensional Josephson junction arrays." *Applied Physics Letters* **58** 2162-2164.

- S. P. Benz and C. A. Hamilton (1996). "A Pulse-Driven Programmable Josephson Voltage Standard." *Applied Physics Letters* **68**(22) 3171.
- W. E. Booij (1997). PhD Thesis "Josephson junctions and Devices Fabricated by Focussed Electron Beam Irradiation." Dept. Materials Science. Cambridge, University of Cambridge 208.
- M. Darula, T. Doderer and S. Beuven (1999). "Millimetre and sub-mm wavelength radiation sources based on discrete Josephson junction arrays." *Superconductor Science & Technology* **12**(1) R1.
- C. A. Hamilton and E. G. Johnson (1972). "Analog computer studies of subharmonic steps in superconducting weak links." *Phys. Letts.* **41A** 393.
- A. K. Jain, K. K. Likharev, J. E. Lukens and J. E. Sauvageau (1984). "Mutual Phase-Locking In Josephson Junction Arrays." *Physics Reports-Review Section Of Physics Letters* **109**(6) 309.
- D. W. Jillie, J. E. Lukens and Y. H. Kao (1977a). "Observations of interactions between two superconducting phase slip centers." *Phys. Rev. Lett.* **38** 915.
- D. W. Jillie, J. E. Lukens and Y. H. Kao (1977b). "Voltage locking in two coupled microbridge Josephson junctions." *IEEE Trans. Magn.* **MAG-13** 578.
- D. W. Jillie, J. E. Lukens, Y. H. Kao and G. J. Dolan (1976). "Observation of voltage locking and other interactions in coupled microbridge Josephson junctions." *Phys. Lett.* **55A** 381.
- D. W. Jillie, M. A. H. Nerenberg and J. A. Blackburn (1980). "Voltage locking and other interactions in coupled superconducting weak links." *Phys. Rev.* **21B** 125.
- Y. Kuramoto (1975). in the proceedings of Proceedings of the International Symposium on Mathematical Problems in Theoretical Physics, Berlin, Springer.
- S. V. Lempitskii (1983). "Stimulation of superconductivity by direct current in a superconductor-normal metal-superconductor junction." *Sov. Phys. JETP* **58** 624.
- K. K. Likharev, L. S. Kuzmin and G. A. Ovsyannikov (1981). "Mutual Phase Locking In Multi-Junction Josephson Arrays." *IEEE Transactions On Magnetics* **17**(1) 111.

- P. E. Lindelof, Bindslev Hansen, J. (1981). "Short range interaction between two superconducting weak links." *Nonequilibrium Superconductivity, Phonons, and Kapitza Boundaries*. K. E. Gray Ed. New York and London, Plenum Press. **65** 593.
- J. E. Lukens, R. D. Sandell and C. Varmazis (1978). "Future Trends in Superconductive Electronics." in the proceedings of AIP Conf.
- D. W. Palmer and J. E. Mercereau (1977). *Phys. Lett.* **61A** 135.
- A. J. Pauza (1993). PhD Thesis "The Fabrication of Josephson Junctions with an Electron Beam." Department of Engineering, University of Cambridge.
- P. A. Rosenthal, M. R. Beasley, K. Char, M. S. Colclough and G. Zaharchuk (1991). "Flux focusing effects in planar thin-film grain-boundary Josephson junctions." *Appl. Phys. Lett.* **59** 3482.
- H. J. T. Smith and M. Dion (1990). *Phys. Rev. B* **42** 206.
- K. Wiesenfeld, P. Colet and S. H. Strogatz (1996). "Synchronization transitions in a disordered Josephson series array." *Physical Review Letters* **76**(3) 404.

# Chapter 7



Annotated image of an SNS junction based device made using an FIB instrument.

Thermal effects in SNS- and  
SIN- junction based devices

## 7.1. Introduction

This chapter investigates how thermal energy in various Superconductor/Normal-metal/Superconductor- (SNS) and Superconductor/Insulator/Normal-metal- (SIN) junction based devices affect their electrical performance, and how the heat flow within the device and its surroundings can be modified. The motivation for this work is that SNS and SIN-based junctions potentially make excellent bolometer-based detectors (Nahum 1993; Booth 1996; Kraus 1996). Such devices are candidates for the next generation of X-ray spectrometers and prototype devices have produced excellent results (Martinis 1996). They work by collecting photon radiation in the normal-metal region of the junction, which raises the electronic temperature. This temperature change causes the electrical characteristics of the junction to change. The sensitivity of the junctions to very small changes in temperature, at the very low base temperatures used, is higher than any existing semiconductor device-based technology.

The first part of this chapter explores how the heat flow in an SIN-based device changes when the bulk substrate is replaced by a thin-membrane, and whether it can be used as a Peltier refrigerator. The second part investigates the heat flow in a SNS junction, the strength of coupling between substrate and device, and the electron and phonon systems in the device. Finally, progress towards a SQUID-based bolometer is explored, and issues that will affect its performance are discussed.

All the work described in this chapter was made with the assistance of Dr. Gavin Burnell.

### 7.1.1. Background

For almost any electrical device, the operating temperature will affect its electrical performance. If the device generates heat, a thermal gradient will be created from the device to its surroundings. The strength of the gradient will be dependent upon the physical and thermal properties of the system. At sufficiently low temperatures the phonon and electronic temperatures will de-couple so allowing the electron temperature to be different from the phonon temperature. For analysing this type of situation it is necessary, therefore, to consider them separately.

## 7.2. Thermal effects in an SIN junction based device

Blamire (Blamire 1991) showed that it is possible to enhance the critical temperature of a thin Al film in a symmetrical SIN-based sandwich (SINIS) device. The temperature enhancement implies that the electrons in the normal-metal (Al) are being cooled. Other researchers, Nahum (Nahum 1994) and Edwards (Edwards 1995), have shown how this effect could be used in a refrigerator (or cryo-cooler) device and has been pursued by various groups (Leivo 1996; Fisher 1997; Jochum 1997; Jug 1997; Pekola 1999). Cooling has been observed by two groups in sub-micron (Manninen 1997) and micron (Fisher 1999) scale junctions.

In this work, the thermal properties of a micron scale SIN junction-based device are investigated. The study focuses on the heat flow in the device, and how it changes when the substrate is replaced by a  $\text{Si}_3\text{N}_4$  membrane.

### 7.2.1. Theory

#### 7.2.1.1. Cooling effect

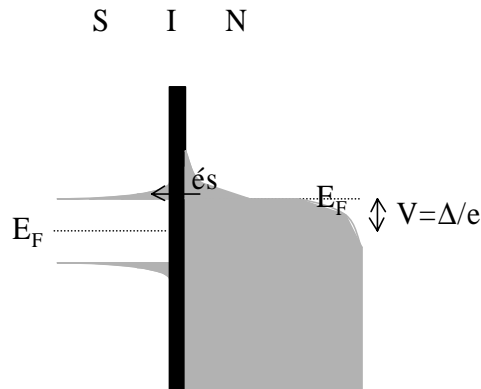


**Figure 7.1: Semiconductor representation of a SIN junction biased ( $V$ ) at the energy-gap ( $\Delta/e$ ) of the superconductor. It shows that only the electrons with energies greater than the Fermi energy ( $E_F$ ) can tunnel into the superconductor.**

The cooling effect can be best described by considering the distribution of electrons in a normal-metal. The equilibrium electron energy population is described by the Fermi-Dirac distribution. In the cooling effect, the states below the Fermi-energy,  $E_F$ , are refilled and the states above  $E_F$  are emptied. This reduces the thermalised spread of electrons, reducing their entropy, and results in a decrease in the electronic temperature. This well

documented mechanism is commonly known as the Peltier effect, and is the cooling mechanism in semiconductor thermoelectric refrigerators.

This can also be applied to an SIN junction. It can be biased so only electrons whose energy  $E$  is larger than  $E_F$  are removed from the normal-metal, as shown in figure 7.1. Alternatively, the junction can be biased in such a way that only electrons with energy less than  $E_F$  can be injected into the normal-metal. By carefully biasing two SIN junctions in series, to form an SINIS device, both effects can occur together, doubling the cooling effect in the normal-metal.

Nahum (Nahum 1994) considered a device with an SIN and SN junction in series. In the SN junction, electrons are injected from the superconductor into the normal-metal at biases below the energy-gap of the superconductor by Andreev reflection (see chapter 2.5.5). A consequence of Andreev reflection is that the energies of the electrons are equal to the Fermi energy of the normal-metal. This means, in effect, that the SN junction does not dissipate heat into the normal-metal.

The  $I$ - $V$  characteristics of the SIN junction depend only upon the temperature of electrons,  $T_e$ , in the normal-metal electrode, as described in chapter 2.4.3. Ignoring the presence of thermal excitations in the superconductor, the dominant contribution to the current is from electrons tunneling from the normal to the superconducting electrode.

From chapter 2.4.2 the current,  $I$ , for  $eV > 0$  is given by

$$I = \frac{1}{R_N} \int_{\Delta}^{\infty} \frac{1}{\exp\left[\frac{E - eV}{k_B T_e}\right] + 1} \frac{E}{\sqrt{E^2 - \Delta^2}} dE. \quad (7.1)$$

$\Delta$  is the energy-gap in the superconductor,  $E$  is energy,  $k_B$  is the Boltzmann constant, and  $R_N$  is the normal state resistance of the junction. When  $(\Delta - eV) > k_B T_e$ , then  $I \approx I_0 \exp[-(\Delta - eV)/k_B T_e]$ , where  $I_0 = (2eR_N)^{-1} (2\pi\Delta k_B T_e)^{1/2}$ . If the junction is biased at a constant current then the temperature responsiveness,  $dV/dT_e$ , is

$$\frac{dV}{dT_e} \approx -\frac{k_B}{e} \ln\left(\frac{I_0}{I}\right). \quad (7.2)$$

When  $eV < \Delta$  only electrons with energy  $E > E_F$  can tunnel from the normal-metal electrode, removing high-energy thermal excitations from the normal electrode, thus cooling the electrons. When  $eV > \Delta$  electrons with  $E < E_F$  are also allowed to tunnel and deposit energy into the normal electrode. The power transfer,  $P_N$ , from the normal electrode is calculated in

the same way as the tunneling current equation 7.1. Each electron transfers  $(E-eV)$  of energy so  $P_N$  is given by

$$P_N = \frac{1}{e^2 R_N} \int_{\Delta}^{\infty} (E - eV) \frac{1}{\exp\left[\frac{E - eV}{k_B T_e}\right] + 1} \frac{E}{\sqrt{E^2 - \Delta^2}} dE. \quad (7.3)$$

This gives the maximum cooling power as  $P_{max}=(k_B T)^2/(e^2 R_N)$  when  $eV=\Delta$ .

### 7.2.1.2. Heating effects and modeling the heat flow in the device

The cooling mechanism, described above, is not the sole contributor to the thermal properties of the device. Thermal energy from the rest of the device, not being cooled, and the surroundings will heat the thermally active region where cooling is taking place. Fisher (Fisher 1998) devised a heat flow model in order to find the maximum thermal load that an SIN junction can absorb while maintaining a given  $T_e$ . This is commonly referred to as the cooling power of the refrigerator,  $P_{REF}$ , and is given by

$$P_{REF} = P_N(T_e) - P_{ENV}(T_e, T_b). \quad (7.4)$$

$T_b$  is the bath temperature (or operating temperature) and  $P_{ENV}$  is the heating power. The base temperature is, therefore, the value of  $T_e$  for which  $P_{REF}=0$ .

For a device sitting on a thick substrate, which is moderately thermally conductive, the thermal load from the environment is dominated by the exchange of energy between conduction electrons in the normal electrode, and lattice phonons in the substrate. The power transferred between the electron and phonon systems is given by

$$P_{e-ph} = \Sigma V_{ol} (T_b^5 - T_e^5). \quad (7.5)$$

$\Sigma$  is a constant that depends on the strength of the electron-phonon coupling, typically  $\sim 1.3 \text{ nW}\mu\text{m}^{-3}\text{K}^{-5}$  (Manninen 1997).  $V_{ol}$  is the volume of the normal-metal region.

Other heating mechanisms occur due to non-ideal behaviour of an SIN junction such as micro-shorts in the insulator barrier and flux threading the junction. The latter was investigated by Ullom and found that the electron-electron interaction distance decreases around a flux vortex, increasing the effects of heating (Ullom 1998). This non-ideal behaviour can be modeled as an ideal junction shunted by a resistance equal to the sub-gap resistance,  $R_D$ , of the junction where

$$R_D = \left. \frac{\partial V}{\partial I} \right|_{V \rightarrow 0}. \quad (7.6)$$

The effect of this non-ideal behaviour is to dissipate a heating power of

$$P_{OHM} = \frac{V^2}{R_D}. \quad (7.7)$$

For most sub-micron junctions, the two heating mechanisms described above are dominant. For larger junction areas, heating due to the effects of quasiparticle scattering processes will become significant. Electrons tunneling into the superconducting electrodes will eventually undergo quasiparticle recombination where they will form Cooper pairs via the emission of phonons with energy  $2\Delta$ , described in detail in chapter 2.6.2. This process dissipates a power  $P_S=IV+P_N$  into the electrodes. Since  $P_S \gg P_N$ , it is essential to minimise the fraction  $\beta$  of  $P_S$  that can couple to the normal-metal electrode by thermal transport through the substrate, or by back-tunneling (direct recombination of quasiparticles in the normal-metal from the superconductor). The relevant length scale over which this effect is significant is the quasiparticle recombination length given by

$$\lambda_R = (D\tau_R)^{\left(\frac{1}{2}\right)}, \quad (7.8)$$

where  $D$  is the diffusion coefficient and  $\tau_R$  is the recombination time for quasiparticles in the superconductor.

Combining equations 7.5 and 7.7 with heating due to quasiparticle recombination gives the overall heating power to be

$$P_{ENV} = P_{e-ph}(T_e, T_b) + P_{OHM} + \beta P_S(T_b). \quad (7.9)$$

The equilibrium value of  $T_e$  can then be found by solving the equation

$$0 = P_N(T_e) - P_{e-ph}(T_e, T_b) - P_{OHM} - \beta P_S(T_b). \quad (7.10)$$

### 7.2.1.3. Modeling of a device on a membrane

One way to reduce the heating power is to either remove the substrate, or replace the substrate directly underneath the device with a material that has a low thermal conductivity. This means the phonon temperature in the device,  $T_{ph}$ , is no longer the same as  $T_b$  so  $P_{e-ph}$  can be reduced. The difference between the heat flow in a device on a thick substrate and a thin-substrate whose thermal conductivity is low is shown in figure 7.2. It shows a heat flow diagram for each configuration of the device. Figure 7.3 shows a schematic of a device on a membrane. Edwards (Edwards 1995) modeled the heat flowing into the device from the rest of the substrate by solving the heat transfer equation

$$\nabla \cdot (\kappa \nabla T_{mem}) = 0. \quad (7.11)$$

$T_{mem}$  is the local membrane temperature.  $\kappa$  is the thermal conductivity of the thin-substrate and is given by

$$\kappa = aT_{mem}^{\frac{5}{2}}. \quad (7.12)$$

If a  $\text{Si}_3\text{N}_4$  membrane is used,  $a$ , a material constant is equal to  $0.0162 \text{ WK}^{-1}\text{m}^{-1}$  (Edwards 1995). Edwards also derived an equation that gave a heating power from the substrate to the device of

$$P_{cond} = \frac{4\pi a d_{mem} \left( T_b^{\left(\frac{7}{2}\right)} - T_{ph}^{\left(\frac{7}{2}\right)} \right)}{7 \ln \left( \frac{r_2}{r_1} \right)}, \quad (7.13)$$

where  $d_{mem}$  is the thickness of the membrane,  $r_1$  and  $r_2$  are the inner and outer radius of the membrane. Leivo (Leivo 1998) has characterised the thermal properties of a silicon nitride membrane, and has shown how the geometry of the membrane and the device affects its thermal conductivity. For this case, the approximation made by Edwards, however, will suffice.

To solve for  $T_e$  in a device on a membrane, two equations have to be solved, shown below:

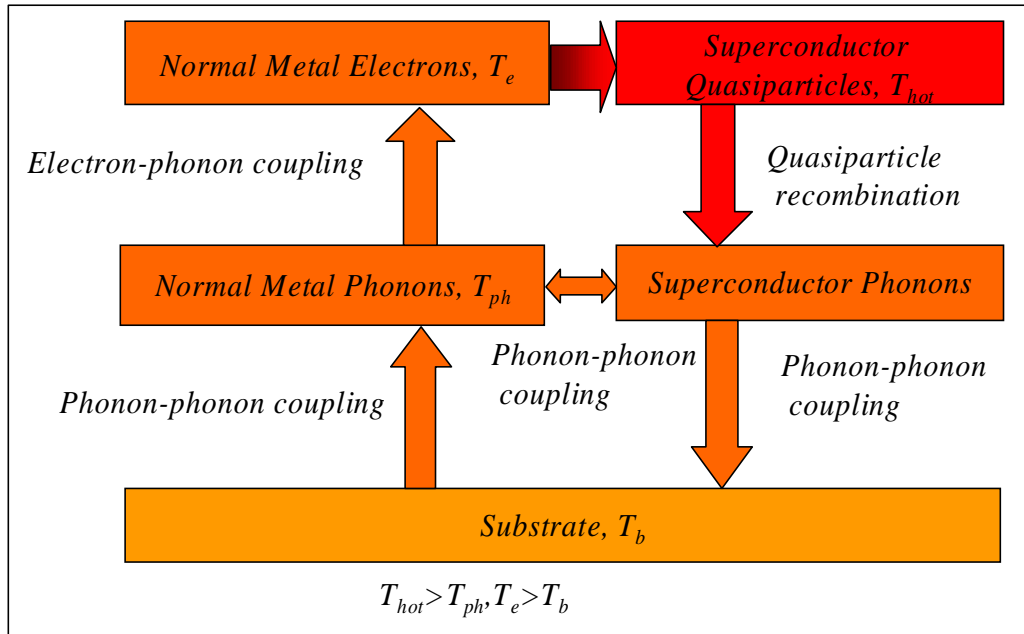
$$0 = P_n(T_e) - P_{e-ph}(T_e, T_{ph}) - P_{OHM} - \beta P_S(T_b) \quad (7.14)$$

$$0 = P_{e-ph}(T_e, T_{ph}) - P_{cond}(T_b, T_{ph}). \quad (7.15)$$

Both equations are based on the equations derived by Fisher (equation 7.10) and Edwards (equation 7.13). Equation 7.14 represents the heat flow at equilibrium from the cooling region of the device to the rest of the device. Similarly, equation 7.15 represents the heat flow at equilibrium from the device on the membrane to the surroundings.

Equations 7.14 and 7.15 were solved for different heating contributions, using common junction parameters from the experiments described below. Results for  $T_b=0.35 \text{ K}$  are shown in figure 7.4. The figure shows the electronic temperature versus junction bias if there were no heating contribution for a device on a substrate (figure 7.4a) and on a membrane (figure 7.4b). From the two plots, cooling is greater for the device on a membrane. Finally, a device on a membrane that has non-ideal behaviour was modeled (figure 7.4c). Ohmic heating and quasiparticle recombination were added ( $R_d=100 \text{ } \Omega$ ,  $\beta=0.5$ ) and shows that these processes dominate.

(a)



(b)

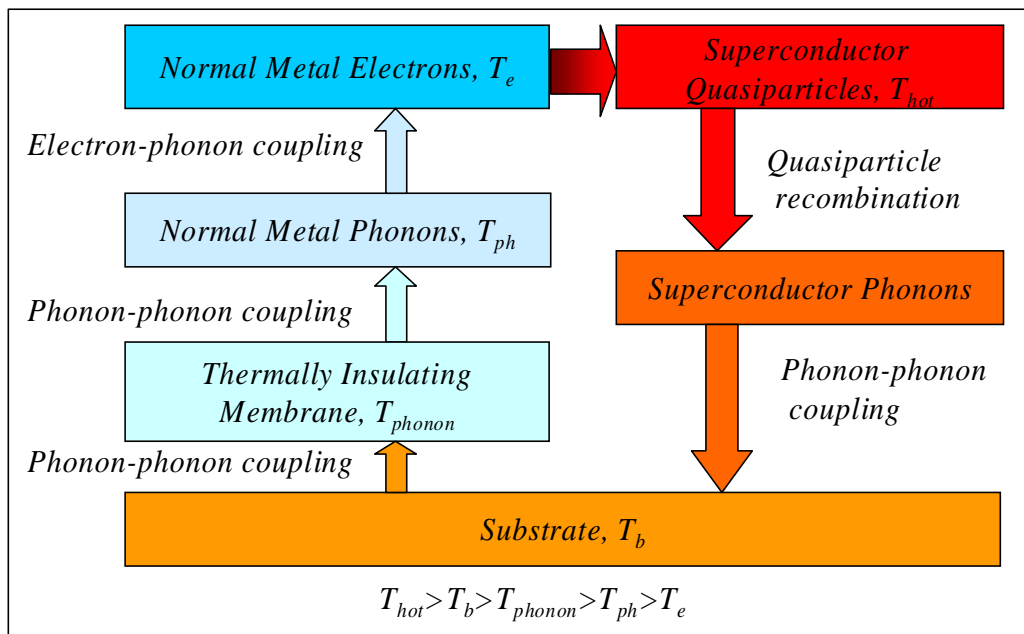


**Figure 7.2: Heat flow diagrams of a SIN junction biased at the energy-gap sitting on (a) a bulk Si substrate and (b) a silicon nitride membrane.**

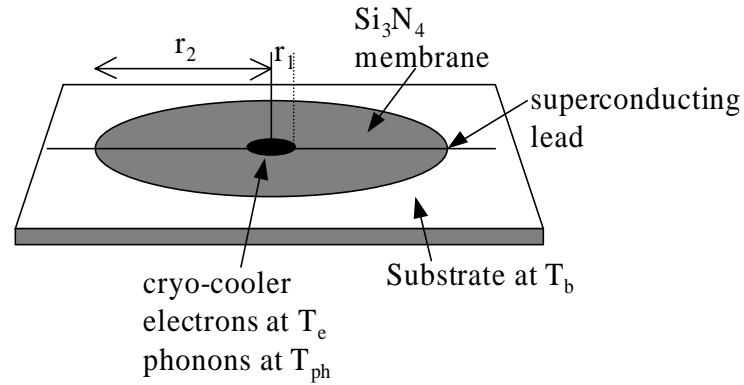


**Figure 7.3:** Schematic of an SIN junction device sitting on a Si<sub>3</sub>N<sub>4</sub> membrane. From Edwards (Edwards, 1995)

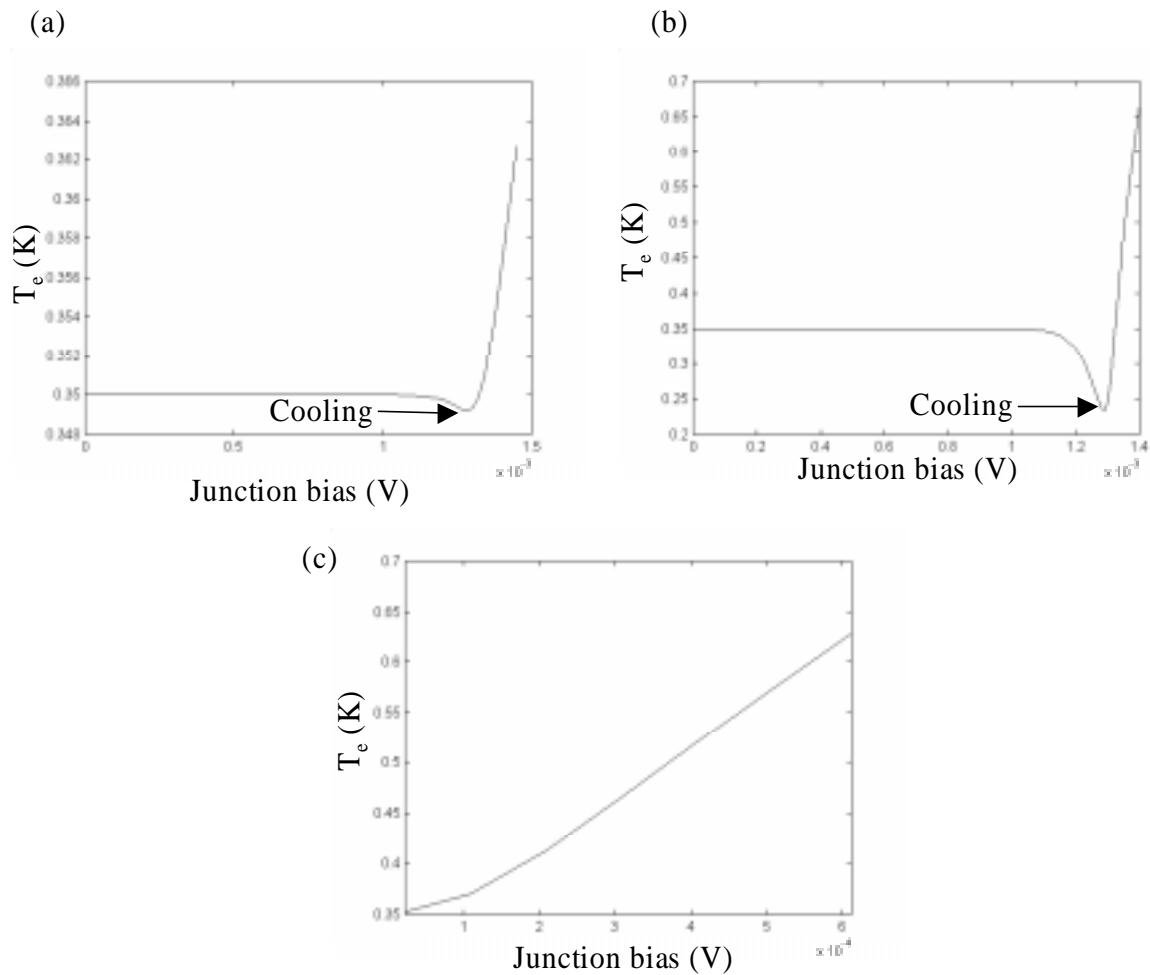


**Figure 7.4:** Theoretical dependencies of the electronic temperature ( $T_e$ ) with the junction bias of an ideal SIN junction for (a) sitting on a bulk substrate (b) sitting on a Si<sub>3</sub>N<sub>4</sub> membrane and (c) an non-ideal SIN junction sitting on a Si<sub>3</sub>N<sub>4</sub> membrane ( $R_d=100 \Omega$ ,  $\beta=0.5$ ).

## 7.2.2. Device fabrication and measurement

### 7.2.2.1. Fabrication and design

A single island SIN junction device was fabricated onto a  $\text{Si}_3\text{N}_4$  coated Si substrate using the fabrication process described in chapters 3.4 and 3.5. The area of each junction was  $100 \mu\text{m}^2$ . Pictures of the device are shown in figure 7.5. The presence of the superconducting Nb layer over the normal-metal in the wiring layer reduced the effects of ohmic heating in the normal-metal, and meant that the cooling region was in the normal-metal region directly above the junction. It was possible to bias 2 junctions in series, therefore, forming a symmetrical SINS'NIS device.

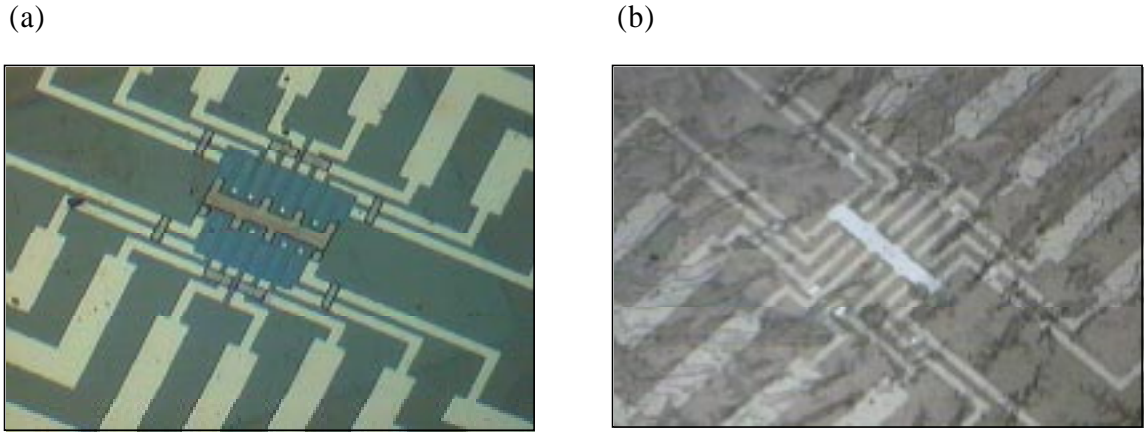


**Figure 7.5: Photographs of a single island SIN junction device sitting on a  $\text{Si}_3\text{N}_4$  membrane from (a) top view and (b) bottom view.**

### 7.2.2.2. Thermometry

To measure the change in  $T_e$  as a function of the device, injector-detector type experiments were performed. Current was injected ( $I_{INJ}$ ) through one junction (injector) while the  $I$ - $V$  characteristics of the sub-gap region of another junction (detector) were measured. Another junction (ground) was the electrical ground for the device. The change in the  $I$ - $V$  characteristics of the detector represents the change in the electronic temperature of the detector's normal-metal, as described in chapter 2.4.3.

The electronic temperature was calculated using the equation

$$\left. \frac{\sigma_{SIN}(V)}{\sigma_N} \right|_{V \rightarrow 0} = A_{SIN} \exp\left(-\frac{\Delta}{k_B T_e}\right) \quad (7.16)$$

where  $\sigma_{SIN}(V)$  is the conductance of the junction at bias  $V$ ,  $A_{SIN}$  is a constant that is dependent on the junction but is independent of temperature.  $\sigma_N$ , the normal state conductance of the junction, is measured from the  $I$ - $V$  characteristics of the junction at high bias. Measurements of  $\Delta$  were made using a similar design with Nb/Al/AlO<sub>x</sub>/Al/Nb (SIS) junctions and it was found to be 1.3 meV (Moseley 1997). Equation 7.16 assumes that the conductance due to leakage currents is negligible, which was found to be the case (Burnell 1998).

To calibrate the thermometry of each junction  $A_{SIN}$  was calculated from equation 7.16 using  $\sigma_{SIN}(V=0)$  and  $\sigma_N$  obtained at 4.2 K. This relatively high temperature was used because the electronic and bath temperatures should be strongly coupled to one another so that the electronic temperature is accurately known. The sample was then cooled to 0.35 K where the injector-detector measurements were made. Various configurations were used of the injector, detector and ground junctions. In order to reduce the effect of self-heating in the detector only the low bias  $I$ - $V$  characteristics of the detector were measured. First, current was injected through the injector junction, both below and above the injector's sub-gap, and the current ( $I_{INJ}$ ) and voltage ( $V_{INJ}$ ) across the injector was measured. Second,  $\sigma_{SIN}$  was calculated as a function of  $V_{INJ}$ , using a LabVIEW<sup>TM</sup> program, written by Dr. Gavin Burnell. Finally, using equation 7.16  $\sigma_{SIN}$  was converted to  $T_e$ .

### 7.2.3. Results and discussion

#### 7.2.3.1. $T_e$ versus $V_{INJ}$

For different injector, detector and ground configurations, graphs of  $T_e$  versus  $V_{INJ}$  are shown in figure 7.6. Each graph clearly shows that the heating processes dominate over the cooling process. As  $V_{INJ}$  was increased in the sub-gap bias range the rate of heating increased until, at above the sub-gap, it became relatively constant. This shows that it is the current passing through the injector that is responsible for the changes in temperature, and not due to self-heating in the detector junction. There is also evidence for self-heating in the detector. For each detector, the electronic temperature at  $V_{INJ}=0$  is around 3 K, far higher than the base temperature (0.35 K) and is discussed in the next section.

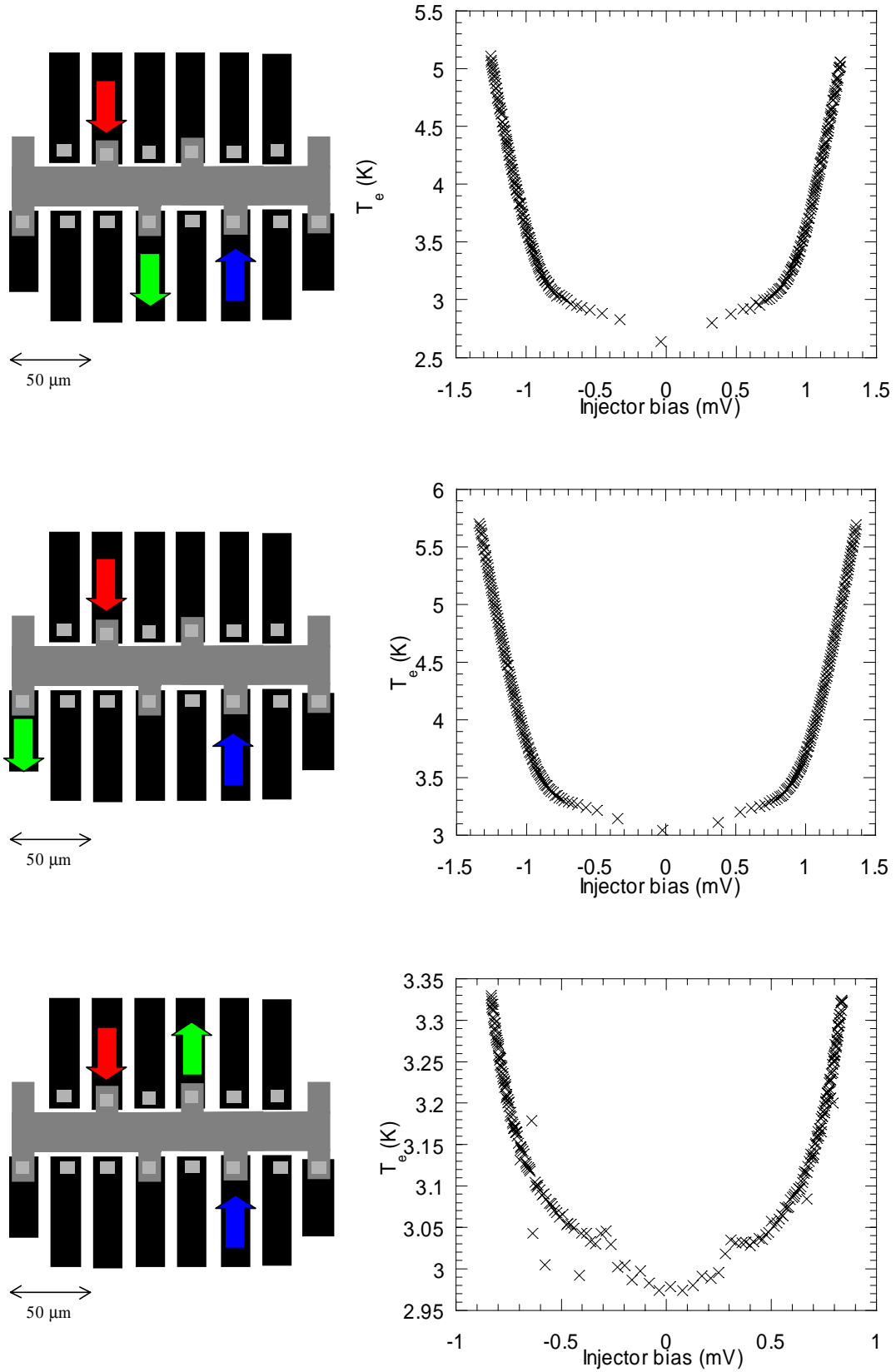
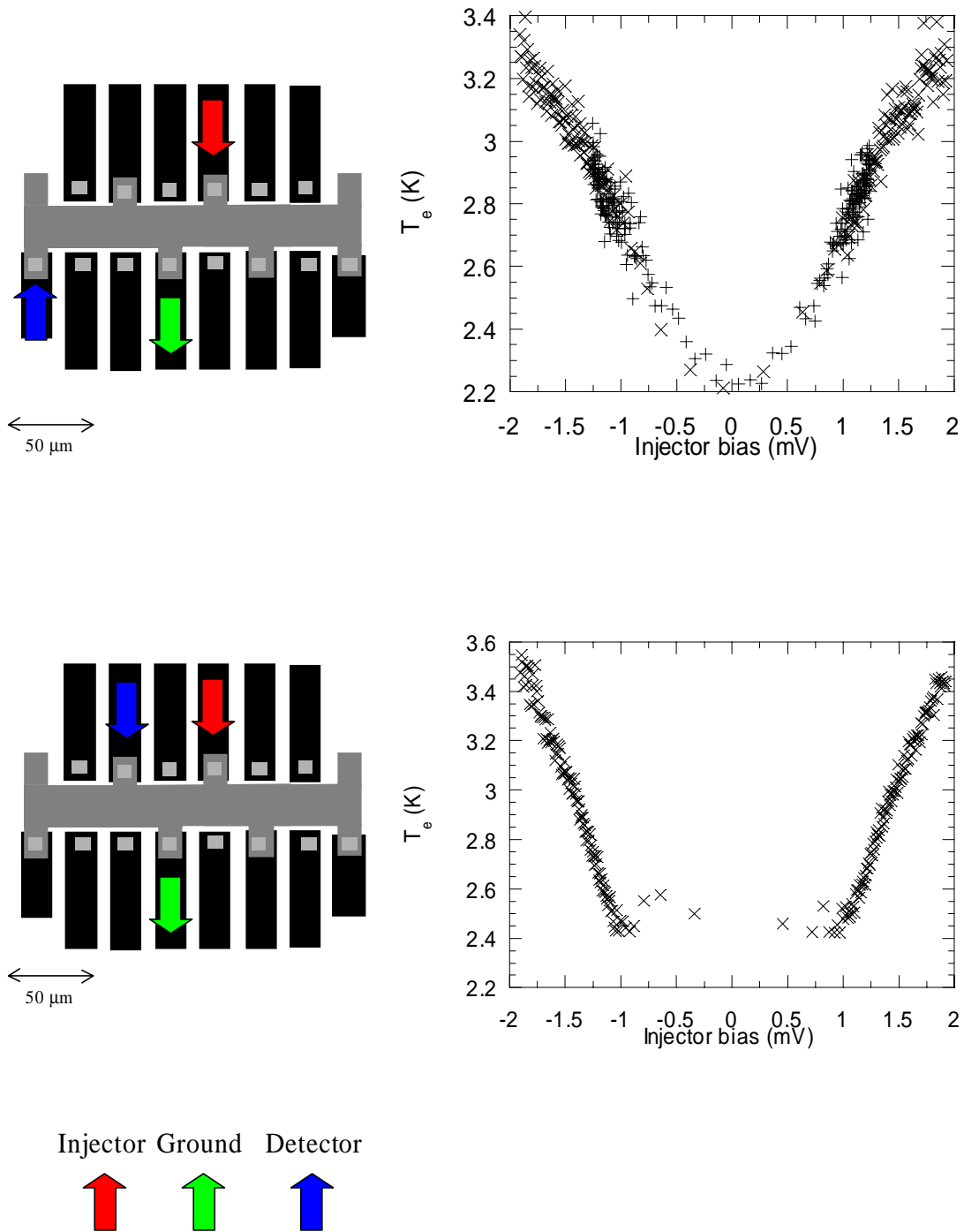


Figure continued overleaf



**Figure 7.6:** For different configurations of injector, detector and ground, the results from a single island SIN junctions device showing the electronic temperature ( $T_e$ ) of the detector junction versus the injector bias.

### 7.2.3.2. Discrepancy between $T_e$ and $T_b$ at $V_{INJ}=0$

The observation that the electronic temperature is far greater than the base temperature may be explained in three ways. First, equation 7.16, which converts  $\sigma_{SIN}(0)$  into  $T_e$ , assumes that the junction is ideal, which is not valid in this situation. Some examples of the poor assumptions used are:  $\Delta$  is constant at the tunnel barrier interface, which Burnell found was not true (Burnell 1998); the quasiparticle population in the normal-metal is described by a Fermi-Dirac function, which may not be true, given the low temperature and non-equilibrium state of the normal-metal. Second, the junction is self-heating due to quasiparticle back-tunneling and recombination around the electrode. Third, the effects of flux threading may heat the electrons and maintain them above  $T_b$ .

Burnell (Burnell 1998) also observed the same discrepancy between  $T_e$  and  $T_b$  in similar SIN junctions, fabricated on r-plane sapphire substrates, and  $T_e$  was found to be 1.8 K at  $T_b=0.35$  K. Burnell attributed this discrepancy to the effects of self-heating in the junction. This explanation is partly supported with the knowledge that  $\lambda_R$  is comparable to the length of the junction, 8  $\mu\text{m}$  (Burnell 1998). This means that quasiparticles in the superconductor's electrode can only move, at most, 8  $\mu\text{m}$  from the junction's interface before re-depositing their heat. The presence of the Nb/Al interface near the junction also reduces  $\lambda_R$  because of the smaller energy gap in Al compared to Nb and means quasiparticles can be trapped around the junction. Fisher *et al.* (Fisher 1999) were able to detect cooling in their junctions with similar areas because they used superconducting Al. Al has a greater quasiparticle recombination length than Nb (Brink 1996).

### 7.2.3.3. Comparison of $\sigma_{SIN}(0)$ with different substrates

In order to make a direct comparison of junctions with and without a membrane the same junctions were measured before the membrane was made. Figure 7.7 shows the  $I$ - $V$  characteristics at 0.35 K of the same junction with and without the membrane. It shows that  $\sigma_{SIN}(V)$  has changed. Further measurements showed that  $\sigma_N$  was unchanged, indicating that the junction was not damaged during the fabrication of the membrane.  $T_e$  was calculated for both cases, and was found to be 2.9 K when the bulk substrate was present, and 3.1 K when it was on the membrane. This clearly shows that the presence of a low thermal conductivity membrane increases the effects of self-heating in the junction; heat from the junction is transported less effectively away from the junction with the membrane. Thus the presence of

a membrane only exaggerates the dominant heating, or cooling, processes taking place in the device.

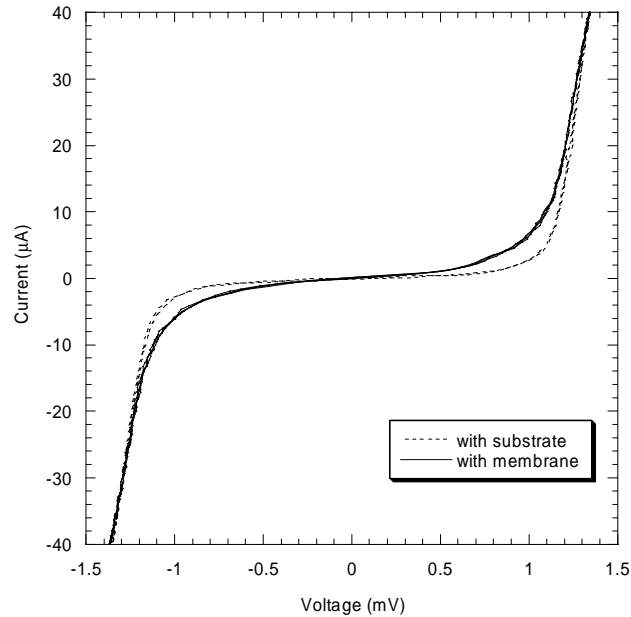


**Figure 7.7:** Comparison of the I-V characteristics at low bias of an SIN junction at 0.35 K sitting on a  $\text{Si}_3\text{N}_4$  membrane with a bulk substrate.

### 7.3. Thermal effects in SNS junction based devices

In this section an investigation is made of the thermal effects in SNS junction based devices. The heat flow in an SNS junction is discussed and compared with the work of Murpurgo *et al.* (Morpurgo 1998).

#### 7.3.1. Background

In recent years, there has been considerable progress in the manufacturing techniques of mesoscopic devices, and this has led to great advancements in the understanding of mesoscopic physics. One important development has been the greater appreciation of the role of Andreev reflection in proximitised normal-metal/superconductor interfaces. As described in chapter 2.5.5, Andreev reflection allows electrical flow across a superconductor/normal-metal interface with no heat dissipation. Experimentalists paid little attention, however, to the fact that the charge carriers in the normal-metal are reflected back

with the superconducting phase of the superconductor. Morpurgo *et al.* (Morpurgo 1997) was the first to show how the reflected phase charge carriers could be utilised to make an interferometer device. This involves two superconductors being in intimate contact with a normal-metal. Phase information from both superconductors pass through the normal-metal region. The distance traveled by the charge carriers in the normal-metal, between the two superconductors, is less than the inelastic electron scattering length,  $\ell_e$ . This means that the system can be treated as a ballistic one where Andreev bound energy states can form. These states change according to the phase difference between the two superconductors. The conductance of the normal-metal will, therefore, change as a function of the phase difference. Applying a magnetic field (typically 1-10 T) will change the phase difference, and produce oscillations in the conductance at a fixed bias. This effect is known as magnetoresistance.

Other recent discoveries associated with Andreev reflection include: reentrant proximity effect (Charlat 1996); sample specific conductivity (Hartog 1996); enhanced shot noise due to Andreev clusters (Dieleman 1997); and tunable superconductivity (Morpurgo 1998). It is the last discovery listed that is pursued here.

### 7.3.1.1. Hot electron tunable superconductivity in a SNS junction

Morpurgo *et al.* made a SNS Josephson junction where the supercurrent flow was regulated by the thermal temperature of the normal-metal. By injecting a normal current through the normal metal, the population of the electronic states in the normal-metal region of the junction was altered, resulting in a change in the supercurrent density. The theoretical details are given by Chang and Bagwell (Chang 1997), but a brief description is given here. The expression for  $I_C$  as a function of the superconducting phase difference,  $\phi$ , is

$$I_S(\phi) = I_{BS}(\phi) + I_{CONT}(\phi) \quad (7.17)$$

$I_{BS}$  is the contribution to the supercurrent given by discrete bound states whose energy, relative to  $E_F$  in the electrodes, is smaller than  $\Delta$ , whereas  $I_{CONT}$  is the contribution of the continuum of states at higher energy. The expressions for these two contributions are:

$$I_{BS}(\phi) = \sum_n I(E_n^+(\phi)p_n^+ + E_n^-(\phi)p_n^-) \quad (7.18)$$

$$I_{CONT}(\phi) = \left( \int_{-\infty}^{-\Delta} + \int_{\Delta}^{\infty} \right) I(E, \phi) p(E, \phi) dE \quad (7.19)$$

Here  $E_n^{+/-}(\phi)$  is the energy of the  $n$ th bound state carrying current in the positive/negative direction.  $IE_n^{+/-}$  is the contribution of these bound states to the supercurrent and  $p_n^{+/-}$  is their occupation probability. Similarly,  $I(E,\phi)$  is the net contribution of the continuum states having energy between  $E$  and  $E+dE$ , and  $p(E,\phi)$  is their occupation probability. Both equations 7.18 and 7.19 show how the supercurrent depends on the occupation of the electronic states.

Murpurgo *et al.* performed an experiment to prove this. They were able to attenuate the  $I_C$  of an SNS junction at 1.7 K as a function of an injected current into the normal-metal. The schematic of their set-up is shown in figure 7.8. It shows a Nb superconducting track containing a 190 nm break. A Au normal-metal track runs perpendicular to the superconducting track, and crosses at the break. This made it possible to inject normal current in the same region traversed by the superconductor. In order to make their device they used standard electron beam lithography and lift-off techniques. The motion of the electrons in the Au was considered to be diffusive ( $\ell_e=40$  nm < dimensions of Au track) so the Andreev energy states were not bound inside the junction. They emphasised that the non-equilibrium state of the electronic distribution, and not the fact that a normal current actually flowed through the junction, was relevant in controlling the supercurrent flow.

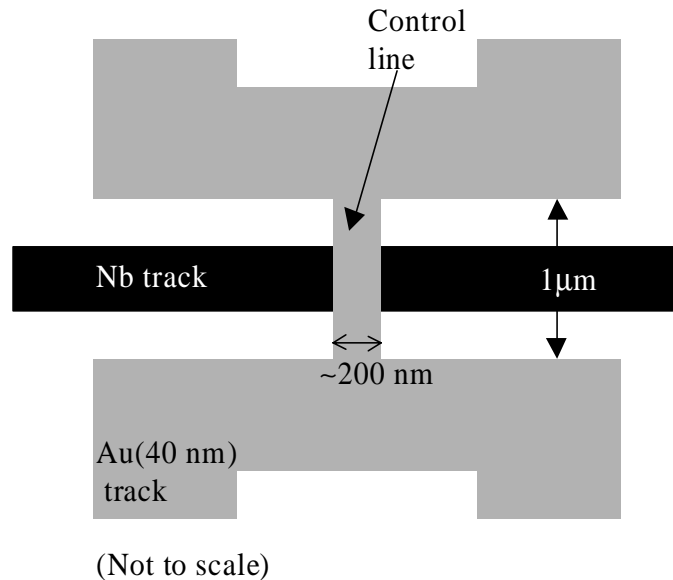


**Figure 7.8: Schematic plan-view of the hot-electron tunable device used by Murpurgo (Murpurgo, 1998).**

Experiments were designed by the author to confirm hot electron tunable superconductivity, and investigate the heat flow in similar devices made using a FIB instrument. All the junctions studied in this section were made with a depth equal to the thickness of the Nb layer (using the area dose method).

### 7.3.2. Heater directly and indirectly coupled to a junction

The first experiment was to investigate how the temperature of a junction varies as it is heated from a nearby normal-metal track, at a bath temperature of 4.2 K. Figure 7.9 shows an annotated schematic of the experiment. In the first configuration the heater, made by milling away the Nb layer from a nearby S/N track, was in electrical contact with the junction. Later, using the FIB instrument the normal-metal linking the junction to the heater was broken so that the normal-metal in both devices no longer made electrical contact. This allowed a comparison to be made of the junction being directly heated, through the normal-metal, and indirectly, through the substrate.

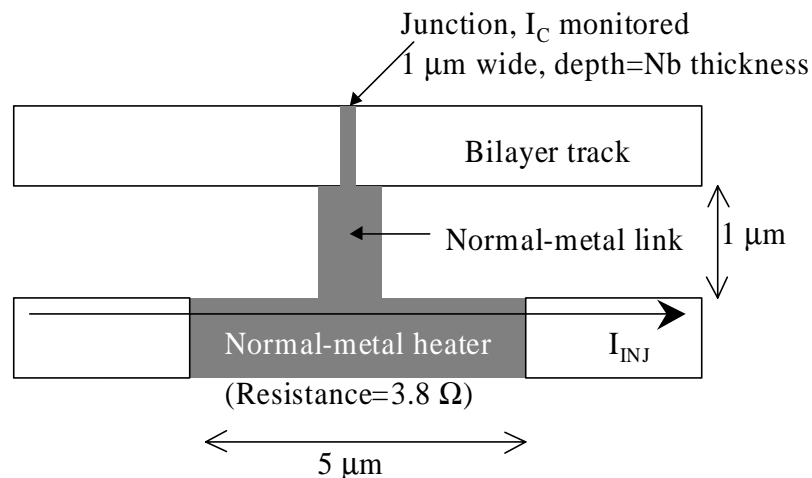


**Figure 7.9: Plan-view schematic diagram of the experimental set-up. The set-up was used to compare the relative heat contributions from the heater to a junction through the substrate with the heat contribution through the normal-metal link.**

Measurements were taken using the 4.2 K dip-probe, described in chapter 3.7.2. The  $I_C$  of the junction, in both the negative and positive current branches, was recorded as a function of the injector current ( $I_{INJ}$ ) through the heater wire. The  $I_C$  gives information about the temperature of the junction region. The exact relationship between  $I_C$  and  $T$  discussed in chapter 5.5 was complicated, and no conversion between  $I_{INJ}$  and  $T$  was attempted here. Figure 7.10 shows the results from both configurations, and clearly indicates that the

responses of the junction were different. For both configurations, the  $I_C$  at  $I_{INJ}=0 \mu\text{A}$  was equal showing that the junction was not damaged when the normal-metal link was broken.

At 4.2 K the electron and phonon systems of the thin-film and substrate are closely coupled, and the change between the responses reflects only the change in the thermal conductivity between the heater and the junction. In the first configuration, where the heater and junction are electrically linked,  $I_C$  decreases more rapidly as more current is injected in the normal-metal heater, than when the electrical link is broken, as in the second configuration. In the second configuration, heat can only be coupled to the junction through the substrate, rather than through the substrate and the normal-metal. The responses show, in both cases, that the thermal coupling between the heater and the junction is mediated most significantly by the substrate.

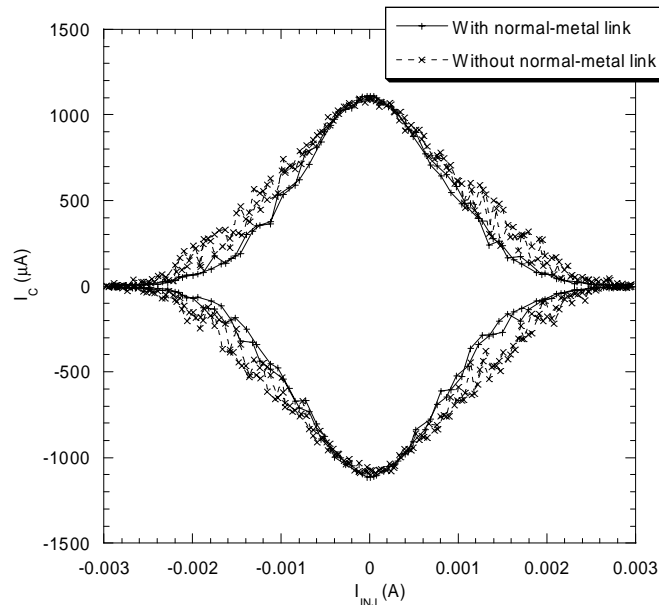


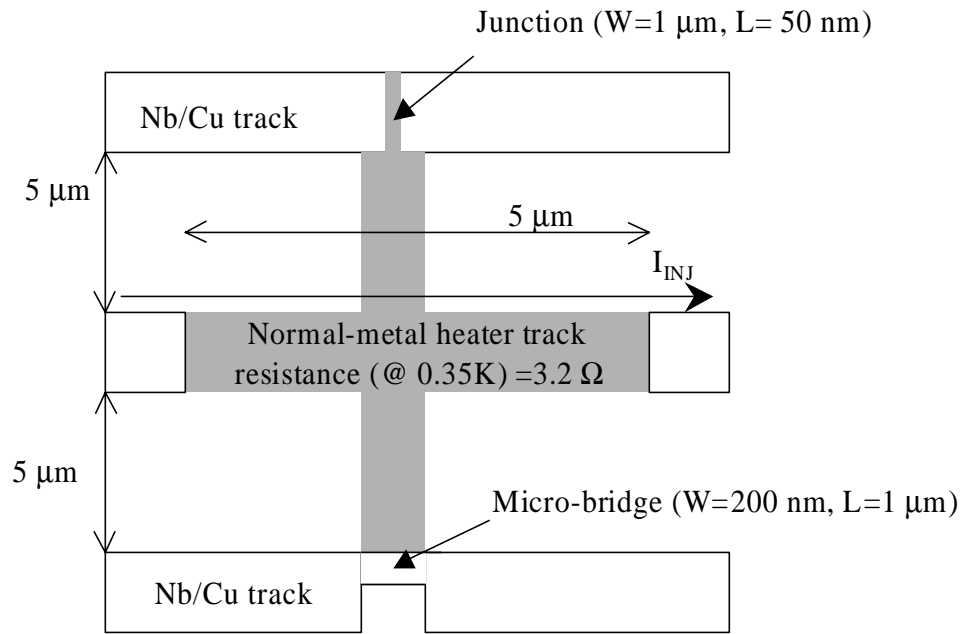
**Figure 7.10: Comparison of the behaviour of the critical current ( $I_C$ ) of a Nb/Cu/Nb junction at 4.2 K as current is injected through the heater ( $I_{INJ}$ ), when a normal-metal link connecting the junction to the heater is present and not present.**

### 7.3.3. Electron-phonon coupling at 0.35K

The previous experiment showed the expected result that the substrate's phonon and the normal-metal electronic and phonon systems were all closely coupled together at 4.2 K.

The aim of this experiment was to deduce whether the phonon and electronic systems were closely coupled at 0.35 K.

Comparing the responses of a junction and a micro-bridge to a heat source allows a comparison of the phonon and the electron temperatures to be made. The  $I_C(T)$  of a junction will depend upon the electronic temperature of the normal-metal and, similarly, the  $I_C(T)$  of a micro-bridge will depend upon the electronic temperature of the superconductor. If heat is generated in the normal-metal thin-film then the electronic temperature of the junction will be directly coupled to the heater via the normal-metal. The electronic temperature of the micro-bridge will be, however, indirectly coupled to the heater via the electron and phonon systems of the superconductor, and the substrate (Wellstood 1994). Consequently, the strength of the electron-phonon coupling can be measured. If there is only weak coupling between them then the relative temperature between the micro-bridge and junction will be different for the same amount of heat generated by the heater.



(Not to scale)

**Figure 7.11: Plan view schematic diagram of the experimental set-up. This was used to compare the responses of a microbridge with a Nb/Cu/Nb junction to a heat source in the normal-metal.**

The annotated schematic of the experiment is shown in figure 7.11. Using the FIB instrument a junction and a thin track of Nb/Cu forming a micro-bridge were made. They were both placed equidistant to a normal-metal heater track, also made using the FIB instrument. As in the previous experiment, the  $I_C$  of the junction and the micro-bridge were measured as a function of the injected current,  $I_{INJ}$ , through the heater track. In addition, the

$I_C$  of the micro-bridge and the junction were measured at different bath temperatures in the range 0.35-9 K, using the Heliox™ probe (described in chapter 3.7.3). The  $I_C(T)$  of the micro-bridge and the SNS junction are shown in figure 7.12. Thus the electronic temperature of the junction and micro-bridge can be measured and compared as a function of  $I_{INJ}$ . The results from the micro-bridge and junction are shown in figure 7.13. Table 7.1 shows the effective temperature at different injected currents for the junction and micro-bridge.

$ I_{INJ} $ (mA)	Effective temperature Junction ( $\pm 0.2$ K)	Effective temperature Micro-bridge ( $\pm 0.2$ K)
1	2.7	2.7
2	4.2	3.9
3	4.8	4.9

**Table 7.1: Comparison of the effective temperatures of a Nb/Cu/Nb junction with a micro-bridge as a current was injected ( $I_{INJ}$ ) through a common normal-metal heater.**

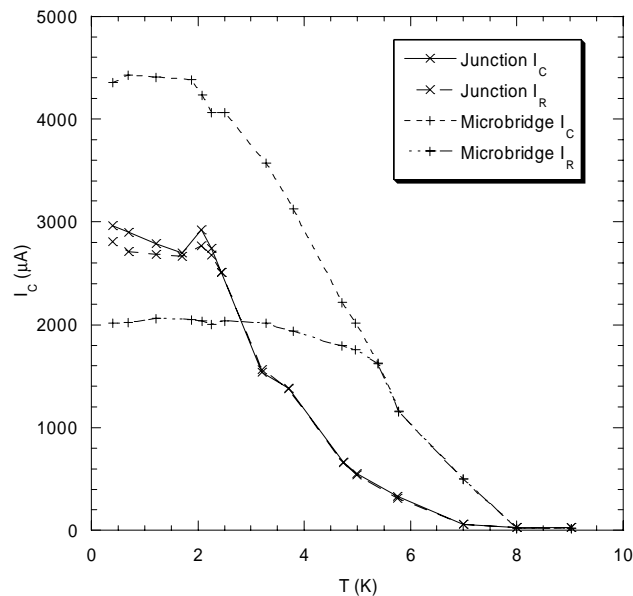


**Figure 7.12: The temperature ( $T$ ) dependencies of the critical current ( $I_C$ ) of the Nb/Cu/Nb junction and the microbridge used for the comparison. At low temperatures hysteresis is present so the return current ( $I_R$ ) at zero bias is also shown.**

The results show that the temperature of the SNS junction and the micro-bridge were not significantly different from one another. This means that the electronic temperature in

the normal-metal was the same as the electronic temperature in the superconductor. The only mechanism to conduct heat between the two electronic systems is through electron-phonon coupling and it is, consequently, concluded that the phonon and electron systems are closely coupled at  $T_b=0.35$  K.

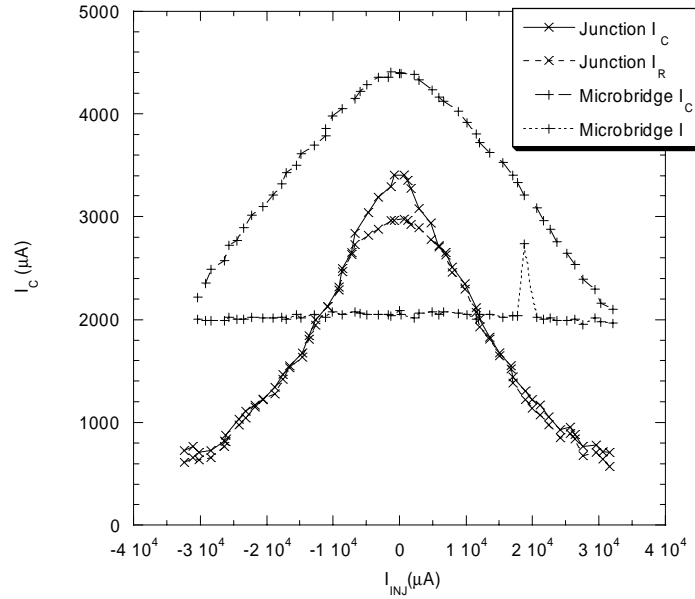


**Figure 7.13: The responses at 0.35 K of the critical current ( $I_C$ ) in a Nb/Cu/Nb junction and a microbridge to an injected current through the normal-metal heater ( $I_{INJ}$ ).**

#### 7.3.4. Heater and junction on a membrane

The two previous experiments have shown that there is strong coupling between the phonon and electron systems in the substrate and thin-film, even at  $T_b=0.35$  K. This experiment was designed to detach the electron and phonon systems of the thin-film from the substrate's. A heater and junction were made on a  $\text{Si}_3\text{N}_4$  membrane using a design similar to the one used in the first experiment. Again, the Heliox<sup>TM</sup> probe was used, and the experimental details are shown in figure 7.14. The  $I_C$  of the junction was recorded as a function of both the current passed through the heater track ( $I_{INJ}$ ) and the base temperature of the sample ( $T_b$ ) and are shown in figures 7.15 and 7.16, respectively. Three observations were made; first, the  $I$ - $V$  characteristics under 3 K were hysteretic; second, there was a lot of

irregularity in the  $I_C(T)$ , shown in figure 7.16; third, the  $I_C$  at  $T_b=0.35$  K was not the same as the  $I_C$  at  $I_{INJ}=0$ .

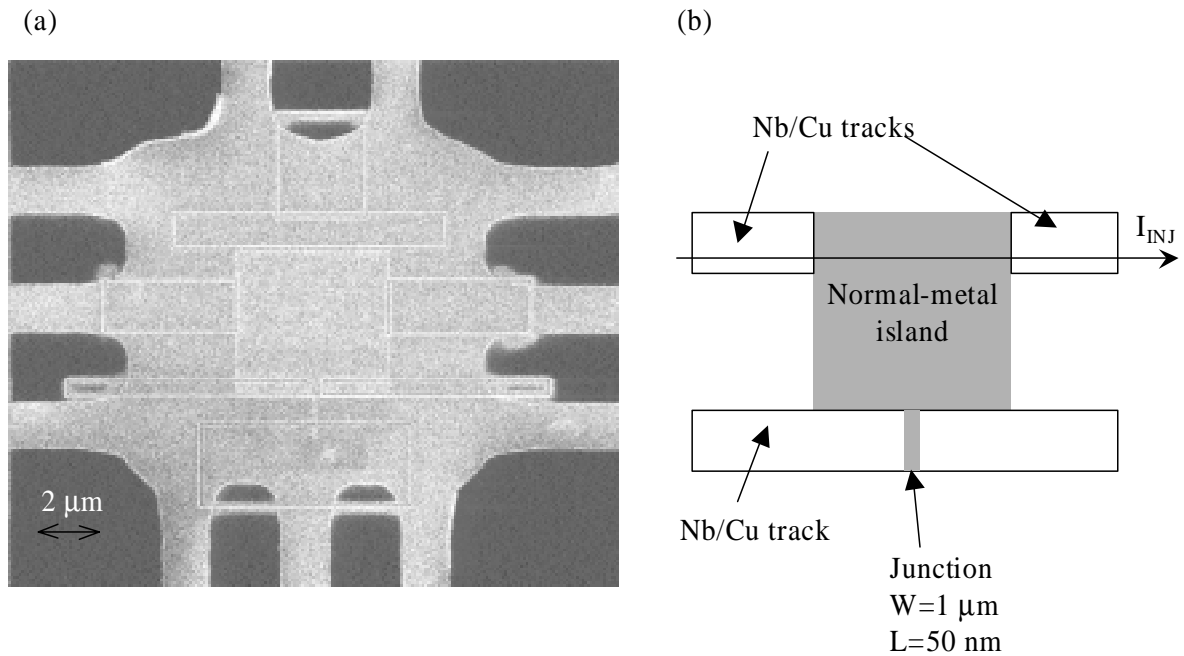


**Figure 7.14: Plan-view FIB image (a) and schematic (b) of the experimental set-up used to measure the response of a Nb/Cu/Nb junction sitting on a  $\text{Si}_3\text{N}_4$  membrane to heat generated in a normal-metal island.**

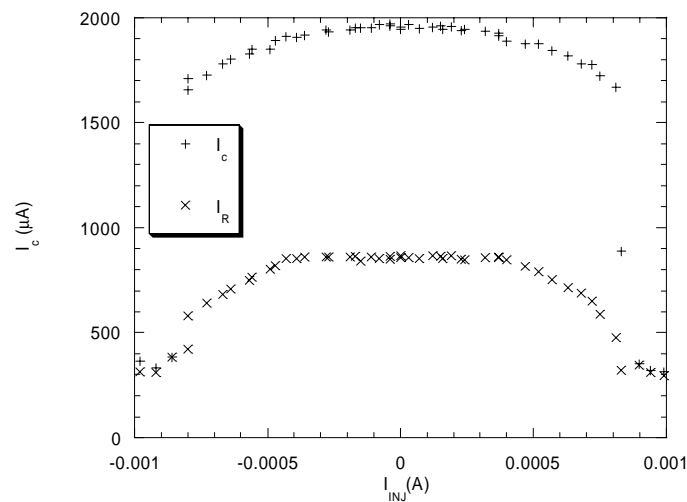


**Figure 7.15: The response at  $0.35 \text{ K}$  of the critical current ( $I_C$ ) in a Nb/Cu/Nb junction sitting on a  $\text{Si}_3\text{N}_4$  membrane to an injected current through a normal-metal island ( $I_{INJ}$ ).**

All of these observations are thought to be due to the effects of self-heating in the junction region. In chapter 5.5 there was strong evidence that self-heating caused

hysteresis in the  $I$ - $V$  characteristics. In this case, the substrate was not present to dissipate the heat away from the junction region, and, as seen in section 7.2, the presence of a silicon nitride membrane means that heat is not transferred as rapidly away from the device. Figure 7.17 compares the  $I$ - $V$  characteristics of the junction at the same base temperature but for different bias ranges. It shows that in the low bias case the  $I_C$  of the junction, and the return current, are higher than in the high bias case. In the high bias case, more heat will be dissipated in the junction region than in the low bias case. This means the actual temperature of the junction will be greater than  $T_b$  and will be higher than in the low bias case. The noise in the  $I_C(T)$  is, therefore, due to the different bias ranges used while recording the  $I$ - $V$  characteristics. Similarly, a reason why the  $I_C$  at  $I_{INJ}=0$  (figure 7.15) is lower than the  $I_C$  at  $T_b=0.35$  K (figure 7.16) is due to the different bias ranges used in the temperature and injection measurements. Another possible reason for this is the injection experiment was done over a period of several minutes so that heat may have built up in the device, and consequently further reduced  $I_C$ .

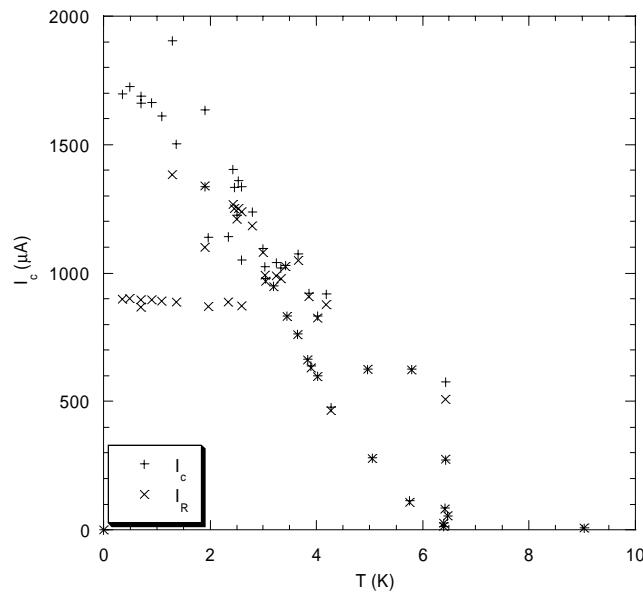


**Figure 7.16: The temperature dependence of the critical current ( $I_C$ ) of the Nb/Cu/Nb. At low temperatures hysteresis is present so the return current ( $I_R$ ) at zero bias is also shown.**

This explanation is supported by another observation, made during the experiments. When a sufficiently large current was passed through the heater track, or through the junction, the apparent  $I_C$  of the junction would decrease and then slowly return to its initial

value, presumably as heat was transported away from the junction region. When a  $\text{Si}_3\text{N}_4$  membrane was used this happened over a time scale of seconds, rather than tenths of seconds when the Si substrate was present.

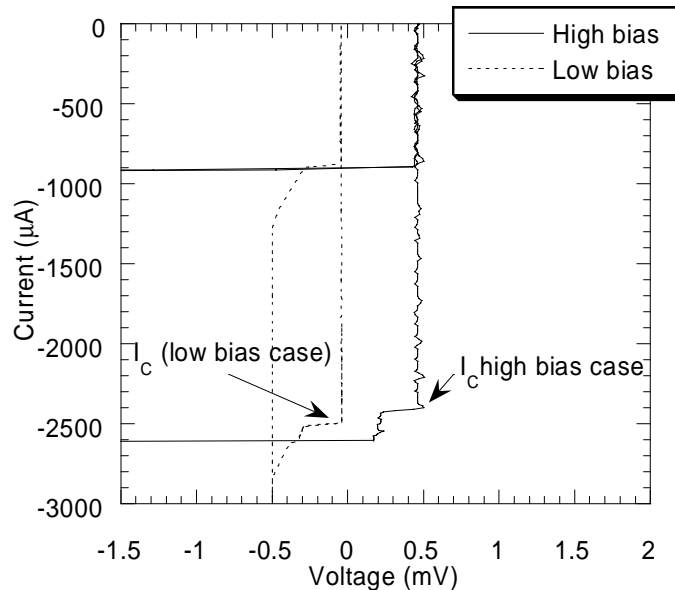


**Figure 7.17: Comparison of the I-V characteristics at 0.7 K of a Nb/Cu/Nb junction sitting on a  $\text{Si}_3\text{N}_4$  membrane at high bias ( $>2$  mV) with the I-V characteristics at low bias ( $<0.5$  mV). For clarity, the high bias case is offset by 0.5 mV. The comparison shows that the critical current ( $I_c$ ) decreases as the bias increases. This may be due to the effects of self-heating in the junction.**

The observation in the second experiment, where the electron and phonons systems appeared to be strongly coupled, can be explained in terms of a self-heating hot-spot in the junction and micro-bridge. This means that the electronic temperature is above 0.35 K, similar to the previous observation in the SIN junction based device.

### 7.3.5. Comparison with Morpurgo's hot electron tunable supercurrent device

The results from all the experiments show that the electron and phonons systems of the substrate, normal-metal and superconductor are strongly coupled, even at  $T_b=0.35\text{K}$ . This means that the modulation of the supercurrent is due to heating and not due to a direct modification of the electron population. Morpurgo argued that phonon heating could be neglected because the electrons injected in the control line from one of the side contacts, shown in figure 7.8, had a rather low probability to scatter inelastically with phonons before

reaching the opposite contact. The electron-phonon scattering time, in their Au normal-metal, was estimated to be 1 ns, meaning that the electron-phonon scattering length was several microns. The side contacts were assumed to act as heat sinks, and absorb the phonons. It is evident from the results reported here that the substrate, being also oxidised Si coated Si, will transfer the heat back into the junction region. The difference between the electron-phonon scattering length in Au, used in their experiments, and Cu, used here, is not thought to be significant due to their similar thermal properties. Although the junction's geometry used by Morpurgo is different to the one studied here, it is the same as the one used by Warlaumont (Warlaumont 1979). Warlaumont's junctions showed a similar  $I_C(T)$  behaviour to the junctions studied here, as reported in chapter 5.5. It is, therefore, probable that the effects of phonon heating in the junction region of Morpurgo's device have been under-estimated.

This explanation does assume, however, that the junctions studied here do not change in character at low temperatures. For junctions studied at 4.2 K, the behaviour is SNS like. At low temperatures the presence of the thin-layer of Nb, present in the junction trench, may mean that the junction becomes weak link-like (ScS). This would mean that the Josephson current flows through the Nb layer in the microbridge and the SNS junction, studied in section 7.3.3. This means that the conclusion reached that the electron-phonon coupling is strong at 0.35 K is invalid as this could not be observed by this experiment. Whether the junction character is SNS- or ScS-like at low temperatures is, however, a matter of speculation.

## 7.4. SNS junction dc-SQUIDS

In collaboration with the author, a new bolometer-based device has been devised and developed (Tarte 2000). It is based on a dc-SQUID design (described in chapter 6.2.2.4) and the schematic and its electrical circuit equivalent are shown in figure 7.18. The SQUID is *symmetrical*, i.e. the electrical properties of the junctions are the same. One junction in the SQUID is connected to a large normal-metal island. When an energetic particle is incident into the normal-metal island, the energy absorbed raises its electronic temperature. Heating the normal-metal will decrease the critical current of the junction that the normal-metal island is connected to, as shown in the previous section. The critical current of the other junction, which is not thermally anchored to the normal-metal island, will not change. Heating the normal-metal island will, therefore, introduce an *asymmetry* between the two

junctions. This has the effect of changing the flux within the SQUID loop and the effective bias point. The change in the bias point changes the current bypassing the SQUID down the resistively shunted feedback loop, which applies Additional Positive Feedback (APF) to the SQUID (Drung 1990).

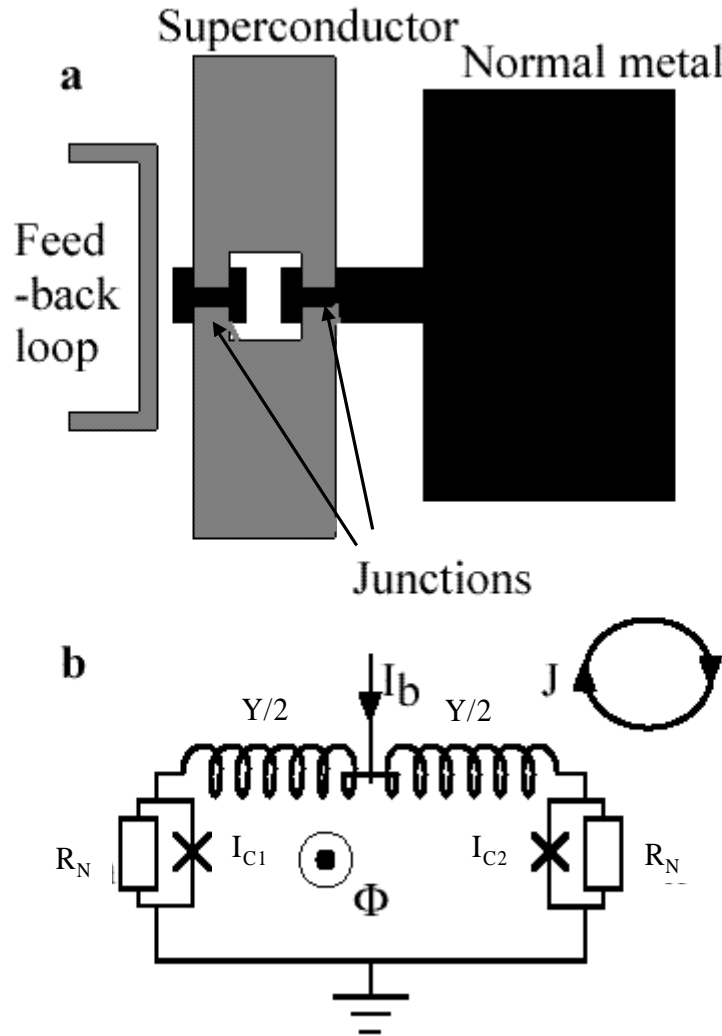


**Figure 7.18:** (a) Schematic diagram of the proposed Asymmetry Modulated SQUID (AMS). The junctions form the SQUID circuit; one of the two normal barriers is connected to a larger island which serves as an absorber in a design aimed at particle energy spectroscopy; a current flowing through the feedback loop modulates the flux in addition to changes in currents circulating the SQUID loop induced by a change in electron temperature of the absorber. (b) Circuit diagram for model of AMS devices based upon resistively shunted junctions. The circulating current ( $J$ ) is induced partly by flux applied to the loop and partly by the asymmetry between the critical currents.

In this section, developments towards making this device are discussed. Further design considerations are made that were not addressed in the original work. These have arisen due to the observations made in the previous sections of this chapter. Dc-SQUIDs have been made, using the FIB instrument, and comparisons of their theoretical to measured performances are made.

#### 7.4.1. Design Considerations

As found in the previous section, the increase in temperature in the normal-metal island will heat both junctions via the phonons in the substrate. It is essential, therefore, for the thermal link between the two junctions to be weak in order to maintain a temperature difference between the two junctions.

Two possible ways to reduce the thermal conductivity between the two junctions are discussed here. First, place the junction with the normal-metal island (detector) on a  $\text{Si}_3\text{N}_4$  membrane and place the other junction (reference) on the bulk substrate. This could be achieved using the conventional lithography techniques already used here. The disadvantage of this method is that the effects of self-heating generated by the junctions will be different. This is due to the different thermal properties between the substrate and membrane, meaning that the electronic temperatures of the two junctions in their stationary state would be different. Second, the junctions are both placed on a bulk substrate and the normal-metal island, still linked to the detector, is placed on a membrane. If the distance between the two junctions and the island are carefully controlled, the heat flow from the normal-metal island will be focussed onto the nearest junction.

In addition, two methods have been hypothesised that should reduce the effects of self-heating in the junctions, and consequently, reduce the electronic temperature in the junction's stationary state. First, reducing the  $I_C$ , by making deeper junction trenches, would reduce the heat dissipated into the normal-metal when the junction is in its finite-voltage state. Second, an additional layer of normal-metal could be placed over the superconducting layer, i.e. N/S/N trilayer, to act as a heat sink.

#### 7.4.2. Development work

The first step in building the device described above was to evaluate the performance of a dc-SQUID made by an FIB instrument. The fabrication method was based on the SNS junction method, described in chapter 4.2.3. First, a rectangular hole was made in the bilayer track, leaving a ring of bilayer track around the hole. Second, rectangular isolation cuts were

made on each side of the hole, to define the width of each junction. Third, the junctions were made, by milling a trench across the whole width of the track, to a depth equal to the thickness of the Nb layer, thus making two junctions with one trench. The last two steps were designed to increase the uniformity of the junctions, which would increase the responsiveness of the SQUID. A scanned image, taken by the FIB, and a schematic diagram of a completed device with the appropriate annotation are shown in figure 7.19.

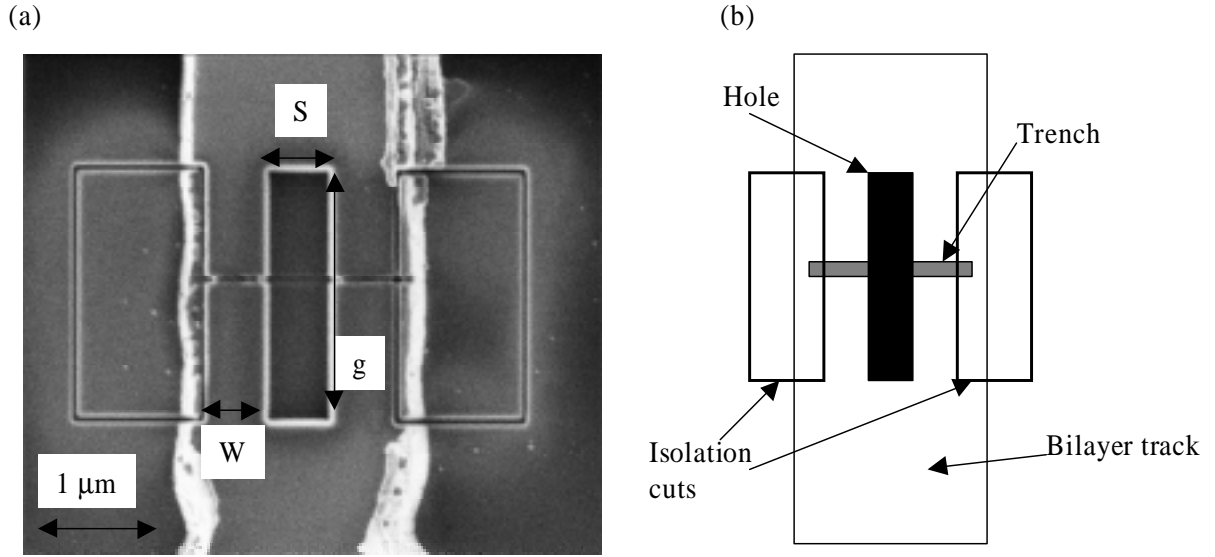


**Figure 7.19: FIB image (a) and schematic (b) plan-views of a dc-SQUID made using an FIB instrument.**

#### 7.4.2.1. dc-SQUID inductance

Enpuku *et al.* (Enpuku 1996) derived an equation for calculating the inductance,  $Y$ , of a rectangular thin-film dc-SQUID. The equation uses the dimensions of the dc-SQUID and  $\lambda_L$ . The equation has successfully calculated  $Y$  for many high-temperature superconductor-based planar dc-SQUIDs (Kang 1998).  $Y$  is the sum of the magnetic inductance ( $Y_M$ ) and the kinetic inductance ( $Y_K$ ) i.e.

$$Y = Y_M + Y_K \quad (7.20)$$

where

$$Y_M = \mu_0 g \frac{K_{(k)}}{K_{(k')}} \quad (7.21)$$

$$Y_K = \frac{2g\mu_0\lambda^2}{d_s w k^2 K_{(k')}} \left\{ \frac{w}{s} \ln \left[ \frac{4ws}{d_s(w+s)} \right] + \frac{w}{2w+s} \ln \left[ \frac{4w(2w+s)}{d_s(w+s)} \right] \right\} \quad (7.22)$$

and  $K_{(x)}$  is the complete elliptic integral of the first kind with a modulus  $k=s/(s+sw)$  and  $k'=(1-k^2)^{1/2}$ .

#### 7.4.2.2. Experiment, results, and discussion

A number of dc-SQUIDs, with different shaped holes, were patterned in Nb(75 nm)/Cu (70 nm) 2  $\mu\text{m}$  wide bilayer tracks. For each device their  $I$ - $V$  characteristics were measured in response to an applied triangular wave-shaped alternating magnetic field. Their voltage responses at a fixed current above the  $I_C$ , i.e.  $I > I_C$ , as a function of the alternating magnetic field were measured, producing a  $V(\phi, I)$  plot of the device. The  $V(\phi, I)$  plots of various devices are shown in figure 7.20.

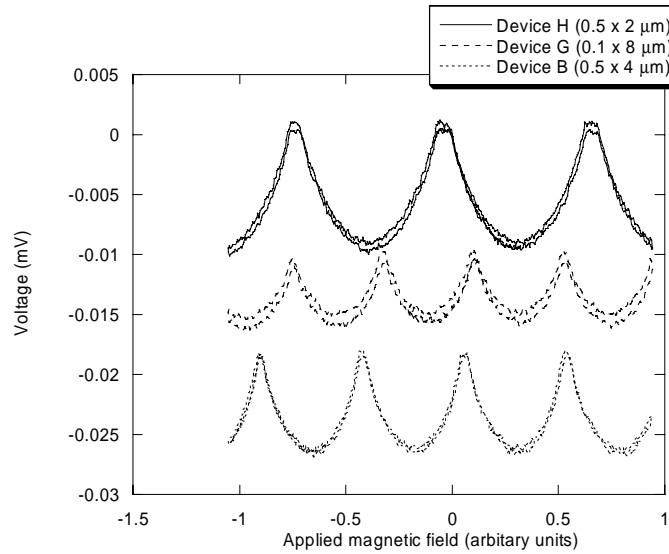


**Figure 7.20:** The voltage responses at a fixed current above the critical current as a function of the alternating magnetic field,  $V(\phi, I)$ , at 4.2 K of various SQUIDs made using an FIB instrument. For clarity, the responses are offset vertically from each other.

The  $I$ - $V$  characteristics of all the devices showed no significant spread in  $I_C$  between junctions in the same device. All the devices showed the expected sinusoidal-like character of  $V(\phi)$  as flux was added to, or removed from, the hole. This confirmed that the devices behaved as SQUIDS. From these results it was possible to calculate the effective area of the hole ( $A_{eff(x,y)}$ ) knowing that,

$$\Phi_0 = \delta B_z A_{eff(x,y)} \cdot \quad (7.23)$$

$\delta B_z$  is the change in magnetic field that is needed to add, or remove, a flux quantum into the hole. The inductance of each device was measured knowing that the relationship between the inductance and the maximum modulated voltage ( $V_{MAX}$ ) is

$$\frac{V_{MAX}}{\Phi_0} \approx \frac{R_N}{Y}. \quad (7.24)$$

For each device, the theoretical inductance, calculated from equation 7.20 and the geometrical area are compared to the apparent inductance and area, calculated from equations 7.23 and 7.24, respectively, and are shown in table 7.2.

JUNCTION ID (9633/1B)	HOLE AREA (S×g) ( $\mu\text{m}^2$ )	$A_{EFF(X,Y)}$ ( $\mu\text{m}^2$ )	THEORETICAL Y (pH)	MEASURED Y (pH)	$V_{MAX}$ ( $\mu\text{V}$ )
B	2 (0.5×4)	1	4.7	9.5	7
C	4 (0.5×8)	4	9.3	26	4
D	1.6 (0.2×0.8)	0.9	14	32	2
F	0.4 (0.1×12)	0.8	4.4	24	16
G	1.6 (0.1×8)	2	17	9.5	6
H	1 (0.5×2)	0.6	2.3	5.7	10

**Table 7.2: Comparison of the measured inductance and effective areas of the holes with the theoretical values.**

The table shows that  $A_{eff}$  and the geometrical areas greatly differ in most cases. Given the huge variation in the range, above and below the geometrical area value, of  $A_{eff}$  it is likely that this is due to experimental uncertainty rather than being due to any systematic differences. The differences between the theoretical and measured inductance, however, are significant. The measured inductance is almost always greater than the theoretical value. This is probably due to the assumption used for making equation 7.24 that the dynamic resistance, the resistance at the bias current, is the same as the junction resistance. To accurately measure the inductance of a SQUID the design would have to be modified. The SQUID would have to be current biased,  $I_B$ , at its most sensitive setting, i.e.  $\delta V \equiv V_{MAX}$ , while a current was injected from one side of the hole to the other, without passing through any of the junctions. The inductance could then be calculated by measuring the change in  $V$  as a function of  $I_{INJ}$ , i.e.  $Y = \Phi_0 / \delta I_{INJ}$ , where  $\delta I_{INJ}$  is the change in the injected current in order to add, or release, a quantum flux from the hole.

### 7.4.3. Closely spaced junctions dc-SQUID

A dc-SQUID where the junctions were placed closely together was made,  $L_{SPACE}=50$  nm, and a FIB scanned image of the device is shown in figure 7.21. The two junctions were partially covered by material ejected from nearby holes that were made after the junctions. The critical current of the thin-track leading to the junctions was smaller than the  $I_C$  of the junctions. This meant that no critical current modulation was seen until the applied magnetic field was strong enough to reduce  $I_C$  below the track's critical current.

The  $I_C$  (B) of the device was recorded and is shown in figure 7.22. It shows that the track's critical current was greater than the  $I_C$  of the junctions when magnetic fields of less than 15 mT were applied. For fields greater than 15 mT,  $I_C$  oscillated with changes in the magnetic field. The change in magnetic field for  $I_C$  to oscillate one complete wave cycle ( $\delta B$ ) was  $1.2 \pm 0.3$  mT. Substituting  $\delta B$  into equation 7.23, the effective area of the hole,  $A_{EFF}$ , was calculated to be  $1.7 \pm 0.4 \mu\text{m}^2$ . This compares favorably to the geometrical area of the hole being  $1.5 \mu\text{m}^2$ .

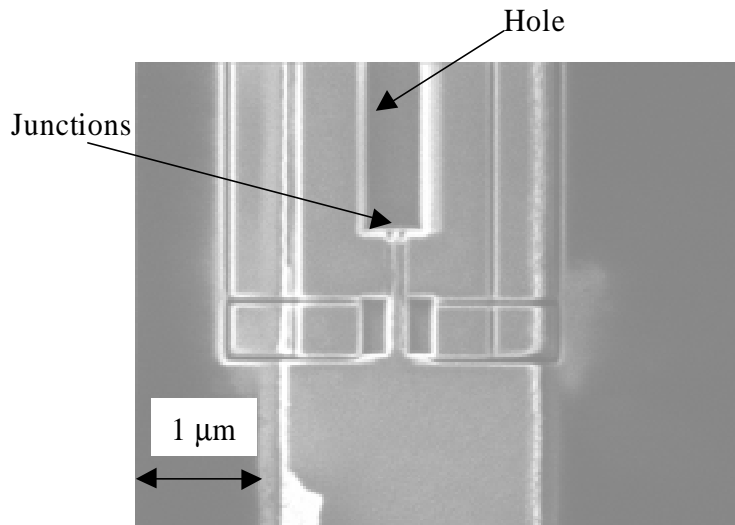


**Figure 7.21: FIB image of a dc-SQUID with closely spaced junctions made using an FIB instrument.**

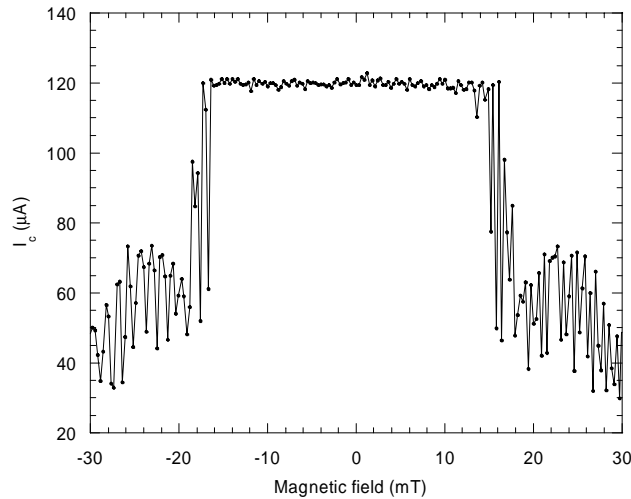


**Figure 7.22: The behaviour of the critical current with magnetic field of a SQUID with closely spaced junctions. The truncated central lobe is due to the low critical current of the central superconducting track linking both junctions. On either side of the central lobe, oscillations appear. The oscillations are due to quantum interference effects between the two junctions.**

#### 7.4.4. Conclusions

A novel dc-SQUID bolometer device was developed and dc-SQUIDs were successfully made using an FIB instrument. The electrical properties of the dc-SQUIDs were in rough agreement with the expected behaviour of conventional planar dc-SQUIDs. Using the FIB instrument it should be possible to investigate new designs of SQUIDs, that have previously been too difficult to make e.g. junction array SQUIDs. It may even be possible to tailor the voltage modulation response to an applied magnetic field, which is useful for electronic applications. The closely spaced junction dc-SQUID, briefly examined in the last section, should show interesting interference effects in its  $V(\Phi, I)$  responses due to the interactions between the quasiparticles in both junctions, described in chapter 6.2.2.2, but this was not investigated.

## 7.5. Summary

In summary, the thermal properties of several SNS- and SIN-junction based devices were studied. It was shown that at an operating temperature of 0.35 K the strength between the electron and phonon systems in the substrate and the thin-film was high. In both cases, this was due to the effects of self-heating in the junctions. Self-heating raised the local temperature of the phonons and electrons, significantly above the operating temperature. It was found that using a low thermally conductive membrane instead of a bulk substrate only exaggerates the heating, or cooling, processes taking place in both types of junctions. The effects of self-heating are, therefore, detrimental to the performance of both types of junctions for use in bolometer based devices. Several methods were suggested that would reduce the effects of self-heating.

Dc-SQUID devices were successfully fabricated, using the FIB instrument. Their electrical behaviour was in general agreement with their theoretical one, calculated from their geometrical dimensions and basic electrical properties.

## 7.6. References

- M. G. Blamire, E. C. G. Kirk, J. E. Evetts and T. M. Klapwijk (1991). "Extreme Critical-Temperature Enhancement Of Al By Tunneling In Nb/AlO<sub>x</sub>/Al/AlO<sub>x</sub>/Nb Tunnel-Junctions." *Physical Review Letters* **66**(2) 220.
- N. E. Booth and D. J. Goldie (1996). "Superconducting Particle Detectors." *Superconductor Science & Technology* **9**(7) 493.
- P. L. Brink, C. Patel, D. J. Goldie, N. E. Booth and G. L. Salmon (1996). "An appreciation of quasiparticle trapping and the proximity effect." *Nuclear Instruments and methods in physics research A* **370** 133.
- G. B. Burnell (1998). PhD Thesis "Quasiparticle and phonon transport in superconducting particle detectors." Department of Materials Science and Metallurgy. University of Cambridge.
- L. F. Chang and P. F. Bagwell (1997). "Control of Andreev-level occupation in a Josephson junction by a normal-metal probe." *Phys. Rev. B* **55** 12578.

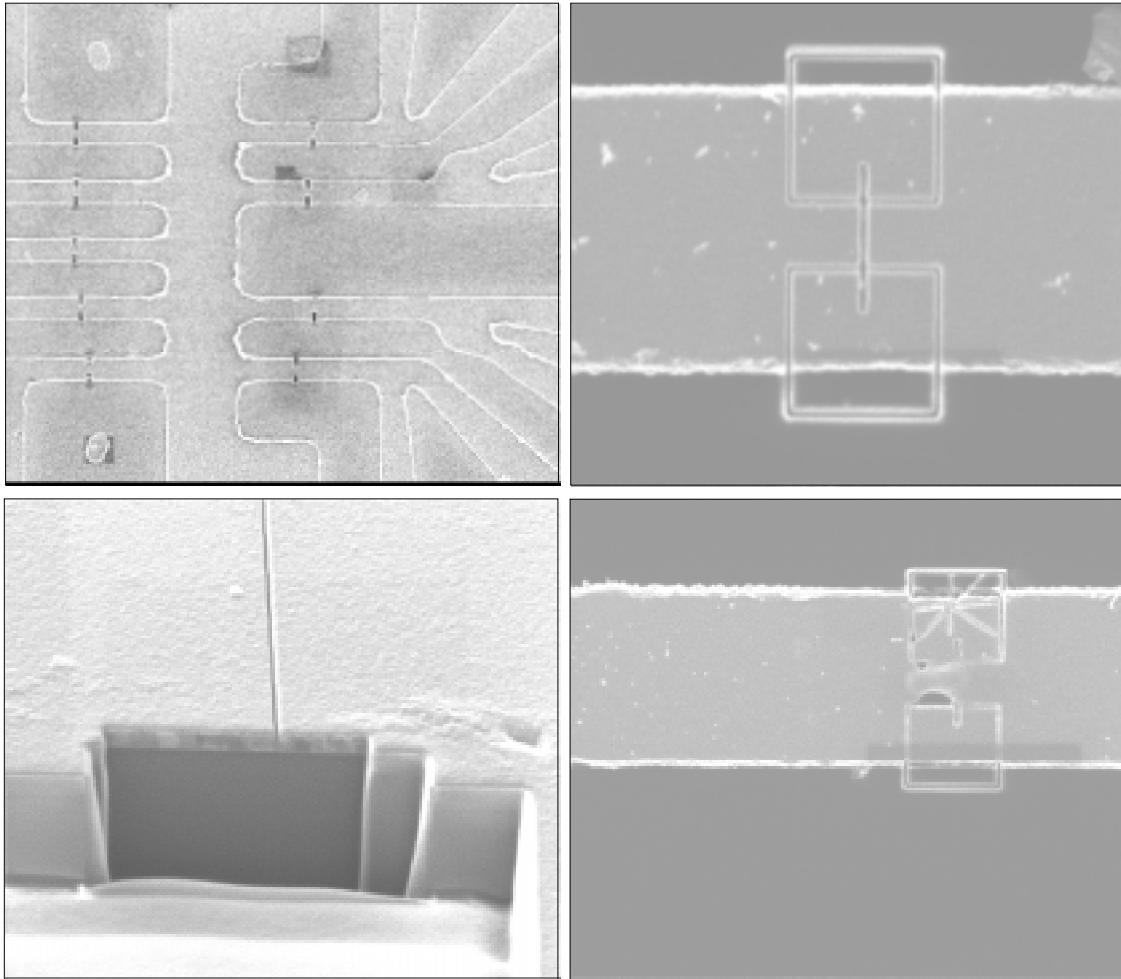
- P. Charlat, H. Courtois, P. Gandit, D. Mailly, A. F. Volkov and B. Pannetier (1996). "Resistive transport in a mesoscopic proximity superconductor." *Czechoslovak Journal of Physics* **46** 3107.
- P. Dieleman, H. G. Bukkems, T. M. Klapwijk, M. Schicke and K. H. Gundlach (1997). "Observation of Andreev reflection enhanced shot noise." *Phys. Rev. Letts.* **79** 3486.
- D. Drung, R. Cantor, M. Peters, H. J. Scheer and H. Koch (1990). *Appl. Phys. Lett.* **57** 406.
- H. L. Edwards, Q. Niu, G. A. Georgakis and A. L. Delozanne (1995). "Cryogenic Cooling Using Tunneling Structures With Sharp Energy Features." *Physical Review B-Condensed Matter* **52**(8) 5714.
- K. Enpuku, T. Maruo and T. Minotani (1996). "Effect of large dielectric constant of SrTiO<sub>3</sub> substrate on the characteristics of high T<sub>c</sub> dc superconducting quantum interference device." *J. Appl. Phys.* **80** 1207.
- P. A. Fisher, J. N. Ullom and M. Nahum (1997). "Progress on the Development of a 100mK Electronic Refrigerator Based on a Normal-Insulator-Superconductor Tunnel Junction." in the proceedings of ISEC '97, Berlin.
- P. A. Fisher, J. N. Ullom and M. Nahum (1998). "Development of a 100 milli-Kelvin electronic refrigerator based on a normal-insulator-superconductor tunnel junction." *Applied Superconductivity* **6** 325.
- P. A. Fisher, J. N. Ullom and M. Nahum (1999). "High-power on-chip microrefrigeration based on a normal-metal/insulator/superconductor tunnel junction." *Appl. Phys. Letts.* **74** 2705.
- S. G. d. Hartog, C. M. A. Kapteyn, B. J. v. Wees, T. M. Klapwijk, W. V. Graaf and G. Borghs (1996). "Sample-specific conductance fluctuations modulated by the superconducting phase." *Phys. Rev. Letts.* **76** 4592.
- J. Jochum, *et al.* (1997). "Modeling the Power Flow in NIS Junctions." in the proceedings of Low Temperature Detectors 7, Munich, Germany.
- B. Jug and Z. Trontelj (1997). "Some Aspects of Electronic Refrigerators Optimization." in the proceedings of ISEC '97, Berlin.
- D. J. Kang (1998). PhD Thesis "High TC dc SQUID Magnetometers." Department of Materials Science and Metallurgy, University of Cambridge.

- H. Kraus (1996). "Superconductive Bolometers and Calorimeters." *Superconductor Science & Technology* **9**(10) 827.
- M. M. Leivo and J. P. Pekola (1998). "Thermal characteristics of silicon nitride membranes at sub-Kelvin temperatures." *Appl. Phys. Letts.* **72** 1305.
- M. M. Leivo, J. P. Pekola and D. V. Averin (1996). "Efficient Peltier Refrigeration By a Pair Of Normal Metal/Insulator/Superconductor Junctions." *Applied Physics Letters* **68**(14) 1996.
- A. J. Manninen, M. M. Leivo and J. P. Pekola (1997). "Refrigeration of a dielectric membrane by superconductor/insulator/normal-metal/insulator/superconductor tunneling." *Applied Physics Letters* **70**(14) 1885.
- J. M. Martinis (1996). "Hot-Electron-Microcalorimeters With 0.25 Mm(2) Area." *Nuclear Instruments & Methods In Physics Research Section A- Accelerators Spectrometers Detectors and Associated Equipment* **370**(1) 171.
- A. F. Morpurgo, S. Holl, B. J. van Wees, T. M. Klapwijk and G. Borghs (1997). "Phase conjugated Andreev backscattering in two-dimensional ballistic cavities." *Phys. Rev. Lett.* **78** 2636.
- A. F. Morpurgo, T. M. Klapwijk and B. J. van Wees (1998). "Hot electron tunable supercurrent." *Appl. Phys. Lett.* **72** 966.
- R. W. Moseley (1997). CPGS report. "Superconducting tunnel junctions." Department of Materials Science and Metallurgy, University of Cambridge.
- M. Nahum, T. M. Eiles and J. M. Martinis (1994). "Electronic Microrefrigerator Based On a Normal-Insulator-Superconductor Tunnel Junction." *Applied Physics Letters* **65**(24) 3123.
- M. Nahum, J. M. Martinis and S. Castles (1993). "Hot-Electron Microcalorimeters For X-Ray and Phonon Detection." *Journal Of Low Temperature Physics* **93**(3-4) 733.
- J. P. Pekola, J. M. Kyynarainen, M. M. Leivo and A. J. Manninen (1999). "NIS chip refrigeration." *Cryogenics* **39** 653.
- E. J. Tarte, R. W. Moseley, M. R. Kolbl, W. E. Booij, G. Burnell and M. G. Blamire (2000). "Asymmetry Modulated SQUIDs." *Supercond. Sci. Technol* (to be published)
- J. N. Ullom, P. A. Fisher and M. Nahum (1998). "Magnetic field dependence of quasiparticle losses in a superconductor." *Appl. Phys. Letts.* **73** 2494.

J. Warlaumont, J. C. Brown and R. A. Buhrman (1979). "Response times and low voltage behavior of SNS microbridges." *Appl. Phys. Lett.* **34** 415.

F. C. Wellstood, C. Urbina and J. Clarke (1994). "Hot-Electron Effects In Metals." *Physical Review B-Condensed Matter* **49**(9) 5942.

# Chapter 8



'Flatlands'

*"Love art. Of all lies, it is the  
least untrue"*

Gustave Flaubert (1821-1880)

## Conclusions

## 8.1. Introduction

In this chapter, the contents of the work presented in the previous chapters will be summarised and the current state of low  $T_C$  junction technology discussed. The primary aim of the work was to show how a Focused Ion Beam (FIB) instrument could make reliable sub-micron scale planar-bridge SNS junctions and related devices. The secondary aims were: understanding the electrical behaviour of planar-bridge SNS junctions and related devices made using an FIB instrument and; understanding the thermal properties of SIN- and SNS-junction based devices for use in bolometer device applications. It will be shown that these aims were fulfilled.

## 8.2. Summary

Planar-bridge (Nb/Cu/Nb) SNS junctions can be reliably fabricated using a standard FIB instrument. This was demonstrated by the responses of junctions to microwaves and magnetic fields, the junctions display the appropriate Josephson behaviour demanded by current technological applications. In addition, the reproducibility in junction behaviour (the variation of critical current was approximately 10%) is the best so far observed for this type of junction. The SNS junction fabrication method has been successfully extended for making high-density SNS junction arrays, dc-SQUIDs, and related devices. Conventional theory satisfactorily explained the electrical behaviour of planar dc-SQUIDs.

A simple model has been devised to explain the normal-state resistance and critical current of a junction. The model was based on the geometry of a junction as defined by the FIB instrument and the film deposition. The model was mostly successful in qualitatively explaining many of the geometrical factors that affect the electrical properties of the junction. The major success of the model was to explain the  $I_C R_N$  product of a junction if the geometrical dimensions of the junction, the intrinsic interfacial resistance of the Superconductor/Normal-metal (S/N) bilayer, and the resistivity of the normal-metal were known.

The effective length of the normal region of a junction is longer than its geometrical length, as defined by the junction trench. The results obtained from the temperature and length dependencies of the critical current and normal-state resistance show that there is an additional 200 nm beyond the geometrical length. The normal region of the junction extends,

therefore, 100 nm into both sides of the S/N bilayer. The discrepancy between the geometrical length and the effective length is thought to be due to the diffusion of quasiparticles in the S/N region.

The study of junctions with varying widths shows that the effective width of a junction in the small limit is less than the geometrical one. This is the result of erosion by the ion beam during fabrication around the edges of the normal-metal in the junction.

The responses of the junctions to magnetic fields were found to be in agreement with the prediction of the planar junction model of Rosenthal *et al.* (Rosenthal 1991).

The variation of the normal-metal thickness study shows that the normal state resistance can be calculated using the geometrical model. The critical current stays constant, however, in the range studied ( $30 < d_N < 140$  nm). Recent work by co-workers using an improved fabrication method has shown, however, that the critical current varies with the normal-metal thickness, which supports the proximity effect explanation.

A model developed by Van Dover *et al.* (Vandover 1981) adequately explained the temperature dependence of the critical current of a junction. The temperature dependencies of hysteresis at both zero- and finite- voltages were also investigated in junctions sitting on a bulk substrate and a thermally insulating membrane. From these studies the effects of self-heating were found to be the cause of hysteresis.

Nb/Cu/Nb junction series arrays, made using an FIB instrument, were successfully manufactured. The reliability of the junctions forming small arrays was found to be similar to the reliability of single junctions. For large arrays, the spread in the electrical behaviour of the junctions forming the arrays increased. Improving the fabrication method should reduce the spread e.g. tailoring the FIB instrument's software for making junction arrays.

For the type of junction series array geometry studied, new observations have been made. The electrical properties of an array have been found to be dependent on the spacing of the junctions and the number of junctions in the array. For all the arrays studied, there was evidence of current redistribution between junctions. A semi-empirical model was made to explain the electrical behaviour of an array in terms of the changing order parameter and quasiparticle interference. For arrays where the spacing between junctions decreases below  $2\lambda_Q$ , the normal-state resistance decreases. Similarly, decreasing the junction spacing below  $2\xi_{ND}$  decreases the critical current. The semi-empirical model was only successful for predicting the trends in the junction spacing dependencies of the critical current and normal-state resistance. For arrays consisting of junctions with spacing below 100 nm, each array

behaved like a single junction. It was thought that this could be explained in terms of the changing nature of the order parameter in the array. It was proposed that this could be exploited to make a novel sensor based on switching a closely spaced junction array from a single junction to a multiple junction configuration. There was no evidence of mutual phase locking in the arrays, although it was believed that dc-injection locking may occur if the electrical behaviour of the junctions were made more uniform.

The thermal properties of several SNS- and SIN-junction based devices were studied. It was shown that at an operating temperature of 0.35 K the strength between the electron and phonon systems in the substrate and the thin-film was high. In both cases, this was due to the effects of self-heating. Self-heating raised the local temperature of the phonons and electrons significantly above the operating temperature. It was found that using a low thermally conductive membrane only exaggerated the heating, or cooling, processes taking place in both types of junctions. The effects of self-heating are, therefore, detrimental to the performance of both types of junctions for use in bolometer based devices. Several methods were suggested that would reduce the effects of self-heating, e.g. placing a heat-sink material around the junction.

### 8.3. Low $T_c$ junction technology

Currently, the development of low  $T_c$  junction technology is being driven by digital circuit needs. This means that the fabrication of low  $T_c$  junctions must be compatible with conventional semiconductor-based chip manufacturing processes. The only proven low  $T_c$  junction fabrication technique that has been scaled up for manufacturing processes uses stacked Nb/ $\text{AlO}_x$  (SIS) junction based technology.

The work presented here described the success of producing reliable SNS junctions and related Josephson based devices. The junctions exhibited excellent Josephson properties with large impedances, making them suitable for use in most applications, although only a preliminary study of the exact details of the electrical behaviour of the junctions was made.

For manufacturing junctions in digital circuits, the fabrication process must be scaled-up. At present, manufacturing devices using an FIB instrument is impractical. The time taken by the FIB instrument to make a device is too long. One way of reducing the time taken would be decrease the milling time. For this to be implemented however, problems relating to the control of the ion beam would need to be overcome. A better alternative is to use electron beam lithography and plasma etching techniques.

The successful use of an FIB instrument in making prototype mesoscopic devices has been demonstrated. Currently making a prototype mesoscopic device and the subsequent development work requires enormous effort. This is mainly because of the demands of photolithography. Typically designing and producing a suitable photographic mask takes weeks. In addition, aligning a mask onto a sample with sub-micron accuracy takes considerable skill. Much of this effort can be circumvented using an FIB instrument. The instrument is relatively easy to use and has excellent control over the dimensions and placing of a device (~10 nm). In conclusion, an FIB instrument has proven to be an invaluable tool for making prototype mesoscopic devices.

## 8.4. References

P. A. Rosenthal, M. R. Beasley, K. Char, M. S. Colclough and G. Zaharchuk (1991). "Flux focusing effects in planar thin-film grain-boundary Josephson junctions." *Appl. Phys. Lett.* **59** 3482.

R. B. Vandover, A. Delozanne and M. R. Beasley (1981). "Superconductor-Normal-Superconductor Microbridges - Fabrication, Electrical Behavior, and Modeling." *Journal Of Applied Physics* **52**(12) 7327.

## Appendix A: Glossary of terms

$\alpha_1, \alpha_2$	junction coupling constants
$\alpha_L$	Landau parameter
$\beta$	fraction of quasiparticle recombination heat power
$\beta_L$	Landau parameter
$\chi$	order parameter phase
$\Delta$	energy gap
$\Delta f$	frequency linewidth
$\Delta_{PN}(E)$	self-energy of the normal-metal
$\Delta_P$	pair potential
$\Delta_{PS}(E)$	self-energy of the superconductor
$\varepsilon_k$	excitation energy
$\Phi$	magnetic flux
$\Phi_0$	1 magnetic flux quantum ( $2.0679 \times 10^{-15}$ Wb)
$\Phi_{eff}$	effective potential
$\phi$	phase difference
$\phi_P$	Usadel parameter
$\Gamma_N$	McMillan energy
$\gamma_b, \gamma_m$	Golubov proximity effect parameters
$\kappa$	thermal conductivity
$\lambda$	BCS electron-phonon coupling strength
$\lambda_L$	London penetration depth
$\lambda_N$	BCS electron-phonon coupling strength
$\lambda_J$	Josephson penetration depth
$\lambda_Q$	quasiparticle diffusion length
$\lambda_R$	quasiparticle recombination length
$\mu_0$	permeability of free space ( $4\pi \times 10^{-7}$ Hm <sup>-1</sup> )
$\theta$	phase
$\rho$	electrical resistivity
$\rho_N$	electrical resistivity of normal-metal
$\rho_S$	electrical resistivity of superconductor
$\Sigma$	electron-phonon coupling constant
$\sigma$	Gaussian spread
$\sigma_L$	lateral spread
$\sigma_N$	normal state electrical conductance
$\sigma_{SIN}$	electrical conductivity
$\tau_E$	inelastic electron-phonon time
$\tau_{eff}$	time for electrons to travel across junction barrier
$\tau_J$	Josephson period time
$\tau_n$	electron tunnelling time
$\tau_Q$	quasiparticle charge relaxation time
$\tau_R$	quasiparticle recombination time
$\tau_S$	magnetic spin flip time
$\tau_T$	mean transition time
$\omega_C$	Debye frequency

$\omega_N$	Matsubara frequency
$\xi$	superconducting coherence length
$\xi_G$	Gor'kov length
$\xi_{NC}$	normal-metal clean limited coherence length
$\xi_{ND}$	normal-metal dirty limited coherence length
$\xi_{SC}$	superconductor clean limited coherence length
$\xi_{SD}$	superconductor dirty limited coherence length
$\Psi$	Cooper pair macroscopic wave function
$\psi$	Ginzburg-Landau order parameter
$\mathbf{A}$	vector potential
$A_{\text{EFF}}$	effective hole area
$A_{\text{SIN}}$	junction constant
$a$	thermal conductivity constant
$B$	applied magnetic field
$B$	fraction of $I_C$ reduction in a closely spaced array
$B_0$	interval between successive minima
$B_{\text{omod}}$	modified interval between successive minima
$C$	normalisation constant
$c^*, c$	BCS annihilation and creation operators
$D$	diffusion coefficient
$d'$	magnetic thickness
$d_{\text{dam}}$	thickness of a damaged layer
$d_{\text{mem}}$	membrane thickness
$d_N$	normal-metal thickness
$d_S$	superconductor thickness
$E_F$	Fermi energy
$E_k$	wavenumber energy
$e$	electronic charge ( $1.60 \times 10^{-19}$ C)
$F$	Green's function
$F_P$	Van Dover prefactor
$F(r)$	local density of the superconducting state
$f$	frequency
$f_k$	Fermi function
$f_S$	free energy density
$f_t$	fluctuating frequency
$G$	Green's function
$G_L$	Ginzburg-Landau free energy density
$G_{N0}$	Ginzburg-Landau free energy of the normal state
$g$	length of slit in a SQUID
$H$	Magnetic field strength
$\hbar$	reduced Planck's constant ( $1.0546 \times 10^{-34}$ Js)
$I_B$	bias current
$I_{BS}$	bound states current contribution
$I_C$	critical current
$I_{\text{CONT}}$	continuum states current contribution
$I_e$	ac current component
$I_H$	current to maintain a hot-spot
$I_{\text{INJ}}$	injected current
$I_Q$	quasiparticle current

$I_S$	supercurrent
$i$	imaginary number
$J_0$	critical current density of a junction
$J_S$	supercurrent density
$j$	integer
$K$	coupling constant
$K_0$	de Gennes kernel
$K_n^{-1}$	de Gennes decay length of the normal-metal
$\mathbf{k}$	wavenumber
$\mathbf{k}_F$	Fermi wavenumber
$k_B$	Boltzmann constant
$L$	geometrical junction length
$L_{eff}$	effective junction length
$L_{ISO}$	length of a rectangular isolating cut
$L_{SPACE}$	distance between junctions
$L_{TL}$	characteristic transmission length
$L_{TR}$	distance between outer Nb electrodes
$\ell_e$	electron mean free path
$M$	trench depth
$m$	mass of a charge carrier
$N_0$	density of states at the Fermi surface
$N_N$	normal-metal density of states
$N_S$	superconductor density of states
$n$	integer
$n_S$	local density of Cooper pairs
$P$	occupation probability
$P_{COND}$	heating power conducted through a membrane
$P_{ENV}$	heating power
$P_M$	microwave power
$P_N$	cooling power
$P_{OHM}$	Ohmic heating power
$P_{REF}$	refrigeration power
$P_S$	quasiparticle heat power
$p$	barrier transmission probability
$q_{ex}$	localised charge
$q_N$	normal-metal de Gennes characteristic length
$q_S$	superconducting de Gennes characteristic length
$R^*$	resistance area product
$R_\phi$	sheet resistance
$R_A$	probability of electron undergoing Andreev reflection
$R_{ARRAY}$	normal state resistance of an array
$R_d$	differential resistance at bias point
$R_{EFF}$	effective resistance
$R_G$	geometrical resistance
$R_N$	normal state resistance of a junction
$R_P$	resistance of a proximitised region
$R_S$	probability of electron undergoing specular reflection
$r$	radius
$S$	width of slit in a SQUID

$T_b$	environment temperature
$T_C$	critical temperature
$T_e$	electronic temperature
$T_{mem}$	membrane temperature
$T_{ph}$	phonon temperature
$t$	time, mill time
$t_{max}$	mill time for $I_C \rightarrow 0$
$t_{min}$	mill time for the superconducting layer to be removed
$U$	energy of wavefunction
$u^*$	effective chemical potential
$V$	voltage
$V_I$	BCS interaction potential constant
$V_{ol}$	volume
$V_{kk'}$	interaction potential
$V_{rad}$	voltage across a Josephson junction induced by e.m. radiation
$V_S$	single Shapiro step interval
$v_F$	Fermi velocity
$v_k^2$	pair occupation probability
$W$	width of junction electrode
$Y$	inductance
$Z$	junction impedance
$Z_e(\omega)$	shunt impedance
$Z_{input}$	FIB user inputted mill depth [ $\mu\text{m}$ ]

## **Appendix B: Conferences Attended and (Un)Published Papers**

### **Conferences Attended**

Condensed Matter and Materials Physics '97 Exeter, UK  
Institute of Physics superconductivity group conference '98 and '99 Birmingham, UK  
International Superconductive Electronics Conference '99 Berkeley, USA

### **Published Papers**

R.W. Moseley, W.E. Booij, E.J. Tarte, and M.G. Blamire (1999) "Direct writing of low T<sub>c</sub> superconductor-normal metal-superconductor junctions using a focused ion beam" *Applied Physics Letters*, **75** 262.

K.Y. Kim, W.E. Booij, R.W. Moseley, Z.H. Barber, M.G. Blamire, and J.E. Evetts (1999) "GMR multilayer device with ring type bridge structure" *IEEE Transactions on Magnetics*, **35** 3646.

R.W. Moseley, A.J. Bennett, W.E. Booij, E.J. Tarte, and M.G. Blamire (1999) "Fabrication of Josephson superconductor-normal metal-superconductor series arrays using a focused ion beam" *Superconductor Science and Technology*, **12** 871.

### **Unpublished Papers**

E.J. Tarte, R.W. Moseley, M.R. Kölbl, W.E. Booij, G. Burnell, and M.G. Blamire (2000) "Asymmetry modulated SQUIDS" to be published in *Superconductor Science and Technology*.

R.J. Kinsey, G. Burnell, R.W. Moseley, and M.G. Blamire (2000) "Active Control of Superconductivity through the Ferromagnetic Exchange Interaction" submitted to *Physics Review B*.